

INTERPRETATION AND CONTROL OF HELICAL PERTURBATIONS IN TOKAMAKS

C.V. Atanasiu, A. Moraru

National Institute for Lasers, Plasma and Radiation Physics, Bucharest, Romania

During the period July-December 2010, the common research between the **Mathematical Modelling for Fusion Plasmas Group of the National Institute for Lasers, Plasma and Radiation Physics (NILPRP)**, Magurele - Bucharest, Romania with the **Max-Planck - Institut für Plasmaphysik (IPP)**, Garching, Germany, and the **Association EURATOM-Hellenic Republic, University of Ioannina**, has been focalized on the following objective:

1 Provision of support to the advancement of the ITER Physics Basis

1.3 MHD stability and plasma control

Specific Objectives:

1. Resistive wall modes (RWMs) stabilization

The target of this research, made in common with IPP Garching, Tokamakphysics Department, is to advance the physics understanding of RWMs stability, including the dependence on plasma rotation, wall/plasma distance, and active feedback control, with the ultimate goal of achieving sustained operation at beta values close to the ideal-wall beta limit through passive and active stabilization of the RWMs. Such objective has its justification in the fact that the stabilization of RWM in ITER, where it is probably not possible to maintain a very fast plasma rotation is still an open problem.

We have continued our research on RWMs made in the first part of 2010, in the frame of the following *milestones*:

- ***M1 To start the adaptation of the software modules of our code for calculation of the wall response (for a real 3D geometry, with holes) to external kink mode perturbations in ASDEX Upgrade in the standard ITM form to be run on GATEWAY (TF-ITM: WP-10 -IMP12-T9)***

Due to the ITM request to use free mathematical libraries only, our mathematical subroutines from NAG and IMSL have been replaced with routines from free libraries, like NETLIB, QUADPACK, etc. Our codes have been run on the GATEWAY platform. It is to note that due to our poor experience in the field of adapting a code to the specific requests of the GATEWAY, we have cooperated and have to cooperate in a direct manner with our colleagues from IPP Garching, specialized in the field.

- ***M2 Defining of a new analytical model to describe the rotational stabilization of the RWM by coupling to a dissipative rational surface (TG-MHD: WP10-MHD-03-03)***

Up to now, we have used the Fitzpatrick seminal model [1] to describe different dissipation mechanisms, like anomalous plasma viscosity, charge-exchange with cold

neutrals, neoclassical flow-damping, sound-wave damping, etc. Unfortunately the results obtained with this model do not correspond to experimentally realistic timescales and plasma rotation values ($O(1\%) \Omega_A$) even it offers some useful information on plasma rotation influence on mode growth rate. Presently, this seems to be a general opinion. Considering the same standard large-aspect ratio, low β , circular cross-section tokamak plasma [2, 3], we have started the developing of an analytical model with a resonant resistive-visco-inertial layer inside of the plasma, more realistic than the Fitzpatrick model. A similar idea has been given by Finn [4]. This internal layer could correspond to a tearing or internal kink mode where we can provide sufficient expertise to treat the singularity of the perturbed flux function at the resonance surface [5].

To provide the physics within the resonant layer, we have used the layer theory of Porcelli [6] to analyze the non-ideal effects inside the resonant layer and have included resistivity and viscosity on the growth rate of the resonant layer. Thus, the cylindrical plasma, with a single resonant surface ($q(r_s)=m/n$), is considered ideal outside the resonant layer but with resistivity and viscosity at the rational surface r_s . The perturbed poloidal flux function $\psi(r)$, sufficiently far from r_s is described by the equation [5, 7]

$$\frac{1}{r} \frac{d}{dr} \left(r \frac{d\psi}{dr} \right) - \frac{m^2}{r^2} \psi - \frac{mj'}{rF} \psi = 0, \quad F = \frac{B_\theta}{r} (m - nq), \quad (2.1)$$

where $' \equiv d/dr$, j is the equilibrium current density, B and B_θ are the unperturbed toroidal and poloidal magnetic field. This equation has been drawn from equation given in Ref. [5] for the toroidal case, by considering a vanishing plasma pressure gradient. The solution of this equation is matched at the resonant surface and at the resistive wall $r=r_w$. Following Bondesson [7], we defined two solutions of this equation: $\psi_0(r)$, the solution with no wall and $\psi_\infty(r)$ the solution with a perfectly conducting wall of radius r_w . The linear combination of these two solutions gives the solution to the RWM problem

$$\psi = a\psi_0 + b\psi_\infty, \quad a = \text{const}, \quad b = \text{const}. \quad (2.2)$$

The boundary condition at r_w is

$$\Delta'_w = \frac{[\psi']_{r_w}}{\psi(r_w)} = \gamma\tau_w, \quad \text{with } [\psi'] = \psi'(r_{w+}) - \psi'(r_{w-}) \text{ and } \psi_0(r_w) = 1, \psi_\infty'(r_{w+}) = -\frac{1}{r_w} \quad (2.3)$$

where γ is the growth rate of the mode. Knowing that the outer solutions (practically, the magnetic vector potential) are continuous across the resonant layer, but present a jump in their first derivatives (the tangential magnetic field), one can use the well known ‘‘Delta prime’’ definition

$$\Delta'_s = \frac{[\psi']_{r_s}}{\psi(r_s)} = \frac{[\psi_0']_{r_s} + \gamma\tau_w [\psi_\infty']_{r_s}}{\psi_0(r_s) + \gamma\tau_w \psi_\infty(r_s)}, \quad (2.4)$$

and applying Newcomb theory [8], it results that the kink mode is unstable.

Eq. (2.1) is used outside the resonant layer and its solutions couple the kink mode to the resonant layer. For the resonant layer Porcelli’s model [6] has been used; he has analyzed the effects of resistivity, momentum and viscosity on the growth rate of the resonant layer. Considering a slab geometry around the resonance layer (such simplification is acceptable for the cylindrical geometry we considered), the Fourier transform of the non-ideal MHD equations is

$$\frac{d}{dk} \left(\frac{k^2}{1 + \delta_\eta^2 k^2} \frac{d\xi(k)}{dk} \right) - \delta_{in}^2 k^2 \xi(k) - \delta_\mu^4 k^4 \xi(k) = 0, \quad (2.5)$$

where,

$\xi(k)$ = Fourier transformed displacement,

$$\delta_{in}^2 = \lambda^2 = (\gamma \tau_A)^2, \quad \tau_A = \Omega_A^{-1} = \text{Alfvén time}, \quad \delta_\mu^4 = \varepsilon_\mu \lambda, \quad \delta_\eta^2 = \varepsilon_\eta / \lambda,$$

λ = the growth rate normalized by the Alfvén time τ_A ,

$\varepsilon_\mu = \nu_\mu \tau_A$ = the inverse of the viscous Reynolds number, normalized by τ_A ,

$\varepsilon_\eta = \nu_\eta \tau_A$ = the inverse of the resistive Reynolds number, normalized by τ_A ,

ν_μ = the rate of collisional transport of transverse ion momentum,

ν_η = the rate of collisional resistive diffusion of magnetic field.

The solution of Eq. (2.5) is

$$\Delta'_{layer}(\gamma) \square - \frac{r_s}{(r - r_s)^2} \frac{\xi(r)}{\xi'(r)} \Big|_{r \rightarrow r_s} \quad (2.6)$$

We have to match the outer solution (Eq. (2.3)) with the layer solution (Eq. (2.6)). In function of different plasma parameters, the response of the layer can be of the following types (after Porcelli):

- 1) Tearing or reconnection: when the resistivity is much greater than inertia and viscosity;
- 2) Ideal: when inertia is much greater than viscosity and resistivity;
- 3) Visco-resistive: when viscosity and resistivity are much greater than inertia;
- 4) Visco-ideal: when inertia and viscosity are much greater than resistivity.

From the matching of the outer and inner solution the known dispersion relation is obtained.

The rotation of the plasma can be introduced by considering stationary plasma with a rotating wall.

For the moment, the obtained results are not very conclusive on determining which of the above mentioned dissipation mechanisms is absolutely necessary for RWM stabilization. We have to continue our investigation by refining the inner solutions of Eq. (2.3).

These two milestones have been carried out in close collaboration with our colleagues from the Tokamak Physics Department of the Max-Planck-Institut für Plasmaphysik, Garching, Germany, during the mobility 15.11.10-15.12.10.

II. Flow stabilization on MHD equilibrium

- **M3 Evaluation of flow stabilization effects on ITER equilibrium states** (TG – MHD: WP10-MHD-03-03)

The goal of this task was to extend the generic linear static (no flow) equilibrium solutions, developed in Ref. [9] and applied to a realistic ASDEX Upgrade equilibria, to an ITER equilibria with sheared flow parallel to the magnetic field. In particular, to apply

the obtained solutions plasmas with ITER shaping, poloidal beta, poloidal current, safety factor on axis, internal inductance and accessible flows with Alfvén Mach numbers on the order of 0.01. The potential stabilizing effect of the flow has been investigated by applying a sufficient condition for linear stability of equilibria with parallel flow.

3.1 Generalized Grad-Shafranov equation

The MHD equilibrium states of an axisymmetric magnetized plasma with incompressible flows parallel to the magnetic field are governed by the generalized Grad-Shafranov equation which in dimensionless form reads [10]-[12]

$$(1-M^2)\Delta^*\Psi - \frac{1}{2}(M^2)'|\nabla\Psi|^2 + \frac{1}{2}\left(\frac{X^2}{1-M^2}\right)' + R^2P_s' = 0 \quad (3.1)$$

along with the Bernoulli relation for the pressure

$$P = P_s(\Psi) - \rho \frac{v^2}{2} \quad (3.2)$$

Here, (z, R, φ) are normalized cylindrical coordinates. The quantities are normalized with respect to the geometric center of the configuration, as follows

$$\bar{R} = R/R_0, \bar{z} = z/R_0, \tilde{u} = u/(B_0 R_0^2), \bar{\rho} = \rho/\rho_0, \bar{P} = P/(B_0^2/\mu_0), \\ \bar{B} = \bar{B}/B_0, \bar{j} = \bar{j}/(B_0/(\mu_0 R_0)), \bar{v} = \bar{v}/v_{A0}, v_{A0} = B_0/\sqrt{\mu_0 \rho_0}.$$

and, for simplicity the tilde was dropped. z corresponds to the axis of symmetry; the function $\Psi(R, z)$ labels the magnetic surfaces; $M(\Psi)$ is the Mach function of the poloidal velocity with respect to the poloidal-magnetic-field Alfvén velocity; $X(\Psi)$ relates to the toroidal magnetic field; for vanishing flow the surface function $P_s(\Psi)$ coincides with the pressure; v is the modulus of the parallel velocity ($v^2 = M^2 B^2$); $\Delta^* = R^2 \nabla \cdot (\nabla/R^2)$, and the prime denotes a derivative with respect to Ψ . Eq. (1) can be simplified by the transformation

$$u(\Psi) = \int_0^\Psi [1 - M^2(g)]^{1/2} dg, \quad (3.3)$$

which reduces (1) to

$$\Delta^* u + \frac{1}{2} \frac{d}{du} \left(\frac{X^2}{1-M^2} \right) + R^2 \frac{dP_s}{du} = 0 \quad (3.4)$$

Note that (3.4) is free of a quadratic term as $|\text{gradu}|^2$ is identical in form with the (quasistatic) Grad-Shafranov equation. Thus, for each choice of the free surface functions $X^2/(1-M^2)$ and P_s , (3.4) is fully determined and can be solved when the boundary condition for u is given. Note that any solution is valid for arbitrary Mach functions $M(u)$ and densities $\rho(u)$. The transformation (3.3) does not affect the magnetic surfaces, it just relabels them. Also, once a solution of (3.4) is found, the equilibrium can be completely

constructed in the u -space; in particular, the magnetic field, velocity, current density, and pressure can be determined by the relations:

$$\bar{\mathbf{B}} = \frac{X}{1-M^2} \nabla\phi + \frac{1}{\sqrt{1-M^2}} \nabla\phi \times \nabla u, \quad (3.5)$$

$$\bar{\mathbf{v}} = \frac{M}{\sqrt{\rho}} \bar{\mathbf{B}}, \quad (M = \pm\sqrt{M^2}), \quad (3.6)$$

$$\bar{\mathbf{j}} = \frac{1}{\sqrt{1-M^2}} \left[\Delta^* u + \frac{1}{2(1-M^2)} \frac{dM^2}{du} |\nabla u|^2 \right] \nabla\phi + \frac{d}{du} \left(\frac{X}{1-M^2} \right) \nabla\phi \times \nabla u \quad (3.7)$$

$$P = P_s(u) - \frac{1}{2} M^2 B^2. \quad (3.8)$$

3.2 The sufficient condition for linear stability

The condition states that a general steady state of a plasma of constant density and incompressible flow parallel to \mathbf{B} is linearly stable to small three-dimensional perturbations if the flow is sub-Alfvénic ($M^2 < 1$) and $A \geq 0$ [12]. In the u -space for axisymmetric equilibria, A assumes the form

$$A = A_1 + A_2 + A_3 + A_4, \quad (3.9)$$

$$A_1 = -(\bar{\mathbf{j}} \times \nabla u)^2, \quad (3.10)$$

$$A_2 = (\bar{\mathbf{j}} \times \nabla u) \cdot (\nabla u \cdot \nabla) \bar{\mathbf{B}}, \quad (3.11)$$

$$A_3 = -\frac{1}{2} \frac{dM^2}{du} (1-M^2)^{-1} |\nabla u|^2 \nabla u \cdot \frac{\nabla B^2}{2}, \quad (3.12)$$

$$A_4 = -\frac{1}{2} \frac{dM^2}{du} (1-M^2)^{-3/2} |\nabla u|^4 g, \quad (3.13)$$

$$g = (1-M^2)^{-1/2} \left(\frac{dP_s}{du} - \frac{dM^2}{du} \frac{B^2}{2} \right), \quad (3.14)$$

and \mathbf{B} and \mathbf{j} as given by (3.5) and (3.7).

For the present stage of our research, we did not find a stabilising effect of the flow and have to continue our investigation.

This work has been carried out in close collaboration with Dr. G.N. Throumoulopoulos from the Association EURATOM-Hellenic Republic, University of Ioannina.

References

- [1] R. Fitzpatrick, Phys. Plasmas **9**, 3459 (2002).
- [2] C.V. Atanasiu, I.G. Miron, "An analytical model for resistive wall modes stabilization", 11th European Fusion Theory Conference, 26-28 September 2005, Aix-en-Provence, France.
- [3] C.V. Atanasiu, I.G. Miron, "A model for resistive wall mode control", EPS30 (P5.157), Rome, Italy, 19-23 June 2006.

- [4] J.M. Finn, Phys. Plasmas **2**, 198 (1995).
- [5] C. V. Atanasiu, S. Günter, K. Lackner, A. Moraru, L. E. Zakharov, A. A. Subbotin, Phys. Plasmas **11**, 5580 (2004).
- [6] F. Porcelli, Phys. Fluids **30**, 1734 (1987).
- [7] A. Bondeson, H.X. Xie, Phys. Fluids **B1**, 2081 (1989).
- [8] W.A. Newcomb, Ann. Phys. **10**, 232 (1960).
- [9] C. V. Atanasiu, S. Günter, K. Lackner, I.G. Miron, Phys. Plasmas **11**, 3510 (2004).
- [10] H. Tasso, G. N. Throumoulopoulos, Phys. Plasmas **5**, 2378 (1998).
- [11] Ch. Simintzis, G. N. Throumoulopoulos, G. Pantis, H. Tasso, Phys. Plasmas **8**, 2641 (2001).
- [12] G. N. Throumoulopoulos, H. Tasso, G. Poulipoulis, J. Plasma Phys. **74**, 327 (2008).
- [13] G. N. Throumoulopoulos, H. Tasso, Phys. Plasmas **14**, 122104 (2007).
- [14] J. Adamek, C. Angioni, G. Antar, C.V. Atanasiu, M. Balden, W. Becker, Review of Scientific Instruments, **81**, 3, 033507 (2010).

Dr. C.V. Atanasiu

National Institute of Laser,
Plasma and Radiation Physics

Scientific Report
To the Contract 1EU/08.08.2008

PROJECT BS_2: Stable organized motion, coherent structures and turbulence in tokamak plasmas

[Project coordinator: Florin SPINEANU, Plasma Theory Group, National Institute for Laser, Plasma and Radiation Physics]

Florin Spineanu, Vlad Madalina, Daniela Nendrean

• EFDA 2010 Work Programme Task Agreement TGS-02 : WP10-TRA-01-04 (L - H transition physics)

Main objective:

Quasi-coherent modes and the stationary state of the Edge Localized Modes.

Milestone:

Stationary parallel dynamics and saturation of the filaments generated in strong Kelvin-Helmholtz events in the H-mode regime

1 Introduction

The H-mode is by necessity the stationary regime of the tokamak working as a reactor, due to the lower rate of loss of the energy contained in plasma. This H-mode is characterised by the presence of a layer of poloidally rotating plasma. The layer is close to the plasma edge, at the last closed magnetic surface. For very general reasons, the layer of strongly sheared poloidal rotation must be accompanied by a strong concentration of current density. This is due to the fact that coincidence of vorticity and current density maxima is a state of lower energy for the plasma. In addition, there are local reasons: the gradients of the density and temperature in the "pedestal" necessitate a current density that can ensure the equilibrium relation $\mathbf{j} \times \mathbf{B} = \nabla p$. The values that have been determined experimentally are high and cannot be justified by reasons related to the neoclassical component (bootstrap, See DIII-D experiments of Burrell).

In the first part of this work, reported previously, it has been shown that the plasma evolves to the break-up of the layer with strong concentration of the density, vorticity and current density into quasi-singular structures (filaments). This evolution is purely growing in an axisymmetric geometry and is governed by an universal instability of the same type as the Chaplygin gas with anomalous polytropic. The break-up of the current layer and formation

of filaments takes place on very short time scales, governed by the Alfvén speed in the direction of the layer (transversal on \mathbf{B}). This is a fast transient process which in axisymmetry is only limited by the generation of the singular filaments. The parallel dynamics is arbitrary, as long as the condition $v_z^{elect} \gg v_{th}^{elect}$ is fulfilled.

However the parallel dynamics is inhibited by the same mechanism which damps the poloidal rotation in tokamak, the *magnetic pumping*. The fast increase of the current and of the flow velocity along the magnetic field lines during the filamentation is accompanied by radial currents (localised to the filaments) due to curvature drifts which, in a collisional plasma, absorb energy from the flow on a time scale of the inverse ion-ion collision frequency. As in the usual neoclassical damping the effect is nonuniform along the line and is effectively equivalent to a force acting against the increase of the flow in the filaments. This may generate oscillatory instead of purely growing states. The effect of thermal channeling due to filamentation contributes to the reduction of the efficiency of the damping mechanism and the regime can again be purely growing but saturates the filaments to a finite amplitude.

The precursors to the ELM event are due to the fact that the nonlinear tearing of the current sheet (coinciding with the vorticity layer) is not purely growing but also has a oscillatory part.

The basic fact in the ion-pressure driven instabilities in tokamak is that the parallel dynamics results from a balance where the electron collisions are essential. This represents the condition that must be invoked in the Hasegawa-Wakatani theory of drift-wave turbulence. When the temperature is high the collisionality is low and one expects that the parallel balance is not satisfactorily described as a dissipative mechanism. Frequently it is invoked the parallel Landau damping but the efficiency of this pseudo-dissipation model is problematic for short time scales as the ones that are implied in the Edge Localised Modes.

We propose to consider the transitory process of increase of the parallel current induced by the centrally advected vorticity in a Kelvin-Helmholtz event as constrained by the poloidal viscosity of neoclassical origin. This mechanism, the usual reason for the decay of poloidal rotation in plasma, is efficient due to the different drifts of electrons and ions in the radial direction, leading to currents that are subjected to resistive dissipation. We propose this mechanism as a source of force opposing the gradient of the parallel current. This will allow to balance in an efficient way the parallel dynamics and will give correct evaluation of the growth rates of the Edge Localised Modes.

2 Equilibrium flows dominated by the neo-classical viscosity

2.1 Parallel and perpendicular flows

From momentum balance it result the equations for the time evolutions of the perpendicular and the parallel velocities of a rotating plasma

$$nm(1 + 2\tilde{q}^2) \frac{\partial u_{\perp}}{\partial t} = -F_{\perp}^R - F_{\perp}^R - F^{neo} - F_{\perp}^a$$

$$nm \frac{\partial u_{\parallel}}{\partial t} = \frac{B_{\theta}}{B_T} F^{neo} - F_{\parallel}^R - F_{\parallel}^a$$

where the forces with superscript R are due to the Reynolds stress in a turbulence and F^a are forces due to additional effects on rotation.

The Reynolds stress is consider the main driving force of the rotation and consists of the advection of the momentum directed along a coordinate, toward the direction of a transversal coordinate. therefore it is dependent of the existence of a *tilting* of the flows of the eddies. In a normal turbulent state, this tilting is supposed to exist as a result of a symmetry breaking, of an origin which is not clear but it is plausible. In the situation of a low-level turbulence the Reynolds stress can however exist if there is a tilting of thermally generated cells consisting of local convection due to temperature gradient-driven ion instability. This is the *tilting instability* studied by Rosenbluth and Shapiro.

The neoclassical viscosity is

$$F^{neo} = -3\mu^{neo} \frac{B_T}{B_0^2} \left\langle \left(\frac{(\mathbf{B} \cdot \nabla) B}{B} \right)^2 \right\rangle \left(u_{\parallel} - \frac{B_T}{B_{\theta}} u_{\perp} - k_{\nu_*} \frac{1}{eB_{\theta}} \frac{dT_i}{dr} \right)$$

where the neoclassical viscosity coefficient is (for velocities which are much less then the sound velocity)

$$\mu^{neo} \approx R_0 q \frac{nmv_{th}\nu_*}{1 + \nu_*} \frac{1}{1 + \varepsilon^{3/2}\nu_*}$$

$$\nu_* = \nu \varepsilon^{3/2} \frac{qR}{v_{th}}$$

and ν is the ion collision frequency.

The coefficient k_{ν_*} describes the relative effect of the **parallel heat flux** on the longitudinal viscosity

$$k_{\nu_*} = 1.17 \quad \text{for} \quad \nu_* \ll 1$$

$$k_{\nu_*} = -0.5 \quad \text{for} \quad 1 \ll \nu_* \ll \varepsilon^{-3/2}$$

$$k_{\nu_*} = -2.1 \quad \text{for} \quad \nu_* \gg \varepsilon^{-3/2}$$

2.2 Particle motion in spatially-varying magnetic field

The equation

$$\ddot{z} = -\frac{\mu}{m} \frac{\partial B}{\partial z}$$

where: z is the distance measured on the line of magnetic field;

$$\mu = \frac{mv_{\perp}^2}{2B}$$

and the magnetic field is taken in a simplified way (valid locally along a single turn of a magnetic line)

$$B = B_0 + B_1 \exp\left(-\frac{z^2}{a^2}\right)$$

Then

$$\frac{1}{2} \frac{d}{dt} (\dot{z})^2 = -\frac{\mu B_1}{m} \frac{d}{dt} \left[\exp\left(-\frac{z^2}{a^2}\right) \right]$$

with the result

$$V(z) = V_0 - \lambda \frac{\mu B/m}{V_0} \exp\left(-\frac{z^2}{a^2}\right)$$

for the small ripple magnetic modulation

$$\lambda = \frac{B_1}{B}$$

One can see that at $z \rightarrow \pm\infty$ the velocity is the same: there is no change in the energy. The reason is: it is necessary to have

- collisions (see for exemple Stix 73)
- or other dissipative mechanism, like the time variation of the magnetic field (which generates electric fields and necessarily acceleration)

The mechanism of decay of the poloidal rotation in tokamak is the viscosity associated to the magnetic pumping. Similarly, there is a magnetic pumping in the ripple modulation.

The energy which can be thermalized in one collision time by magnetic pumping is approximately

$$\frac{1}{6} |\lambda|^2 \left(\frac{3}{2} nT \right)$$

This can be large compared with the kinetic energy of rotation. The modulation of the magnetic field is of the order

$$\lambda \sim \frac{r}{R} \equiv \varepsilon$$

In this result it is considered the rotation of the plasma as a rigid body and for this reason the energy which is affected is the full energy of the plasma. In reality we have only a filament of plasma in the present case. The lost energy will be, however, a similar proportion.

Power lost by magnetic pumping We shall assume the following values for the geometry and plasma

$$\lambda = \frac{r}{R} \equiv \varepsilon = 0.3$$

$$n = 10^{20} \text{ (m}^{-3}\text{)}, \quad T = 10 \text{ (KeV)}, \quad B_T = 3 \text{ (T)}$$

The energy which is thermalized at every **collision time** τ_{ii} by the *magnetic pumping* in every unit volume

$$\begin{aligned} \delta E_\tau &= \frac{1}{6} |\lambda|^2 \left(\frac{3}{2} n T \right) \\ &= 4 \cdot 10^3 \text{ (J/m}^3\text{)} \end{aligned}$$

Let us consider a plasma rotation velocity (in the poloidal direction) representing a fraction α from the thermal ion velocity

$$\alpha = \frac{v^{rotation}}{v_{thi}}$$

Then, the number of “collision times” in the time interval necessary for a rotation with the velocity $v^{rotation}$ is

$$\begin{aligned} N &= \frac{\tau_{rotation}}{\tau_{ii}} \\ &= \frac{2\pi a}{\alpha v_{thi}} \frac{1}{\tau_{ii}} \end{aligned}$$

This has sense only if $N > 1$ which puts a inferior bound to $\alpha > \alpha_0 \sim 0.0024$. Here

$$\begin{aligned} \nu_{ii} &= 3.42 \cdot 10^{-5} \frac{n}{T^{3/2}} [Z] \\ &\simeq 4 \cdot 10^3 \text{ (sec}^{-1}\text{)} \end{aligned}$$

$$N = \frac{10^{-2}}{\alpha}$$

The energy lost by magnetic pumping in a plasma volume:

$$\begin{aligned} \Delta E &= N \cdot \delta E_t \cdot Vol \\ &= \frac{10^{-2}}{\alpha} 4 \cdot 10^3 (\delta r (2\pi a) (2\pi R)) \end{aligned}$$

The conclusion of this semi-quantitative analysis is that the loss of energy from a plasma that has poloidal rotation, loss which is related to the magnetic pumping effect, can be the source of the saturation of the filamentation event and can act as a force that is opposed to the breaking-up of the layer of rotating plasma. Since this layer of high vorticity is also a layer of higher current density, the force will produce a spatial oscillation along the poloidal direction, instead of a tearing. This should be associated with the quasi-coherent modulations which are observed in experiments.

3 Parallel dynamics during transient filamentation in ELMs

The variables are ω (vorticity) and J_{\parallel} . These are the equations:

$$\begin{aligned} \frac{d\omega_{\parallel}}{dt} &= \frac{B^2}{\rho} \nabla_{\parallel} \left(\frac{j_{\parallel}}{B} \right) - \frac{2\mathbf{B} \cdot (\nabla p \times \nabla B)}{\rho B^2} + \frac{\mu}{\rho} \nabla^2 \omega_{\parallel} \\ \frac{\partial j_{\parallel}}{\partial t} &= \frac{1}{\mu_0} \nabla_{\parallel} (B \omega_{\parallel}) + \frac{\eta}{\mu_0} \nabla^2 j_{\parallel} \end{aligned}$$

From these equations one derives a local relationship between the parallel current and the vorticity oriented along the magnetic field lines, which is precisely the case of the filaments. For a highly conducting plasma one gets for a local perturbation

$$j_{\parallel} = -\frac{k_{\parallel} B}{|k_{\parallel} B|} \left(\frac{\rho}{\mu_0} \right)^{1/2} \omega_{\parallel}$$

We note that the nature of the equation obeyed by the vorticity seems to permit an oscillatory behaviour of this quantity. However this should be combined with propagation of perturbations along the poloidal direction, where the spatial modulations should follow the initial periodic formation of the seeds of filaments, from Kelvin-Helmholtz events.

The opposition encountered by an increasing filament of current and vorticity is due to the magnetic pumping. This is because the formation of the filament implies the increase of the parallel current in some particular (periodically disposed) points on the rotation H -mode layer and this increase is equivalent to pushing the plasma along the magnetic field line. The filamentation due to “drop-on-ceil” instability should be purely growing, while the increase of the flow along the line is a transient process. Plasma is suddenly pushed along the line due to the concentration of the density in the vortex and it has to traverse regions of different magnetic field. It is then subject to the magnetic pumping and the effect is a force that acts as a damping of the motion. This leads to a dynamic balance of the two opposite tendencies:

1. increase of parallel velocity of plasma associated with the concentration of density during filamentation and vortex formation
2. damping of the parallel motion due to the magnetic pumping effect. The decay of the poloidal rotation in a low beta plasma is related to the motion of the plasma through the spatially-periodic magnetic field of the tokamak. This is the dissipative process of magnetic pumping and its effect is realized via the ion viscosity.

It is considered that at the initial moment a radial electric field exists in plasma. There is a poloidal rotation of plasma due to the interaction of this field with the confining magnetic field. Moving through this periodic magnetic field the drifts of the particles will create a radial electric current. This is because the drifts of the electrons and the ions are different in magnitude.

The drift kinetic equation is solved for the neoclassical distribution function in the first order in the neoclassical small parameter, δ . The radial current is obtained from the velocity space integral of the particle radial drift, weighted by the first order distribution function.

The electrons and ions moving along a magnetic line experience different deviations induced by the gradient of B and by the curvature (guiding centre drifts). The charge separation is a current with nonvanishing radial component and symmetric periodic amplitude along the line. This current (transversal on the line) in an ideal plasma is simply oscillatory, following the regions of low or high B . The collisionality, even small, opposes a resistivity to this current density and induces an irreversible loss of energy, leading in time to the damping of the poloidal flow component, the one that is confronted with the variation of B .

The current density induced by the drift separation

$$j_D = en(v_{Di} - v_{De})$$

leads to a loss of energy $\Delta\mathcal{E} \sim \eta_\perp \langle j_D^2 \rangle t$ averaged over the excursion of the particles that explore the low- B and the high- B regions along the line in the time t . The average loss of energy per unit of time $\partial(\Delta\mathcal{E})/\partial t$ is noted ε and its time integral is bounded from above by the total “poloidal” energy of the flow. An estimation is

$$j_D \sim en \frac{1}{\Omega_i} (\mu_i \nabla B + v_{\parallel i}^2 (\hat{\mathbf{n}} \cdot \nabla) \hat{\mathbf{n}}) - en \frac{1}{\Omega_e} (\mu_e \nabla B + v_{\parallel e}^2 (\hat{\mathbf{n}} \cdot \nabla) \hat{\mathbf{n}})$$

We can neglect the ion field-curvature term due to smaller $v_{\parallel i}$ and the electron ∇B drift

$$j_D \sim en \frac{\mu_i \nabla B}{\Omega_i} - en v_{\parallel e}^2 \frac{1}{\Omega_e R}$$

from which we get an estimation of the power loss

$$\varepsilon \sim e^2 n^2 \eta_\perp \left(\frac{1}{\Omega_i} \langle \mu_i \nabla B \rangle - v_{\parallel e}^2 \frac{1}{\Omega_e R} \right)^2$$

and of the maximal variation of the electron parallel velocity

$$v_{\parallel e} \sim \sqrt{\Omega_e R} \left| \frac{\varepsilon^{1/2}}{en\eta_\perp^{1/2}} - \frac{1}{\Omega_i} \langle \mu_i \nabla B \rangle \right|^{1/2}$$

The effect on the variation of the vorticity by stretching during filamentation is

$$\frac{d\omega_\parallel}{dt} = \frac{B^2}{\rho} \nabla_\parallel \left(\frac{j_\parallel}{B} \right)$$

Taking $\omega_\parallel \sim v/d$ where v is in the layer (poloidal) and d is the width of the layer,

$$\frac{\partial v}{\partial t} \Big|^{damping} = \frac{dB}{ne\rho} \frac{\partial}{\partial z} \sqrt{\Omega_e R} \left| \frac{\varepsilon^{1/2}}{en\eta_\perp^{1/2}} - \frac{1}{\Omega_i} \langle \mu_i \nabla B \rangle \right|^{1/2}$$

This new term must be added to the equation for the velocity v in the layer, and acts like a force opposing the concentration of current density in a filament.

$$\frac{\partial v}{\partial t} + v \frac{\partial v}{\partial x} = -\frac{e}{m_i c} \left(V_z^{(0)} + \frac{e}{m_e c} A \right) \frac{\partial A}{\partial x} - \frac{\partial v}{\partial t} \Big|^{damping}$$

The most important effect is the inhibition of the Chaplygin (drop-on-ceil) instability.

4 Conclusion

The parallel dynamics during the transient filamentation of the current and vorticity sheet at the tokamak edge is the result of a balance between the increased flow along the line and the damping of the motion *magnetic pumping*. This provides the basis for an explanation of the oscillatory precursors of the ELMs: before the filamentation becomes purely growing, the damping from magnetic pumping compensates periodically the increase in the parallel current and the flow due to the vorticity concentration.

References

- [1] F. Spineanu, M. Vlad, “Parallel dynamics during transient filamentation in ELMs”, 2nd EFDA Transport Task Force Meeting, Culham, UK, September 2009.
- [2] F. Spineanu, M. Vlad, “Parallel dynamics during transient filamentation in ELMs”, 3rd EFDA Transport Task Force Meeting and 15th EU-USA Transport task Force Meeting, Cordoba, Spain, 7 - 9 September 2010.

Scientific Report

To the Contract 1EU-2/11.08.2008
For July - December 2010

Project BS-3A: *Anomalous Transport in Plasma: Role of collisions, turbulence and wave-plasma interaction in transport. Application to ITER.*

Coordinator: Lect. Dr. N. I. Pometescu

Plasma Theory Group: Nicolae Ion Pometescu, Gyorgy Steinbrecher

- **General Objectives**

The aim of this project is to make progress in understanding the transport in fusion plasma from devices like ITER. The role of collisions, turbulence and wave-plasma interactions and also the correlation between them for driving transport of particles and energy will be analysed. Complex features like long-range correlations, intermittency in plasma edge turbulence, edge transport barriers, core impurity transport with different dominant core turbulence and different radio-frequency heating scheme will be analysed. For that are used both analytical and numerical methods. Previously developed stochastic models will be adapted to study long-range correlations, self-similarity and intermittency. Gyrokinetic semi-Lagrangian codes with collision term will be adapted to the study of the particle transport in tokamak.

The results obtained in this project will be applied to existing large plasma devices but are oriented specially to be applied to plasma in ITER device.

For the year 2010 the objectives are:

1. Impact of central electron heating on both electron and ion temperatures, and on particle and impurity densities.
2. Numerical experiments with low dimensional kinetic models of the impurity transport.
3. Study of the turbulent structures and intermittency by stochastic differential equations.
4. Characterization of long-range correlations and multi-scale physics in L-mode plasmas and during edge improved confinement regimes.

- **Specific Objectives**

In this stage of the project, July-December 2010 we have attained the following specific objectives from the previous mentioned objectives:

1. Impact of central electron heating on both electron and ion temperatures, and on particle and impurity densities.
2. Numerical experiments with low dimensional kinetic models of the impurity transport.
3. Study of the turbulent structures and intermittency by stochastic differential equations.
- 4a. Long-range correlations influence on the impurity transport.

- **Resume of the stage**

1. *Impact of central electron heating on both electron and ion temperatures, and on particle and impurity densities.*

Milestone 1b: *Study of the dispersion equation for multi-species plasma with ITG turbulence in the presence of the radio-frequency heating*

The influence of the radio-frequency heating on the impurities transport was studied through comparative analysis of two discharges in JET: the reference discharge #69808 without RF power and discharge #68383 with the maximum ICRF power of 8.3 MW applied to electrons in Hydrogen Minority Heating scheme.

2. *Numerical experiments with low dimensional kinetic models of the impurity transport.*

This objective is continued from 2009. In the previous stage, the statistical properties of the electrostatic field, generated with low dimensional kinetic codes, were studied. It was found that it is possible to approximate the stochastic electrostatic field by a 2 dimensional self-similar processes. A C++ code was written that generates random electric field with self-similarity and long-range correlation properties. The particle transport induced by a random electrostatic field, generated by this algorithm was studied by numerical methods. The statistical post-processing of the results of the particle transport simulations was performed by a new class of stable numerical processing method. The elaboration of the mathematical methods for the interpretation of the first principle gyrokinetic simulations is important for the optimization of the strategy of the time consuming first principle simulations, necessary for the optimization of the large tokamaks, like ITER and DEMO.

4b. *Long range correlations, reduced stochastic models.*

New class of reduced stochastic models for the simulation of transitions in stochastic dynamical systems, transitions that can be identified with L-H transitions, was elaborated. The main part of the model consists of a noise driven stochastic model. The heavy tail exponent of the models is related to that exponent p of the L^p spaces whose norm is finite. An important parameter of the model is the exponent p_{crit} : for $p < p_{crit}$ we have finite L^p norms of the relevant variable of the affine model. The L-H transition take place exactly

when the critical exponent crosses the value $p_{\text{crit}} = 1$. The $p_{\text{crit}} > 1$ corresponds to the L mode and the $p_{\text{crit}} < 1$ to the H mode. In the $p_{\text{crit}} < 1$ case the model exhibits also an increased intermittency, which can be associated with the increase of the type I ELM activity. The hysteresis effect will be manifest if the driving noise of the linear model is generated by a dynamical system associated to the magnetic field line dynamics.

- **Scientific description**

Specific Objective I

1. *Impact of central electron heating on both electron and ion temperatures, and on particle and impurity densities.*

Coordinator: Lect. Dr. Nicolae Pometescu.

Co-operations: TG-T WP10-TRA-03-03, Université Libre de Bruxelles and Chalmers University, Sweden

Milestone 1b: *Study of the dispersion equation for multi-species plasma with ITG turbulence in the presence of the radio-frequency heating*

Experiments have shown that auxiliary heating can influence impurity accumulation and transport and, by consequence, the plasma confinement. In JET, various type of discharges at ITER relevant collisionality had shown that the density profile of Ni ($Z=28$) impurity is flattening when ion cyclotron resonance heating (ICRH) is applied [1].

Influence of ICRH on the impurity density profile was intensively studied but the present understanding of impurity transport and accumulation is still insufficient to predict the behaviour of elements over wide Z range. Also, some discrepancies between calculated peaking factor and experimental measurements rest to be explained and clarified.

The Weiland multi-fluid model with trace impurity approximation is used to describe ITG/TE mode turbulence and the equation for the impurity/ion density perturbation due to ITG modes in plasmas with radio-frequency heating, obtained in [2].

The profiles for impurity and electron density and temperature profiles are given to fit the experimental data from shots 69808 and 68383 in JET [3, 4]. The reference discharge 69808 is without RF power and the discharge 68383 is with the maximum ICRF power of 8.3 MW in H Minority Heating. The influence of the heating on the density perturbation profile is taken into account by the specific profiles of electron density and electron /impurity temperature profiles for the two shots.

In order to represent the radial variation of the impurity density perturbation for the two shots we find the eigenfrequency modes for ITG instability. This imply to solve the equation resulting from the quasineutrality condition. The resulting dispersion equation, which is of great complexity, was solved in different approximations. In the present work

we assumed one ion species with charge number Z_i and one impurity species (Ni) with charge number $Z=28$.

In the present study the discussion focussed on the inner region of plasma with $0 < r/a < 0.6$, where the contribution from trapped electrons was neglected. Also, the ion (Hydrogen) temperature profile is assumed the same with impurity temperature profile. In this case, from the dispersion equation result four eigenvalues. Between the four eigenmodes we choose the unstable mode with the real and imaginary part represented in figure 1 and figure 2, respectively.

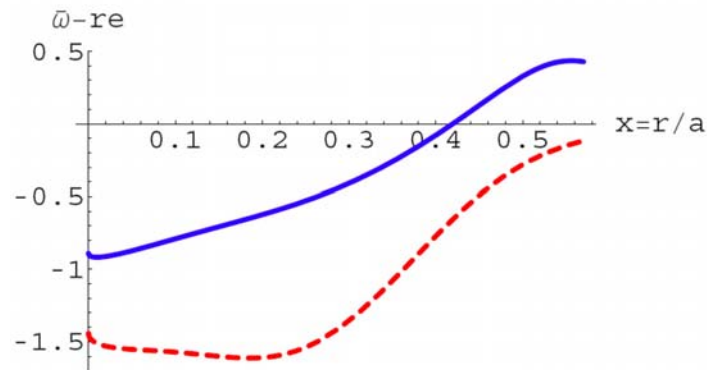


Figure 1: Real part of the frequency in discharge #69808 (full line) and discharge #68383 (dashed line)

As can be seen, in the presence of RF heating the growth rate becomes smaller than in the case without RF heating which means a more 'quiet' ITG instability.

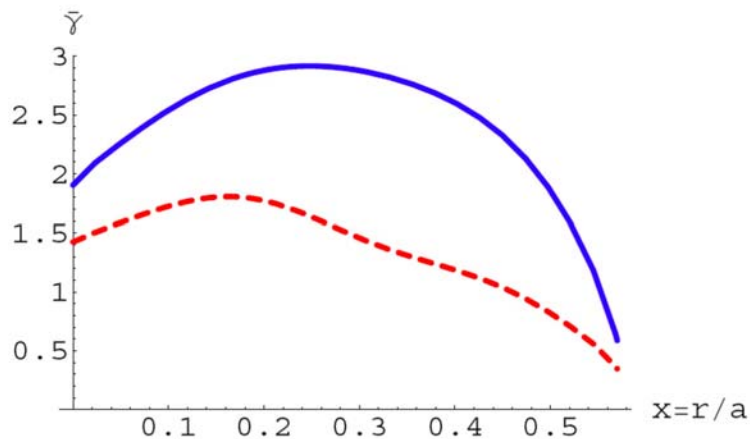


Figure 2: Growth rate of ITG mode in discharge #69808 (full line) and discharge #68383 (dashed line)

The Ni-impurity diffusivity D_z and convective velocity V_z are calculated for ITG mode eigenvalue with previously determined characteristics plotted in figures 1 and 2 for a

fixed turbulence scale.

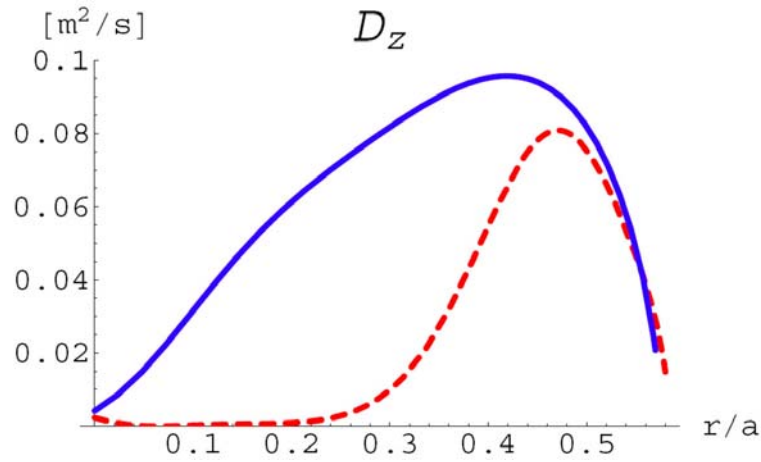


Figure 3: Diffusivity in discharge #69808 (full line) and discharge #68383 (dashed line)

In figures 3 and 4 are shown the radial profiles of D_z and V_z in the two shots. We note that in the region with $0 < r/a < 0.5$ the diffusivity in the presence of RF heating is smaller than diffusivity in absence of RF heating, with a very small value of the latest in the interval $0 < r/a < 0.3$ and a maximum value at $r/a = 0.47$ that correspond to the position where start the plateau for the density profile in the presence of RF heating. In the case without RF heating the diffusivity reach its maximum at $r/a = 0.43$ and is much greater than in the presence of RF heating for $0 < r/a < 0.4$.

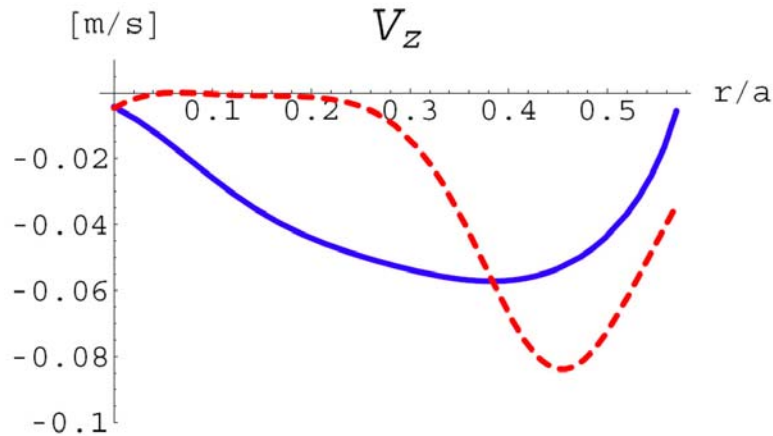


Figure 4: Convective velocity in discharge #69808 (full line) and discharge #68383 (dashed line)

As for the diffusivity, the presence of RF heating reduced nearly to zero the magnitude of the convective velocity in the region with $0 < r/a < 0.3$. Hence, in the central region of the

plasma the transport due to ITG instability is practically suppressed as was confirmed by experimentally observations.

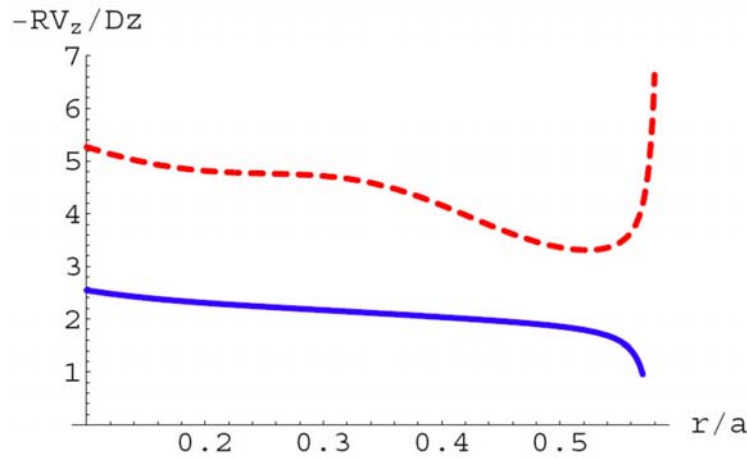


Figure 5: Normalized impurity density peaking factor in discharge #69808 (full line) and discharge #68383 (dashed line)

The normalized impurity density peaking factor (assuming a source-free plasma) of Ni-impurities as function of radial coordinate is shown in figure 5. The density peaking factor in the case without RF heating decrease linearly with r/a in the region with $0 < r/a < 0.5$.

In the case with RF heating the density peaking factor decrease with r/a also for $r/a < 0.5$ but with a plateau for $0.2 < r/a < 0.3$.

The results obtained in the present approximation [5] are relevant for ITG mode in the region with $r/a < 0.5$ and can be used as a starting point for more precise calculations in iterative procedure.

Specific Objective II

2. Numerical experiments with low dimensional kinetic models of the impurity transport.

Coordinator: Prof. Dr. György Steinbrecher

Co-operations: TG-T WP10-TRA-05-01, C.E.A. Cadarache, France

This objective is continued from 2009. In the previous stage, the statistical properties of the electrostatic field, generated with the low dimensional kinetic codes, were studied. In this period it was found, by empirical numerical simulations, that it is possible to approximate the stochastic electrostatic field by a 2 dimensional generalization of the classical one-dimensional self-similar processes. Similar results on higher dimensions were reported in Ref. [6]. In order to perform test particle transport simulations in an efficient way a C++ code was written that generate random electric field with self-

similarity and long-range correlation properties. The theoretical foundations of this algorithm were exposed in Refs. [7,8]. The particle transport induced by a random electrostatic field, generated by this algorithm, with prescribed statistical properties, extracted from numerical first principle low dimensional gyrokinetic simulations, was studied by numerical methods. The statistical post processing of the results of the particle transport simulations was performed by a new class of stable numerical processing method, elaborated on the basis of the results from ref. [9]. In the framework of this new class of numerical filtering methods, it is possible to extract information on the whole spectrum of anomalous diffusion exponents, when the mean square displacement of the test particle is represented as

$$\left\langle |\mathbf{R}_\omega(t)|^2 \right\rangle_\omega = \int_0^2 t^\alpha d\rho(\alpha) \quad (1)$$

where the averaging is performed over an ensemble of random trajectories. The representation (1) contains also the usual asymptotic large time behavior in anomalous transport:

$$\left\langle |\mathbf{R}_\omega(t)|^2 \right\rangle_\omega = O(t^\beta) \quad (2)$$

where the exponent β is the dominant exponent in the representation given in Eq.(1). In the work [9] we proved that in the cases when we have no a priori information on the existence of dominant exponent, the reconstruction of the spectrum of all of the diffusion exponents, given by the nonnegative measure $d\rho(\alpha)$, is an ill posed, unstable problem. A possibility to stabilize this set of problems is given by the results in Ref.[9] that proves that it is possible to reconstruct $d\rho(\alpha)$ in weak sense, that means to derive tight upper and lower bounds on the mean values:

$$\int_0^2 f(\alpha) d\rho(\alpha) \quad (3)$$

Here $f(\alpha)$ is a smooth function, for instance a Gaussian centered around a given point. The results of this analysis on simulated data shows that the maximal, dominant exponent is not well separated and a naïve fit give rise to biased determination of the leading exponent. The dependence of the mean values (3) on the test particle mass was studied. Qualitative explanation of the results was given, by using recent results from ref. [10] on the occurrence of stable distributions.

The elaboration of the mathematical methods for the interpretation of the first principle gyrokinetic simulations is important for the optimization of the strategy of the time consuming first principle simulations, necessary for the optimization of the large tokamaks, like ITER and DEMO.

Specific Objective III

4b. Long range correlations, reduced stochastic models.

Coordinator: Prof. Dr. György Steinbrecher

Co-operations: EFDA WP – III.2.1, C.E.A. Cadarache, CNRS Marseille, France

Milestone: *Comparative study of different plasma regimes and description of the transition in term of global parameters.*

New class of reduced stochastic models for the simulation of transitions in stochastic dynamical systems, transitions that can be identified with L-H transitions, was elaborated. The main part of the model consists of a noise driven stochastic model, whose aspects were studied in the refs. [7,11,12]. The main aspect in this class of models is related to the fact that the mean values of the moments of the output of random dynamical system (or, in functional analytic terms, the L^p norms [12]) depends in a very sensitive way on the intensity of the driving multiplicative noise as well as on its correlation times. We insist on the fact that in our analysis we used, beside usual L^p Banach spaces with $p \geq 1$, also a class of unusual L^p Banach spaces with $0 < p < 1$. The heavy tail exponent of the models is related to that exponent p of the L^p spaces whose norm is finite. An important parameter of the model is the critical exponent p_{crit} . Only for $p < p_{\text{crit}}$ we have finite L^p norms of the relevant variable of the affine model. The critical exponent p_{crit} , that is identical to the heavy tail exponent of the model, depends on the parameters like intensity of the driving noise, the correlation time of the driving noise. The L-H transition take place exactly when the critical exponent crosses the value $p_{\text{crit}} = 1$. Interestingly, this transition is exactly the transition from classical L^p spaces ($p \geq 1$) to “exotic L^p spaces”, with $0 < p < 1$. We recall that in generic cases of the distributions, L^p spaces with $0 < p < 1$ are in a sense pathological: their dual is reduced to the null vector. The $p_{\text{crit}} > 1$ corresponds to the L mode and the $p_{\text{crit}} < 1$ to the H mode. Observe that in the $p_{\text{crit}} < 1$ case the model exhibits also an increased intermittency, which can be associated with the increase of the type I ELM activity.

The hysteresis effect will be manifest if the driving noise of the linear model is generated by a dynamical system associated to the magnetic field line dynamics. We mention that the results of ref. [12] are obtained under very general assumptions related to the driving multiplicative noise. In this case the hysteresis is related in fact to the hysteresis effect of the driving multiplicative noise, produced by the complex fractal structure, stickiness of the magnetic island chains. This model is a stochastic generalization of the models from refs. [13, 14].

- **Conclusions**

1. *Impact of central electron heating on both electron and ion temperatures, and on particle and impurity densities.*

The influence of the RF heating on the Ni-impurity transport was studied from comparative analysis of two discharges in JET: the reference discharge #69808 without RF power and discharge #68383 with the maximum ICRF power of 8.3 MW which is applied to electrons in Hydrogen Minority Heating scheme. This goal was accomplished by using the multi-fluid Weiland model with trace impurity approximation and input profiles of density and temperature from the two shots. For the most unstable determined eigen modes were evaluated diffusivity, convective velocity and peaking factor for the two shots, respectively. The results obtained in the present approximation [5] are relevant in JET for ITG mode in the region with $r/a < 0.5$ and can be used as a starting point for more precise calculations in iterative procedure.

2. *Numerical experiments with low dimensional kinetic models of the impurity transport.*

Numerical experiments on the impurity transport were performed and new post-processing method for the study of the diffusive properties of the transport of particles was elaborated. This new method allows a very stable determination of the spectrum of the diffusion exponents, in contradistinction with the classical methods that find only the lowest and the highest exponent

4b. *Comparative study of different plasma regimes and description of the transition in term of global parameters.*

A noise driven intermittency model, was adapted to the elaboration of reduced stochastic models of the hysteresis effects, L-H transitions and occurrence of intermittency in the edge plasma. The study of the statistical properties of the intermittent events in the edge plasma turbulence is essential in the evaluation of the intermittent heat loads on the plasma facing components of large tokamaks.

The proposed objectives were attained. The study of these milestones will be continued.

- **References**

[1] Puiatti M E, Valisa M, Angioni C, Garzotti L, Mantica P, Mattioli M, Carraro L, Coffey I and Sozzi C, 2006, Phys. Plasmas, **13**, 042501

- [2] H Nordman, R Singh, T Fülöp, L-G Eriksson and *all*, „*Influence of radio frequency ponderomotive force on anomalous impurity transport in tokamaks*”, Phys. Plasmas **15**, 042316 (2008)
- [3] Carraro L, Angioni C, Giroud C, Puiatti M E, Valisa M, Buratti P, Buttery R, Coffey I, Garzotti L, Van Eester D, Lauro Taroni L, Lawson K, Lerche E, Pantica P, Mattioli M and Naulin V, 2007, *Proceedings of the 34th EPS Conference on Controlled Fusion and Plasma Physics*, Warsaw, July 2-July 6, 2007 ECA Vol 31F, O-4.028
- [4] Valisa M, Angioni C, Carraro L, Coffey I, Predebon I, Puiatti m E, Lauro Taroni L, Alper B, Belo P, Giroud C, Van Eester D, Lerche E, Naulin V, Tala T, Tsala M and JET-EFDA contributors, 2009, *Proceedings of the 36th EPS Conference on Plasma Physics*, Sofia, June 29-July 3, 2009 ECA Vol 33E, P-2.169
- [5] N. Pometescu, *Diffusion coefficient and convective velocity profiles of Ni-impurity in JET plasmas with ICRH*, poster session at “Theory of Fusion Plasmas, Joint Varenna-Lausanne International Workshop”, Varenna, Italy, August 30 – September 3, 2010
- [6] Dif-Pradalier et all, “*Nonlocal dynamics of turbulence, transport and zonal flows in tokamak plasmas*”. Preprint UCSD THC/P4-06.
- [7] Steinbrecher G., Weysow B., “*Generalized Randomly Amplified Linear System Driven by Gaussian Noise. Extreme Heavy Tail and Algebraic Correlation Decay in Plasma Turbulence*”, Physical Review Letters **92**, 125003 (2004).
- [8] G. Steinbrecher, B. Weysow “*New representation and generation algorithm for fractional Brownian motion*”, Roumanian Journal of Physics, **55**,1120-1130, (2010).
- [9]. G. Steinbrecher, R. Scorei, V. Cimpoiasu, I. Petrisor “*Stable Reconstruction of the T2 Distribution by Low Resolution NMR Measurement and the Classical Markov and Hausdorff Moment Problem*”. Journal of Magnetic Resonance, **146**, 321-334 (2000).
- [10] D. Buraczewski, E. Damek, Y.Guivarc’h I”*Convergence to stable laws for a class of multidimensional stochastic recursions*”, Probab. Theory and Relat. Fields **148**, 333-402, (2010).
- [11]. X. Garbet, G. Steinbrecher, “*On-off intermittency. Exact results*”. Presented at the “Solvay Workshop <A Tribute to Radu Balescu>”, Brussels, 6-8 March 2008.
- [12] G. Steinbrecher, X. Garbet. B. Weysow, “*Large time behavior in random multiplicative processes*”.[arXiv:1007.0952v1](https://arxiv.org/abs/1007.0952v1) [[math.PR](https://arxiv.org/abs/1007.0952v1)], (2010)
- [13] D. A Gates et all, “*Neoclassical islands in COMPASS-D*”, Nucl. Fusion **37**, (1997), 1593-1606.
- [14] R. J. Buttery et all, “*Onset of the neoclassical tearing modes on JET*”. Nucl. Fusion **43**, (2003) 69-83.

Scientific Report

To the Contract 1EU-2/11.08.2008
For the period July-December 2010

Project BS-3B: *Anomalous Transport in Plasma. Stochastic processes and transport in turbulent plasma*

Plasma Theory Group: M. Negrea, I. Petrisor, D. Constantinescu

• **General Objectives**

The scope of the project is to explain some features of the anomalous transport and to develop the analytical and numerical skills to evaluate correctly the transport in fusion device like ITER. The project aims also to deep insight the physics of plasma turbulence. Both analytical and numerical methods are used to achieve the objectives. The test particle diffusion in an electromagnetic stochastic field is studied in the framework of the decorrelation trajectory method (DCT). In this kind of stochastic field we must determine the mean square displacements and the radial and poloidal diffusivities using the numerical method and the DCT method. The comparison of the results obtained by these two methods might then allow us to confirm the DCT approach results. These results are important for “Validation of physics-based transport models” and “Plasma edge characterization and modeling”, objectives for ITER. Some characteristics of the anomalous transport of magnetic field lines and charged particles, features that cannot be described in the context of the standard diffusion paradigm, will be explained using the memory effects. The long memory effects will be studied using fractional models and limited (short) memory effects will be studied using delay systems or hysteresis systems.

The results obtained in this project will be applied to existing large plasma devices but oriented specially to be applied to plasma in ITER device.

For the year 2010 the objectives are:

1. Simulations of MHD turbulence (TG-T, ULB)
 - 1.1. Study of turbulent zonal flow including test particle and field line transport. Stochastic magnetic field line diffusion and particle diffusion in MHD.
2. Study of anomalous transport (TG-T, WP10-TRA-05-03, ULB, Association of Hellenic Republic)
 - 2.1. Stochastic modelling with application to the edge turbulent transport. Calculus of the diffusion coefficients for test particles in the edge region of tokamak plasma using the decorrelation trajectory method and numerical simulation.
 - 2.2. Study of the fractional diffusion equation with a coupling between position and momentum space; methods to solve this equation analytically and/or numerically in order to study the radial transport.
 - 2.3. Studies of the sawtooth oscillations based on the relaxation oscillation theory and on mapping models.
 - 2.3. a) Study of the sawtooth oscillations based on the relaxation oscillation theory

2.3.b) Study of the sawtooth oscillations based on mapping models

- **Specific Objectives**

In this stage of the project, the period July - December 2010, we have attained the following specific objectives from the previous mentioned objectives:

Specific Objectives

1.1. Study of turbulent zonal flow including test particle and field line transport. Stochastic magnetic field line diffusion and particle diffusion in MHD

2.2. Study of the fractional diffusion equation with a coupling between position and momentum space; methods to solve this equation analytically and/or numerically in order to study the radial transport.

2.3. a) Study of the sawtooth oscillations based on the relaxation oscillation theory.

- **Resume of the stage**

Specific Objective 1.

Study of turbulent zonal flow including test particle and field line transport. Stochastic magnetic field line diffusion and particle diffusion in MHD

The work is related to the building of the electromagnetic fluctuations, and both the electric and the magnetic fields are obtained through the numerical resolution of the MHD equations derived from first principles. In order to obtain the diffusion coefficients we used the specific incompressible MHD equations for the Kolmogorov flow.

Specific objective 2.2.

Study of the fractional diffusion equation with a coupling between position and momentum space; methods to solve this equation analytically and/or numerically in order to study the radial transport.

The transport models in position and velocity space are formulated in terms of the probability for a particle to be situated in the position “ x ” and to have the velocity “ v ” at the moment “ t ”. We introduce the velocity in the transport model in order to incorporate the strong background magnetic field (through the usual Vlasov equation), to include the collisions (through a diffusion term) and the effect of the turbulent electric field which could be responsible for the anomalous diffusion (through a fractional Riesz derivative).

Specific objective 2.3

2.3. a) Study of the sawtooth oscillations based on the relaxation oscillation theory.

In the previous work the sawtooth oscillations of the plasma parameters (for example the repetitive and rapid crash of the central electron temperature) were explained using the magnetic stochasticity hypothesis: the sawtooth oscillations are localized in regions where the magnetic reconnection is accomplished and the increased turbulent transport in the plasma core causes the observed crash of the plasma temperature. In the present approach we use a different approach, based on a low-dimensional model describing the evolution of the

perturbed magnetic field and of the pressure gradient. This model is useful to understand qualitatively their reaction to changes in the driving parameters (e.g. heating power) or to illustrate the possible action of control techniques (e.g. pellet injection for ELM mitigation).

- **Scientific description**

Specific Objective 1.

1.1. Study of turbulent zonal flow including test particle and field line transport.

Stochastic magnetic field line diffusion and particle diffusion in MHD

Coordinators: Lect. Dr. Negrea Marian and Lect. Dr. Iulian Petrisor

The work is related to building of the electromagnetic fluctuations, and both the electric and the magnetic fields are obtained through the numerical resolution of the MHD equations derived from first principles. In order to obtain the diffusion coefficients we used the specific incompressible MHD equations for the Kolmogorov flow. The Kolmogorov force, which is usually oriented on the x-direction, depends on the y-coordinate: $\mathbf{f} = (A_f \sin(k_f y), 0, 0)$. The MHD velocity and the magnetic fields are taken to be divergence free. We have started to study simultaneously the first order guiding centre equation and the Lorentz force system specific to ions impurities, $\alpha (\mathbf{e} + \mathbf{v} \times \mathbf{b})$. A friction force, $\chi (\mathbf{u} - \mathbf{v})$ depending on the difference between the test particle velocity and the MHD velocity, which mimics the collisions between the tracers and the velocity MHD field, was taken into account. We have made some longer MHD Kolmogorov flow simulations with Kolmogorov parameters $A_f = 1$, $k_f = 1$ and different values of the z-component of the average homogeneous magnetic field b_{0z} . For a preliminary test, in order to study the particle behaviour, the simulation with a magnetic field on the toroidal axis $b_{0z} = 0.9$ was chosen. The Reynolds number is considered about 250 and the following five different cases for the particles are analyzed:

- Three different types of “charged particles” given by the coefficients (α, χ) , i.e.: $(\alpha, \chi) = \{(2, 1), (2, 10), (2, 100)\}$;
- Two types of first guiding centre approximation with $v_{\text{parallel}} = \{1, 10\}$.

For specific parameters that impose the relative velocity we have obtained the mean square displacements in realistic cases specific to ITER, the average kinetic energy for the fluid (averaged over the periodic box) and the average kinetic energy for the three types of charged particles. One first observation is that the transport along the y direction can be super-diffusive for the physical particles. As expected, because there is an external magnetic field along the z axis, both guiding centre approximations and magnetic field lines show ballistic/super-diffusive regimes on this direction. It is also expected that for very large numbers of particles, and large enough χ the average kinetic energy of the test particles will match that of the fluid. More particles and longer integration times are needed for a better conclusion. The work, which is in progress, has been done in collaboration with Dr. D. Carati and Dr. C. Lalescu from ULB.

Specific objective 2.2.

Study of the fractional diffusion equation with a coupling between position and momentum space; methods to solve this equation analytically and/or numerically in order to study the radial transport.

Coordinator: Conf. Dr. Dana Constantinescu

The transport models in position and velocity space are formulated in terms of the probability for a particle to be situated in the position “x” and to have the velocity “v” at the moment “t”.

We introduce the velocity in the transport model in order to incorporate the strong background magnetic field (through the usual Vlasov equation), to include the collisions (through a diffusion term) and the effect of the turbulent electric field which could be responsible for the anomalous diffusion (through a fractional Riesz derivative). We studied some analytical and numerical methods to solve the fractional transport equation. We obtained the analytical form for the solutions of the fractional transport equation with constant coefficients. The solutions are expressed in terms of special functions (Mittag-Leffler functions). The algorithm we use for obtaining the numerical solution is based on the approximation of the Riesz derivative by the Grunwald-Letnikov fractional derivative of the same order. Using this algorithm we built a code which can be applied for symmetric and asymmetric Riesz derivatives of any order (for physically relevant models the order is between 0 and 2). The results obtained using this code are in agreement with the analytical ones

We studied also the influence of the parameters involved in equations, mainly of the order of the fractional derivatives. In the fractional transport model without collisions, which includes the fractional α -Riesz derivative in space and the δ -Riesz derivative in velocity, it was shown that the solution exhibits Levy flights of order α in space and of order δ in velocity, so the transport is anomalous both in space and velocity. In the fractional diffusion model we studied the influence of the symmetry/asymmetry of the Riesz derivative. The asymmetric case seems to be relevant for fusion plasma where asymmetric transport is usually observed. We observed that pulse initial conditions exhibit a ballistic drift to the right or to the left (depending on the asymmetry of the derivative) reminiscent of the rapid propagation phenomena in perturbative plasma experiments.

The results were obtained in collaboration with Loukas Vlahos and Heinz Isliker, Aristotle University, Thessaloniki. The work is in progress.

Specific objective 2.3.

Studies of sawtooth oscillations based on relaxation oscillation theory and on mapping models.

2.3. a) Study of the sawtooth oscillations based on the relaxation oscillation theory

Coordinator: Conf. Dr. Dana Constantinescu

In the previous work the sawtooth oscillations of the plasma parameters (for example the repetitive and rapid crash of the central electron temperature) were explained using the magnetic stochasticity hypothesis: the sawtooth oscillations are localized in regions where the magnetic reconnection is accomplished and the increased turbulent transport in the plasma core causes the observed crash of the plasma temperature.

In the present approach we use a different approach, based on a low-dimensional model describing the evolution of the perturbed magnetic field and of the pressure gradient. This model is useful to understand qualitatively their reaction to changes in the driving parameters (e.g. heating power) or to illustrate the possible action of control techniques (e.g. pellet injection for ELM mitigation). A systematic study of the dynamical dependence on the parameters of the system (the normalized power input into the system, the current diffusion coefficient, the diffusion of the magnetic field of the mode, the normal heat diffusion and the heat diffusion due to perturbations) was achieved. The bifurcations in the parameters space (leading to different evolutions of the system) were carefully analyzed. A special attention was paid to the identification combination of the parameters' values for which the sawtooth

oscillations appear. It was also analyzed the influence of some slight modifications of the parameters' values on the dynamics of the system.

A paper containing the main results was proposed for publication in *Physics of Plasmas*. The results were obtained in collaboration with Olgierd Dumbrajs (Institute for Solid State Physics, University of Latvia, Association Euratom-UL, Latvia) V. Igochine, K. Lackner, R. Meyer-Spasche, and H. Zohm (Max-Planck Institut für Plasmaphysik, Association Euratom-IPP, Germany).

- **Conclusions**

- 1.1. Study of turbulent zonal flow including test particle and field line transport. Stochastic magnetic field line diffusion and particle diffusion in MHD**

- For specific parameters that impose the relative velocity we have obtained the mean square displacements in realistic cases specific to ITER, the average kinetic energy for the fluid (averaged over the periodic box) and the average kinetic energy for the three types of charged particles. One first observation is that the transport along the y direction can be super-diffusive for the physical particles.

- 2.2. Study of the fractional diffusion equation with a coupling between position and momentum space; methods to solve this equation analytically and/or numerically in order to study the radial transport.**

- We studied the influence of the parameters involved in equations, mainly of the order of the fractional derivatives. In the fractional transport model without collisions, which includes the fractional α -Riesz derivative in space and the δ -Riesz derivative in velocity, it was shown that the solution exhibits Levy flights of order α in space and of order δ in velocity, so the transport is anomalous both in space and velocity.

- 2.3. a) Study of the sawtooth oscillations based on the relaxation oscillation theory**

- A systematic study of the dynamical dependence on the parameters of the system (the normalized power input into the system, the current diffusion coefficient, the diffusion of the magnetic field of the mode, the normal heat diffusion and the heat diffusion due to perturbations) was achieved. The bifurcations in the parameters space (leading to different evolutions of the system) were carefully analyzed.

- **Bibliography**

- [1] C.C. Lalescu, D. Carati, M. Negrea, I. Petrisor, *Virtual particle transport in turbulent MHD Kolmogorov flow*, to be presented to the Conference "Particles in turbulence" ,16-18 March 2011, Potsdam (Germany).

- [2] M. Negrea, I. Petrisor, Dana Constantinescu, *Aspects of the diffusion of electrons and ions in tokamak plasma*, Rom. Journ. Phys., Vol. 55, Nos. 9–10, P. 1013-1024, Bucharest, 2010.

- [3] Dana Constantinescu, M. Negrea, I. Petrisor, *The study of the sawtooth oscillations in tokamaks using mapping models*, Rom. Journ. Phys., Vol. 55, Nos. 9–10, P. 951–960, Bucharest, 2010.

Raportul Stiintific si Tehnic (RST)

**National Institute of Laser,
Plasma and Radiation Physics**
V. Stancalie

WP10-ITM-ISIP-ACT10
WP10-ITM-ISIP-ACT1
WP09-ITM-ISIP-T3

The longer term goal of the ITM-TF is to provide the European fusion community with a validated suite of simulation tools for ITER exploitation and to provide the basis for a complete simulation environment for fusion plasmas generally available for use also for modelling on current devices and in support of theory and modelling in general. IMPs have dual responsibilities in that they should continue to develop and manifest the physics foundations for Integrated Modelling in standalone packages targeting the code platform environment while they are also supporting the integration efforts towards scenario modelling tools.

The ITM Portal acts as an interface between users and the various tools available on the ITM Gateway.

Various problems arising from the usage of the ITM Portal were dealt with in the context of the ISIP-ACT10 task. Some of the solutions were posted as Wiki entries in the Portal Wiki system.

A closer look to the ACL (Access Control List) mechanism of Gforge was required in order to make it easier for the users to work with.

In order to demonstrate setting ACLs under GForge a new project called “Test GForge ACLs”(with repository “gforge_acl”) was created. This project started with the default settings associated with any new ITM software project (created after 28 January 2009).

Furthermore, a new user called “testsvn” was created and given ITM membership rights similar to those of regular ITM users.

Notes:

- In order to be able to manipulate the access rights of a particular user he/she must become a member of the project (it is not possible to change the rights for a user who is not a member of a project)
- Groups are not part of GForge. The “itm_members” pseudo-group is just a trick that can be translated as “every itm member becomes a restricted, hidden, member of the project”. Therefore it is somewhat equivalent to manually adding each user to the project, the only difference being that these users are not actually visible and only “itm_members” virtual user is shown.
- When ACLs are modified it take a maximum of 30 minutes (typically 15) in order to become effective.

The following test use cases were considered:

1) Add write permission for a user who already has read permission as member of a group

Since “testsvn” is member of itm_members group, it already has read access to the repository. However, it does not have write access to any directory.

In order to give write permissions to “testsvn” the user must first join the project. When the project admin approves the request, he can make the “testsvn” user member of “Software Developer” role, thus giving it write access to the repository, without the need to further define additional ACLs.

2) Limit access to a subdirectory to single users and/or subgroups

For the purpose of this test, it is assumed that the “testsvn” user is not a member of the project , but is still a member of the “itm_members” pseudo-group (like it was the case prior to the changes indicated at 2.1. above).

In order to limit read access for “itm_members” to the “/tags” subdirectory, two new ACLs are required:

- a) For directory “/” itm_members is set to “no access”
- b) For directory “/tags” itm_members is set to “read”

At this point, user “testsvn” can checkout from http://gforge.efda-itm.eu/svn/gforge_acl/tags and read everything under this directory, but the user is unable to checkout from /trunk or any other directories that are not under /tags. This applies for every member of itm_members that is not a member of the project.

In order to give write access to user “testsvn” to the repository/parts of the repository, the user must first join the project and approved as a “Software developer”. Afterwards, for each defined ACL, the project admin must click on “Edit permissions” and “Submit”. This confirms adding the new user to the defined set of ACLs. Of course, read or write access can be given to the user. By default, the user will have write access.

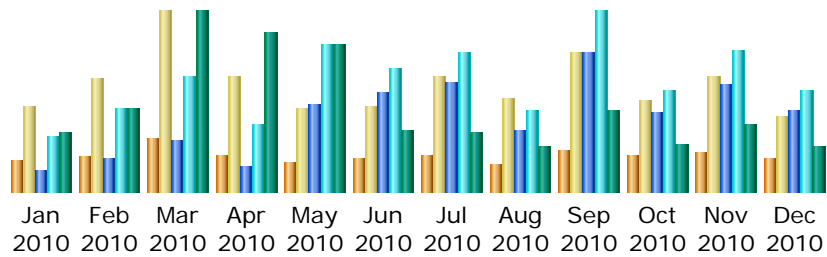
3) Cancel read access for a single user to a specific directory

In order to cancel the read access for a particular user, the corresponding ACL must be set to “no access”. This will simply remove the user from the ACL and thus it must be used with care since the user may be member of another top-level ACL that would give him read/write access. Also, the user must be member of the project in order to manipulate his ACLs. Warning: Since all users are members of itm_members, it is not possible to define something like “All itm_members have read access to /tags, however testsvn does not”. In order to do this, it is necessary to manually add each user to the project, except “testsvn”, thus manually doing what the “itm_members” pseudo-group did. Of course, in this case the “itm_members” must be removed from the project members.

Since a certain user can appear twice (or more) into an ACL, due to its membership to various groups, it became clear that a certain order must be applied. Otherwise, it is uncertain what permissions a particular user will have when the ACL is formed by combining various user groups.

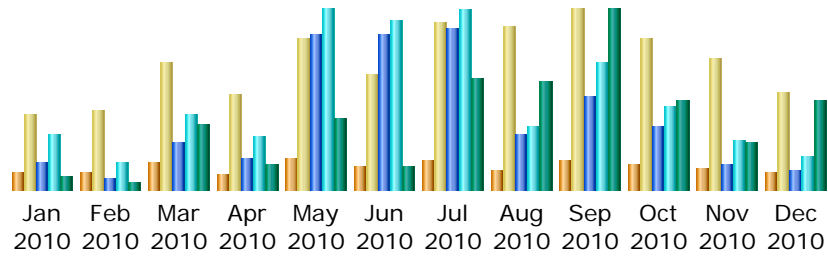
This was achieved by writing and applying a patch on the file used to generate the actual ACL from inside Gforge.

The following tables offer a view on the overall traffic on Portal and Gforge machines:



Month	Unique visitors	Number of visits	Pages	Hits	Bandwidth
Jan 2010	178	468	8654	22851	275.37 MB
Feb 2010	197	634	13582	34242	389.20 MB
Mar 2010	292	1002	20866	48314	850.67 MB
Apr 2010	199	637	10476	28058	753.21 MB
May 2010	166	467	36025	61641	697.60 MB
Jun 2010	187	470	41667	51452	287.69 MB
Jul 2010	195	635	45528	58112	279.26 MB
Aug 2010	149	515	25302	33634	212.06 MB
Sep 2010	228	778	57847	75040	386.61 MB
Oct 2010	196	512	32640	42396	225.44 MB
Nov 2010	214	642	44546	58827	317.10 MB
Dec 2010	183	420	33415	41859	211.68 MB
Total	2384	7180	370548	556426	4.77 GB

Table 1. ITM Portal usage report for the period Jan-Dec 2010



Month	Unique visitors	Number of visits	Pages	Hits	Bandwidth
Jan 2010	54	225	13976	29658	2.65 GB
Feb 2010	51	236	5852	14356	1.68 GB
Mar 2010	84	379	24520	40233	14.42 GB
Apr 2010	48	286	16063	28230	5.56 GB
May 2010	96	453	82663	95508	15.54 GB
Jun 2010	67	345	81925	89226	5.26 GB
Jul 2010	86	503	85433	95038	24.37 GB
Aug 2010	60	489	29588	33131	23.70 GB
Sep 2010	85	541	49711	67527	39.75 GB
Oct 2010	76	452	33283	44119	19.78 GB
Nov 2010	61	393	13297	25904	10.35 GB
Dec 2010	54	294	10040	17841	19.81 GB
Total	822	4596	446351	580771	182.87 GB

Table 2. ITM Gforge usage report for the period Jan-Dec 2010

The Portal and Gforge usage has considerably increased since the first months of the year. This will most likely require in the future new techniques for storing and offering access to the data. Combined with complex ACLs inside Gforge, this requires a lot of computing power since the ACLs must be verified and enforced on each file accessed from SVN.

A Catalog Querying Tool was developed and installed on the Portal machine in order to give web access to the Catalog Database. Currently there is no data stored in the database but its structure is available inside a MySQL database.

The web interface allows for searching through the database tables and to paginate results. Details will be available for each data entry. In order to allow easy integration of this tool with other, more complex tools, a web service interface was used for actually accessing the data. Therefore, the graphical interface is decoupled from the data access mechanism. The graphical interface is represented by a set of PHP pages displaying the data, while the query mechanism is represented by a web service based interface, that directly communicates with the MySQL engine.

RAPORTUL STIINTIFIC SI TEHNIC IN EXTENSO

(RST)

Atomic Data Calculation in support of AMNS activity

EFDA Task Agreement TFL

Code:

WP10-ITM-AMNS-ACT2

WP10-ITM-AMNS-ACT3

Atomic, Molecular, Nuclear and Surface Data in ITM

I. Introduction

The aim of the project is to **contribute to atomic data calculation in support of AMNS activity and to further development and maintenance of a module for implementing AMNS data to ITM-TF codes (WP10-ITM-AMNS-ACT2, WP10-ITM-AMNS-ACT3).**

Methods and codes exist for a wide range of electron-impact excitation and ionization processes; however, it is important to exercise these codes for situations required in plasma modelling. In particular, more attention must be given to excited initial states, as metastables may be very long-lived in the light elements (different from the case of high-Z elements) and their presence has a significant impact on power loss. It is proposed that collision data for $e^+He(n=2,3,4)$ should be revisited, especially near threshold. The same applies to other light targets: H, He, Li and Be and their ions and at least the $n=2$ initial state for B and C and their ions. (But checking what has been done for this to-date in ADAS.) Benchmark calculations at the highest level of theory should be done at least for He. These calculations are expensive as excitation from excited states can access many states of high angular momentum already at very low plasma temperature. Scaling rules and simplified methods for computation of processes beginning with excited states should be investigated as well, e.g., based on the distorted-wave (DW), plane-wave (PW), classical trajectory Monte Carlo (CTMC), or Exchange Classical Impact Parameter (ECIP) methods. However, calculations on the two-electron e^+H process already serve as a warning against the DW and PW methods at $n=4$ or $n=5$.

The present work refers to the calculation of atomic data for plasma spectroscopy in strong collaboration with the Atomic Data Analysis Structure International Project (**ADAS**). For **2010** the

project aims to provide collision calculation results in a standardised format necessary for module implementation. The following milestones have been envisaged for 2010: 1/ delivery of cross sections and collision strengths for electron-impact excitation of C atoms; 2/ delivery of cross-sections and collision strengths for electron-impact excitation of C IV ion ; 3/ delivery of a module to provide our atomic data to ITM-TF codes. As member of **ADAS** consortium, our group contributes to the development of **ADAS database**.

II. Summary of Results

Carbon ions and atoms are released from the walls into the edge plasma by a number of processes (physical sputtering, chemical erosion, radiation enhanced and thermal sublimation). Such impurities have a detrimental effect on plasma heating, and must be rapidly removed. A detailed knowledge of carbon transport properties is thus required, which can be obtained through spectroscopic monitoring. To deduce relevant physical quantities from the measurements requires accurate cross section data. We use the R-matrix method to calculate data for transitions between $n \leq 4$ states in carbon atoms. Two independent calculations were carried out. In the first, 28 target states were included in the R-matrix expansion. These are all 22 states with configurations $1s^2 2s^2 2p^3 l$ ($l = 0, 1, 2$), $1s^2 2s^2 2p^4 s$ and $1s^2 2s 2p^3$ that lie below the first ionisation threshold, together with the further three $1s^2 2s 2p^3$ states that lie just above this threshold and the three double excited $1s^2 2p^4$ states that lie still higher energies. In the second calculation, an additional 20 states with configurations $1s^2 2s^2 2p^4 l$ ($l = 1, 2, 3$) and $1s^2 2s^2 2p^5 s$ were included in the R-matrix expansion. Hence, in the first 28-state calculation all states with $n \leq 3$ were included in the expansion while in the second 48-state calculation all states with $n \leq 4$ were included. Results from a series of calculation are given as figures.

Data for electron-impact excitation of C^{2+} are of importance in the interpretation of both laboratory and astrophysical plasmas. For example, C^{2+} data have been used at the JET fusion experiment to model impurity inflow into the edge plasma from the surfaces with which the plasma interacts. The radiative transitions of primary importance are between levels of the $2s3l$ configurations. However, collisional mixing with the $2s4l$ levels as well as radiative cascades from them are important factors. Thus, collisional data through $n = 4$ are needed for accurate modelling of the flux of impurities into the plasma. Wave functions of the 1S (ground state), 3P and 1P states for the beryllium

isoelectronic sequence have been obtained in various approximations. The HF^{2p} orbitals for the ^{1P} and ^{3P} states are similar except for Be, where the ^{2p} orbital is quite diffuse for the ^{1P} state. The difference between the experimental $E(^1P) - E(^3P)$ and the HFE($^1P) - E(^3P)$ is 0.62 eV for Be and 1.17 ~ 1.40 eV for B⁺ ~ F⁵⁺. The disagreements are attributed to the correlation effects between the 2s and 2p electrons. This is confirmed by calculations. It is shown that a limited basis SCF calculation reproduces the above feature of the HF results if we treat the orbital exponents as the variational parameters. The use of the Slater values for the orbital exponents is shown to be inadequate especially for the Be ^{1P} state.

Separate account has been done to Fe-peak element: Co³⁺ ion. Results for electron impact excitation of forbidden lines in this ion have been obtained. Our work represents the first detailed collision calculation on this ion

Finally, the development of modules that take AMNS data from the ITM-TF data repository and provide them in a standardized format to ITM-TF codes, is needed. With this respect our group contributed in particular at the consolidation of the ITM AMNS database with Carbon and implementing a module for devolving AMNS data to the ITM database via the AMNS CPO, e.g. writing the C++ wrapper.

2. Scientific progress report

3.1. Provision of atomic data for the AMNS activity

3.1.1. Carbon atoms

The current state of plasma modelling requires data for the excitation of highly excited levels of the target ion/atom. Such calculations are extremely difficult to perform, as a large number of target excited states have to be included. Moreover the energy range in which the atomic data are required necessitates a calculation over very many partial waves, including a large number of continuum orbitals representing the scattered electron. In the work reported here the R-matrix computer packages have been used to calculate cross sections and collision strengths for important transitions to the $n = 3$ and $n = 4$ level of carbon.

Two independent calculations have been carried out for **C atoms**. These are:

a) Calculation **A**: 28 target states have been included in the R-matrix extension. These are all 22 states with configurations $1s^2 2s^2 2p^2$, $1s^2 2s^2 2p 3l$ ($l = 0, 1, 2$), $1s^2 2s^2 2p 4s$ and $1s^2 2s 2p^3$ that lie below the first ionization threshold, together with the further three $1s^2 2s 2p^3$ states that lie just above this threshold and the doubly excited $1s^2 2p^4$ states that lie at still higher energies.

b) In the second calculation, Calculation **B**, an additional 20 states with configurations $1s^2 2s^2 2p 4l$ ($l=1,2,3$) and $1s^2 2s^2 2p 5s$ have been included in the R-matrix expansion. Hence, in the first 28-state calculation all states with $n \leq 3$ are included in the expansion while in the second 48-state calculation all states with $n \leq 4$ are included. The energy levels of the states lying below the ionization threshold and included in the two calculations have been obtained.

The energy levels of these states lying below the ionization threshold and included in the two calculations are illustrated in figure 1.

For scattering calculation we used FARM based on a combination of propagation techniques to propagate the R-matrix from the boundary of internal region of the R-matrix box, to a radius where a Gailitis expansion of the asymptotic wave function can be applied. An estimate can also be made of the contribution to the cross section from higher partial waves omitted from the calculation.

Finally, the collision strengths for the $1s^2 2s^2 2p^2 \rightarrow 1s^2 2s^2 2p 3l$ transitions are given as a series of figures. The aim of the calculation was to provide cross sections and collision strengths over a wide temperature range.

Some evidence of resonance structures at low energies have been pointed out.

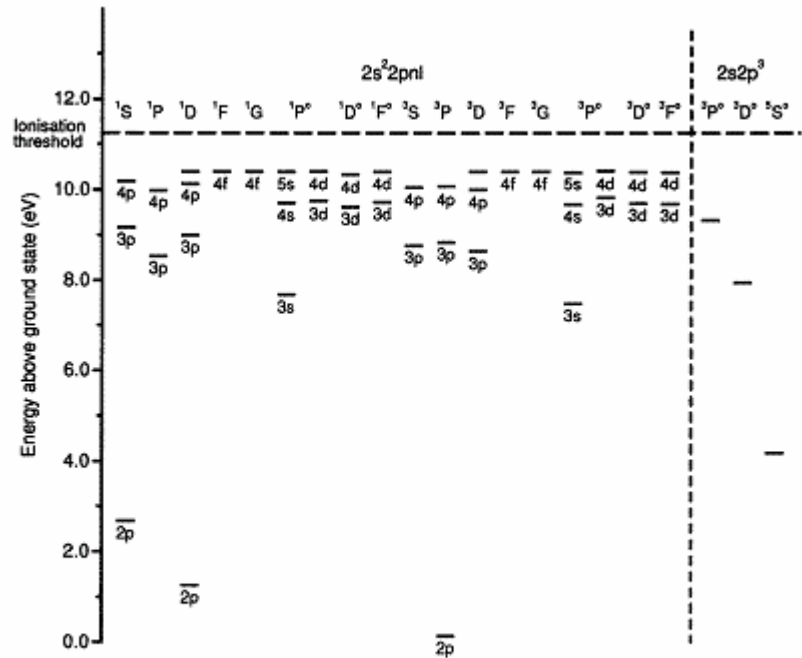


Figure 1. Energy levels of carbon below the first ionization threshold.

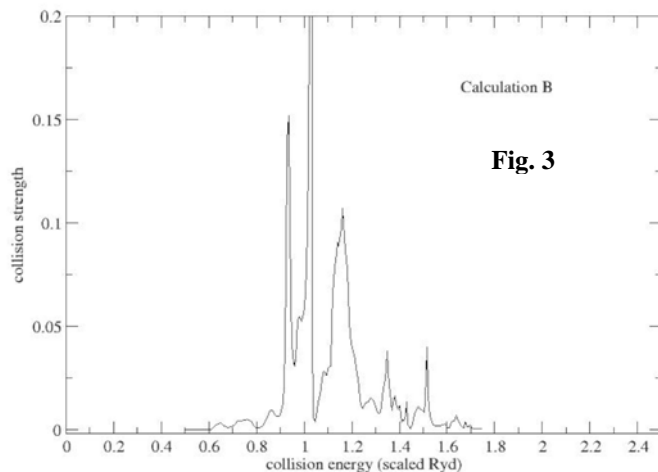
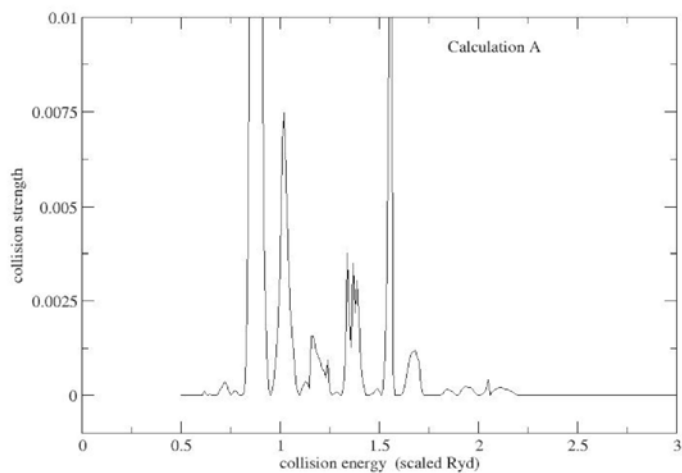


Fig. 3

Figures 2 and 3 give collision strengths as output from the calculation A and Calculation B, respectively.

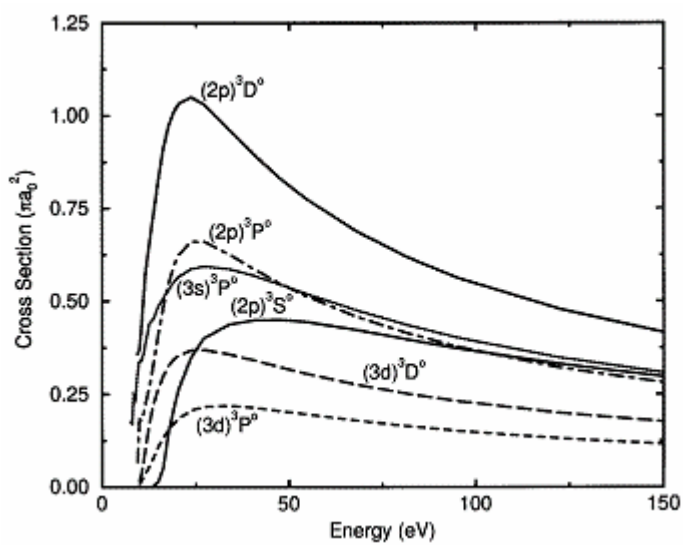


Fig.4

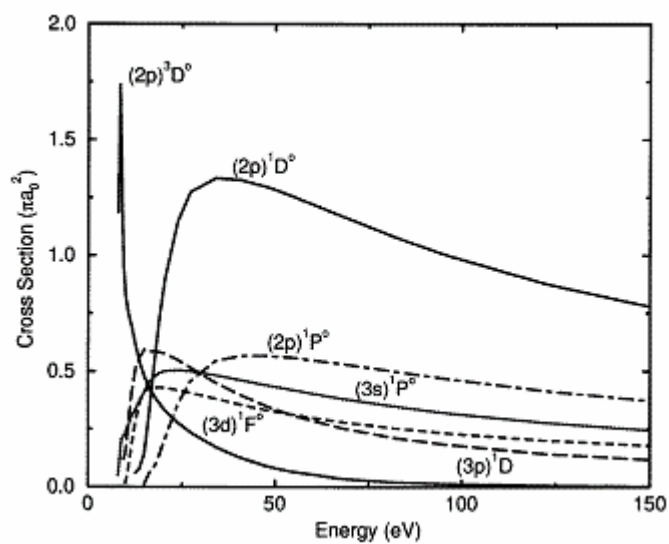


Fig.5

Cross sections as a function of collision energy for the most important transitions from the $1s^22s^22p^2$ 3P ground state are shown in Fig.4. In Fig.5, the cross sections as a function of collision energy are plotted for the most important transitions from the $1s^22s^22p^2$ 1D ground state. The two calculations yielded an enormous quantity of data in the form of cross sections, effective collision strengths and transition rates. Cross sections as a function of collision energy for the most important transitions from the $1s^22s^22p^2$ 1S ground state are shown in Fig.6.

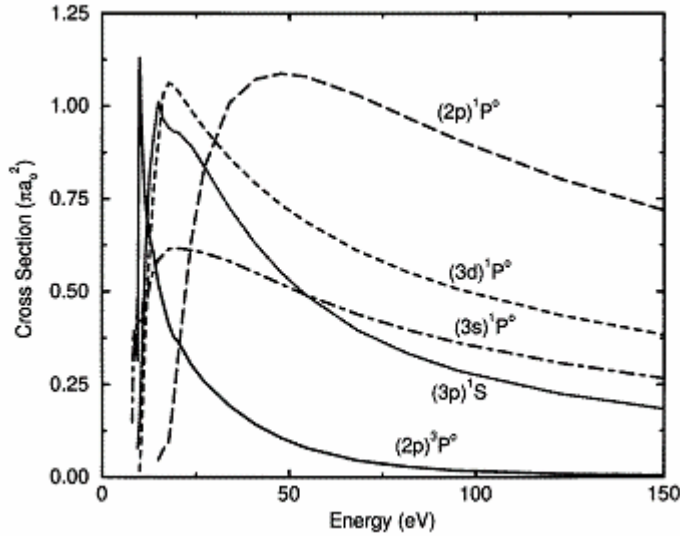


Fig.6

3.1.2. Cobalt ions (Co^{3+})

Transition probabilities of the iron group elements are of great importance in the calculation of non-local thermodynamic equilibrium (LTE) line formation. The open d-shells which occur in the low ionization stages of Fe, Ni and Co give rise to many low-lying target states that are strongly coupled in low and intermediate energy collisions. This complexity of the resonance structure for low energy electron scattering determines the complexity of atomic data calculation. With this respect, current theoretical methods and computational tools place more emphasis on the accurate representation of target electron wave functions than the study of other processes. The cross sections and rates must be determined at typically tens of thousands of energy values. When colliding electron penetrates the charge distribution of the target, many higher lying levels of the target can be virtually excited. Then the resultant collision complex can be accurately represented by accounting for these virtually excited states.

We have carried out the first detailed calculations of electron-impact excitation of forbidden transitions amongst states with $3d^6$, $3d^54s$ and $3d^54p$ configurations in Co^{3+} . We have initiated the LS-coupling calculation where the only 136 states arising from these three configurations are retained. In summary, we have performed three target model calculations: a) 3 LS-coupled *R*-matrix calculation including $3d^6$,

$3d^54s$ and $3d^54p$ states in the N -electron wave function expansion; b) we included in the R -matrix expansion all 136 LS coupled states which arise from six target configuration $3d^6$, $3d^54s$, $3d^54p$, $3p^43d^8$, $3p^43d^74s$ and $3p^43d^74p$ looking at the effect of configuration interaction. c) 9-state LS –coupled R -matrix calculation. Starting with the 136-level model, we included in the R -matrix expansion all 184 LS coupled states which arise from nine target configuration $3d^6$, $3d^54s$, $3d^54p$, $3p^43d^8$, $3p^43d^74s$, $3p^43d^74p$, $3p^53d^7$, $3p^53d^64s$ and $3p^53d^64p$.

We explored the effect of including configuration interaction wave functions both in the target states expansion and in the $(N + 1)$ -electron quadratically integrable functions expansion. The target states have been represented by elaborate configuration interactions in an attempt to account for electron correlation effects where it is essential to include the $3p^2 \rightarrow 3d^2$ core excitation in both the target and scattering wave functions. We found that this give rise to very distinctive two-particle one hole resonances at higher energies.

Finally, we mention that preliminary calculation including 272 states with a maximum 841 channels which includes the $3p^63d^54d$ configuration has been started. This large calculation requires more timing consuming with serial version of the R -matrix package program. In a future study we plan also include the states arising from the $3p^63d^54d$ configurations and to calculate collision strengths and effective collision strengths between all the states.

3.2. Delivery of a standardised module

The purpose is to provide the ITM-TF as a whole with up-to-date Atomic, Molecular, Nuclear and Surface (AMNS) data. Delivery of the data to codes is made by ITM developed standardized modules, where traceability (including provenance) of data is ensured.

To aid to data delivery, a module for the ITM codes have been written. This module makes use of the existing atomic data for carbon. In 2010 the ITM data structure Atomic data was finalised; a module taking Carbon data from the AMNS database and write them to the and ITM AMNS database via the data structure was devolved (more elements are in the pipeline); and a first version modules for reading AMNS data from the ITM database and deliver them to ITM codes were written.

Standardised module delivering AMNS data in a standardised form to ITM codes have been developed in Fortran90. They are now able to take data from an ITM database via the AMNS CPO. The existing modules are written in F90 and work on a C++ wrapper has started. This work will be completed in 2011, including documentation. Developed module need to be updated as more AMNS data are put into the ITM database. Extension to other programming languages supported by the ITM are also envisaged.

References

1. Stancalie V, „Forbidden transitions in excitation by electron impact in Co^{3+} : an R-matrix approach”, *Phys. Scr.* in press;
2. V.F. Pais , „ Web Services Usage in Distributed File Systems” *Fusion Engineering and Design* 85 , pp. 419-422 , **2010**,
3. V.F. Pais, S. Balme, H.S.Akpangny, F. Iannone, P. Strand, „Enabling remote access to projects in a large collaborative environment” *Fusion Engineering and Design* 85, pp. 633-636, **2010**
4. Guillerminet B, Iannone F, Imbeaux F, Manduchi G, Maslennikov A, Pais V, Strand P., „Gateway: New high performance computing facility for EFDA task force on integrated Tokamak modelling” *Fusion Engineering and Design* 85, pp. 410-414, **2010**
5. V. Stancalie, V. Pais, A. Mihailescu, O. Budriga, A. Oprea, „Recent Progress in the Theoretical Investigation of Laser-Atom, Laser-Plasma Interactions” *Romanian Reports in Physics* 62, pp. 528-545, **2010**

Scientific Report

**To the Contract IEU-1/11.08.2008
For the year 2010**

Project BS-13 : *Theoretical modeling of the RWM feedback control considering neoclassical toroidal viscosity and error field penetration*

Specific Objective II

a) *Derivation of the evolution equations for the plasma angular motion at the level of the plasma boundary and inner non-ideal MHD layers (that develop at the corresponding inner rational surfaces) to prove global plasma deceleration and NTV braking of the plasma rotation;*

b) *Electromagnetic and NTV torques calculation for shapes of the flux surfaces structure that include toroidicity, ellipticity, triangularity. The influence of the above parameters in finding the optimal less destabilizing error field spectrum will be calculated.*

Coordinator: Dr. I.G. Miron (CS III)
EFDA Task Agreement: WP10-MHD-03-03-xx-01

We continue our work by deriving a 2-dimensional dynamic theoretical model that proves the phenomena of global tokamak plasma deceleration and neoclassical toroidal viscosity braking of the plasma toroidal rotation as a result of the non-resonant (coupled) error field penetration. The term *global* refers to the locations of all the internal non-ideal, inertial layers that develop around every magnetic surface inside the plasma. The resistive wall mode dispersion relation obtained within the frame of the first objective will still be used with a well-thought substitution of the RWM's growth rate by the time derivative due to the dynamic treatment of the involved phenomena. The natural (flux) coordinates are used with the corresponding metric coefficients that are functions of the toroidicity, ellipticity and triangularity parameters. Mode coupling is considered, the theoretical model being a multimode model. An inhomogeneous resistive wall and an active system consisting of a number of rectangular, radially thin coils and detectors centred at the same local coordinates system are considered, the magnetic flux measured by the detector being amplified and fed back into the coils. To make possible an analytic treatment of the problem, the high plasma aspect ratio and the thin resistive wall approximations are used. Moreover, the resistive wall and the radial feedback coils and detectors are supposed to lie on magnetic surfaces.

Starting from the perturbed equation of motion of the plasma, we have obtained the toroidal component of the 2-dimensional dynamic equation of every non-ideal, inertial layer (IL) inside the plasma:

$$\frac{d\Omega_\varphi}{dt} + \frac{\eta_2}{\rho_m r_s^2 d_s^2} (\Omega_\varphi - \Omega_{\varphi 0}) = \frac{1}{8\pi^2 R_0^3 \rho_m r_s^2 d_s} T_{\varphi EM} \quad (1)$$

The above equation has been derived using flux coordinates under the $\mathcal{O}(\varepsilon^2)$ approximation, where $\varepsilon = a/R_0$, a being the plasma boundary "radial" flux coordinate and R_0 the major radius. Ω_φ is the toroidal angular velocity of the IL, ρ_m the plasma mass density, r_s the "radial" flux coordinate of the corresponding magnetic surface and $d_s = \delta_s / r_s$, where δ_s is the "radial" half-width of the layer. The second term in the left hand corresponds to the perturbed NTV torque with η_2 the perpendicular viscous coefficient [1]. By neglecting the

gyroviscous components of the perturbed stress tensor, the perpendicular component is the only component that does not cancel under IL volume integration. Ω_{φ_0} is the unperturbed IL toroidal angular velocity. $T_{\varphi EM}$ is the perturbed electromagnetic torque that corresponds to the coupling of the perturbation modes due to the error field action as the marginal stability of the perturbations is approached. The increased perturbation effects augment the perturbed NTV torque that decelerates and finally brakes the IL toroidal rotation.

Using the (r, θ, φ) flux (natural) coordinates that keep the magnetic field lines straight in (θ, φ) plane (to assure the only magnetic safety factor $q(r)$ radial dependence), and the parameterization of the perturbed magnetic field as $\mathbf{b} = \nabla \times \psi \mathbf{n}$, the following expression for perturbed electromagnetic torque have been obtained:

$$T_{\varphi EM} = (2\pi / \mu_0) \sum_m \text{Im} \int_0^{2\pi} \left[(mn_3 + i \partial n_3 / \partial \theta) \psi_s^{mn*} \Delta \psi_s \exp(-im\theta) \right] d\theta \quad (2)$$

$\mathbf{n} = \mathbf{B} / B$, where \mathbf{B} is the equilibrium magnetic field, n_3 its covariant toroidal component and m is the poloidal mode number subject to the summation of the Fourier components that the perturbations develop. n is the toroidal mode number. The index s refers to the flux coordinate r_s where the IL is positioned at. * denotes the complex conjugate of a number.

To use the resistive wall mode relations previously obtained within the frame of the first objective, we choose the natural relation between the two parameterizations (ψ and ϕ) of the perturbations, $\psi = \mathbf{n} \cdot \nabla \phi$, where $d\mathbf{b} / dt = \nabla \times (\mathbf{v} \times \mathbf{B})$ and the perturbed plasma velocity is $\mathbf{v} = (1/B) \nabla (d\phi / dt) \times \mathbf{B}$. Finally, we have obtained the following expression for the perturbed electromagnetic torque:

$$T_{\varphi EM} = -(4\pi^2 / \mu_0 R_0 r_s q_s^2) \sum_m \alpha_s^m (m - nq_s) \sum_{j=-3, j \neq 0}^3 [(m+j)(m+j-nq_s) / j] \text{Re} (\phi_{ts}^{mn} \phi_{ts}^{m+jn*}) \quad (3)$$

$$\times \left\{ [r_s / R_0 + a\epsilon (r \Lambda'_{js})'] \delta_{|j|1} - (2a\epsilon / r_s) [(j^2 - 1) \Lambda_{js} - r_s (1 - r_s q_s' / q_s) \Lambda'_{js}] (1 - \delta_{|j|1}) + \vartheta(\epsilon^2) \right\}$$

$\phi_{ts}^{mn} \equiv [d\phi^{mn} / dt]_{r=r_s}$, where $-\phi_{ts}^{mn}$ is the (m, n) Fourier component of the perturbed scalar electric potential at $r = r_s$. $\Lambda_{js} \equiv \Delta_s \delta_{|j|1} + E_s \delta_{|j|2} + T_s \delta_{|j|3}$ ($j=1, 2, 3$ and δ Kronecker delta).

Δ_s , E_s and T_s are the Shafranov shift, ellipticity and triangularity of the q_s corresponding magnetic surface. Their explicit expressions relative to their values at the boundary of the plasma were given earlier within the frame of the first objective.

α_s^m refers to the obtained single mode expression [2] for the jump in flux coordinates, $\Delta \psi_s$:

$$\alpha_s^m = \left\{ \mu_0 \pi R_0 q^2 \tilde{J}'_{\parallel} / (rq') \cot[-\mu_0 \pi R_0 q^2 \tilde{J}'_{\parallel} / (2mq')] \right\}_{r=r_s} \quad (4)$$

\tilde{J}_{\parallel} is the poloidally integrated equilibrium parallel current density. The well-known Wesson current profile is used. ' denotes the radial derivative. The expression (3) clearly shows the mode coupling prevalence in explaining the influence of the perturbed electromagnetic torque on the plasma stability. Due to the axisymmetry conditions, there is no explicit toroidal coupling. However, the perturbed quantities, ϕ_{ts}^{mn} , satisfy toroidally coupled equations due to the toroidal resistive inhomogeneity of the passive and active feedback systems. In $\vartheta(\epsilon)$ approximation, $j \neq 0$ from the above expression indicates that single mode theory (i.e. resonant error field) is unable to explain the involved phenomena. The resonant component influence has $\vartheta(\epsilon^2)$ magnitude, thus the adjacent mode coupling prevails.

With the vacuum parameterization of the perturbed magnetic field $\mathbf{b} = \nabla \chi$, in $\vartheta(\epsilon^2)$ approximation, from the continuity of the perturbed normal magnetic field across any IL we have obtained:

$$\begin{aligned} \chi_{w-}^{mn} = & -\frac{1}{c_{2,sws}^{m0}} \left\{ c_{1,sws}^{m0} \chi_{s+}^{mn} + \sum_{j=-3, j \neq 0}^3 \left[c_{1,sws}^{mj} - c_{2,sws}^{mj} \frac{c_{1,sws}^{m+j,0}}{c_{2,sws}^{m+j,0}} + (m+j)I_{2s}^j + \vartheta(\varepsilon^2) \right] / a \right\} \chi_{s+}^{m+j,n} \\ & + \frac{1}{r_s R_0 q_s} \left[m(m-nq_s) \phi_{s-}^{mn} + \sum_{j=-3, j \neq 0}^3 ((m+j)(m+j-nq_s) I_{1s}^j + \vartheta(\varepsilon^2)) \phi_{s-}^{m+j,n} \right] \end{aligned} \quad (5)$$

The obtained jump condition of the tangential perturbed magnetic field across the IL gives:

$$\chi_{s+}^{mn} = -(1/mR_0q_s) \{ (m-nq_s) r_s \phi_{ts-}^{mn} - [m - \alpha_s^m r_s (m-nq_s) + \vartheta(\varepsilon)] \phi_{ts-}^{mn} \} \quad (6)$$

The coefficients of the above equations are obtained from the derivation of the 2-dimensional RWM dispersion relation and are defined within the frame of the first objective.

Finally, keeping into account the dynamic form of the plasma and feedback equations, a long and straightforward calculus leads to a $2L$ dynamic system of equations that gathers the full plasma-IL-vacuum-feedback system behavior in terms of time derivatives of the perturbed magnetic fluxes across the IL:

$$\sum_{h,k} \sum_{\alpha=0}^4 \left(P_{mn}^{hk\alpha} \partial^\alpha \phi_{ts-}^{hk} / \partial t^\alpha + \tilde{P}_{mn}^{hk\alpha} \partial^\alpha \phi_{ts-}^{hk} / \partial t^\alpha \right) = 0 \quad (7)$$

$$\sum_{h,k} \sum_{\alpha=0}^3 \left(F_{mn}^{hk\alpha} \partial^\alpha \phi_{ts-}^{hk} / \partial t^\alpha + \tilde{F}_{mn}^{hk\alpha} \partial^\alpha \phi_{ts-}^{hk} / \partial t^\alpha \right) = 2R_0q_s \sum_{h,k} \bar{\beta}_{0w-}^{hk0} \chi_{c+}^{hk} \quad (8)$$

$L = (m_2 - m_1 + 1)(n_2 - n_1 + 1)$ and $h, m = m_1, \dots, m_2$, $k, n = n_1, \dots, n_2$. $P_{mn}^{hk\alpha}$ and $\tilde{P}_{mn}^{hk\alpha}$ are explicitly derived coefficients as functions of all the plasma bulk and IL parameters taken into account: ρ_s (mass density), η_2 , δ_s (layer width), q_s , r_s , p_s (pressure), Δ_s , Δ'_s , E_s , E'_s , T_s , T'_s and $\Omega_{\varphi 0}$ (unperturbed plasma rotation). $F_{mn}^{hk\alpha}$ and $\tilde{F}_{mn}^{hk\alpha}$ are explicit analytic derived coefficients as functions of all the feedback parameters taken into account (the same parameters that we have used to derive the 2-dimensional RWM dispersion relation) and $\Delta_{w,f,d}$, $\Delta'_{w,f,d}$, $E_{w,f,d}$, $E'_{w,f,d}$, $T_{w,f,d}$, $T'_{w,f,d}$. The right hand term in (8) includes the non-resonant error field contributions, χ_{c+}^{hk} . Due to the fact that the error field is static, the coefficients $\bar{\beta}_{0w-}^{hk0}$ are not time dependent. In the following we apply the same mathematical method we have built for the cylindrical model we have derived in a previous work. By applying the Laplace transformation of the system (7) and (8), $\bar{f}(\tau) = \int_0^\infty f(t) \exp(-t\tau) dt$, we get:

$$\begin{aligned} \sum_{j,k} \left[\left(\sum_{\alpha=0}^4 \tau^\alpha P_{mn}^{jk\alpha} \right) \overline{\phi_{ts-}^{hk}} + \left(\sum_{\alpha=0}^4 \tau^\alpha \tilde{P}_{mn}^{jk\alpha} \right) \overline{\phi_{ts-}^{hk}} \right] &= 0 \\ \sum_{j,k} \left[\left(\sum_{\alpha=0}^3 \tau^\alpha F_{mn}^{jk\alpha} \right) \overline{\phi_{ts-}^{hk}} + \left(\sum_{\alpha=0}^3 \tau^\alpha \tilde{F}_{mn}^{jk\alpha} \right) \overline{\phi_{ts-}^{hk}} \right] &= 2R_0q_s \sum_{j,k} \frac{1}{\tau} \bar{\beta}_{0w-}^{hk0} \chi_{c+}^{hk} \end{aligned} \quad (9)$$

The following initial conditions have been used: $\phi_{ts-}^{hk(i)}(t=0+) = 0$, $\phi_{ts-}^{hk'(i)}(t=0+) = 0$ for $i \geq 0$, where $(i) \equiv \partial^i / \partial t^i$. At $t=0$, the magnetic error field provides the only perturbations spectrum. Using the method and the notations presented in [3], the Leibniz expansion of the determinant of the above system of equations gives

$$\Delta_s \equiv \sum_{i=1}^{7L+1} \tau^{i-1} \sum_{\substack{l_1, \dots, l_{2L}=1 \\ \text{distinct}}}^{2L} \text{sgn}(l_1, \dots, l_{2L}) \sum_{\substack{\alpha_1, \dots, \alpha_{2L}=0 \\ \alpha_1 + \dots + \alpha_{2L} = i-1}}^4 \prod_{p=1}^{2L} \Gamma_{p\alpha_p}^{l_p} \quad (10)$$

with

$$\begin{aligned} \Gamma_{p\alpha}^{l_p} = & P_p^{l_p\alpha} H(L-l_p)H(L-p) + \tilde{P}_p^{l_p\alpha} H(l_p-L-1)H(L-p) + \\ & + F_p^{l_p\alpha} H(L-l_p)H(p-L-1)H(3-\alpha) + \tilde{F}_p^{l_p\alpha} H(l_p-L-1)H(p-L-1)H(3-\alpha) \end{aligned} \quad (11)$$

H is the Heaviside unit step function. The relations between the index ordering and the mode numbers can be found in [3]. The relation (10) easily allows to numerically obtain the roots $\{\tau_i\}_{i=1,\dots,7L}$ of $\Delta_s = 0$. In the same manner, to obtain the solutions $\phi_{is-}^{l_i}$, the $\Delta_s^{l_i}$ determinant is built by replacing the corresponding column with the inhomogeneous (error field) column. Using (10), $\Gamma_{p\alpha}^{l_p}$ is replaced by:

$$\begin{aligned} \Gamma_{p\alpha}^{l_p} &= P_p^{l_p\alpha} H(L-l_p)H(L-p)(1-\delta_{l_p l_i}) + \tilde{P}_p^{l_p\alpha} H(l_p-L-1)H(L-p) + \\ &+ F_p^{l_p\alpha} H(L-l_p)H(p-L-1)H(3-\alpha)(1-\delta_{l_p l_i}) + \left(2R_0 q_s \sum_{l_p} \tilde{\beta}_{0w-}^{l_p} \mathcal{X}_{c+}^{l_p} \right) H(L-l_p)H(p-L-1)\delta_{l_p l_i} \quad (12) \\ &+ \tilde{F}_p^{l_p\alpha} H(l_p-L-1)H(p-L-1)H(3-\alpha) \end{aligned}$$

The solutions are $\overline{\phi_{is-}^{l_i}} = \Delta_s^{l_i} / (\tau \Delta_s)$. Using the partial fraction decomposition and the inverse Laplace transformation, we finally have obtained:

$$\phi_{is-}^{l_i}(t) = \left(\Delta_s^{l_i} / \Delta_s \right)_{\tau=0} + \sum_{j=1}^{7L-L_0} \left[(\tau - \tau_j) \Delta_s^{l_i} / (\tau \Delta_s) \right]_{\tau=\tau_j} \exp(\tau_j t) \quad (13)$$

L_0 is the number of eventually zero coefficients that correspond to the highest consecutive polynomial exponents. According to the *Initial Value Theorem*, it can be easily proved that the above solution satisfies the initial conditions we have used. Using solutions (13), the electromagnetic torque (3), can now be calculated. By introducing the obtained expression of (3) in the 2-dimensional dynamic equation of the IL (1), we are finally able to provide the following analytic solution for the IL toroidal angular velocity:

$$\begin{aligned} \Omega_\varphi(t) &= \Omega_{\varphi 0} \left[1 + \exp(-\eta_2 t / \rho_m r_s^2 d_s^2) \right] \\ &+ \frac{d_s}{4\mu_0 r_s R_0^4 q_s^2} \sum_m \alpha_s^m \sum_{j,k=0}^{7L-L_0} \frac{e_{jk}^{mn} + e_{kj}^{m*}}{\eta_2 + \rho_m r_s^2 d_s^2 (\sigma_j + \sigma_k^*)} \exp[(\sigma_j + \sigma_k^*)t] \quad (14) \end{aligned}$$

$\{\sigma_i\}_{i=0,\dots,7L-L_0} = (0, \{\tau_i\}_{i=1,\dots,7L-L_0})$ are the roots of $\sigma \Delta_s = 0$ and e_{jk}^{mn} are explicit expressions of plasma and feedback parameters:

$$\begin{aligned} e_{jk}^{mn} &= (m - nq_s) \gamma_j^{mn} \sum_{\substack{p=-3 \\ p \neq 0}}^3 \frac{1}{p} (m+p)(m+p-nq_s) \gamma_k^{m+p,n} * \\ &\times \left\{ [r_s / R_0 + a\varepsilon(r\Lambda_{ps}')'] \delta_{|p|1} - (2a\varepsilon / r_s) [(p^2 - 1)\Lambda_{ps} - r_s(1 - r_s q_s' / q_s)\Lambda_{ps}'] (1 - \delta_{|p|1}) + \vartheta(\varepsilon^2) \right\} \quad (15) \end{aligned}$$

where $\gamma_j^{l_i} = \left[(\sigma - \sigma_j) \Delta_s^{l_i} / (\sigma \Delta_s) \right]_{\sigma=\sigma_j, j=0,\dots,7L-L_0}$.

It can be clearly seen that all the error field poloidal modes couple with the IL corresponding poloidal mode within this multimode model description. On the other hand, a non-resonant error field couples with all the poloidal modes whose magnetic surfaces the inertial layers develop at. The intrinsic toroidal mode coupling effects are contained within the $\gamma_j^{l_i}$ terms and they are due to the passive and active feedback system toroidal resistive inhomogeneity. Within the single mode theory, only a $\vartheta(\varepsilon^2)$ term would remain in the second right hand term of (14) and the $\vartheta(\varepsilon)$ term would disappear as well as the main and global error field destabilizing effect.

The data used to plot the $\Omega_\varphi(t)$ dependencies is: $a = 0.15m$, $R_0 = 0.92m$, $q_a = 2.95$, $q_0 = 1.03$, $\Omega_{\varphi 0} = 5kHz$, $\rho_s = 6.5 \cdot 10^{-7} kg/m^3$, $\eta_2 = 15 \cdot 10^{-5} kg \cdot m^{-1} s^{-1}$, $B_{\varphi 0} = 0.35T$, $r_d = 0.16m$, $r_w = 0.175m$, $r_f = 0.2m$, $N = 5$, $G_d = 15$, $G_p = 25$, $\delta_f = 0.005m$, $\delta\theta_f = \delta\varphi_f = \pi/200$, $\Delta\theta_f = \pi/6$, $\Delta\varphi_{w2} = \pi/6$, $\Delta\varphi_f = 0.9 \cdot \Delta\varphi_{w2}$, $\Delta\theta_d = \pi/9$, $\Delta\varphi_d = 0.8 \cdot \Delta\varphi_{w2}$, $\{\theta_p\}_{p=1,\dots,7} = (0, \pi/6, \pi/3, \pi/2, 3\pi/2, 5\pi/3, 11\pi/6)$, $\delta_{w1} = \delta_{w2} = 0.012m$. The above data is characteristic for the HBT-EP tokamak plasma.

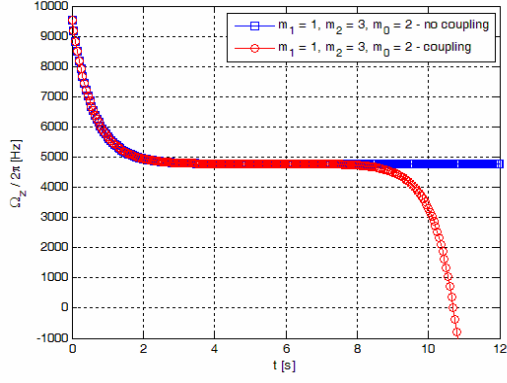


Fig. 1

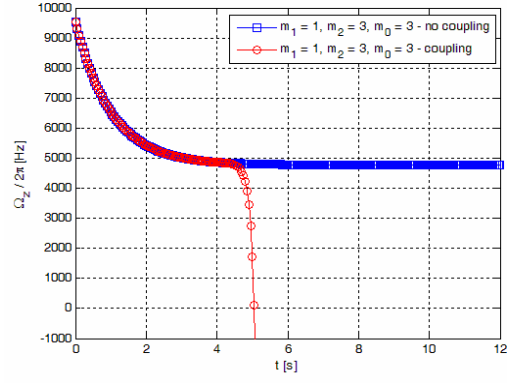


Fig. 2

The main achievement of the 2-dimensional theoretical model we have presented has been accomplished. Figures 1 and 2 clearly illustrate the deceleration and braking of the plasma rotation at the level of the inertial layers we have considered. Figure 1 shows the deceleration of the rotation of the IL developed around the magnetic surface that corresponds to the (2,1) internal mode, whereas Figure 2 illustrates the same effect for the boundary marginal (3,1) mode. The (1,1) or (2,1) modes have the same dependency type. The influence of the error field mode coupling is obvious compared to the no-coupling case. In fact, the coupling of the modes is responsible for the increase of the NTV torque influence that finally brakes the plasma rotation. The solution (14) exhibits the explicit dependence on η_2 .

Unfortunately, due to its intrinsic limitations, the Matlab code we have built is significant time consuming. A more elaborated numerical code would provide more accurate results for more neighboring modes taken into account.

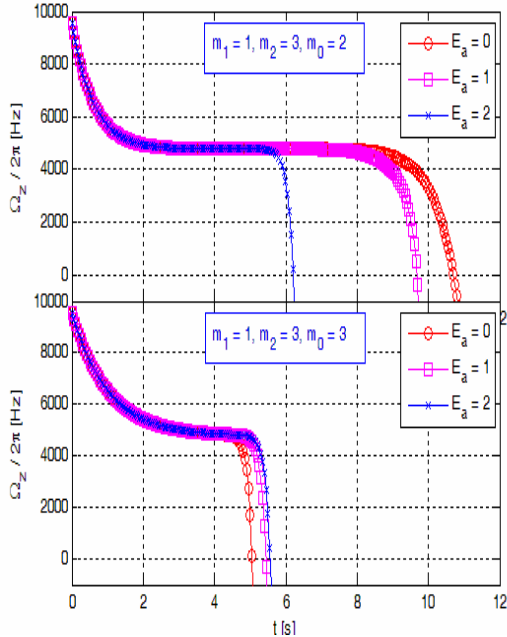


Fig. 3

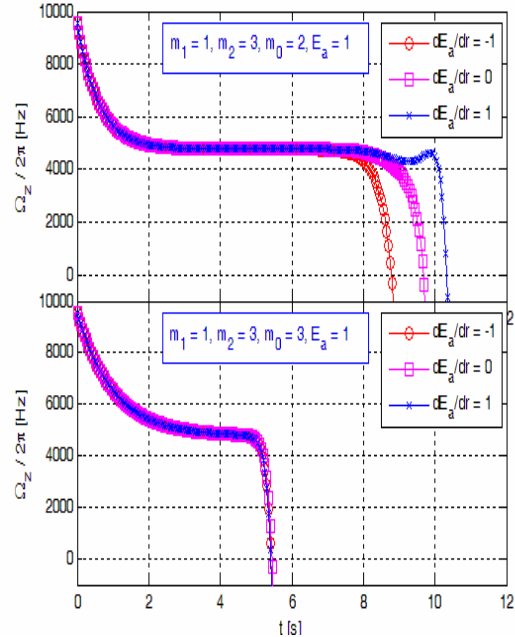


Fig. 4

Figure 3 shows the dynamic dependence of $\Omega_\phi(t)$ as the plasma boundary ellipticity, $E_a = 2R_0 [Z|_{\omega=\pi/2} - (R-R_0)|_{\omega=\pi}] / [Z|_{\omega=\pi/2} + (R-R_0)|_{\omega=\pi}]^2$, varies. (R, ω, Z) are the orthogonal cylindrical coordinates and ω is the poloidal geometrical angle related to θ by $\omega = \theta - (r/R_0) \sin \theta - a\epsilon [\Delta' \sin \theta + (E/r - E')/2 \sin 2\theta + (2T/r - T')/3 \sin 3\theta] + \vartheta(\epsilon^2)$. For internal plasma modes (2,1) or (1,1) the ideal configuration for less destabilization corresponds to $E_a = 0$, i.e. the cylindrical form for the plasma column. On the contrary, for the more unstable external kink mode (3,1), the $E_a > 0$ condition provides less

destabilization. However, for $E_a > 0$ (condition required by other stability considerations, beyond the present study) the less destabilizing configuration implies $dE_a/dr > 0$ (Figure 4) for all the internal modes. The increased ellipticity of the magnetic surfaces as their "radial" coordinate grows provides less instability. Consequently, the combined effect of ellipticity and its radial derivative assumes that the optimal error field spectrum involves the prevalence of higher internal mode amplitudes compared to the external kink (or RWM) mode amplitude. A lower (3,1) mode amplitude minimizes the coupling with its adjacent internal modes and the result is a slower deceleration of the corresponding IL.

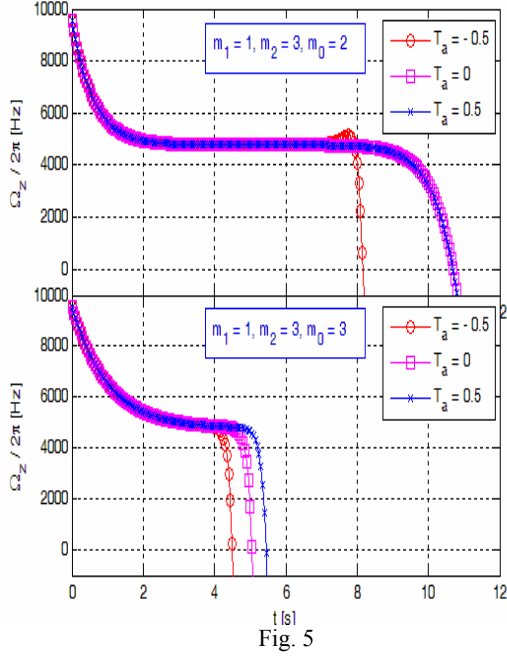


Fig. 5

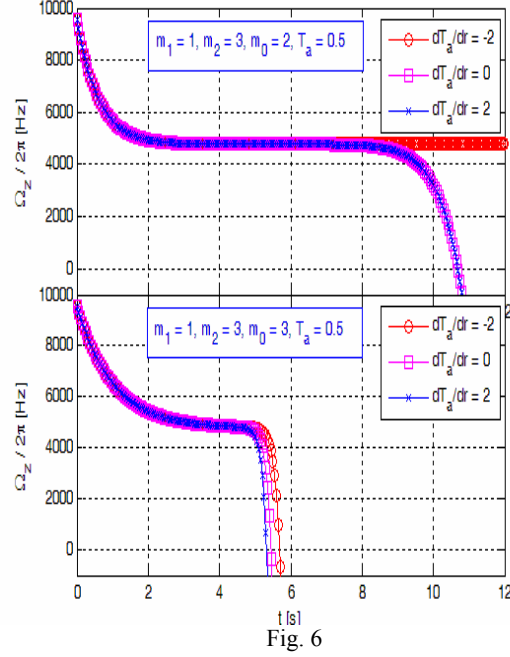


Fig. 6

Figures 5 and 6 show the IL toroidal angular velocity $\Omega_\phi(t)$ dynamic dependencies for different plasma boundary triangularities $T_a = (R_0/Z|_{\omega=\pi/2})(R-R_0)|_{\omega=\pi}/Z|_{\omega=\pi/2} + 1$ and dT_a/dr , respectively. The less destabilizing configuration corresponds to $T_a \geq 0$ for internal modes and $T_a > 0$ for the (3,1) mode (Figure 5). Unlike the ellipticity case, the $dT_a/dr < 0$ condition is less destabilizing for all the modes (Figure 6). Again, under the $T_a > 0$ and $dT_a/dr < 0$ conditions, the optimal error field spectrum assumes a lower (3,1) mode amplitude condition to be fulfilled. All the above analysis achieved for every mode of instability taken into account provides the parametric data in order to find the optimum non-resonant error field spectrum as to obtain the less destabilizing configuration.

Conclusions

An axisymmetric 2-dimensional theoretical model has been built to prove the global plasma deceleration and NTV braking of the plasma rotation. An analytic expression for any inertial layer toroidal angular rotation has been provided. A multimode treatment has been considered. Within the large aspect ratio assumption, it has been demonstrated that the error field modes coupling effect prevails and the single mode theory is unable to provide realistic results. The influence of toroidicity, ellipticity and triangularity parameters in finding the less destabilizing configuration has been showed.

References

- [1] S.I. Braginskii, *Rev. Plasma Phys.* **1** (1965) 205.
- [2] C.C. Hegna and J.D. Callen, *Phys. Plasmas* **1** (1994) 2308.
- [3] I.G. Miron, *Plasma Phys. Control. Fusion* **50** (2008) 095003.

Scientific Report for the year 2010
To the Contract 1EU-3/11.08.2008 Sub-Project BS-6

Authors: V. Anita, C. Costin, G. Popa, L. Sirghi, M. L. Solomon

Subject: Plasma diagnostics

Specific Objective: Characterisation of Pilot-PSI plasma beam by electrical methods (electrostatic analysers) WP10-PWI-04-04

A multiple tungsten plane probe system (61 probes disposed in 2D with circular symmetry – see Fig. 1) was installed in the centre of Pilot-PSI target (at FOM, The Netherlands). A laser beam was used to centre the probe system on the axis of the device. Mainly, two types of measurements were made: *i*) measurements of the plasma current drawn by the grounded collectors and *ii*) measurements of floating potential of the collectors. The measurements were performed for different experimental conditions: hydrogen gas flow of 3 slm, magnetic field strength of 0.4, 0.8 and 1.2 T and different plasma-source currents 80, 100, 120 and 140 A. The frequency of the simultaneous data acquisition (National Instruments data acquisition system) was either 50 KSamples/sec/ch, 500 KSamples/sec/ch or 1 MSamples/sec/ch.

Multi-probe system – current measurements at the target.

We correlated our experiments with temperature measurements on the surface of the target by using a non contact method with an infrared camera. A quartz vacuum window and a plane mirror permitted to focus the infrared radiation from the target surface on the entrance lens of the infrared temperature measurement camera. These measurements revealed a very high increase of the target surface temperature in the centre and a sharp decrease on the edge of the target. The surface temperature is influenced by both the plasma source current and the applied magnetic field strength. The measured values varied between 320 °C (at 80 A and 0.4 T) and 2500 °C (at 140 A and 1.2 T). These measurements indicate very difficult conditions for electrical diagnosis devices in Pilot-PSI.



Fig. 1. Front picture of the multi-probe system with 61 collectors

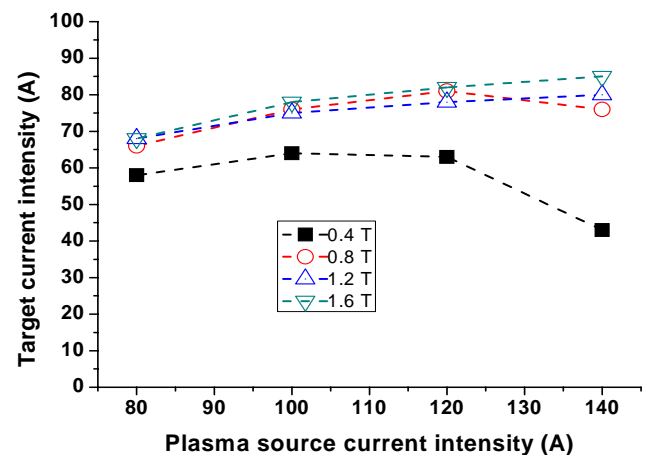


Fig. 2. Target current intensity versus plasma-source current (magnetic field strength as parameter)

The currents flowing through a compact copper target (grounded) were measured with Tektronix digital oscilloscope DPO4034 - 4 channels, 350MHz and 5Gs/s sample rates. In the case of $B = 0.4$ and 0.8 T the registered target current was maximum at the plasma-source current of 120 A. In the case of 1.2 and 1.6 T the target current increased continuously with the increase of the plasma-source current (Fig. 2). Although the currents collected by the grounded target are negative (showing electron dominated currents), they are plotted in Fig. 2 in absolute value.

The 61 plane probe system (0.63×10^{-6} m² single electrode area) was used to measure the radial variation of the current density on the target. The probes were protected by a carbon plate of 38 mm in

diameter, in contact with high density plasma. Figure 3 presents the variation of the probe current density with the radial position from the centre of the plasma beam, having the discharge current intensity and the applied magnetic field as parameters. All the probes were grounded.

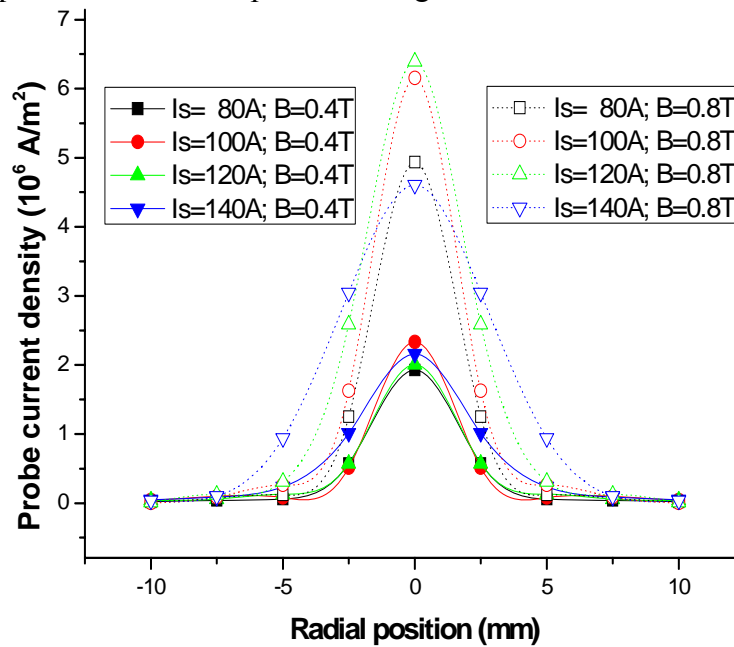


Fig. 3. Radial variation of the probe current (with discharge current intensity I_s and applied magnetic field strength B as parameters)

The measurements revealed a very non uniform current density distribution on the target surface, with the maximum value in the centre of the plasma beam. The current density on the compact target increased with the discharge current for the same applied magnetic field (from $5.11 \times 10^4 \text{ A/m}^2$ at 80 A to $7.08 \times 10^4 \text{ A/m}^2$ at 140 A and 1.2 T, as example). The current density measured on the probe in the centre of the plasma beam increased with the plasma-source current from 80 to 120 A but decreased at 140 A, for the same applied magnetic field intensity (from $7.2 \times 10^6 \text{ A/m}^2$ at 80 A to $4.87 \times 10^6 \text{ A/m}^2$ at 140 A and 1.2 T).

Two 2D distributions of the current intensity measured for a magnetic field strength of 0.8 T are plotted in Fig. 4. The negative values of the measured currents are related to the electron dominated current received by the grounded collectors. The 2D distributions showed a good cylindrical symmetry and a strong radial gradient of the current could be noticed in all cases. The maximum of the current distribution is recorded almost in the centre of the target. The increase of the magnetic field creates a better plasma confinement, reflected in a strong amplification of the measured electric current intensity and steep radial gradients. The maximum values of the measured currents intensity were $\sim 2.4 \text{ A}$ at 0.4 T and $\sim 4.8 \text{ A}$ at 0.8 T, in the centre of the plasma column.

The multi-plane probe system worked well up to 1.2 T but the central probe was melted at 1.6 T as a consequence of the high current density determined by the confinement of the plasma beam at this high magnetic field.

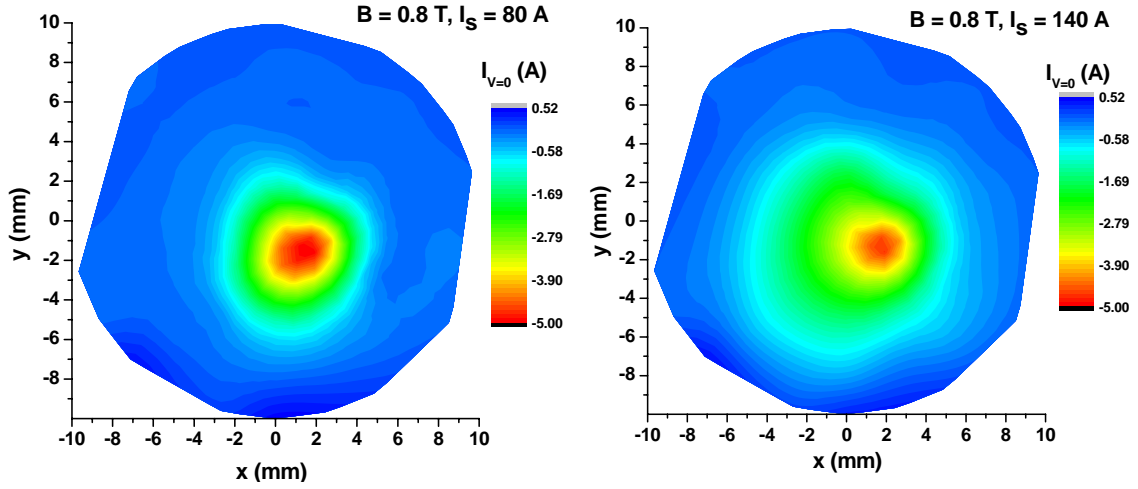


Fig. 4. 2D distributions of the current intensity for two plasma-source currents of 80 and 140 A ($B = 0.8$ T)

Multi-probe system – floating potential measurements at the target.

The 2D floating potential distributions measured for a magnetic field strength of 0.8 T are plotted in Figure 5. A good cylindrical symmetry is also noticed on the 2D floating potential distributions. The measured floating potential ranges between ~ 0 V at the side of the beam and -70 V at 0.4 T up to ~ -165 V at 0.8 T in the centre of the plasma column. An increase of the total discharge current was observed to decrease the floating potential at the target. The magnetic field dependence is explained by a decreasing cross field conductivity. Both floating potential and current intensity followed the time evolution of the magnetic field during its switching-on/off. To determine the electron temperature and density in the plasma column, Thomson scattering measurements were made by FOM researchers simultaneously with the electrical measurements.

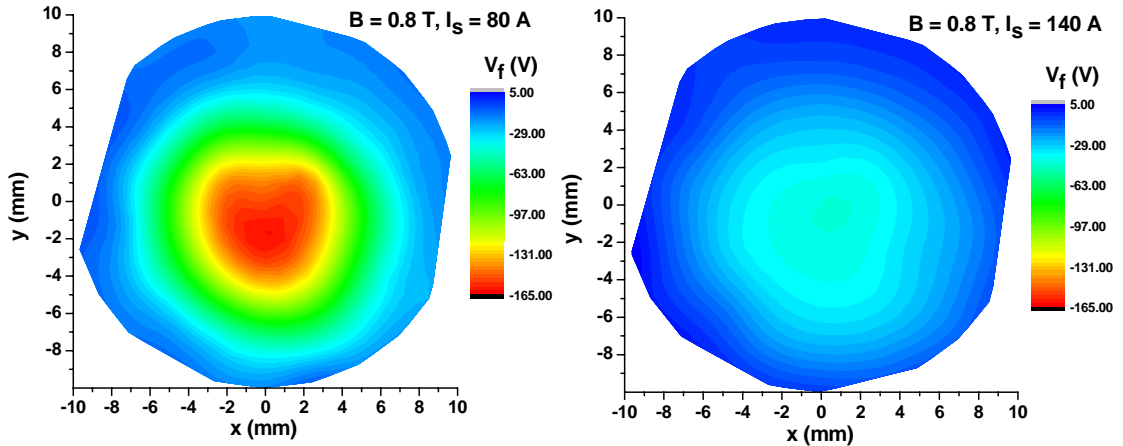


Fig. 5. 2D distributions of the floating potential for two plasma-source currents of 80 and 140 A ($B = 0.8$ T)

Cross-correlation signal analysis.

In signal processing, cross-correlation is a measure of similarity of two waveforms as a function of a time-lag applied to one of them. For two continuous functions, f and g , the cross-correlation is defined as:

$$(f * g)(t) = \int_{-\infty}^{\infty} f^*(\tau) g(t + \tau) d\tau$$

where f^* denotes the complex conjugate of f . Similarly, for discrete functions, the cross-correlation is defined as:

$$(f * g)[n] = \sum_{m=-\infty}^{\infty} f^*[m] g[n + m]$$

If the cross-correlation signal has a well defined peak it means that the two functions are similar and the time-lag value corresponding to the peak indicates the delay between the two functions. In the case of the cross-correlation of a signal with itself (called auto-correlation), there will always be a peak at a lag of zero.

This analysis technique was applied to study the time correlation between the current intensity signals measured by different collectors of the analyzer. The main purpose of this analysis was to study the rotation of the magnetized plasma column. As it can be seen in Fig. 1, the tungsten probes were arranged on four concentric circles of different radii (2.5, 5, 7.5 and 10 mm). We chose a collector on each circle and we calculated the cross-correlation between the signals measured on that collector and six other collectors in his neighbourhood, from the same circle (3 collectors before and 3 after him). An example of the obtained cross-correlation signals for 7 collectors disposed on the 3rd circle is presented in Fig. 6. The auto-correlation signal of the reference collector ch 309 is plotted in light blue. It can be noticed that all 6 signals are correlated with the reference one and the delay between each two neighbour signals is 1 μ s. This confirms that the plasma column rotates and the distance between two adjacent collectors from the third circle is covered in 1 μ s. The corresponding rotation velocity at the radial position of 7.5 mm is about 2.6 km/s. It has to be mentioned that the data acquisition frequency was 1 MHz meaning that the time delay between two consecutive acquired data on the same channel was 1 μ s. This places the result of the cross-correlation analysis at the limit of the time resolution, reflected in an imprecision of the calculated plasma rotation velocity of about 50%.

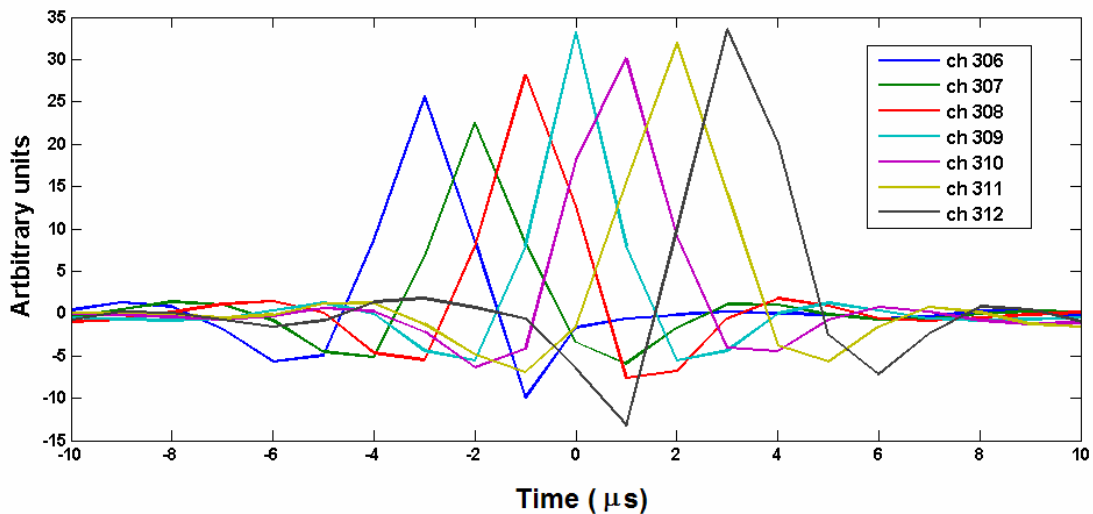


Fig. 6. Cross-correlation analysis of the signals measured on the collectors from the third circle of the multi-probe system

From the floating potential measurements we could estimate the radial electric field and calculate the \mathbf{ExB} drift velocity. The radial profile of the electric drift velocity is a parabolic one having the maximum value of ~ 10 km/s obtained for a radial position of ~ 5 mm. For the radial position of 7.5 mm (third circle) the electrical drift velocity is ~ 7 km/s. The real rotation velocity is smaller compared to the electric drift velocity because the first one is influenced also by the diamagnetic drift, the collisions between particles, etc. The rotation of the plasma column could also be observed representing successive (1 μ s delay) 2D current intensity distributions.

Measurements with 3-grid electrostatic analyzer.

An ion energy electrostatic analyzer with 3 grids has been manufactured and also mounted in the centre of Pilot-PSI target (Fig. 7). The stainless steel grids and the collector (disks of 10 mm in diameter) were mounted in a stainless steel Faraday cup. The active area of the analyzer was limited to a circular opening of 0.5 mm in diameter of a carbon diaphragm mounted in front of the grids. A biasing circuit and data acquisition system for analyzer I-V characteristics was built based on a source measuring unit (SMU) mounted on the XPI device of National Instruments. The SMU was controlled by a home-made LabView software.

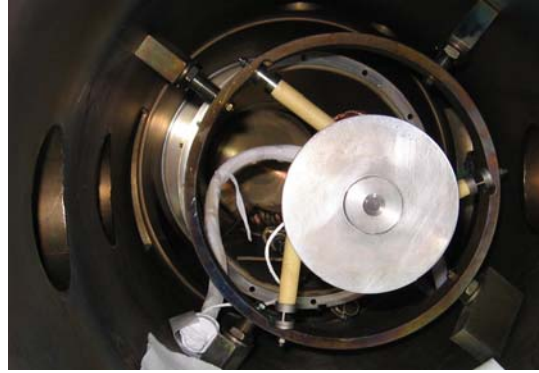


Fig. 7. Ion energy analyzer mounted on the target of Pilot-PSI

The electrostatic analyzer was biased with respect to the ground. The potential of the hydrogen plasma column during the confinement in the magnetic field was negative, varying between -10 V and -40 V as function of the magnetic field intensity and discharge current intensity. The plasma potential decreased with the increase of the discharge current and increased with the increase of the magnetic field intensity. We have successfully acquired current-voltage characteristics of the analyzer. The acquired data were processed off-line by a home-made software. The I-V characteristics revealed that the ion energy distribution function with respect to the ground is centred at the electrostatic energy of ions at plasma potential, i.e. 10-15 eV for $B = 0.4$ T. A typical I-V characteristic and ion energy spectra are shown in Fig. 8. Unfortunately, due to certain limitations of the I-V data acquisition system we could not resolve the fine structure of the ion energy spectrum, but the experimental data are indicating that the thermal ion energies are spread into less than 1eV.

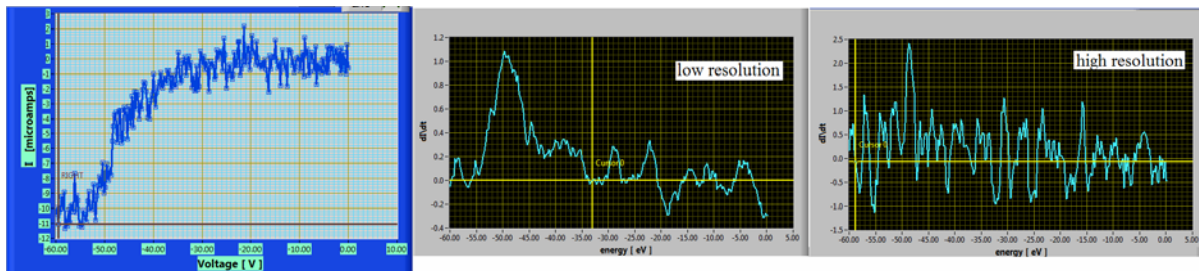


Fig. 8. Typical I-V characteristic of the analyzer and the corresponding low- and high-resolution ion energy spectra. Increase of the spectrum resolution was done on the expense of the signal-to-noise ratio. The spectra show a peak at the potential energy of the analyzer separation grid. The width of the peak indicates the ion temperature

The electrostatic analyzer was used only at $B = 0.4$ T and it was melted by plasma at a discharge current of 120 A. The main problem of this device was the overheating, which led to the melting of the grids. Further design research has to be made in order to improve the analyzer.

Publications

- [1] M. L. Solomon, V. Anita, C. Costin, I. Mihaila, L. Sirghi, G. Popa, M. J. van de Pol, R. S. Al, G. J. van Rooij, J. Rapp, "2D distributions of current and floating potential at the target surface in Pilot-PSI", *37th European Physical Society (EPS) Conference on Plasma Physics*, 21-25 June 2010, Dublin, Ireland (poster presentation)
- [2] M. L. Solomon, V. Anita, C. Costin, I. Mihaila, L. Sirghi, G. Popa, M. J. van de Pol, G. J. van Rooij, J. Rapp, "Current and floating potential distributions measured by a multi-probe system at the end plate surface in Pilot-PSI", *15th International Conference on Plasma Physics and Applications (CPPA)*, Iasi, Romania, 1-4 July 2010 (poster presentation P6-07)
- [3] M. L. Solomon, V. Anita, C. Costin, I. Mihaila, G. Popa, H. J. van der Meiden, R. S. Al, M. van de Pol, G. J. van Rooij, J. Rapp, "Multi-channel analyzer investigations of ion flux at the target surface in Pilot-PSI", *Contrib. Plasma Phys.* **50**(9), 898-902 (2010)

Project BS-14 : Understanding of the ExB drift nonlinear effects on transport and structure generation in turbulent tokamak plasmas

Coordinator: Dr. M. Vlad (CS-I)

Plasma Theory Group: F. Spineanu, M. Vlad, D. Nendrean

The milestones for 2010 are

- 1. Density evolution of impurities and particles in turbulent tokamak plasmas*
- 2. Zonal flow generation and particle trapping in the structure of the turbulent potential*

A part of the research proposed in this project represents our Association contributions to EFDA Work Programme for the Transport Task Group at the following topics:

- WP10-TRA-01: Physics of L-H transition, WP10-TRA-01-02: Role of the multi-scale mechanism in the L-H transition
- WP10-TRA-05: Statistical properties of the edge turbulent transport, WP10-TRA-05-01: Turbulent structures and intermittency

The work on these two topics is scheduled along the entire year 2010. The main results obtained are summarized below.

Main results

1. Density evolution of impurities and particles in turbulent tokamak plasmas

A new mechanism of impurity accumulation/loss was found in 2009. It is a nonlinear effect determined by the ratchet pinch velocity in toroidal geometry due to the poloidal motion of the impurity ions induced by the motion along magnetic lines and by the flows generated by the moving potential. This poloidal motion determines a time oscillation of the peaking factor. The latter is defined as the ratio of the radial pinch velocity multiplied by plasma radius and the diffusion coefficient. The time oscillation is determined by the variation of the confining magnetic field on the magnetic surface.

The work scheduled for the first part of 2010 concerns the improvement of the description of the geometrical aspects in our model. We have modified the model by introducing the toroidal geometry. We have developed a code for determining the macroscopic trajectories of the impurity ions, taking into account the toroidal geometry, the parallel motion and the turbulence. Impurity density is obtained from these “macroscopic” trajectory simulation by a Monte Carlo method. A subroutine for determining the fraction of trapped and free trajectories was written and tested.

The work in the second part of the year had the aim of developing the module for determining the local transport coefficient and the pinch velocity. The latter are considered in the stochastic equation for the trajectories as given functions of the magnetic surface and of the toroidal position on it. Scale separation between the fundamental diffusion process and the ion “macroscopic” trajectory permitted to introduce a two step averaging procedure. The turbulent advection was first averaged taking into account trajectory trapping in the structure of the

stochastic potential (eddy motion). It was shown that the complex nonlinear process can be described by determining separately the transport characteristics of the trapped and free ions. The decorrelation trajectory method was adapted for the calculations in this module. Realistic models for plasma turbulence were developed. The toroidal geometry is included in the Eulerian correlation of the stochastic field, which is calculated from the radial, poloidal and toroidal wave number spectrum. The model includes space anisotropy, dominant poloidal waves and potential motion with the diamagnetic velocity. The influence of these characteristics of the turbulence on ion macroscopic trajectories was studied.

The objectives for 2010 were achieved and the code is prepared to determine the strength of the new mechanism of impurity accumulation/loss we have found, which is one of the objectives planned for 2011.

2. Zonal flow generation and particle trapping in the structure of the turbulent potential

We have studied the connection between the stochastic trapping of the trajectories (eddy motion) and the evolution of the drift type turbulence in the strongly nonlinear regime.

Test modes on turbulent plasmas were studied taking into account the process of ion trajectory trapping in the structure of the background potential. The case of drift turbulence was considered, and the frequency ω and the growth rate γ were determined as functions of the statistical properties of the background turbulence. The main characteristics of the evolution of the turbulence were deduced from γ and ω .

We have shown that trajectory trapping has a strong and complex influence on the evolution of the turbulence. Trapping determines the increase of potential cell and the decrease of the spectrum width that forms quasi-coherent structures. The reversed effect appears later in the evolution: ion trapping combined with the motion of the potential with the average diamagnetic velocity destroys the large potential structures and produces the damping of the drift modes. In the same time, the fluctuations of the diamagnetic velocity and the ion flows determine the growth of zonal flows modes.

A different physical perspective on the nonlinear evolution of drift turbulence is obtained. The main role is played by the trapping of the ions in the stochastic potential that moves with the diamagnetic velocity. The trapped ions determine the evolution of the turbulence toward large wave lengths (the inverse cascade). They also determine a slower increase of the amplitude of the potential fluctuations and the evolution to more ordered states. The influence of the ion flows produced by the moving potential appears later in the evolution of the turbulence. The ion flows determine the damping of the small k modes, the decay of the growth rate and eventually the damping of the drift modes with any k . The ion flows also determine transitory zonal flow modes (with wave number on the poloidal direction, $k_y=0$ and $\omega=0$) in connection with the fluctuation of the diamagnetic velocity due to the background turbulence. Thus, in this perspective, there is no causality connection between the damping of the drift turbulence and the zonal flow modes. Both processes are produced by ion trapping in

the moving potential, which determines ion flows. The drift turbulence does not saturate but has an intermittent evolution.

These results represent the first theoretical (analytical) evaluation of the evolution of the turbulence in the strongly nonlinear regime and they bring an important contribution to the understanding of plasma turbulence.

1. M. Vlad, F. Spineanu, „*Zonal flow generation and particle trapping in the structure of the turbulent potential*”, 3rd EFDA Transport Topical Group Meeting combined with the 15th EU-US Transport Task Force Meeting, Cordoba, Spain, 7-10/09/2010
2. M. Vlad, F. Spineanu, „*Nonlinear effects in the diffusion of charged particles in 3-dimensional stochastic magnetic fields*”, ISRSSP 2010, August 25-27, Sofia, invited paper.
3. M. Vlad, F. Spineanu, „*Drift turbulence beyond quasilinear stage*”, to be submitted.
4. M. Vlad, F. Spineanu, „*Nonlinear evolution of drift turbulence: inverse cascade, zonal flows, intermittency*”, XVth International Conference on Plasma Physics and Applications, 1-4 July, Iasi, invited paper.
5. M. Vlad, “Nonlinear effects produced by the ExB drift on transport and structure generation in turbulent tokamak plasmas”, Association Day, 2 July 2010.

1 Impurity density evolution in turbulent tokamak plasmas

Impurity transport in magnetically confined plasma is one of the important problems in fusion research. This process is not completely understood and it represents a very active research field (see for example some of the most recent papers [1]-[15]). The turbulence is shown to produce a diffusive transport as well as an average velocity (pinch), which often leads to peaked impurity profiles even when the particle source is peripheral. The turbulent particle pinches are determined by the magnetic field gradient [16]-[19] or by the temperature gradient [20]. The first mechanism was shown to be dominant in tokamak plasmas.

We have found a new type of pinch, *the ratchet pinch*, which is presented in a series of papers [21], [22], [23]. It appears in turbulent plasmas due to the gradient of the confining magnetic field as an average velocity directed parallel or anti-parallel to ∇B , depending on the characteristics of the turbulence. We have shown that the pinch effect is dominant compared to the diffusive transport in the nonlinear stage of the turbulence characterized by trajectory trapping (or eddying).

The parallel motion of the ions determines a decorrelation time τ_{\parallel}^i that is the largest characteristic time in the ordering of the drift turbulence. Consequently, it should have a negligible effect in the transport of the ions. However, due to the toroidal geometry of the tokamak magnetic configuration, an indirect effect is shown to appear, which is mass-charge dependent.

The turbulent fluctuations in tokamak plasmas are strongly elongated along the magnetic field lines. The field lines rotate on the nested magnetic surfaces. Consequently, parallel motion brings periodically the particles from the low to the high magnetic field side of the magnetic surface. A part of the ions that have small parallel velocity are reflected on banana orbit and do not reach the high field side. The average period is τ_{\parallel}^i . This time is large and does not influence the distribution of displacements up to decorrelation, which determines the pinch velocity and the diffusion coefficient. Thus local approximation (with constant magnetic field) can be used for determining these parameters. The distribution of displacements at large time has to include this periodic change of the transport coefficients, induced by their dependence on the magnetic field. This process was not analyzed until now.

A different periodic poloidal motion of the particles appears in the nonlinear stage of the drift turbulence. The trapped particles are advected by the moving potential with the effective diamagnetic velocity while the free ones move in the opposite direction. These particle flows compensate such that the total flux is zero.

The "macroscopic" effect of the pinch velocity appears in the peaking factor $p = aV_R/D$, which is the measure of direct to diffusive transport. For quasilinear turbulence, this ratio is $p = a/2L_B$. As L_B is constant on the magnetic surface, the peaking factor does not depend on the poloidal motion of the ions in this case. In the nonlinear stage of turbulence, the ratchet velocity is approximately constant on the magnetic surface since it scales in K as K^{-1} . The diffusion coefficient is smaller in the high field side and it determines a peaking factor that scales as

$$p \sim B^{\gamma-1} \tag{1}$$

where γ is the trapping scaling exponent that depends on the Eulerian correlation of the stochastic potential and determines the diffusion coefficient ($D \cong V\lambda_c K^{-\gamma}$). The values of γ are in the range $0 < \gamma < 1$, so that the peaking factor is always largest in the high field side of the magnetic surface.

The direction of the pinch velocity is toward the symmetry axis of the torus. A periodic poloidal motion determines a pinch velocity that change periodically from inside to outside of the plasma. For uniform poloidal rotation, the larger values of p inside torus determine a loss mechanism. If the poloidal rotation is not uniform, the loss mechanism can be amplified (for smaller rotation velocity inside the torus) or it can be attenuated or even transformed in an accumulation mechanism (if the rotation velocity is smaller outside the torus). The shape of the plasma also contributes to this mechanism.

The toroidal geometry makes the magnetic lines shorter inside torus than outside. Thus the poloidal motion determined by the magnetic structure contribute to the accumulation of impurities. The diamagnetic velocity is smaller inside the torus and thus it has a loss effect. As shown in Section 3, zonal particle flows are important when the number of trapped and free particles are comparable. The poloidal motion is determined by both velocities. The first depends on particle mass while the second depends on the characteristics of the turbulence. The rotation velocity produced by the parallel motion decreases with the increase of the mass number and thus it is expected that the diamagnetic velocity dominates for large mass particles leading to smaller accumulation rate than in the case of small A particles.

1.1 Code for calculating the pinch velocity and the diffusion coefficient

We have developed a code based on the decorrelation trajectory method for calculating the pinch velocity and the diffusion coefficient for impurities with given mass and charge in toroidal geometry. More precisely, the average effect of the turbulence on the space-time scale of the macroscopic trajectories are determined.

The transport model includes a moving potential with the poloidal velocity V_*^{eff} . The potential has Gaussian distribution and given Eulerian correlation. Finite correlation lengths along magnetic field lines are included. The Eulerian correlation is modelled starting from given spectra of the wave numbers in the poloidal, radial and toroidal directions. This permits to include in the model different correlation length on the three directions (space anisotropy) and dominant waves. The Eulerian correlation can be small scale (with Gaussian shape) or large scale (with slow space decrease, of algebraic type). The toroidal correlation length can be as large as the dimension of the magnetic surface. In these conditions the wave structure of the potential dominates.

The connection of this module for the average effect of the turbulence to the equation of the macroscopic trajectories implies conceptual modification of the decorrelation trajectory method. It is not necessary to determine the diffusion coefficient and the pinch velocity, but rather the mean square displacement and the average displacement during the macroscopic time step. Only in the case of scale separation these quantities are expressed in terms of diffusion coefficients and pinch

velocity. Moreover, the trapping in the structure of the stochastic potential is fully taken into account by averaging separately on the trapped and free trajectories.

These results are local. It is sufficient to take into account the space variation of the magnetic field only as a constant gradient. The configuration of the magnetic field influences the macroscopic trajectories both directly and through the parametric dependence of the turbulence effects on the confining magnetic configuration.

In conclusion, we have realized the computer code that is necessary for the quantitative analysis of the strength of the new mechanism that produces impurity loss/accumulation, which we have identified. It is a nonlinear effect that appears due to the poloidal motion of the impurity ions. The latter has two components: particle motion along magnetic lines in toroidal geometry and particle poloidal flows induced by the drift turbulence. Depending on the ratio of the two components, impurities can be accumulated or lost. The accumulation rate depends on impurity mass through the parallel velocity.

2 Zonal flow generation and particle trapping

Turbulence evolution in magnetically confined plasmas is a complex problem that is not yet understood besides the huge amount of work on this topic (see [24] and the references there in). Most studies that go beyond the quasilinear stage are based on numerical simulations. They show the generation of large scale structures and of zonal flows that lead to turbulence damping.

The aim of this paper is to study the nonlinear evolution of the drift turbulence on the basis of test modes on turbulent plasmas. A Lagrangian approach of the type of [25] is developed using the results we have obtained in the last decade on the statistics of test particle trajectories. Semi-analytical statistical methods (the decorrelation trajectory method [26] and the nested subensemble approach [27]) have been developed for the study of test particle stochastic advection. These are the first methods that describe trajectory trapping or eddying that is specific to the $\mathbf{E} \times \mathbf{B}$ drift in turbulent plasmas. It was shown that trapping determines memory effects, quasi-coherent behavior and non-Gaussian distribution [27].

A new understanding of important aspects of the physics of drift type turbulence in the non-linear phase is obtained. The main role in the processes of inverse cascade, zonal flows and intermittency is shown to be played by ion trapping.

We consider the drift instability in slab geometry with constant magnetic field. We start from the basic gyrokinetic equations for the distribution of electrons and ions.

The solution for the potential in the zero Larmor radius limit is $\phi(\mathbf{x}, z, t) = \phi_0(\mathbf{x} - \mathbf{V}_*t, z)$, where ϕ_0 is the initial condition and $\mathbf{V}_* = T\partial_x[\ln(n_0)]/eB$ is the diamagnetic velocity produced by the gradient of the average density $n_0(x)$. This shows that the potential is not changed but displaced with the diamagnetic velocity.

The finite Larmor radius effects combined with the non-adiabatic response of the electrons destabilizes the drift waves. The frequency ω and the growth rate γ of

the modes are

$$\omega = k_y V_*^{eff}, \quad V_*^{eff} = V_* \frac{\Gamma_0}{2 - \Gamma_0}, \quad (2)$$

$$\gamma = \frac{\sqrt{\pi}}{|k_z| v_{Te}} \frac{k_y^2 (V_* - V_*^{eff}) V_*^{eff}}{2 - \Gamma_0}, \quad (3)$$

where $\Gamma_0 = \exp(-b)I_0(b)$, $b = k_\perp^2 \rho_L^2 / 2$ and ρ_L is the ion Larmor radius. The wave number components are k_i , $i = x, y, z$ and $k_\perp = \sqrt{k_x^2 + k_y^2}$. These are the characteristics of the linear (universal) drift instability on quiescent plasmas.

We consider a turbulent plasma with given statistical characteristics of the stochastic potential and we study linear test modes. The growth rates and the frequencies of the test modes are determined as functions of the statistical characteristics of the background turbulence with potential $\phi(\mathbf{x}, t)$. A wave type perturbation of the potential $\delta\phi(\mathbf{x}, z, t) = \phi_{k, \omega} \exp(i\mathbf{k} \cdot \mathbf{x} + ik_z z - i\omega t)$ is introduced. It is small ($\delta\phi \ll \phi$) and thus it has a negligible influence on particle trajectories. The solutions for the perturbations of electron and ion densities are obtained using the characteristics method as integrals along particle trajectories in the background potential of the source terms determined by the density gradient. The characteristics $\mathbf{x}^\alpha(\tau), z^\alpha(\tau)$ are the trajectories obtained by integrating the equation of motion backwards in time with the condition at time t , $\mathbf{x}^\alpha(t) = \mathbf{x}$, $z^\alpha(t) = z$

$$\frac{d\mathbf{x}^\alpha}{d\tau} = -\nabla\phi(\mathbf{x}^\alpha, z^\alpha, \tau) \times \mathbf{e}_z, \quad \frac{dz^\alpha}{d\tau} = v_z^\alpha. \quad (4)$$

The background turbulence produces two modifications in the response. One consists in the stochastic $\mathbf{E} \times \mathbf{B}$ drift that appears in the trajectories and the other is the fluctuation of the diamagnetic velocity due to the fluctuations of the density δn in the background turbulence. Both effects are important for ions while the response of the electrons is approximately the same as in quiescent plasma. The perturbed distribution function is averaged over the stochastic trajectories. The dispersion relation (quasi-neutrality condition) of a mode with frequency ω and wave number \mathbf{k} is obtained

$$2 + i\sqrt{\pi} \frac{\omega - k_y V_*}{|k_z| v_{Te}} = i\Pi \Gamma_0 [\omega + V_* (k_y + ik_i k_j R_{ij})]. \quad (5)$$

The background turbulence appears in this equation in the average propagator

$$\Pi = \int_t^{-\infty} d\tau \langle \exp(-i\mathbf{k} \cdot \mathbf{x}^\alpha(\tau)) \rangle \exp(i\omega(t - \tau)) \quad (6)$$

and in the tensor R_{ij} , which is the integral of a Lagrangian correlation

$$R_{ji}(\tau, t) \equiv \int_\tau^t d\theta' \int_{-\infty}^{\tau - \theta'} d\theta \langle v_j(\mathbf{x}^i(\theta'), z, \theta') \partial_2 v_i(\mathbf{x}^i(\theta), z, \theta) \rangle, \quad (7)$$

where v_j is the $\mathbf{E} \times \mathbf{B}$ drift velocity component. The average propagator (6) contains the effects of the stochastic trajectories and the tensor R_{ij} yields from the fluctuations of the diamagnetic velocity.

2.1 DRIFT TURBULENCE EVOLUTION

The growth rate and the frequency of the drift modes give an image of the turbulence evolution starting from a weak initial perturbation with very broad wave number spectrum. We show that a sequence of processes appear at different stages as transitory effects and that the drift turbulence has an oscillatory (intermittent) evolution.

2.1.1 Trajectory diffusion and damping of small k modes

The time variation of the potential thus consists of an average translation with the velocity V_d , which is the average of V_*^{eff} over wave-numbers, and in the change of its shape. The statistics of trajectories is Gaussian for small amplitudes of the stochastic velocity $V \ll V_d$ and the diffusion of trajectories is isotropic. The solution of the dispersion relation (5) shows that ω and V_*^{eff} are not changed [Eqs. (2)] and that the growth rate becomes:

$$\gamma = \frac{\sqrt{\pi}}{|k_z| v_{Te}} \frac{k_y^2 (V_* - V_*^{eff}) V_*^{eff}}{2 - \Gamma_0} - k_i^2 D \frac{2}{2 - \Gamma_0}. \quad (8)$$

This is the well known result of Dupree [25] which shows that a stabilizing contribution is produced by the ion diffusion in the background turbulence, which leads to the damping of the large k modes.

2.1.2 Trajectory structures and large scale correlations

The increase of the turbulence amplitude V above V_d determines ion trapping or eddying. As we have shown, this strongly influences the statistics of trajectories. The distribution of the trajectories is not more Gaussian due to trapped trajectories that form quasi-coherent structures. At this stage the trapping is weak in the sense that the fraction of trapped trajectories n_{tr} is much smaller than the fraction n_{fr} of free trajectories.

The probability of displacements $P(\mathbf{x}, t)$ has a pronounced peaked shape compared to the Gaussian probability. It can be modeled by $P(x, y, t) = n_{tr}G(\mathbf{x}; \mathbf{S}) + n_{fr}G(\mathbf{x}; \mathbf{S}')$, where $G(\mathbf{x}; \mathbf{S})$ is the 2-dimensional Gaussian distribution with dispersion $\mathbf{S} = (S_x, S_y)$. The first term has a small constant dispersion that is the size S of the trajectory structures and describes the trapped trajectories. The free trajectories are described by the second term, which has diffusive dispersion $S'_i = S_i + 2D_i t$, $i = x, y$. This distribution modifies the average propagator a factor \mathcal{F} that is determined by the average size of the trapped trajectory structures

$$\mathcal{F} \equiv \exp\left(-\frac{1}{2}k_i^2 S_i^2\right). \quad (9)$$

The solution of the dispersion relation (5) leads only to the modification of the effective diamagnetic velocity

$$V_*^{eff} = V_* \frac{\Gamma_0 \mathcal{F}}{2 - \Gamma_0 \mathcal{F}}, \quad (10)$$

while the growth rate equation is not modified. The decrease of the effective diamagnetic velocity produces the displacement of the position of the maximum of γ toward small k . The maximum of γ moves to smaller k values of the order of $1/S_i$ and the size of the unstable k range decreases. The maximum growth rate decreases.

Thus, ion trapping determines the increase of the correlation length of the potential and the decrease of the average frequency (proportional with k_2). In this nonlinear stage, turbulence evolution becomes slower and leads to ordered states (narrower spectra with maximum at smaller k).

2.1.3 Ion flows and turbulence damping

The evolution of the potential determines the increase of the fraction of trapped ions. This produces another effect on the test modes. The potential continues to move with the average diamagnetic velocity V_d . This determines an average flux of the trapped particles $n_{tr}V_d$. As the $\mathbf{E} \times \mathbf{B}$ drift has zero divergence, the probability of the Lagrangian velocity is time invariant, *i. e.* it is the same with the probability of the Eulerian velocity. The average Eulerian velocity is zero and thus the flux of the trapped ions that move with the potential has to be compensated by a flux of the free particles. These particles have an average motion in the opposite direction with a velocity V_{fr} such that $n_{tr}V_d + n_{fr}V_{fr} = 0$. The velocity on structures method that we have recently developed shows that the probability of the displacements splits in two components that move in opposite direction. Thus, opposite ion flows are generated by the moving potential in the presence of trapping. They modify both the effective diamagnetic velocity and the growth rate

$$V_*^{eff}(n) = V_*^{eff}(0) + nV_*, \quad (11)$$

$$\gamma = \frac{\sqrt{\pi}}{|k_z|v_{Te}} \frac{k_y^2 (V_* - V_*^{eff}) (V_*^{eff} - nV_*)}{2 - \Gamma_0 \mathcal{F}} - k_i^2 D_i \frac{2 - \Gamma_0 \mathcal{F} n_{tr}}{2 - \Gamma_0 \mathcal{F}} \quad (12)$$

where $n \equiv n_{tr}/n_{fr}$. The drive term of the drift instability (the first term in Eq. (12), γ_1) is still a parabolic function of V_*^{eff} but the range of positive γ_1 is reduced to the interval (nV_*^{eff}, V_*^{eff}) . This determines the decrease of the maximum of γ_1 . The effective diamagnetic velocity (11) shows that it increases for all values of k and becomes larger than V_* first for small k . This determines the damping of these modes. As n increases modes with larger k are damped and, for $n = 1$, $\gamma_1 < 0$ for any k .

2.1.4 Generation of zonal flow modes

The fluctuations of the density produced by the background turbulence (7) determine an additional term in the growth rate: $\approx k_i k_j R_{ij} V_*$. The component R_{11} is very interesting because it generates modes with $k_2 = 0$ and $\omega = 0$, if this term is positive. These are static oscillations in the direction of the average density gradient, which are known as zonal flow modes and have been intensely studied in the last decade in connection with internal transport barriers (see [28] and the references therein). We have found that R_{11} essentially depends on n . It increases when the ion flows

become important up to a positive maximum and then it decreases to zero. It is essentially determined by the anisotropy that is generated by the difference in the average velocity of the trapped ions V_d and the average velocity of the free ions $V_{fr} = -nV_d$. When $n = 1$, the ion flows are symmetrical and R_{11} vanishes. A clear connection of the zonal flow modes with the ion flows induced by the moving potential appears.

In conclusion, a different physical perspective on the nonlinear evolution of drift turbulence is obtained. The main role is played by the trapping of the ions in the stochastic potential that moves with the diamagnetic velocity. The trapped ions determine the evolution of the turbulence toward large wave lengths (the inverse cascade). They also determine a slower increase of the amplitude of the potential fluctuations and the evolution to more ordered states. The influence of the ion flows produced by the moving potential appears later in the evolution of the turbulence. The ion flows determine the damping of the small k modes, the decay of the growth rate and eventually the damping of the drift modes with any k . The ion flows also determine transitory zonal flow modes (with $k_y = 0$ and $\omega = 0$) in connection with the fluctuation of the diamagnetic velocity due to the background turbulence. Thus, in this perspective, there is no causality connection between the damping of the drift turbulence and the zonal flow modes. Both processes are produced by ion trapping in the moving potential, which determines ion flows. The drift turbulence does not saturate but has an intermittent evolution.

References

- [1] C. Estrada-Mila, J. Candy, and R.E. Waltz, Phys. Plasmas **12**, 022305 (2005).
- [2] V. Naulin, Phys. Rev. E **71**, 015402(R) (2005).
- [3] H. Weisen et al., Nuclear Fusion **45**, L1-L4 (2005).
- [4] M. Priego, O. E. Garcia, V. Naulin and J. Juul Rasmussen, Phys. Plasmas **12**, 062312 (2005).
- [5] A. Eriksson and J. Weiland, Phys. Plasmas **12**, 092509 (2005).
- [6] X. Garbet, N. Dubuit, E. Asp, Y. Sarazin, C. Bordelle, P. Ghendrih, G. T. Hoang, Phys. Plasmas **12**, 082511 (2005).
- [7] K. Hallatschek, W. Dorland, Phys. Rev. Lett. **95**, 055002 (2005).
- [8] N. H. Bian, O. E. Garcia, Phys. Plasmas **12**, 042307 (2005).
- [9] N. Kasuya, K. Itoh, Phys. Plasmas **12**, 090905 (2005).
- [10] C. Angioni, A. G. Peeters, Phys. Rev. Lett. **96**, 095003 (2006).
- [11] L. Garzotti, M. Valovic, X. Garbet, P. Mantica, V. Parail, Nuclear Fusion **46**, 994 (2006).

- [12] T. Hauff, F. Jenko, *Plasmas* **14**, 092301 (2007).
- [13] S. Futatani, S. Benkadda, Y. Nakamura, K. Kondo, *Phys. Rev. Lett.* **100**, 025005 (2008).
- [14] N. Dubuit, X. Garbet, T. Parisot, R. Guirlet and C. Bourdelle, *Phys. Plasmas* **14**, 042301 (2007).
- [15] C. Angioni et al., *Phys. Plasmas* **14**, 055905 (2007).
- [16] V. V. Yankov, *JETP Lett.* **60**, 171 (1994).
- [17] M. B. Isichenko, A. V. Gruzinov, and P. H. Diamond, *Phys. Rev. Lett.* **74**, 4436 (1995).
- [18] R. D. Baker and M. N. Rosenbluth, *Phys. Plasmas* **5**, 2936 (1998).
- [19] X. Garbet et al, *Phys. Rev. Lett.* **91**, 035001 (2003).
- [20] J. Weiland, A. B. Jarmen, H. Nordman, *Nucl. Fusion* **29**, 1810 (1989).
- [21] M. Vlad, F. Spineanu and S. Benkadda, *Phys. Rev. Lett.* **96**, 085001 (2006).
- [22] M. Vlad, F. Spineanu and S. Benkadda, *Phys. Plasmas* **15** (2008) 032306 (9pp).
- [23] M. Vlad, F. Spineanu and S. Benkadda, *Plasma Phys. Control. Fusion* **50** (2008) 065007 (12pp).
- [24] Krommes J. A., *Phys. Reports* **360** (2002) 1.
- [25] Dupree T. H., *Phys. Fluids* **15** (1972) 334.
- [26] Vlad M., Spineanu F., Misguich J.H., Balescu R., *Phys.Rev.E* **58** (1998) 7359.
- [27] Vlad M. and Spineanu F., *Phys. Rev. E* **70** (2004) 056304.
- [28] Diamond P. H., Itoh S.-I., Itoh K., Hahm T. S., *Plasma Phys. Control. Fusion* **47** (2005) R35-R161.

BS18 A

RST in extenso

Titlul complet al Proiectului BS 18A:

Study of the thermal treatment influence in formation of the stable Be-C, Be-W and C-W alloys . TVA gun electron beam irradiation influence. (BS-PS)

(Studiul influenței tratamentului termic în formarea de compusi stabili Be-C, Be-W și C-W. Influența iradierii cu fascicule de electroni produse de tunul TVA)

Etapa II (15 Decembrie 2010)

TVA gun thermal treatment of the Be/C, Be/W and C/W coatings

Task: TA PWI 2010, Chapter 6: Determination of expected alloys and compounds in ITER relevant conditions and their influence on PWI processes and fuel retention

Sub-task: TA WP10-PWI-06-01-02/MEdC/PS: TVA gun electron beam irradiation influence on mixed films prepared using TVA method

Task Force on Plasma Wall Interaction

Area: SEWG ITER Material Mix

Principal investigator: Cristian P. LUNGU,

Research team: A. Anghel, C. Porosnicu, I. Jepu, A.M.Lungu, P. Chiru, C. Ticos, C. Luculescu

National Institute for Laser, Plasma and Radiation Physics, Association
EURATOM MEdC

ABSTRACT

Since the operation conditions for the nuclear fuel removal in a fusion power plant like ITER involves wall baking at higher temperatures of the plasma facing components - i.e. 515 K for the first wall and 623 K for the divertor area - it is important to know how this thermal treatment procedures will affect the materials' properties. It was observed that by heating at 623 K, the carbon from the graphite substrate diffuses into the deposited beryllium film forming a mixed layer of Be, BeO and Be₂C at the interface, while the oxygen present at the Be-C interface diffuses to the surface of the film. Comparing the results obtained by Nuclear Reaction Analysis we observed that the deuterium implanted after annealing was retained in deeper layers in the case of thermally treated samples due to the structural changes induced in the films by the Be/C mixed layer formation and the effects of the oxygen diffusion into the thermal treated films.

1. Introduction

In magnetic confinement fusion devices, plasma facing components are subject to heat and particle fluxes that strike the first wall either continuously or in bursts. The effect on the wall surface is usually tolerable in present facilities but in future fusion power reactors the power load will be much higher and the duration of the plasma discharges much longer. The potential scale of the damage to the first wall challenges fusion research and technology, particularly for the development of the divertor. Even when most of the power of the plasma is exhausted in volumetric processes, some plasma facing components will have to withstand peak temperatures of more than 1300 K, despite being actively cooled.

On the other hand, it was established that baking the inner walls of the chamber at 515 K and 623 K for the divertor area is a solution for the nuclear fuel removal from the plasma facing components [1-3].

It is important to expand the knowledge how the thermal treatments and the heat loads will influence the materials which will be used as plasma facing components (Be, W, C) and their compounds. In this report, the influence of thermal treatment on Be-C mixed material formation and deuterium retention under controlled laboratory conditions is studied.

Sample preparation

The beryllium films were deposited on mirror polished fine grain graphite substrates using the thermionic vacuum arc (TVA) technology developed by the research group.

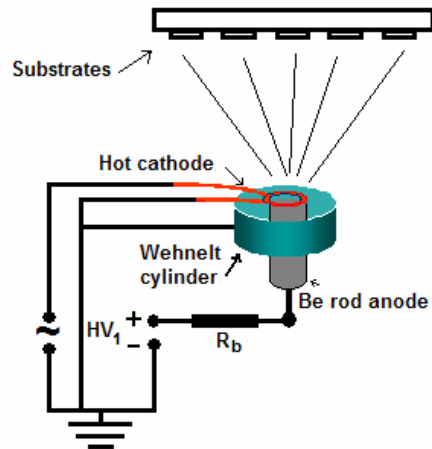


Fig. 1 Schematic representation of the thermionic vacuum arc (TVA) deposition method

The TVA technique involves preparation of thin films from the pure vapors of the metal to be deposited without using any buffer gas [4-5]. The TVA principle scheme is presented in Fig. 1, as well as in the previous published papers [4-5].

Thermal treatment, deuterium ion implantation and retention analysis

After the deposition, the composition of each sample was analyzed by Rutherford Backscattering Spectrometry (RBS) using a 2.6 MeV $^4\text{He}^+$ ion beam in the Tandem Accelerator available at IPP – Garching, Germany [6], confirmed by X-ray Photoelectron Spectroscopy – XPS, [7] and then annealed at 623 K in high vacuum conditions, at around 10^{-5} Pa, using the thermal desorption spectroscopy (TDS) setup in IPP-Garching. The temperature ramp rate was $\approx 0.25 \text{ K}\cdot\text{s}^{-1}$ from room temperature to 635 K. Counting that the mixing of beryllium and carbon in the interface area it is a time dependent process, the samples were kept at this temperature for different time scales, 30, 60 and 90 minutes respectively. Other samples were annealed up to the temperature of 1000 K. After annealing, the composition depth profiles of the samples were determined by RBS (using the SIMNRA code) and XPS depth profile measurements.

Deuterium ion implantation into thermally treated samples was performed in the High Current Ion Source at IPP-Garching. The energy of the D ion beam was 600 eV D_3^+ , meaning 200 eV/D. The implantation fluences were up to $\sim 2 \times 10^{23} \text{ D}\cdot\text{m}^{-2}$. This value corresponds to the expected fluence to the ITER first wall after 400 s discharge with the flux of $\sim 3 \times 10^{19} \text{ D}\cdot\text{m}^{-2} \cdot\text{s}^{-1}$. The incident angle was normal to the target surface, and the implantation temperature was set as room temperature.

After the implantation, the deuterium retained profiles were determined using the $\text{D}(^3\text{He}, \text{p})^4\text{He}$ nuclear reaction before the TDS measurements.

Results

Figure 2 shows a typical depth profile of the as-deposited beryllium films on graphite substrates using the TVA technique. It can be seen that the only impurity found in the film was the oxygen, below 5 at %, present as BeO as the XPS measurements revealed. An increase in the oxide amount was observed at the films surface, due to atmosphere exposure of the samples

after the deposition, but also at the Be-C interface, due to the residual oxygen content present in the chamber in the beginning of the deposition process.

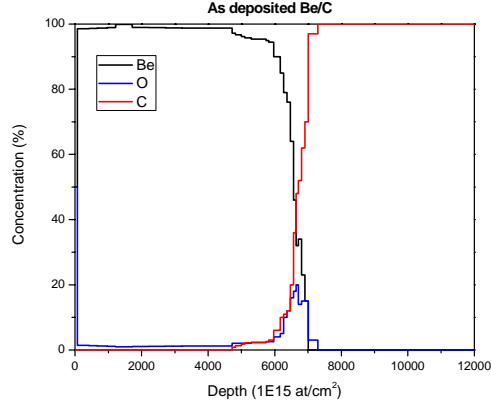


Fig. 2 Elemental composition depth profile of an as deposited Be film obtained by RBS.

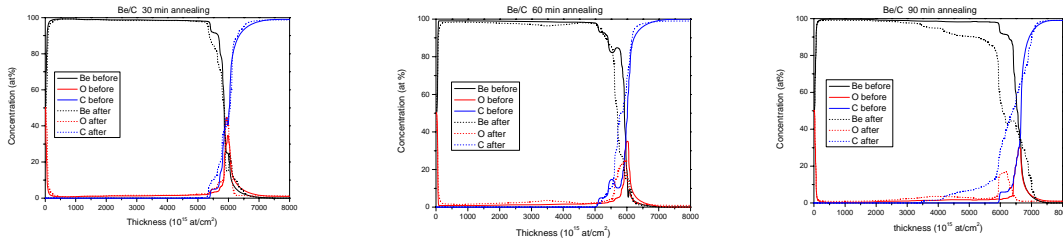


Fig. 3 Elemental composition depth profiles of Be films annealed at 623 K for 30, 60 and 90 min time scales obtained by RBS.

Figure 3 shows the RBS elemental depth profiles obtained for the samples thermally treated in high vacuum at 623 K during 30, 60 and 90 min respectively. As it can be seen, even the annealing of the samples for only 30 minutes induces changes at the interface, where a mixture of Be, Be_2C and C was found. It is known that at the chosen temperature of 623 K, beryllium carbide (Be_2C) formation starts, in agreement with [8]. Also, it was observed that the oxygen coming from the graphite substrate migrates into the Be film leading to the formation of a thicker beryllium oxide layer at the interface. Increasing the annealing time to 90 minutes, the mixed material layers present at the interface becomes thicker as well as the oxide.

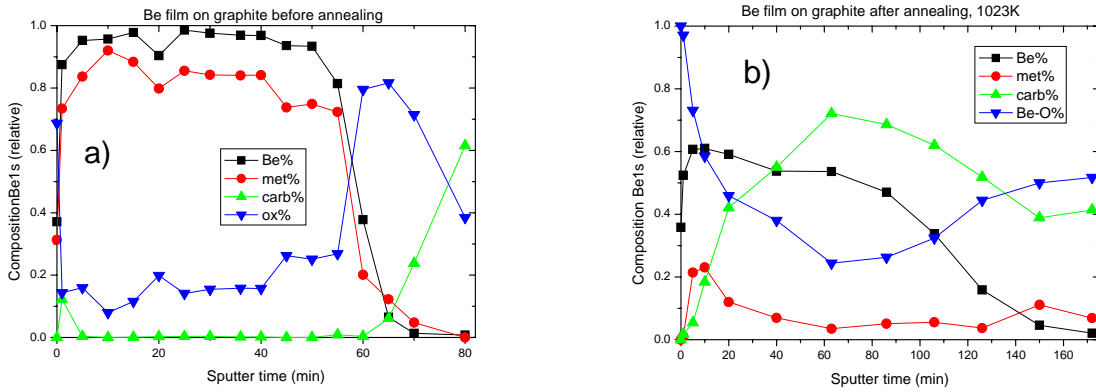


Fig. 4 XPS depth profiles of Be films on graphite before (a) and after (b) annealing at 1023 K

After annealing the samples at ~ 1023 K it was found out that the entire Be film became a mixture of metallic Be, BeO and Be₂C. In Fig. 4, the XPS depth profile shows, for comparison, the distribution of chemical states of Be in the film before and after annealing to 1023 K. These results are in good agreement with the RBS measurements performed.

No significant differences were observed in deuterium retention between the samples annealed at 623 K due to the thickness of the Be films of $\cong 500$ nm, which was larger than the deuterium implantation range of about 200 nm. The smaller differences observed, meaning a decrease in the total amount of deuterium retained in the film while increasing the annealing time, are attributed to the surface oxide layer which acts like a barrier.

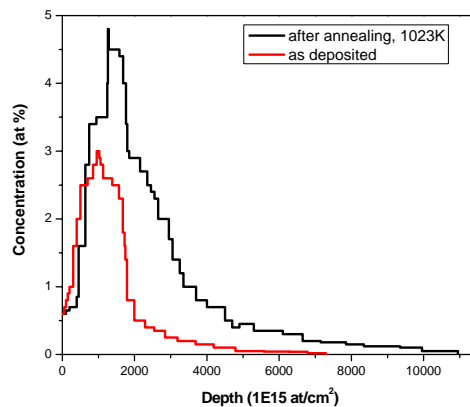


Fig. 5 Deuterium depth profiles before and after thermal treatment at 1023 K.

A significant change in the retention behavior was observed for the samples annealed at 1023 K. For explanation, Fig. 5 shows the deuterium depth profiles obtained by NRA measurements before and after the thermal treatment. For that sample a fluence of 5×10^{18} D·cm⁻² was used for implantation and the NRA measurements revealed that for the as-deposited sample a total amount of $2,9 \times 10^{16}$ D·cm² was retained while for the annealed sample the deuterium amount increased to 1×10^{17} D·cm⁻². Also, in the case of thermally treated sample, the distribution of the deuterium in the film changes by means that the implantation depth becomes higher compared to that of the pure beryllium film. This behavior is related not only to the Be-C mixed material formation but also to the increase in the BeO concentration in the near surface area.

Further investigations regarding the deuterium retention as well as the desorption behavior of films thinner than D ions implantation depth range (≈ 100 nm) are ongoing in order to obtain information about the influence of mixed material formation by thermal treatment at 623 K.

Conclusion

The influence of thermal treatment at 623 and 1023 K of beryllium films deposited on graphite by TVA method by means of changes induced at the interface as well as the deuterium retention was investigated.

It was found out that by annealing the samples at 623 K a mixed material layer appears at the interface. The thickness of this mixed layer increases while increasing the annealing time. Also an increase of the beryllium oxide amount present in the film was observed while the annealing time increases. This behavior is caused by the migration toward the Be film of the oxygen present in the graphite substrate and the large affinity between beryllium and oxygen. The XPS measurements confirmed that the mixed layer consists of pure Be, BeO and Be₂C. By deuterium retention measurements only small changes caused by the surface beryllium oxide layer were observed.

By thermal treatment of the samples at ~ 1023 K the mixed material layer extends to the whole film, changing the retention behavior. The total deuterium amount retained in the annealed films increases with an order of magnitude for the same implantation fluence.

References

- [1] R A Pitts, A Kukushkin, A Loarte, A Martin, M Merola, C E Kessel, V Komarov and M Shimada, Phys. Scr. T138 (2009) 014001.
- [2] T Tanabe, N Bekris, P Coad, C.H Skinner, M Glugla, N Miya, J. Nucl. Mater., 313-316 (2003) 478.
- [3] N. Bekris, C. H. Skinner, U. Berndt, C. A. Gentile, M. Glugla, A. Erbe, W. Pilz, J. Nucl. Mater 329-333 (2004) 814.
- [4] C. P. Lungu, I. Mustata, V. Zaroschi, A. M. Lungu, A. Anghel, P. Chiru, M. Rubel, P. Coad G. F. Matthews and JET-EFDA contributors, Phys. Scr. T128 (2007) 157.
- [5] A. Anghel, I. Mustata, C. Porosnicu, C. P. Lungu, J. Nucl. Mater. 385 (2009) 242
- [6] J. Roth, D. S. Walsh, W. R. Wampler, and M. Mayer, Nuclear Instruments and Methods in Physics Research Section B: Beam Interactions with Materials and Atoms, 136-138, (1998), 689.
- [7] K. Schmid, A. Wiltner, Ch. Linsmeier, Nuclear Instruments and Methods in Physics Research Section B: Beam Interactions with Materials and Atoms, 219-220, (2004), 947
- [8] F. Kost, Ch. Linsmeier, M. Oberkofler, M. Reinelt, M. Balden, A. Herrmann, S. Lindig, J.Nucl. Mater. 390-391 (2009) 975.

Presentation and publications in connections with the project

Presentations

1. Cristian P. Lungu, TVA gun electron beam irradiation influence on mixed films prepared using TVA method, Report on task agreement WP10-PWI-06-01-02/MEdC/PS at TF-PWI annual Meeting, 3-5 Nov 2010, Vienna, Austria

Publications (Journals):

1. A. Anghel, C. Porosnicu, C. P. Lungu, K. Sugiyama, C. Krieger, J. Roth, Influence of Thermal Treatment on Beryllium/Carbon Formation and Fuel Retention, J. Nucl. Mat, accepted
2. K. Sugiyama, J. Roth, A. Anghel, C. Porosnicu, M. Baldwin, R. Doerner, K. Krieger, C.P. Lungu, Consequences of Deuterium Retention and Release from Be-containing Mixed Materials for ITER Tritium Inventory Control, J. Nucl. Mat, accepted

Publications (Books):

3. C. P. Lungu, I. Mustață, C. C. Porosnicu, I. Jepu, A. Anghel, Caracterizarea filmelor compozite combinatoriale obținute prin metoda arcului termoionic în vid, București, Editura Academiei Oamenilor de Știință din România, 2010, ISBN 978-606-92500-1-3 (in Romanian)

Director de proiect: Dr. C. P. Lungu

Comunicari la Conferinte internationale.

1. Cristian P. Lungu, TVA gun electron beam irradiation influence on mixed films prepared using TVA method, Report on task agreement WP10-PWI-06-01-02/MEdC/PS at TF-PWI annual Meeting, 3-5 Nov 2010, Vienna, Austria

Publications (Journals):

1. A. Anghel, C. Porosnicu, C. P. Lungu, K. Sugiyama, C. Krieger, J. Roth, **Influence of Thermal Treatment on Beryllium/Carbon Formation and Fuel Retention**, J. Nucl. Mat, accepted
2. K. Sugiyama, J. Roth, A. Anghel, C. Porosnicu, M. Baldwin, R. Doerner, K. Krieger, C.P. Lungu, **Consequences of Deuterium Retention and Release from Be-containing Mixed Materials for ITER Tritium Inventory Control**, J. Nucl. Mat, accepted

Books:

1. C. P. Lungu, I. Mustăță, C, C.Porosnicu, I. Jepu, A. Anghel, **Caracterizarea filmelor compozite combinatoriale obținute prin metoda arcului termoionic în vid**, București, Editura Academiei Oamenilor de Știință din România, 2010, ISBN 978-606-92500-1-3 (in Romanian)

BS18 B

RST in extenso

Titlul complet al Proiectului BS 18B:

Study of the ternary system formation Be-C-W using thermionic vacuum arc method; Influence of hydrogen/deuterium inclusion into the prepared films on the retention process. D-retention in mixed materials containing H, D and He (BS-PS)

(Studiul formării sistemelor ternare Be-C-W folosind metoda arcului termoionic in vid; Influența incluziunilor de hidrogen/deuteriu în filmele preparate asupra procesului de retenție. Retenția deuteriului în materiale cu conținut de H, D și He

Etapa II (15 Decembrie 2010)

Production of Be-C-W mixed layers with different relative concentrations in the presence of O₂, H₂ /D₂, He

Task title: TA PWI 2010, Chapter 6: Determination of expected alloys and compounds in ITER relevant conditions and their influence on PWI processes and fuel retention

Sub-task: Sub-task: TA WP10-PWI-06-02-02/MEdC/PS: D-retention in mixed materials containing H, D and He

Task Force on Plasma Wall Interaction

Area: SEWG ITER Material Mix

Principal investigator: Cristian P. LUNGU,

Research team: C. Porosnicu, A. Anghel, I. Jepu, A.M.Lungu, P. Chiru, C. Ticos, C. Luculescu

National Institute for Laser, Plasma and Radiation Physics, Association
EURATOM MEdC

ABSTRACT

The Inconel cladding tiles of the ITER-like-wall to be tested at JET will be coated by a beryllium layer. Carbon containing tiles will be also present. These materials are sputtered in the high flux ($10^{22} \text{ m}^{-2}\text{s}^{-1}$ or higher) of the deuterium-tritium plasma. Ionized by the energetic electrons and with hydrogen isotope ions they will be implanted or re-deposited, creating composite layers.

In order to study the deuterium retention and release, mixed layers were prepared using the thermionic arc method.

Deuterium implantation was performed using a high current ion source at room temperature using a deuterium ion beam with energy of 200eV/D. Thermal Desorption Spectroscopy (TDS) analyses were correlated with the beryllium/carbon relative concentrations of the prepared films. The relative Be-C concentration influence both the retention and the desorption mechanisms. For low beryllium concentration into the mixed Be-C layer the amount of deuterium was lower. The TDS spectra proved that the different samples different behavior was caused by different individual trapping sites for each of these two elements.

Introduction

Beryllium and carbon fiber composites (CFC) are candidate materials to be used on the ITER main chamber wall and divertor [1-2]. The tiles next to the divertor area will be subject to high flux ($10^{22}\text{m}^{-2}\text{s}^{-1}$ or higher) of the deuterium-tritium plasma. Due to the sputtering and chemical erosion of these candidate materials, beryllium and hydrocarbon species particles can migrate into the plasma. They will be ionized by the energetic electrons and implanted or re-deposited on the divertor and on the shadowed areas together with hydrogen isotope ions.

Composite thin film depositions are used in order to obtain structures that have similar characteristics as the films deposited in different fusion reactor's areas. This type of films can be obtained under working conditions of the thermonuclear reactors, where parts of the walls are made of beryllium tiles or beryllium coated inconel tiles, and other reactor regions are made of carbon. The high energy plasma determines the migration and mixture of these elements.

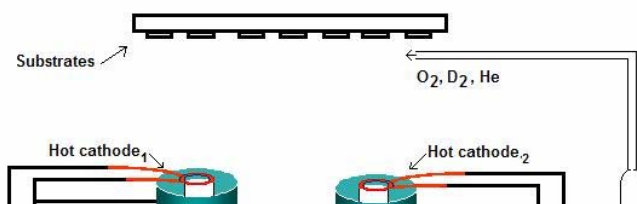
Beryllium carbide will easily be formed under reactor exposure conditions and therefore investigations on deuterium retention in Be-C systems are necessary. TVA deposition system has been upgraded and fabrication of Be-C-W in the presence of O_2 , H_2 / D_2 , He co-deposition films is now available.

Sample preparation

The deposition method used is based on vacuum evaporation, thermionic vacuum arc (TVA) method, presented in detail in Ref [3], as well as in the former reports. During the entire coating process, a negative bias voltage was applied on the tiles, with a value of -700V, which ensured a compact coating by rejecting the electrons and accelerating the positive ions from plasma [4].

In order to obtain films that have different Be-C-W relative concentrations, a setup that uses two simultaneous TVA discharges was developed. The distance between the anodes was 20 cm and the sample holder-anodes distances were around 25 cm, as the particle flux depends on the distance and the incident angle. The two anodes and the substrates were positioned so that a different particle flux was present for each sample in a deposition batch. A stainless steel pipe of 3 mm in diameter provided O_2 , D_2 or He gases near the substrates as shown in Fig. 1.

a)



b)



Fig. 1 The schematic representation of the deposition system and the electrical connections used to obtain the Be-C-W composite films with O₂, D₂ and He co-depositions (a) and a photograph of the prepared samples (b)

Mirror polished fine grain graphite plates of dimensions 12 mm x 14 mm were used as substrates. In the first batch, the films were deposited at room temperature, while for the next an oven was used to heat the substrates at 725K. This way, the atoms and the ions from the plasma, reach the substrate without causing thermal shocks at the onset of the deposition due to the high mobility of the particles that arrive at the substrate. The lack of thermal shocks decreases the possibility of getting defects caused by mechanical stress [5].

Rutherford Backscattering Spectroscopy (RBS) and X-ray photoelectron spectroscopy (XPS) analyses were performed on the samples to assess the concentration of the two materials as well as the presence of oxygen and impurities and the films' composition and thickness.

For RBS measurements it had been used a ⁴He energy beam of 2.6 MeV. The beam's energy value was chosen taking into account the interaction cross section of ⁴He and beryllium to avoid the non-Rutherford interaction that may cause errors in the data interpretation. The fitting of the experimental data was done using SIMNRA code, developed at IPP Garching. [6]

The nuclear reaction D(³He, p)⁴He offers information about the implanted deuterium inside the film. For the detection of the resulting particles (α and protons), two detectors are being used, positioned at 102° for protons and 135° for α particles. The protons detector gives information about the total amount of deuterium inside the film, while the α particles detector is used to obtain the deuterium depth profile of the deuterium trapped inside the film. For these measurements, the energies used for the ³He beam were 690 and 800 keV. [6]

Film composition

The main aspect underlined by RBS measurements is the fact that samples with different C-Be ratios were obtained. Also, from the depth profiles obtained from RBS measurements it can be observed that for the room temperature substrates the film was oxidized only at the surface due to the air exposure after the deposition and at the interface, trapped inside before the deposition. For the heated substrates the oxygen present at the interface diffuses into the material, oxidizing the beryllium and the carbon in the whole film. (Fig. 2).

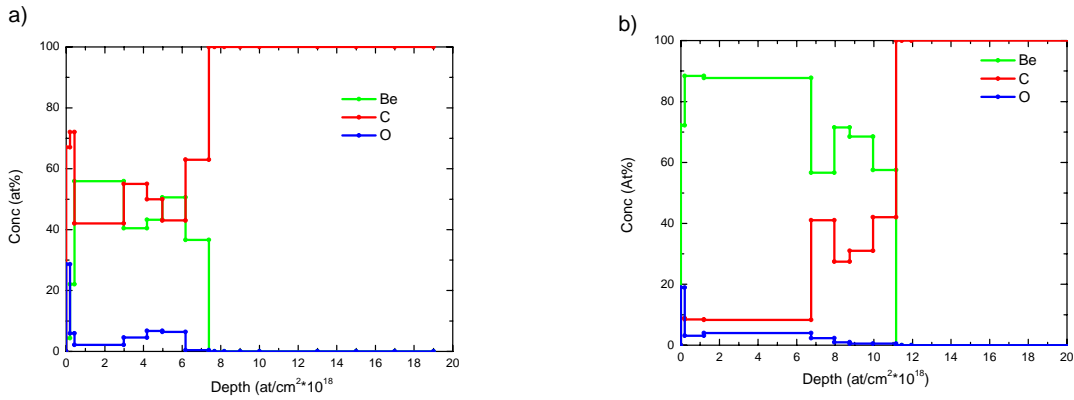


Fig. 2 Elemental depth profiles deduced from the RBS spectra for deposited films at room at 725 K heated substrate (b).

XPS depth profiling spectra were recorded as function of time during sputtering using Ar ions with a density of $1\mu\text{A}/\text{mm}^2$ at 3kV accelerating voltage, at normal angle incidence. XPS analysis was performed for one sample deposited at 725K (Figure 3).

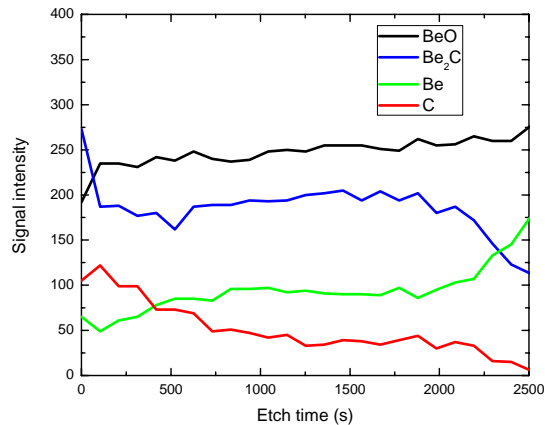


Fig. 3 XPS depth profile for Be-C composite film deposited at 725 K

Analysing the 105 – 120 eV binding energy range, and assigning the Be1s peak at about 111 eV to the metallic Be and the peak at about 113 eV to the Be₂C stable compound [7], the presence of the Be₂C inside the whole film is being highlighted. Also, there can be observed oxidized beryllium (assigning the 115 eV peak to the BeO compound), among the metallic beryllium and atomic carbon.

Retention and desorption studies on Be-C films

Due to the higher purity and low oxidation level, the samples deposited at room temperature were selected to be subjected to deuterium retention and desorption studies.

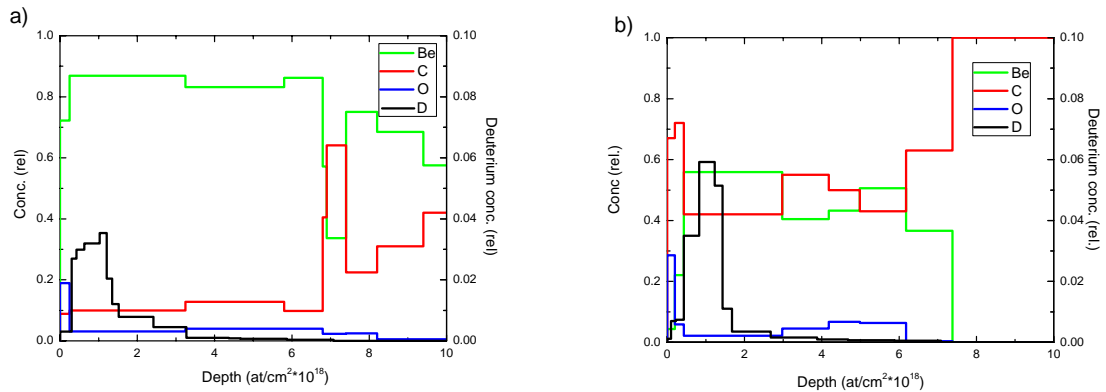


Fig. 4 Deuterium depth profiles for samples with different Be-C relative concentration for high beryllium concentration (a), and for high carbon concentration (b)

Deuterium implantation experiment was performed using the high current ion source of IPP Garching [8]. The energy of D ion beam was 600 eV D₃⁺ (200 eV/D), and the incident direction was normal to the target surface. The implantation was carried out at a room temperature with the flux of $\sim 3 \times 10^{19}$ D/m²s. After certain continuum implantation (2.09×10^{21} D/m²), the amount of D retention was determined by nuclear reaction analysis (NRA). NRA analysis proved that the deuterium depth profile is highly influenced by the relative Be-C concentration. For high Be concentration, deuterium goes deeper inside the film (Fig. 4a).

The total amount of deuterium retained (measured using the protons detector) as a function of the carbon concentration is shown in the Figure 5 and highly depends on the Be-C relative concentration. For high carbon concentration the amount of deuterium retained is lower. So, for the films that have 5% carbon composition the total amount of deuterium retained is 32% from the amount implanted, for the samples containing more than 50%, the

percentage of the deuterium amount retained is less than 10%. It is presumed that this behavior occurred because of the carbon or carbide presence.

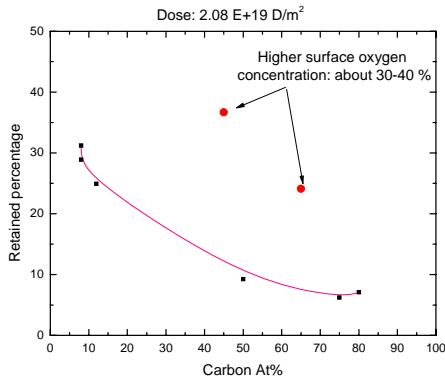


Fig. 5 The total amount of deuterium retained as a function of the carbon concentration

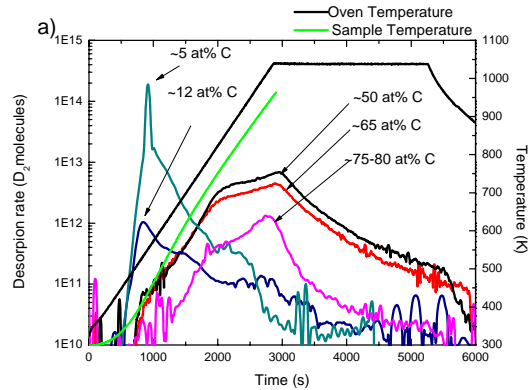


Fig. 6 D₂ Thermal desorption spectra for films with different beryllium - carbon relative concentrations, implanted at room temperature.

The samples corresponding to the two experimental points that do not follow the trend were analyzed before TDS and from the RBS depth profile it was observed that the films presented at the surface very high oxygen concentration (about 40%) inside the whole film. It can be assumed that a BeO layer was formed modifying the retention mechanisms. How the samples accumulated oxygen is still unclear and although it is improbable, it is assumed that oxidation occurred during implantation process. These samples were not used for further studies.

Thermal desorption spectroscopy (TDS) experiment was performed for the implanted samples using the TESS facility at IPP Garching [9]. The experiment consists in heating the sample with 15K/min ramp, up to 1000K followed by a 20 minutes hold. Then the sample was allowed to cool by itself. During the entire heating process, the amount of deuterium released from the film (as D₂ and HD molecules) was measured.

TDS profiles for the Be-C samples showed clear dependence of deuterium release on the beryllium - carbon relative concentration. For implantation at room temperature and for high Be concentrations it was observed a pronounced D₂ desorption peak between 425 and 475 K, which corresponds to deuterium desorption from beryllium related trapping sites. At higher carbon/carbide concentrations this beryllium related desorption peak decreases and a

correspondingly increasing peak between 925 and 975 K appears, which is attributed to retention of the carbon/carbide related trapping sites [10] (figure 6).

Conclusion

Composite beryllium-carbon-tungsten films with co-deposited O₂, D₂, and He gases were prepared using the thermionic vacuum arc technique, coating graphite substrates from two different sources, ignited simultaneously. Their characteristics are presumed to be similar with the future resulting inner wall surface after the thermo-nuclear plasma exposure inside ITER.

XPS analysis proved beryllium-carbide formation inside the composite samples. The ratio in some samples was around 30%. Substrate temperature during deposition influences the oxygen concentration inside the films.

Deuterium implantation was performed for the samples obtained at room temperature. Using Nuclear Reaction Analysis (NRA) was determined the retention of deuterium and deuterium depth profiles of the prepared samples.

The relative Be-C concentration influence both the retention and the desorption mechanisms. For low beryllium concentration into the mixed Be-C layer the amount of deuterium was lower. The TDS spectra proved that the different samples different behavior was caused by different individual trapping sites for each of these two elements.

References

- [1] R.Aymar, P. Babaraschi and Y. Shimomura, *Plasma Phys. Control. Fusion* **44** (2002) 519
- [2] G. F. Matthews, P. Edwards, T. Hirai, et al., *Phys. Scr.* **T128** (2007) 137
- [3] C. P. Lungu, I. Mustata, V. Zaroschi et al., *Phys. Scr.* **T128** (2007) 157
- [4] Anghel, I. Mustata, C. Porosnicu, et al., C. P. Lungu, *J. Nucl. Mater* **385** (2009) 242-245
- [5] C. P. Lungu, I. Mustata, V. Zaroschi, et al., *Phys. Scr.* T128 (March 2007) 157–161
- [6] M. Mayer, SIMNRA User's Guide, Tech. Report IPP 9/113, Max-Planck-Institut für Plasmaphysik, Garching, 1997
- [7] P. Goldsträß and Ch. Linsmeier, *Nuclear Instruments and Methods in Physics Research Section B: Beam Interactions with Materials and Atoms* 161-163 (2000) 411-414
- [8] K. Krieger and J. Roth, *J. Nucl. Mater* 290-293 (2001) 107-111
- [9] J. Roth, V.Kh. Alimov, A.V. Golubeva, et al., *J. Nucl. Mater.* **363-365** (2007) 822-826

- [10]K. Sugiyama, J. Roth, A. Anghel, C. Porosnicu, M. Baldwin, R. Doerner, K. Krieger, C.P. Lungu, Consequences of Deuterium Retention and Release from Be-containing Mixed Materials for ITER Tritium Inventory Control, J. Nucl. Mat, in print

Presentations and publications in connection with the project

Presentations

1. Cristian P. Lungu, D-retention in mixed materials containing H, D and He, Report on task agreement WP10-PWI-06-02-02/MEdC/PS at TF-PWI annual Meeting, 3-5 Nov 2010, Vienna, Austria

Publications (Journals):

1. C. Porosnicu, A. Anghel, K. Sugiyama, K. Krieger, J. Roth, C.P.Lungu, Influence of beryllium carbide formation on deuterium retention and release, J. Nucl. Mat, accepted
2. K. Sugiyama, J. Roth, A. Anghel, C. Porosnicu, M. Baldwin, R. Doerner, K. Krieger, C.P. Lungu, Consequences of Deuterium Retention and Release from Be-containing Mixed Materials for ITER Tritium Inventory Control, J. Nucl. Mat, accepted

Publications (Books):

1. C. P. Lungu, I. Mustățã, C. C.Porosnicu, I. Jepu, A. Anghel, **Caracterizarea filmelor compozite combinatoriale obținute prin metoda arcului termoionic în vid**, București, Editura Academiei Oamenilor de Știință din România, 2010, ISBN 978-606-92500-1-3 (in Romanian)

Director de proiect: Dr. C. P. Lungu

Comunicari la Conferinte internationale.

1. Cristian P. Lungu, **D-retention in mixed materials containing H, D and He**, Report on task agreement WP10-PWI-06-02-02/MEdC/PS at TF-PWI annual Meeting, 3-5 Nov 2010, Vienna, Austria

Publicatii (Reviste ISI):

1. C. Porosnicu, A. Anghel, K. Sugiyama, K. Krieger, J. Roth, C.P.Lungu, Influence of beryllium carbide formation on deuterium retention and release, J. Nucl. Mat, accepted
2. K. Sugiyama, J. Roth, A. Anghel, C. Porosnicu, M. Baldwin, R. Doerner, K. Krieger, C.P. Lungu, Consequences of Deuterium Retention and Release from Be-containing Mixed Materials for ITER Tritium Inventory Control, J. Nucl. Mat, accepted

Publicatii (Carti):

1. C. P. Lungu, I. Mustața, C, C.Porosnicu, I. Jepu, A. Anghel, **Caracterizarea filmelor compozite combinatoriale obținute prin metoda arcului termoionic în vid**, București, Editura Academiei Oamenilor de Știință din România, 2010, ISBN 978-606-92500-1-3 (in Romanian)

RST in extenso

PRODUCTION OF BERYLLIUM COATINGS FOR INCONEL CLADDING TILES FOR THE ITER-LIKE WALL PROJECT

Etapa II (Decembrie 2010)

Activitatea 1:

Be coatings on IWGL, IWC and DPC inconel tiles

Activitatea 2:

Be coatings on test coupons.

Activitatea 3:

Thickness characterization

Abstract

The project's aim is the coating of about 800 inconel tiles to be used on the first wall of the JET fusion device in Culham, UK. During the 2010 were planned coating activities of 8 μm beryllium thick films on inconel tiles, beryllium coatings on test samples and film thickness characterization. Starting with January 2010, UKAEA sent to the Nuclear Fuel Plant (NFP) – Pitesti the Inconel tiles in few lots. Because during the 2009 were not performed beryllium coatings due to the postponed schedule was necessary, at the beginning of 2010, the re-testing of the deposition systems. New beryllium coatings were performed on test samples, repeating the The next step consisted in deposition on real Inconel dump-plates in the presence of specialists from JET (Les Pedrick) and EFDA (Zoita Vasile)

The third step consisted in 8 μm thickness beryllium film deposition using thermal evaporation method on IWGL Clading, IWC and Dump Plates Inconel tiles.

Were performed thickness tests, adherence tests as well smear tests on the plastic bags used for the coated tiles packing.

The coated tiles were collected by a transport company under the CCFE-Culham management. In total 816 Inconel tiles were coated with beryllium.

Introduction

The ITER-like Wall Project, part of the "JET programme in support of ITER", to be implemented on JET included R&D activities to develop a method of depositing Be layers on an interlayer plus a Be over layer onto Be tiles and characterization of the Be coating purity by surface and structure analysis techniques as well.

The JET main wall will be made of solid Be tiles. In order that the erosion rate of the Be wall to be assessed, it is necessary to be measured erosion of a few microns of beryllium. The "markers" tiles will be distributed in the areas of interest such as Outer Poloidal Limiters (OPL) and Inner Wall Guard Limiters (IWGL).

The "marker" is a Be tile with a stripe of an easily detected heavy metal deposited on it as a thin interlayer, and with a few microns layer of the bulk-like Be on top of that. If the outer layer is eroded at the same rate as the bulk, then the erosion rate can be determined by detecting the distance of the interlayer from the final surface, for erosion of less than the film thickness.

According to the Individual Task Description for the Article 6.3 Order JW6-OEP-MEC-09C the main objectives are the following:

A. To produce Be-coatings on Inconel tiles in accordance with the technical specifications and the JET requirements contained in ILW-EDM-1223-T002

The aims of this task is the manufacturing of Be coatings on inconel samples provided by JET using thermal evaporation method developed at Nuclear Fuel Plant (NFP) in Pitesti

Beryllium coatings on inconel using thermal evaporation in vacuum

The activities for qualification procedure of the thermal evaporation deposition method started in 2008, examining the qualification documents:

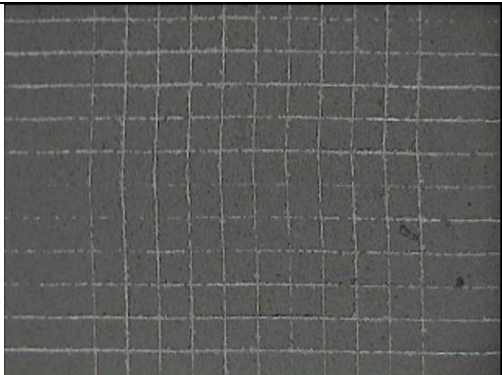
1. The qualification plan: Beryllium coatings on Inconel tiles;
2. Quality inspection of Beryllium coatings;
3. Beryllium coatings: technical preparation procedure;
4. Beryllium coatings: Operating procedure;
5. Handling, identification and packing the materials;
6. Beryllium thickness adjustment;
7. Repairing of the inconel tiles coated with Beryllium.

There have been produced Be films coatings on stainless steel test samples and zirconium alloy tiles, material used in serial production at NFP Mioveni-Pitesti. There have been made new adherence tests to ensure the coatings reproducibility. The samples were measured using the MICRODERM device of NFP. The values obtained were between the limit values requested by the project (the thickness of the Be films 7-9 μm).

During 2008, there have been made Be films coatings for method qualification, on inconel tiles and witness samples, sent by UKAEA, Culham, England, respectively: 2 IWGL Tiles, 4 IWC Tiles, 2 DPC Tiles, 100 Inconel witness samples of 6 x 29.5 x 1.2 mm³ and 25 inconel witness samples of 15x20x1.2 mm³.

The tiles and the witness samples have been placed in the deposition chamber, using for Be films coatings the thermal evaporation method, observing the operating procedure approved by UKAEA. .

Figs. 1 shows the photographs of IWGL tiles coated with Be and Fig. 2 shows inconel witness samples after the adherence test.

	
<p>Fig.1 Inconel IGWL tiles coated with Be by thermal evaporation in vacuum method</p>	<p>Fig.2 Inconel witness samples after the adherence test</p>

Thickness measurements (from which resulted that the Be thickness layer was in the range 7-9 microns) and the adherence measurements (from which resulted that the films' adherence is proper) have been made in the presence of UKAEA specialists.

An Inconel sample set coated with Be has been sent to UKAEA for impurities' measurements in the coated layers.

Starting with January 2010, CCFE sent to the Nuclear Fuel Plant (NFP) – Pitesti the Inconel tiles in few lots. The agreed coating schedule was:

Be Coating Schedule

Tile System	Latest Arrival Date
IWGL Cladding	8-Feb-2010
IWC	31-Mar-2010
Dump Plates	30-Apr-2010

Because in 2009 were not performed beryllium coatings due to the postponed schedule was necessary, at the beginning of 2010, the re-testing of the deposition systems. New beryllium coatings were performed on test samples, repeating the procedures carried out during the qualification of the evaporation method.

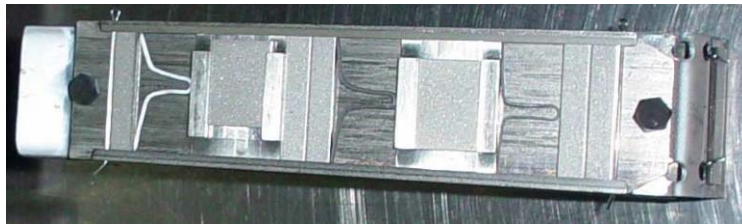


Fig. 3 Photograph of the witness samples mounted on the coating holder.

First, were used as substrates, Inconel plates of 5 mm x 10 mm and 15 mm x 20 mm sizes. Thickness was found in the range of 7.09 – 7.97 μm and adherence tests were satisfactory, as shown in Fig. 4. (The documents accompanied the witness samples and the pre-production lot)

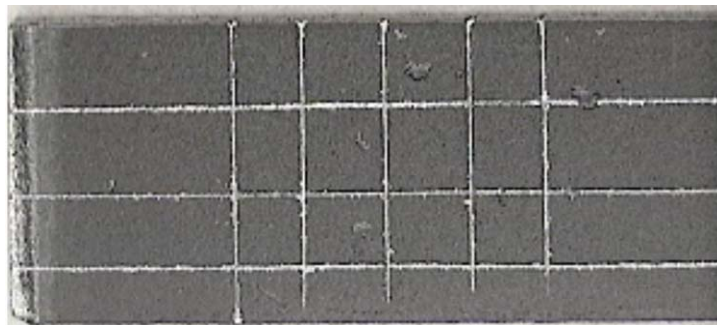


Fig. 4 The adherence test performed on the witness samples.

The next step consisted in deposition on real Inconel dump-plates in the presence of specialists from JET (Les Pedrick) and EFDA (Zoita Vasile)

The third step consisted in 8 μm thickness beryllium film deposition using thermal evaporation method on IWGL Cladding, IWC and Dump Plates Inconel tiles.

The first lot of 84 off IWGL Inconel tiles was collected on March 13.2010

The updated Be coatings plan was established at 13.05.10:

1. Lot 1 Dump Plate (DP) carrier tiles (196 tiles): 07.05.10
2. Inner Wall Cladding (IWC) tiles (200 tiles): 04.06.10
3. Lot 2 Dump Plate (DP) carrier tiles (196 tiles): 30.06.10
4. Lot 3 Dump Plate (DP) carrier tiles (88 tiles): 30.07.10



Fig. 5 Adjusting Inconel tiles on the jigging device

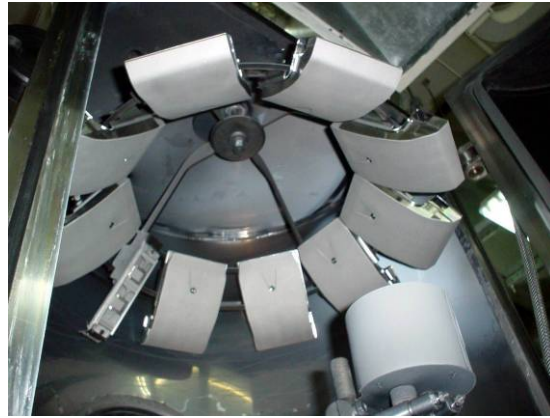


Fig. 6 Inconel tiles after beryllium coatings

After be coatings on all Inconel tiles transferred at NFP Pitesti (working in 2 or three shifts in order to reduce the coating period) were performed thickness and adherence tests on the coated tiles and witness samples, respectively. Smear tests were performed on the plastic bags used for the coated tiles packing. Every production lot was accompanied by the following documents:

- a. Packing list for Consignment to JET (Inconel tiles)
- b. Certificate of Conformity for Consignment to JET (Inconel tiles)
- c. INVOICE (not for payment)

The last coated Inconel tiles lot (680 tiles – 10 wooden crates) was collected by a transport company under the CCFE-Culham management. The total number of coated tiles was 816.

G. Burcea, F. Din1, A. Tomescu, L. Pedrick, C. P. Lungu , I. Mustata, V. Zaroschi, and JET-
EFDA contributors, **Beryllium coatings on Inconel tiles**, SOFT international Conference,
September 2010, Porto, Portugal.

SCIENTIFIC REPORT

Task title: Removal of codeposited materials from gaps with a plasma torch /
Indeprtarea materialelor codepuse de pe suprafete plane si castelate cu torta
de plasma

Code: WP10-PWI-02-04-01/MEdC/BS

Outline

1. General objectives of the project
2. The objectives of the activities in the **Sem II 2010**
3. Summary of obtained results
4. Description of the work. Results
5. Conclusions
6. Future work

1. General objectives of the project

The long-term material co-deposition is associated with the tritium retention issues, which become most prominent in PFCs with gap structure. Cleaning with the plasma torch at atmospheric pressure is based on the scanning of the surface with a small size plasma source. *The purpose of this project is to investigate the removal of carbon and mixed layers from flat and castellated surfaces with plasma torch working in nitrogen/argon/reactive gases.*

2. The objectives of the activities in the present stage of the project

In the frame of the project, for the second part of the year 2010, the Romanian team focused on the following activities:

- Experiments of cleaning with plasma torch working in nitrogen/argon/reactive gases;
- Cleaning of carbon and mixed layers from laboratory/Tokamak coated flat and castellated surfaces;

3. Summary of the obtained results / Rezumatul rezultatelor obtinute

The previous experiments realized in the frame of the task focused on plasma torch operation in nitrogen/argon/reactive gases. The present contribution focuses on cleaning, with plasma torch working in nitrogen/argon/reactive gases, of carbon and mixed layers

from flat and castellated surfaces. First, experiments to establish the optimum parameters for high removal rate of carbon from flat graphite surfaces were realized. The cleaning experiments were performed with plasma torch operated in argon/ammonia, argon/oxygen, argon/hydrogen, nitrogen, nitrogen/hydrogen and nitrogen/oxygen. The assessment of the cleaning efficiency was performed with profilometry measurements. The removal rates of carbon were calculated from the removal profiles. In nitrogen, the optimum parameters for the highest removal rates were obtained at the following parameters: distance between plasma torch and substrate = 5 mm, RF power = 400 W, nitrogen flows = 3000 sccm, scanning speed = 5mm/s. The effectiveness of cleaning experiments over graphite substrates, performed with plasmas generated in reactive gases, has been assessed by profilometry measurements. Plasmas in argon and argon/hydrogen have a low effect on surfaces; when these gases are admixed in nitrogen or argon gases a quenching effect appears, which decreases the plasma length and diminishes the active species arriving at surface. The oxygen plasma is the fastest in removal of laboratory made co-deposited layers; nevertheless, the operation with oxygen or mixtures with high oxygen concentration leads to instabilities and to severe shortening of torch lifetime, which are unacceptable drawbacks. The important finding is that plasma torch operated with nitrogen/oxygen mixtures, with about 10% oxygen, at high powers (400 W) and moderate gas flow rates (3000 sccm nitrogen, O₂ flow = 300 sccm) presents a very high removal rate (up to 10⁻² g/min), which is up to ten times higher than the rates obtained until now.

The cleaning experiments performed on gaps coated with a-C:H/metal layers showed the same behaviour, previously observed with simple carbon layers: the cleaning goes deep inside gaps up to 20 mm, is faster at the top margin of the gaps, and it is very effective on its bottom. The AFM experiments proved the roughening of surface, while EDAX proved that the metal phases become dominant on surface, thus being less removed compared to carbon phases.

4. Description of the work. Results

a) Cleaning of carbon layers

The experiments of carbon removal were realized by scanning of flat graphite surfaces with the plasma torch at atmospheric pressure working in different gases (nitrogen/argon/reactive gases). A computer controlled XY translation table assisted the scanning procedure. Figure 1 shows the image of the flat graphite sample during cleaning experiments. Figure 2 shows images of a graphitic surface before and after scanning along parallel lines, with nitrogen plasma (...) for an increased number of scans.

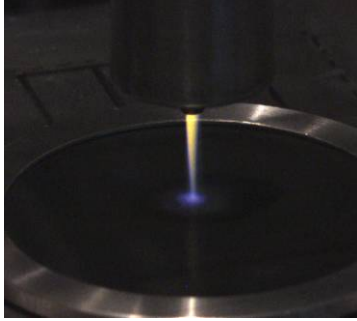


Figure 1. Image of the graphite sample during cleaning experiments

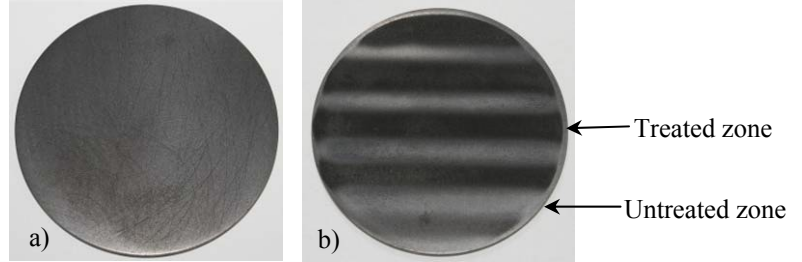


Figure 2. Image of the graphite sample before (a) and (b) after plasma torch cleaning

A study of the cleaning efficiency was performed on the graphite sample regarding the influence of the gas nature, the torch-surface distance, RF power, mass flow rates and the number of scans.

The gases used for the cleaning experiments were argon/ammonia, argon/oxygen, argon/hydrogen, nitrogen, nitrogen/hydrogen, and nitrogen/oxygen. After scanning with plasma torch, profilometry measurements on these samples were realized. The section of the profile allowed the calculation of the mass of the removed material, from where dividing by processing time the removal rate was obtained.

The cleaning with Ar was inefficient; the effect on the surface was too low to obtain measurable profiles. Contrary, carbon removal rates were easy calculated from obtained profiles in nitrogen. Figure 3 presents the profile of the graphite surface after scanning in different N_2 flows and different RF powers. Figure 4 shows the removal rates of carbon after different N_2 flows and different RF powers.

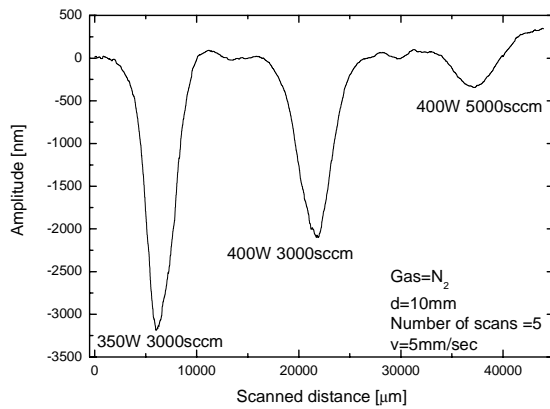


Figure 3: Graphite surface profile after different N_2 flows and different RF powers

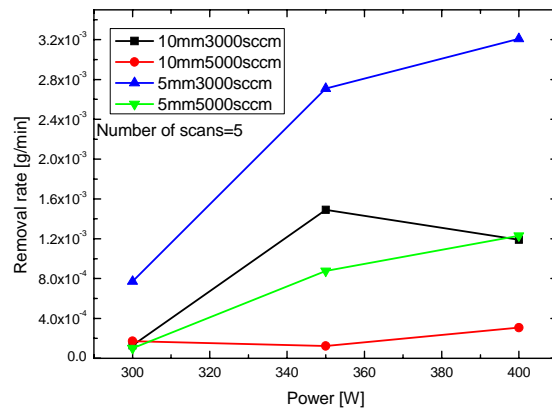


Figure 4: Carbon removal rates after different N_2 flows and different RF powers

From these experiments, we concluded that the optimum parameters for nitrogen plasma cleaning are: distance 5 mm; high power of 400 W; small and moderate flow rates (3000 sccm). These values were selected for experiments where reactive gases were added to the nitrogen.

The deepness of the profiles obtained from argon/ammonia, argon/oxygen, argon/hydrogen, and nitrogen/hydrogen were very low due to the low etching rate of these gases at 5 mm distance. They did not permit the determination of the removal rate.

In Figure 5a and 5b the profiles of graphite samples after scanning with the plasma torch working in nitrogen/oxygen mixed gases are presented, for an increasing O₂ mass flow rate. A better comparison between profiles is done in Figure 6, where the profiles are aligned with respect to their minimum. The dependence of the removal rate upon the O₂ mass flow rate is presented in Figure 7. It is seen that an optimum value of 10% O₂ in the nitrogen leads to the highest removal rate of $9.5 \cdot 10^{-3}$ g/min.

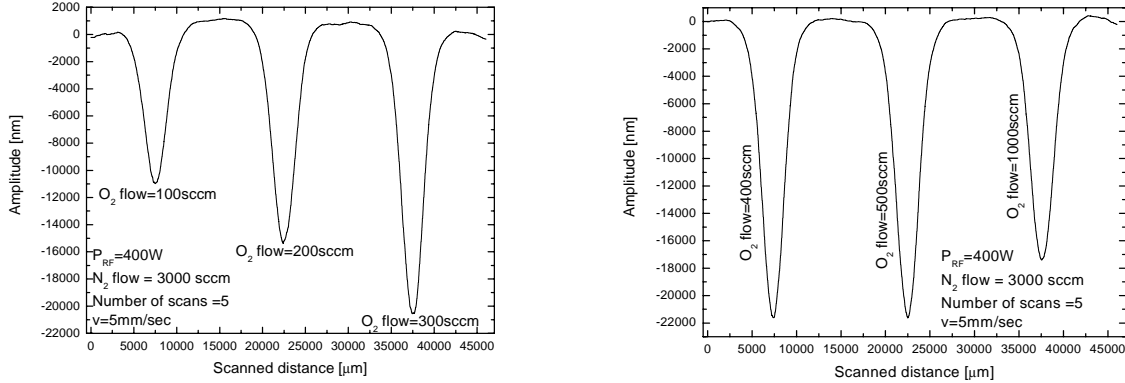


Figure 5: Graphite surface profiles after scanning with different O₂ flows

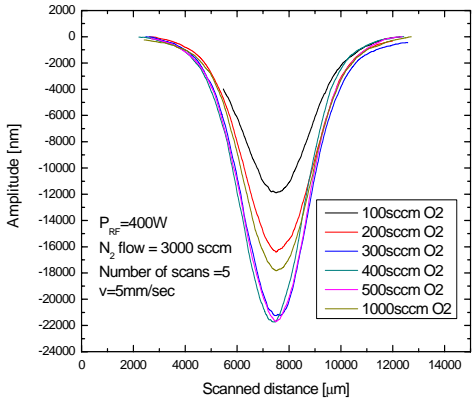


Figure 7: Profiles after scanning with different O₂ flows

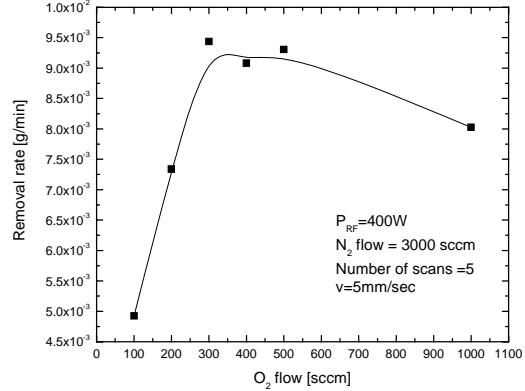


Figure 8: Carbon removal rates after scanning with different O₂ flows

b) Cleaning of mixed layers

Cleaning experiments of mixed layers (a-C:H/W, a-C:H/Al) on flat and castellated surfaces were performed in nitrogen and nitrogen/oxygen mixed gases with different number of scans. Optimum parameters were chosen for the carbon removal rate in the experiments involving cleaning of mixed layers: RF power = 400 W, distance between plasma torch and substrate = 6 mm, scanning speed = 5 mm/s, nitrogen mass flow rate = 4000 sccm.

Imaging, AFM and EDAX measurements were realized on the scanned samples.

In Figure 12 are presented images of flat mixed thin layers (600 nm, tungsten/a-C:H) before scanning (a, b), during scanning procedure (c) and after scanning procedure (d). From Figure 12d it is observed that the mixed layer is apparently removed after 1 scan with the plasma torch working in nitrogen. The same effect occurs after scanning

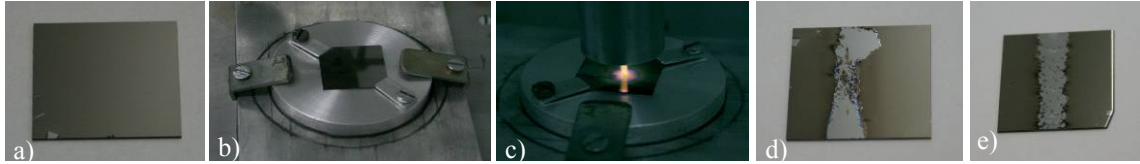


Figure 12: Images of flat mixed layers: a) before cleaning; b) mounted on holder; c) during scanning procedure and d),e) after cleaning

with the plasma torch working in nitrogen/oxygen (Figure 12e).

Figure 9 shows the AFM images of the treated flat thick mixed layers (5 microns, a-C:H/W) with the plasma torch working in nitrogen. The roughness of the samples increases with the number of scans indicating the material removal.

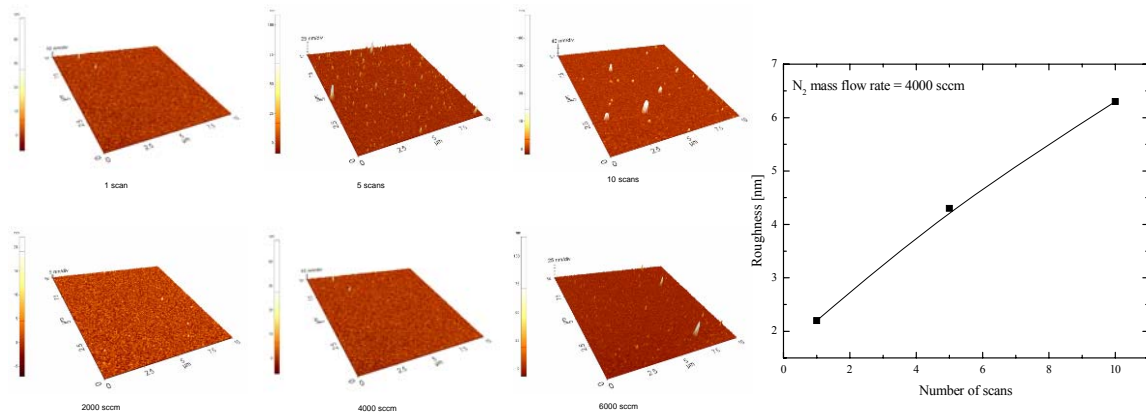


Figure 9: AFM images of the flat mixed layers (tungsten/a-C:H) surfaces and the roughness of these surfaces

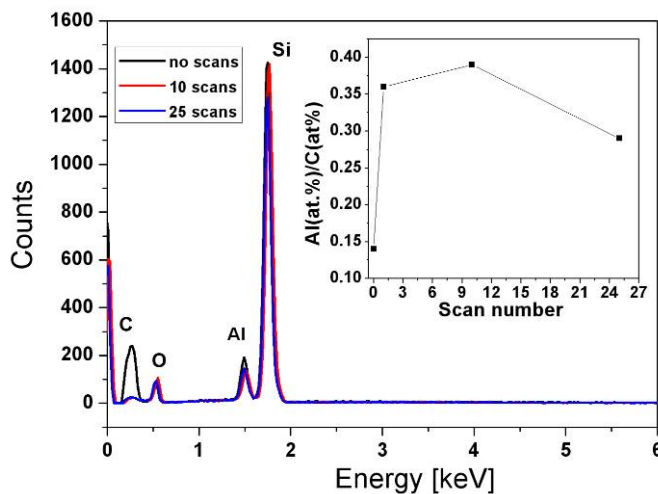


Figure 11: EDAX investigations of a sample coated with hydrogenated carbon and aluminium mix

The results of EDAX investigations (Figure 11) show a stronger reduction of the C component due to plasma treatment comparative to the Al one. Modifications of EDAX signal correspond do an increase of Al (at %) /C (at %) from 0.14 (for untreated probe) to 0.39 (for 10 plasma scans). This leads to the conclusion that plasma treatment removes mainly the C from the co-deposited layer.

Next experiments were realized on castellated surfaces. The castellated surfaces are delimited by two cubes (figure 13). Silicon surfaces coated with the tungsten/a-C:H mixed layers were mounted on inside the faces of cubes. For these experiments the best parameters were chosen for the cleaning of carbon (RF power = 400 W, N₂ flow = 3000 sccm, O₂ flow = 300 sccm and distance between plasma torch and graphite surface = 5mm) and scanning with increased number of scans were performed.

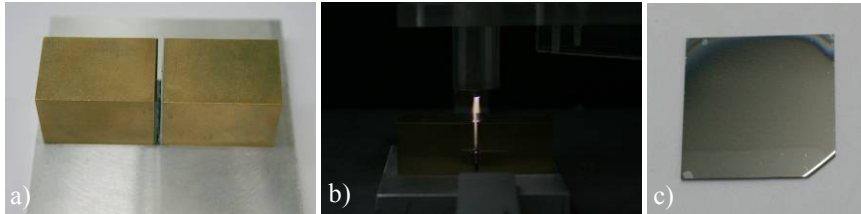


Figure 13: Images of castellated mixed layers: a) mounted on holder before cleaning; b) during scanning procedure and c) after cleaning

The cleaning experiments showed the same behaviour, previously observed with simple carbon layers: the cleaning goes deep inside gaps up to 20 mm, is faster at the top margin of the gaps, and it is very effective on its bottom.

5. Conclusions

Cleaning experiments on flat graphite samples and on flat and castellated surfaces covered with mixed layers were performed. On flat graphite samples, the best cleaning results are in nitrogen and nitrogen/oxygen. Removal rates increase with the number of scans. In nitrogen/oxygen mixed gases, with 3000 sccm nitrogen mass flow rate, the removal rate increases with the oxygen mass flow rate, and reaches an optimum of around 10^{-2} g/min at 300 sccm; after this value the removal rate decreases again. On flat mixed layers scanned with the plasma torch, the roughness increases with the number of scans. EDX investigation showed that after scanning the C/Al ratio in the mixed layer decreases.

6. Future work

The following activities will be related to study of the cleaning process in order to increase the efficiency. Such as, are of high importance the evaluation of the influence of surface temperature on the cleaning. A correlation of ante and post cleaning surface properties (chemical state, roughness, reflectivity) with the parameters of the cleaning process (feeding gas, power, distance), is necessary, as well.

Publications

1. E.R. Ionita, C. Stancu, T. Acsente, B.Mitu, G. Dinescu, C. Grisolia, *Plasma torch cleaning of carbon layers from deep gaps at atmospheric pressure*, 26 th Symposium on Fusion Technology (SOFT 2010), Porto, Portugal, 27 September – 1 October, 2010.

2. E.R. Ionita, C. Stancu, M. Teodorescu, T. Acseente, G. Dinescu, *Extension of plasma torch operation with reactive gases for wall cleaning purposes*, 6th Euratom MEdC Association Days Meeting, 2nd July, 2010, "Alexandru Ioan Cuza" University, Iasi, Romania
3. G. Dinescu et al. *Removal of codeposited materials from gaps with a plasma torch*, presentation at Joint Meeting of EFDA Taskforce Walls Interactions SEWGs and Emerging Technology System Integration (ETS) 8-11 June 2010, Garching, Germany
4. C. Stancu, M. Teodorescu, A. C. Galca, G. Dinescu, *Carbon layers cleaning from inside of narrow gaps by a RF glow discharge*, poster at Twelfth International Conference on Plasma Surface Engineering", PSE 2010, Garmisch-Partenkirchen, Germania, 12-17septembrie 2010, paper submitted to Surface and Coatings Technology.

SCIENTIFIC REPORT

Task title: LABORATORY MODELS FOR CODEPOSITED LAYERS / MODELE DE LABORATOR PENTRU STRATURI CODEPUSE

Code: WP10-PWI-02-04-02/MEdC/BS

Outline

1. General objectives of the project
2. The objectives of the activities in the **Sem II 2010**
3. Summary of obtained results
4. Description of the work. Results and conclusions
5. Future work

1. General objectives of the project

Laboratory made co-deposited layers are of high importance for the validation of fuel removal techniques (by laser, discharge, etc) and of monitoring techniques. Various groups have applied lasers, oxidation, and discharges in order to remove codeposited layers, but the results are difficult to compare, because each group has utilized its own synthesized material. ***The purpose of the project is to realize and characterize a family of materials, similar to the codeposited layers, in order to be used as laboratory models for the fuel removal or monitoring experiments.*** The problem is complex, because two or three materials are to be incorporated in the same layer, and these materials must be relevant for the fusion technology. As example of possible models one may mention amorphous hydrogenated layers, diamond like layers, carbon layers admixed with metals.

2. The objectives of the activities in the present stage of the project

The deposition of mixed carbon/metal layers/hydrogen must be approached in connection with the plans of using metals (tungsten, beryllium) for next JET experiments and ITER. The project main objectives are:

- Realization and characterization of model co-deposited layers for their use in conjunction with fuel removal techniques
- ***Studies of the deposition and chemical transformation of Al/C + hydrogen layers, or (if possible to work with) Be/C + hydrogen layers, or similar layers***

At the current stage of the project there was in view the second objective; for its accomplishment there were pursued the following activities:

- Optimization and the monitoring of the deposition technique
- Study of the transformation of the model codeposited layers induced by gases

3. Summary of the obtained results

The sequential deposition method developed previously in the project proved its ability in producing mixed (composite) a-C:H/Me layers as laboratory models for fusion reactors codeposited layers. This process consist in repeating for N_{CYC} times the following steps: deposition of W by magnetron sputtering (MS) in Ar (t_W seconds) \rightarrow transport of substrate (t_{TR} seconds) to PECVD plasma source (during this time interval C_2H_2 is admitted in the process chamber) \rightarrow deposition of a-C:H in PECVD process in Ar + C_2H_2 mixture (t_C seconds) \rightarrow transport of substrate (t_{TR} seconds) to MS plasma source (when C_2H_2 is evacuated from the process chamber). The value of transport time is an important process parameter, influencing the proper condition of the gaseous atmosphere during deposition and the reasonable duration for depositing thick layers of a-C:H/Me. For evaluating the repeatability of the deposition cycles during deposition of one sample and also of different samples deposited in the same conditions there was implemented a setup for monitoring the sequential deposition process by means of optical emission spectroscopy, using a low cost, low resolution (0.2nm) optical multichannel analyzer (OMA). The monitoring wavelengths were established on the basis of an optical emission spectroscopy (with both high and low resolution) study of MS and PECVD processes. The optical monitoring proved also to be useful for substrate cleaning process and for target pre sputtering, prior starting the sequential deposition process.

The degradation (fast change of colour followed by severe delaminating) of laboratory models for codeposited layers containing Be (i.e. a-C:H/Al mixed layers, Al used as Be substitute) soon after their exposure to ambient atmosphere was investigated. For this purpose, there was monitored the optical transmission of a-C:H/Al mixed layers deposited on glass substrates, during their interaction with atmospheric air and its components (O_2 , N_2 , Ar, and Ar carrying water vapours).

It results that the optical changes are due to a combined chemical effect of the atmospheric air components (without Ar), the main contribution being that of water vapours. The mechanical instability of the a-C:H/Al layers on the substrate is also mainly influenced by the water vapours contained in the atmospheric air. It was also observed the stabilizing effect of a-C:H/Al layers on the substrate by post deposition treatment with N_2 .

4. Description of the work. Results and conclusions

4. 1. Optimization of the deposition technique; implementation of sequential process optical monitoring

The sequential deposition method developed previously in the project proved its ability in producing mixed (composite) metal/carbon layers as laboratory models for fusion reactors codeposited layers. Shortly, the mixed layers are grown by repeating for N_{CYC} times the following steps: deposition of W by magnetron sputtering (MS) in Ar (t_W seconds) \rightarrow transport of substrate (t_{TR} seconds) to PECVD plasma source (during this time interval C_2H_2 is admitted in the process chamber) \rightarrow deposition of a-C:H in PECVD process in Ar + C_2H_2 mixture (t_C seconds) \rightarrow transport of substrate (t_{TR} seconds) to MS plasma source (when C_2H_2 is evacuated from the process chamber). The value of transport time is constrained by the followings: a) long t_{TR} are desirable in order to assure the optimal gaseous atmosphere during the deposition steps; b) too long t_{TR} values will lead to unacceptable long duration of the deposition process when thicker layers are required, (for example, using the following process parameters: $t_W=4s$, $t_C=9s$, $t_{TR}=5s$, $N_{CYC}=850$, $P=80W$, 70 sccm Ar and 5 sccm C_2H_2 , the deposition rate is 4.7 nm per cycle, leading to more than 5 hours process duration for obtaining a 4 μ m thick a-C:H/W composite layer).

For evaluating the repeatability of the deposition cycles during deposition of one sample and also of different samples deposited in the same conditions there was implemented an monitoring

setup for the sequential deposition process, by means of optical emission spectroscopy. Based on the optical monitoring method there was also evaluated the optimal value of t_{TR} .

4.1.1. Optical monitoring method and experimental setup

The optical monitoring setup is based on a low cost, low resolution (0.2nm) Optical Multichannel Analyzer (OMA, Ocean Optics HR4000) and on the feature of the associated Spectra Suite software to record the time evolution (trend) of the optical intensity corresponding to a specified wavelength (the recorded curves will be named *line trends*). The light is collected from the substrate vicinity, in the same solid angle for both PECVD and MS processes, using a 60 μ m diameter UV-VIS optical fiber.

The identification of the wavelength values useful in monitoring the sequential deposition process [1] was performed recording low (using OMA) and high resolution (using a Horiba Jobin Yvon spectrograph FHR-1000, 0.02 nm resolution) optical emission spectra of both PECVD and MS discharges ignited using 5sccm C_2H_2 mass flow rate, 70 sccm Ar, 80W RF power process parameters; supplementary, there were performed OES investigations over PECVD plasma ignited in sole C_2H_2 . Fig. 1 presents the low resolution spectra for the PECVD and magnetron discharges. For the sole C_2H_2 PECVD discharge (Fig. 1a.) there can be observed spectral features proving the dissociation of C_2H_2 in plasma: the emission bands of the CH and C_2 radicals (transitions $A^2\Delta-X^2\Pi$ at 431nm and $d^3\Pi_g - a^3\Pi_u$ of the Swan band system at 516.5 nm) and the hydrogen H_α atomic emission line (656.3 nm). Addition of Ar to the C_2H_2 PECVD discharge leads to “masking” of the CH and C_2 spectral signatures by the intense ArI lines (Fig. 1b and Fig.2). Still, the atomic H_α emission line is well resolved by OMA in both spectra recorded for the C_2H_2 and Ar+ C_2H_2 PECVD; for this reason *the hydrogen H_α emission line (656.285nm) was selected for optical monitoring the PECVD process during the a-C:H deposition step.*

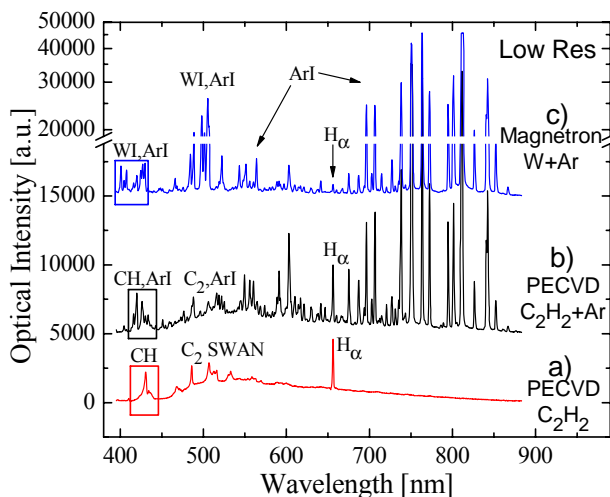


Fig. 1. Low resolution spectra of: a) PECVD discharge in C_2H_2 ; b) PECVD discharge in Ar and C_2H_2 mixture; and c) tungsten magnetron discharge in Ar.

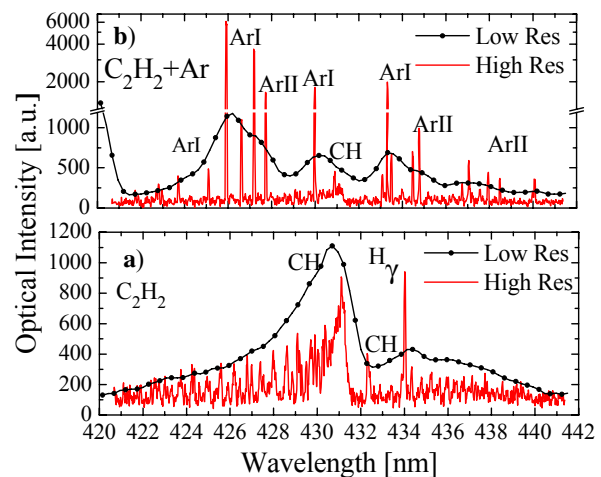


Fig. 2. High and low resolution spectra over the 420-442 nm spectral range for: a) C_2H_2 PECVD discharge; and b) Ar and C_2H_2 mixture PECVD discharge.

The spectrum recorded during magnetron discharge step is presented in Fig.1c. High resolution investigation of the magnetron discharge (not presented here) recorded in the 400-430nm interval revealed that only the peak situated around 401 nm contains the only WI spectral signatures, without Ar lines contributions. Thus, the *WI 400.87nm wavelength was selected for optically monitoring of the tungsten deposition steps.* Also, for both deposition steps, *the 763.51nm argon emission line was selected as references of plasma emission.*

Fig. 3 presents the optical line trends recorded at the beginning of a sequential process in which was deposited a 400nm thick a-C:H/W layer ($t_w = 8s$, $t_c = 5s$, $t_{TR} = 5s$, $N_{CYC} = 80$, $P_{RF} = 80W$). A good repeatability of the deposition steps can be observed. The optical monitoring proved also to be useful for substrate cleaning process and for target pre sputtering.

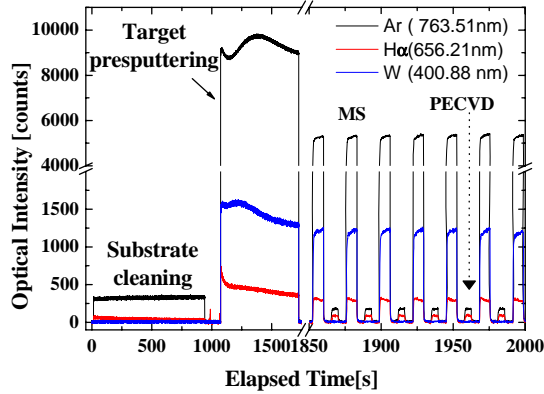


Fig. 3. Example of optical line trends recorded during optical monitoring of the sequential deposition process

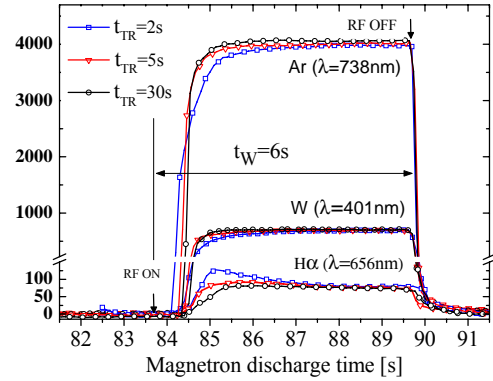


Fig.4. Evolution of the optical line trends during magnetron discharge step for diverse values of the transport times ($t_{TR} = 2s, 5s, 30s$); plasma exposure times are constant ($t_c = 7s$, $t_w = 6s$).

4.1 2. Optimization of the deposition technique

During the sequential deposition process the Ar flow is constant and the gas composition is controlled via the admission and evacuation times for acetylene which are strictly linked to the substrate transport time t_{TR} . Fig.4 presents the superposed optical line trends during the tungsten deposition step in processes with differing transport times ($t_{TR} = 30s, 5s, \text{ and } 2s$), while plasma exposure times are kept constant ($t_c = 7s$, $t_w = 6s$). For $t_{TR} = 30s$ the optical line trends of W and Ar becomes stationary in short time; the level of H α line correspond to the hydrogen insufficient pumped or desorbed from the reactor walls. Deposition processes using such long t_{TR} are inconvenient for thick films deposition. For $t_{TR} = 2s$ it can be observed an overshoot of the H α trend line, simultaneously with an overdamping of the W one, indicating the presence of C₂H₂ in the target vicinity at the beginning of the metal deposition step and poisoning of the magnetron target (carbides formed on the metal target surface present a lower sputtering yield comparative with the pure metal [2]), leading to sputtering of a tungsten carbon compound instead of sole W. For $t_{TR} = 5s$, the evolution of W and Ar monitoring lines is more close to that for $t_{TR} = 30s$ while the overshoot of H α line is almost absent. The value $t_{TR} = 5s$ was considered as being an acceptable compromise for assuring proper gas composition in performing deposition of thick composite a-C:H/W layers in reasonable process durations.

4.2. Studies of the deposition and chemical transformation of Al/C + hydrogen layers

After deposition, laboratory models of Be containing codeposited layers (a-C:H/Al mixed layers, Al used as Be substitute) presents a fast change of colour (in a few minutes) followed by severe delaminating (in a few hours) during their exposure to ambient atmosphere. It is necessary to point that pure a-C:H or Al layers do not present such changes in contact with ambient atmosphere.

The effect of atmospheric air and its components, i.e O₂, N₂, Ar, and Ar carrying water vapours during interaction with of a-C:H/Al layers deposited on glass substrates was studied by in situ monitoring of layers optical transmission.

4.2.1 Experimental setup. Investigation procedure.

The interaction of a-C:H/Al mixed layers with gases was performed “in-situ” immediately after their deposition. For this purpose, the sequential deposition setup was reconfigured as it is presented in Fig.5: the MS and PECVD plasma sources were mounted on the same axis while the substrate holder was modified (it presents an axial hole of 25mm diameter) such as to allow the light passing through it. After deposition of the a-C:H/Al layer, the reactor is evacuated to 1E-5 mbar and filled up to the atmospheric pressure with the reacting gas. The optical radiation provided by a tungsten lamp, after passing through the a-CH/Al mixed layer, is collected by a large (30 mm diameter) lens and the *optical trends* of several optical wavelengths (586nm, 634nm, 662nm, 713nm, 734nm and 823nm) are recorded using the procedure described in sect. 4.1.

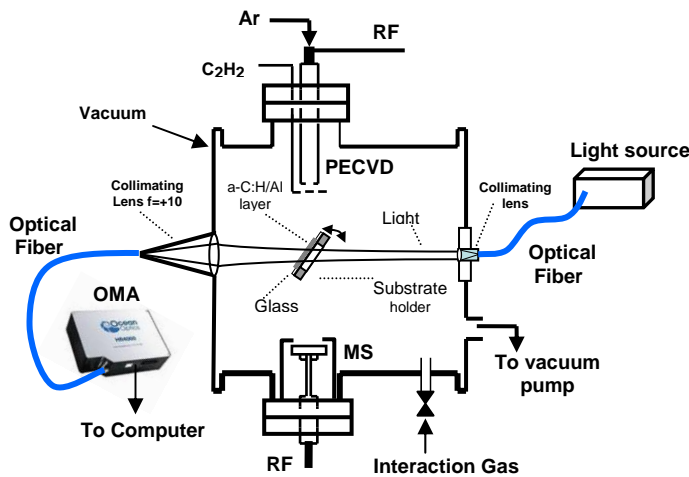


Fig. 5. Experimental setup for deposition of a-CH/Al layer and their optical study during interaction with different gases.

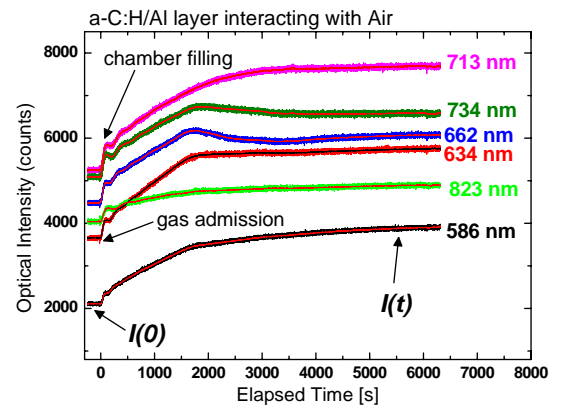


Fig. 6. Optical line trends recorded during interaction of a-CH/Al layer with ambient air.

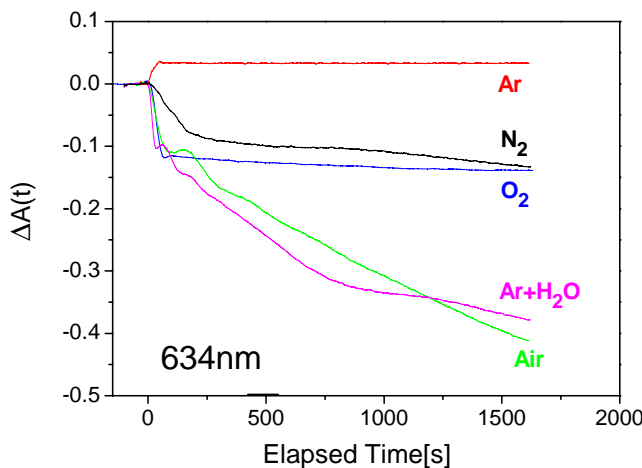


Fig.7: Variation of a-C:H/Al layers optical absorbance during treatment with ambient air gaseous components.

absorbance $A = \alpha d$ (where α is the absorption coefficient and d is the layer thickness) can be expressed as $\Delta A(t) = A(t) - A(0) = \ln[I(0)/I(t)]$, where $I(0)$ and $I(t)$ are the transmitted light intensities before and after gas admission in the reaction chamber.

Fig. 7 presents the time dependence of absorbance variation $\Delta A(t)$ for all the mentioned reacting gases, at the monitored wavelength 638nm. It can be observed that Ar do not produce any effect over the a-C:H/Al layer optical absorbance (the small variation during the chamber filling

4.2.2. Results and discussions.

An example of optical trends during interaction of the mixed layer with ambient air is presented in fig.6. It can be observed a “step” variation of the transmitted light intensity ($I(t)$) during the reaction chamber filling (2 minutes), which was attributed mainly to interaction of the gas with the deposited layer, followed by slower variation.

Considering the evolution of transmitted light intensity during the stationary pressure states (before and after filling the chamber with gas) and based on Beer Lambert law, the time variation of the a-CH/Al layer

which is due to the optical system misalignment caused by windows displacements when the pressure changes from low to atmospheric value is negligible). This is not the situation for a-C:H/Al composite layers interacting with N₂ or O₂; after chamber filling with every of those gases, the optical absorption of the layer decreases constantly. Comparing with the Ar which is an inert gas it results that the change in a-C:H/Al layer absorbance is produced by the chemical interaction between N₂ or O₂ with the composite layer. Still, the effect of these gases is not so severe like that produced by atmospheric air, which is comparable only with that of the Ar and H₂O vapors mixture.

The delaminating effect of the atmospheric air components for the a-C:H/Al layers is illustrated in fig.8. It is easy to observe (fig.8a and 8b) the similar effect (total delaminating) produced by atmospheric air and the mixture of Ar+H₂O. Immediately after interaction with O₂, the a-C:H/Al layer is still adherent to the substrate (fig.8.c) but it delaminates rapidly after exposure in ambient air. The a-C:H/Al layers which reacted with N₂ are adherent to the substrate for much longer time (fig.8.e), even after days.

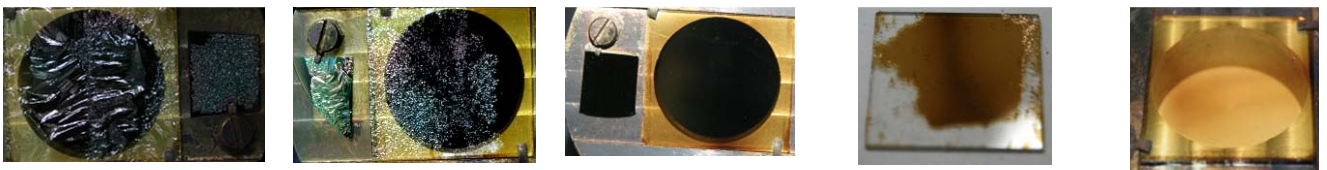


Fig.9: Adherence of the a-C:H/Al layers after interaction with atmospheric air components:

- | | | | | |
|--|---|---|--|---|
| <p>a) Immediately after interaction with ambient air.</p> | <p>b) Immediately after interaction with Ar+H₂ mixture.</p> | <p>c) Immediately after interaction with O₂ (sample still in reaction chamber).</p> | <p>d) The composite sample from fig.9c after 5 minutes exposure in ambient air.</p> | <p>e) The composite sample interacted with N₂ after 30 minutes exposure in ambient air.</p> |
|--|---|---|--|---|

It results that the optical changes of the a-C:H/Al layers are due of a combined chemical effect of the atmospheric air components (without Ar), the main contribution being that of water vapours. As regarding the mechanical stability of the a-C:H/Al layers on the substrate, the main contribution to their delaminating is due to water vapours contained in the atmospheric air. These results are also confirmed by FTIR investigations performed over the a-C:H/Al layers (presented in WP10-PWI-02-04-02/MEdC/BS report).

References.

1. T. Acsente, E. R. Ionita, C. Stancu, C. Luculescu, G. Dinescu, *Properties of composite a-C:H/metal layers deposited by combined RF PECVD/Magnetron sputtering techniques*, Provisionally accepted for publication in Thin Solid Films as a E-MRS 2010 Symposium L article
2. K. Wasa, M. Kitabatake, H. Adachi, *Thin Film Materials Technology - Sputtering of Compound Materials*, © 2004 William Andrew Publishing

SCIENTIFIC REPORT

Task title: PRODUCTION OF CONTROLLED LABORATORY CO-DEPOSITED LAYERS FOR FUEL REMOVAL STUDIES / PRODUCEREA DE STRATURI SUBTIRI PENTRU STUDII DE CURATARE CU PLASMA

Code: WP10-PWI-02-04-03/MEdC/BS

Outline

1. General objectives of the project
2. The objectives of the activities in the 2nd semester 2010
3. Summary of obtained results
4. Description of the work. Results and conclusions

1. General objectives of the project

Removal of the material codeposited on Tokamaks walls and PFC is very important for safe working of plasma fusion machines. In this context, there were performed fuel removal experiments using different approaches (atmospheric pressure plasma jets, laser ablation, discharges). *The purpose of this project is realization of stable composite layers of hydrogenated carbon with metal inclusions, with well predefined composition, to be used for fuel removal experiments using different approaches.* Also the project points on investigation of the time stability of the composite layers in presence of ambient open atmosphere.

2. The objectives of the activities in the present stage of the project

The deposition of mixed carbon/metal layers with pre-defined composition is necessary linked to the plans of using metals (tungsten, beryllium) for next JET experiments and ITER. The project objectives are:

- Definition of parameters for which layers with pre-defined carbon/metal content are obtained; composition characterization.
- Submission of composite layers for validation of fuel removal procedures
- *Identification of the agents of the fast chemical change in metal (aluminum)/carbon + hydrogen layers at contact with the ambient*

At the current stage of the project there was in view the last objective and for that accomplishment was pursued the following activities:

- FTIR (Fourier Transform Infrared Spectroscopy) investigation of the a-C:H/Al after their interaction with atmospheric air and its components (N₂, O₂, water vapors).

3. Summary of the obtained results / Rezumatul rezultatelor obtinute

Summary of the obtained results

After deposition, the a-C:H/Al mixed layers (used as laboratory models for Be containing codeposited layers, Al being used as Be substitute) present a fast change of color followed by severe delaminating during their exposure to ambient atmosphere, while the pure a-C:H or Al layers do not present such changes. The chemical transformation of the a-C:H/Al mixed layers were studied by FTIR (Fourier Transform Infrared Spectroscopy) investigation of a-C:H/Al samples after their interaction with the mentioned gases. The results proved that the fast degradation of a-C:H/Al layers after exposing them to open atmosphere are due to their chemical interaction with O₂ and water vapors from the ambient. These results are correlated with the that obtained in the frame of WP10-PWI-02-04-02/MEdC/BS project (where the effect of atmospheric air and its components over the a-C:H/Al layers was studied by in situ monitoring of layers optical transmission during the interaction).

4. Description of the work. Results and conclusions

4.2. Studies of the deposition and chemical transformation of Al/C + hydrogen layers

The a-C:H/Al samples were deposited on double polished 001 Si substrates using the following parameters for the sequential deposition process: carbon step deposition duration $t_C=6s$, metal deposition step (magnetron sputtering of Al target) $t_{Al}=7s$, transport time of the substrate between plasma sources $t_{TR}=5s$, number of deposition cycles $N_{CYC}=200$, applied RF powers (to both plasma processes) $P_{RF}=100W$. The thickness of the deposited layers is 200nm. FTIR investigations were performed using a JASCO 6300 spectrometer in the 7800-400 cm^{-1} range, with a resolution of 4 cm^{-1} and an average number of 128 scanning.

4.2.1. Results and discussions.

The recorded infrared spectra represent the cumulate contribution of the interference produced at the interface silicon substrate and deposited a-C:H/Al layer and the absorption due to chemical bonds present in the layer. Fig.1 presents the FTIR transmission spectrum of an reference hydrogenated amorphous carbon (a-C:H) layer; the deposition of this layer was performed sequentially without depositing the metal component (i.e. $P_{RF}=0W$ during metal deposition step); after deposition, the layer was exposed to open atmosphere. In the spectrum are visible the typical stretching bands of CH₂ and CH₃ in the spectral region 2800 – 3100 cm^{-1} (2876 cm^{-1} symmetric CH₃; 2926 cm^{-1} anti symmetric CH₂; 2953 cm^{-1} anti symmetric CH₃) and the C-H bending bands (symmetric at 1373 cm^{-1} and anti-symmetric at 1445 cm^{-1}) specific to the methyl group.

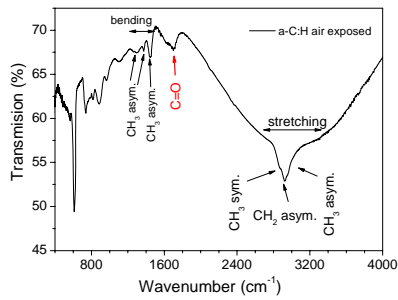


Fig.1. FTIR transmission spectrum of a reference a-C:H layer.

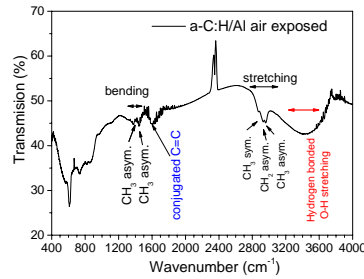


Fig.2. FTIR transmission spectrum of a-C:H/Al mixed layer after interaction with ambient air.

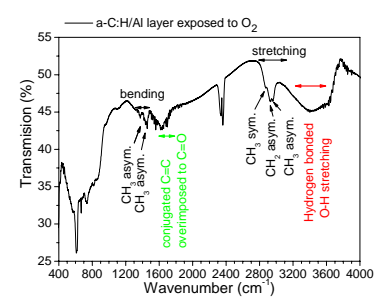


Fig.3. FTIR transmission spectrum of a-C:H/Al mixed layer after interaction with O₂.

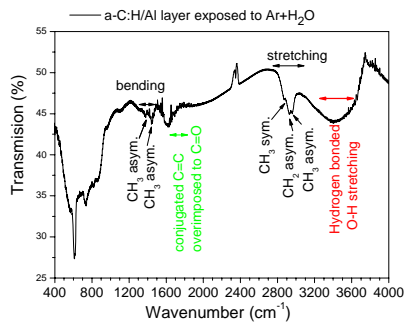


Fig.4. FTIR transmission spectrum of a-C:H/Al mixed layer after interaction with Ar+H₂O.

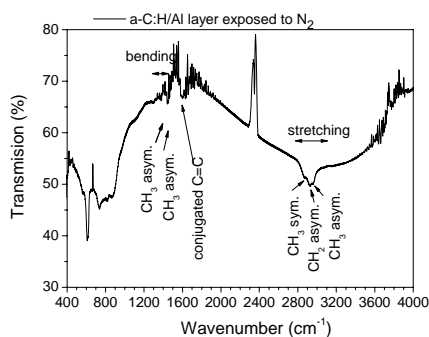


Fig.5. FTIR transmission spectrum of a-C:H/Al mixed layer after interaction with N₂.

In comparison with the reference a-C:H layer, in the structure of mixed a-C:H/Al layer exposed to ambient atmosphere (Fig.2) there can be remarked the absence of the C=O bond and the presence of an large absorption band around 1600cm⁻¹ wavelength, specific to the conjugated C=C bonds. Supplementary, there can be remarked an extreme large absorption band in the spectral range 3000–3600 cm⁻¹; the presence of this band is possible to be associated with an overlapping of the absorption produced by the stretching in the primary and secondary amines NH₃ and NH₂ (3300 – 3400 cm⁻¹) and absorption band produced by OH groups (3200 – 3600 cm⁻¹). This large absorption band, centered on 3400 cm⁻¹, is also present in the FTIR spectrum of the a-C:H/Al mixed layer exposed to Oxygen atmosphere (Fig.3); supplementary, in this situation can be observed the enlargement of the absorption band around 1600cm⁻¹, specific to apparition of C=O bonds in the layer structure. The FTIR spectrum of a-C:H/Al mixed layer exposed to a mixture of Ar + water vapors (fig.4) presents the same features like the spectrum of a-C:H/Al mixed layer exposed to oxygen; the main difference consists in a slight enlargement of the 1600cm⁻¹ absorption band. The FTIR spectrum, presented in fig.5, recorded for the a-C:H/Al mixed layer exposed to a mixture of N₂ atmosphere, do not present the 3400 cm⁻¹ absorption band, proving that exposure to N₂ of the mixed layer do not promote apparition of the NH₃ and NH₂ bonds. It results that the 3400cm⁻¹ band (observed in a-C:H/Al samples treated in air, O₂ and Ar+H₂O mixture) originate from the layer oxidation and apparition of OH bonds.

Concluding, the chemical changes in a-C:H/Al exposed to ambient atmosphere are due O₂ and water vapors.

4.4. Deposition of composite samples

Using the sequential deposition method there were deposited samples with predefined W/C concentration ratio as requested for cleaning experiments. The samples thickness was in the range of 2-4 μm, with a maximum content of 40 at. % tungsten.

The prepared samples were submitted to the following Euratom partners:

- For the plasma-torch cleaning experiments (MEdC, G. Dinescu)
- For CIEMAT Spain (F. Tabares)
- For CNRS Toulouse, centre LAPLACE (L. Pitchford)
- Université Paris 13, CNRS (Michael Redolfi – May 2010).

4.4. Conclusions

FTIR investigation of mixed a-C:H/Al layers (used as laboratory models for Be containing codeposited layers, Al being used as Be substitute) proved that fast degradation of these layers after exposing them to open atmosphere are due O₂ and water vapors from the ambient. This result is correlated with that obtained by the study performed in the frame of WP10-PWI-02-04-02/MEdC/BS project (by in situ monitoring the optical transmission of the a-C:H/Al mixed layers)

X-RAY MICRO-TOMOGRAPHY STUDIES CFC SAMPLES FOR POROSITY NETWORK CHARACTERIZATION

- WP10-PWI-01-02-01/MEdC (BS_20A) -

Ion Tiseanu, Teddy Craciunescu, Cosmin Dobrea, Adrian Sima

EURATOM-MEdC Association, Romania

National Institute for Lasers, Plasma and Radiation Physics, Bucharest, Romania

1. Introduction and objectives

The carbon reinforced carbon fibre (CFC) monoblocks of the ITER divertor vertical target must sustain high heat fluxes of 10 MW/m^2 during 400 s (normal operation) and up to 20 MW/m^2 during 10 s (off-normal event). CFCs have a unique combination of high conductivity, low Z and resistance to damage induced by the high heat loads. Given the demanding environmental requirements of the ITER divertor, specially developed CFCs are needed as plasma facing components (PFC) materials.

The problem of fuel (tritium) retention in a carbon material is a major concern due to its radioactivity and inventory constraints within the ITER installation. So far, most data on fuel retention were obtained in all-carbon machines, so that comparison with carbon free machines (all-W ASDEX Upgrade, future ITER like Wall in JET) needs to be performed for better prediction in ITER conditions. Scaling of the retention rate as function of plasma/machine parameters (injection rate, incident flux/fluence, PFC materials, PFC temperature) is only poorly characterized. Albeit the main retention mechanisms have been identified (such as the co-deposition with C and/or Be, bulk diffusion and trapping in CFC and W) their relative contributions in ITER conditions are still uncertain being subject of active research, from laboratory experiments, modeling as well as integrated tokamak experiments [1,2]. According to earlier investigations, the retention in the material bulk was considered to be less critical than the retention in co-deposited layers. Even if the DITS experiment showed that bulk retention concerns only ~10% of the total permanent retention in Tore Supra [3,4], techniques are envisaged to remove the deposits from removed areas (and thus recover the fuel stored in these deposits), when it will be definitely impossible to recover the fuel trapped in the bulk of the CFC constituting the PFCs. This bulk retention was demonstrated to be due to a-C:H layers deposited in the pores of the CFC ([5]~10-15% of voids due to porosity for the CFC N11).

It is expected that an accurate 3D porosity description of the CFC materials would provide an essential input for the quantization of the fuel retention in the material bulk. Here, the problem of the quantitative characterization of the porosity structure of CFC materials is addressed by means of high resolution X-ray micro-tomography (μ XCT). The non-invasive inspection was pursued on samples with or without refractory/marker metal coating, on non-irradiated or on *post-mortem* samples. The main challenge is posed by the required micron range of the spatial resolution for rather macroscopic samples.

2. Experiments and Results

2.1 Experimental setup

Most experiments were carried out at our newly upgraded X-ray tomography facility [6] (Fig. 1). The system is equipped with a last generation Nano-focus X-Ray source for non-

destructive inspection. The source is operational in both micro- and nano-focus mode, at a tube voltage up to 225 kV and a maximum power of 10÷20 W. X-Ray images can be acquired by using three different high resolution detector types: Image Intensifier (XII) for rapid non-destructive examinations, Flat Panel (FP) detectors and a linear detector for the high density sample analysis. The linear detector using 1,024 scintillator - photo diode assemblies is characterized by a great dynamic margin that leads to high definition and high contrast images. Positioning and turning around of the sample are insured by a set of seven high precision motorized micrometric manipulators. Automation, control and data acquisition were obtained by means of in-house software package. The tomographic reconstruction for the cone-beam scanning is based on an optimized implementation of the modified cone beam filtered back-projection algorithm. Using a parallelization technique on multiprocessors workstations, experimental data consisting of large radiographic images (1220x1216 pixels) are processed for building the 3D reconstructions of typically 1024x1024x1024 voxels.

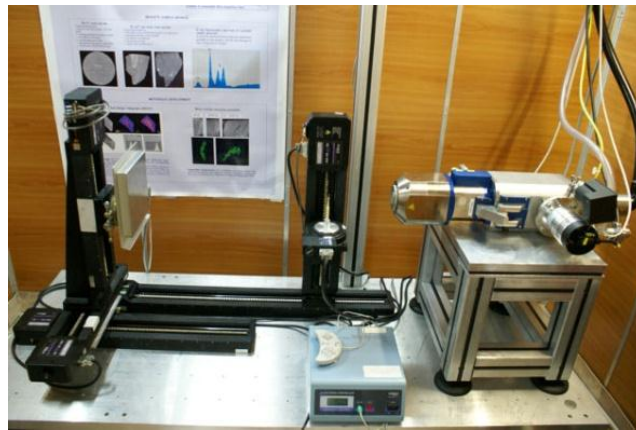


Figure 1 – View of the NILPRP Nano-CT facility.

The most important characteristics of the X-Ray tomographic system are presented in Table 1.

Table1 – Main parameters of the NILPRP Nano-CT facility

Micro/nanofocus X-Ray source	Max. high voltage: 225 kV Feature recognition: <1 μm Min object-focus distance: 0.2 mm X-Ray cone: 170° X-ray target power: ~10÷30 W
X-Ray detection:	
Detector number of elements/effective area	768x576 / 169x169 mm ² 7" XII 1024x1024/ 50x50 mm ² CMOS FP 1248x1248/ 120x120 mm ² a-Si FP
Digital Output	10 to 16 bits
Sample micrometric manipulator	
-X stages	-travel up to 800 mm, loading capacity up to 30 kg
-Z stage	-travel 300 mm, loading capacity up to 6 kg
-θ stage	-accuracy 0.03°, loading capacity up to 10 kg
Magnification factor	< 2000
Spatial resolution	≥ 500 nm
Scanning time	< 15min. per 720 views
3D reconstruction time	< 12 min for 1024x1024x1024 voxels
Scanning method	Cone Beam CT; short scan CT

(180° + fan angle) and Oblique
View Cone Beam

X-ray fluorescence analysis for the determination of samples composition was performed with our newly developed instrument *Tomo-Analytic* [7]. The instrument combines a 3D X-Ray microtomograph with a microbeam fluorescence system. The microbeam fluorescence component is a configurable elemental composition mapping tool, including optical X-ray beam collimation.

2.2 CT optimization

We have measured three types of CFC samples: former ITER reference CFC NB31, JET CFC DMS780 and a series of CFC N11 samples in the frame of the DITS post-mortem analysis. For reference a porosity free fine-grain graphite EK98 sample was also scanned.

Moderate resolution measurements of CFC samples at voxel resolution of approximately 7 μm , with an estimated minimum detectable feature of $\sim 7\text{-}10$ μm , were devoted to the optimization of the X-ray source and detection parameters (Fig. 2).

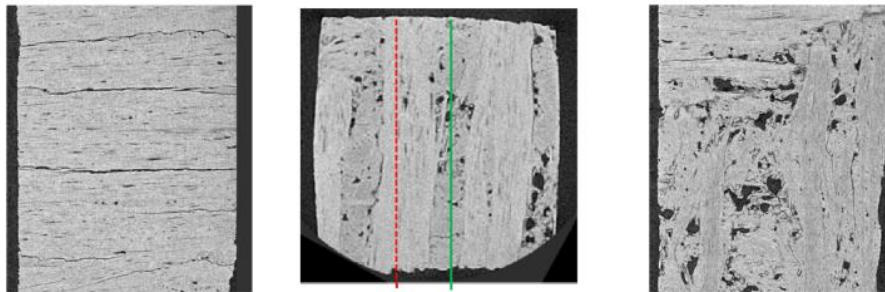


Figure 2 - An axial cross section on a NB31 CFC sample at voxel resolution of 6.6 μm is represented in the central panel. A cut through the main fibre direction along dotted red line (left panel). The longitudinal cross section along the green solid line (right panel) shows a distinctive feature of NB31- the pan-fibre composed of tiny fibres (needling) somewhat randomly distributed and going perpendicularly to the main pitch-fibre direction.

Once the optimum parameters have been determined, high resolution measurements (~ 2.5 $\mu\text{m}/\text{voxel}$) were performed by the proprietary, recently developed, “offset tomography” (Off-CT) technique. Using multiple scans of the investigated object, Off-CT is able to almost double the magnification factor and therefore doubling the space resolution for a given detector size. While the maximum resolution of 2.5 $\mu\text{m}/\text{voxel}$, on a relatively large sample (5x5x5 mm^3), is a remarkable performance, the images noise might be a perturbation factor for the accurate porosity factor evaluation. In order to reduce the image noise two steps were considered: 1) reduction of reconstruction artefacts like “ring artefacts” [8] and “beam hardening artefacts” [9] and 2) upgrade the irradiation head of our X-ray tube with a high power diamond target for improved photon statistics. The diamond target allows for a ten-fold increase in the thermal conductivity as compared to the conventional transmission targets. As a result, high energy electron beams can be kept in focus to maintain the small focal spot size required for high image resolution. Using a JIMA mask, the test pattern of 2 μm can be clearly resolved even for a target power up to 20 Watts. As part of the optimization experiments, we have also installed a low contrast X-ray target which consists on a thin molybdenum layer on a beryllium window. This configuration has been used for the scanning of relatively small and X-ray transparent samples currently provided within the DITS project.

A set of up to 1440 radiographies at equidistant angles have been used for the high resolution fully 3D tomography. Figure 3 shows a representative tomographic image with voxel resolution of 2.5 μm of CFC of type NB31.

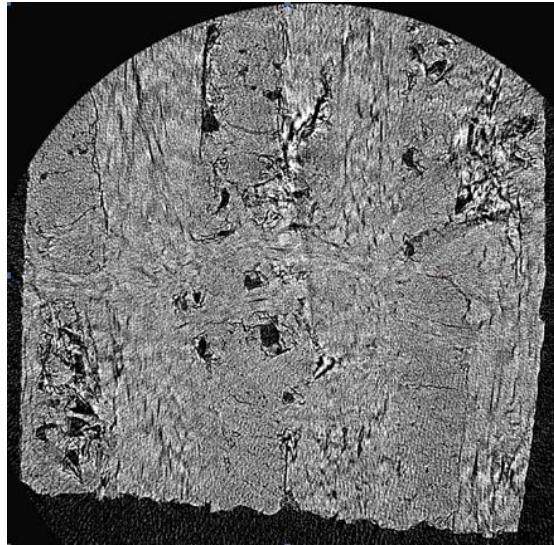


Figure 3 - Tomographic cross-section at 2.5 μm /voxel for NB31 CFC sample. The tomographic reconstruction was obtained using the Off-CT scanning technique.

2.3 Porosity determination method

To determine the main CFC network porosity characteristics the 3D reconstructed volumes were further processed. For the quantitative analysis of the porosity structure in terms of total void fraction, network connectivity, wall thicknesses we used the powerful 3-D visualization and measurement software: VGStudioMax, Volume Graphics GmbH, Heidelberg, Germany, www.volumegraphics.com. The data post-processing process comprises several steps: 1) finding the optimal choice for the threshold level, in order to create a correct border between CFC and porous regions. A detailed inspection of this demarcation is performed while navigating through the reconstructed volume along transversal, longitudinal and sagittal cross-sections (Fig. 4); 2) following validation, the reconstructed volume is segmented and the porous structure is extracted as an independent object which can be represented also as a 3D structure; 3) determination of the absolute value of the porosity factor by using the volume analysis module. The defect analysis tool can be used to determine other parameters as: voids volume, size and projected area distribution.

The porosity factor calculation procedure was applied for three types of CFC samples relevant for the fusion technology. The porosity factor values (Table 2) are in good agreement with the manufacturer nominal specifications. It can be remarked that the N11 porosity factor measured in the frame of the Deuterium Inventory in Tore Supra DITS *post-mortem* analysis is significantly higher than the one of the new, more advanced NB31 and DMS780 and the recently developed NB41CFC materials. An effort has been made to obtain very high resolution radiographies for the NB41CFC sample. Figure 5 shows two images obtained at 1.66 micron/pixel and even at 0.63 micron/pixel. At 1.66 microns/pixel one can see very well the pitch fiber structure while at 0.63 microns/pixel one can distinguish individual carbon fibers.

Table 2 – The porosity factor for three CFC samples

Material	NB31	DMS780	N11	NB41
Porosity factor (%)	8.1	9.4	10.5÷12	6.4

It is remarkable the improvement of the porosity factor associated with the most advanced NB41 CFC material.

One should note that the currently available DITS N11 CFC samples have a relatively small volume (2x2x6 mm³). These samples result from the cutting of CFC N11 Tore Supra tiles (20x20x6 mm³) in three slices of 2 mm each. The sample whose upper surface was in contact with the plasma is labeled "top", the one the closest to the Cu heat sink is the "bottom" sample."

This might explain the rather large uncertainty of the porosity factors. We also plan to scan N11 samples with statistically significant volumes.

Certainly, our current 3D micro-tomography reconstructions for the relatively large samples (5x5x5 mm³) of NB31 and DMS780 CFC could be considered a good basis for the characterization of the initial porosity of the new CFC ITER reference material NB41.

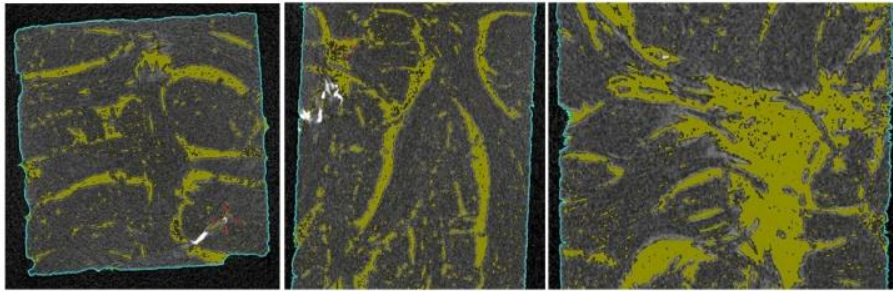


Figure 4 – Transversal, longitudinal and sagittal cross-section through the tomographic reconstruction of a DITS “top” sample after image thresholding for porosity factor calculation. Scanning parameters: HV=80 kV, I=150 μA, target: Mo, focus spot size: <1.5 μm, voxel resolution: 2.75 μm, cross-section width: 2 mm.

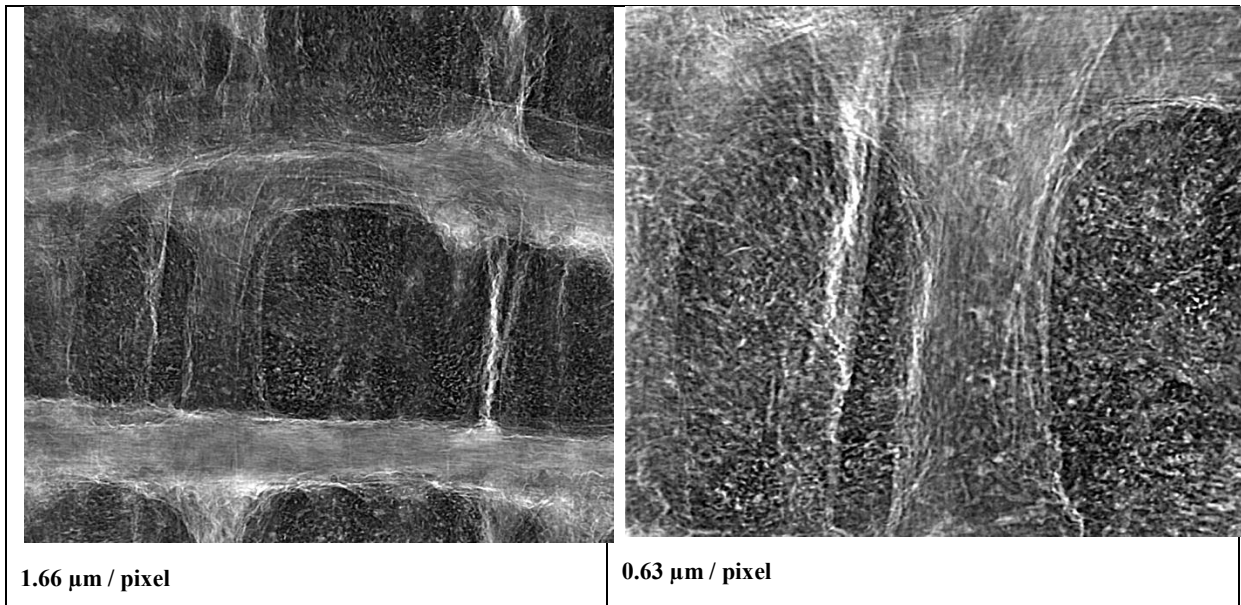


Figure 5 – High resolution digital radiography on NB41 CFC sample . At 1.66 microns/pixel one can see the pitch fiber structure. At 0.63 microns/pixel one can distinguish individual carbon fibers.

2.4 Tomography on CFC samples with metallic insertions (coatings)

Besides the evaluation of the porosity factor, tomographic reconstructions provided additional useful information concerning the morphology of the CFC samples. For example the penetration of metallic structures (Cu, Ti) along fibre interspaces can be revealed. The presence of Cu and Ti is due to the way the fingers of the TPL are built: the Cu heat sink and CFC tiles are joined using "Active metal Casting" [9]. Figs. 5-6 illustrate the investigation of the Cu heat sink region for DITS CFC samples. Despite the wide range of the X-ray attenuation coefficients displayed by this region which induces strong artefacts the tomographic analysis reveals a strong connectivity of the pores along the main fibre direction. It can be also observed that the pores are coated by a thin Ti layer and the metallic structures advance along main fibre direction interspaces up to 3 mm. To obtain an enhanced visualization of this phenomenon, additional image post-processing was performed. The image fusion obtained by summing the transversal, longitudinal and sagittal cross-section is presented in Fig. 7. The identification of the material composition was certified by the X-ray fluorescence analysis (see again Fig. 7).

In another sample of the TS N11 CFC one have observed a metallic deposit on the rounded plasma facing region (Fig. 8).

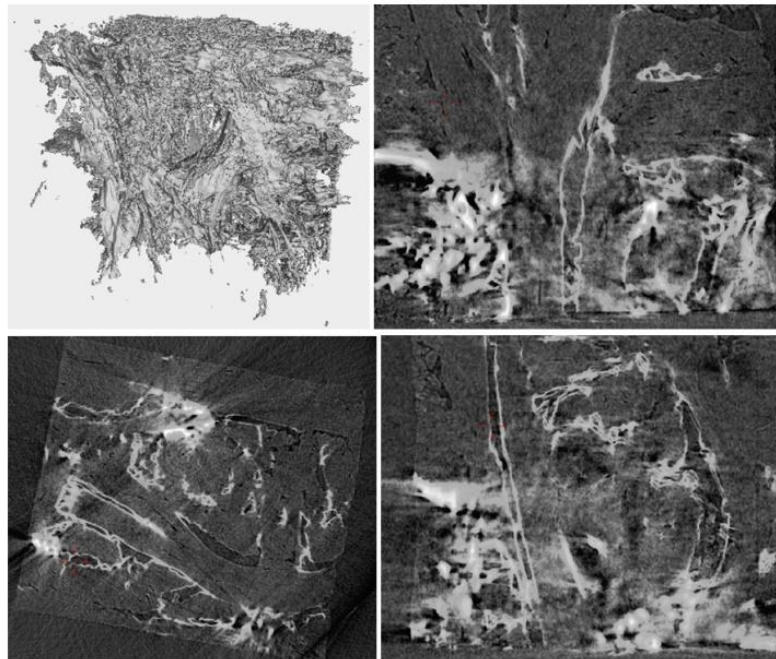


Figure 5 – Tomographic analysis of the Cu heat sink region of DITS “bottom” sample: 3D reconstructed volume (top-left), longitudinal (top-right), transversal (bottom-left) and sagittal (bottom-right) cross-section. Bright regions correspond to metallic structures present in the gaps between the main fibres. Scanning parameters: HV=90 kV, I=200 μ A, target: Mo, focus spot size: <1.5 μ m, voxel resolution: 2.75 μ m, cross-section width: 2 mm.

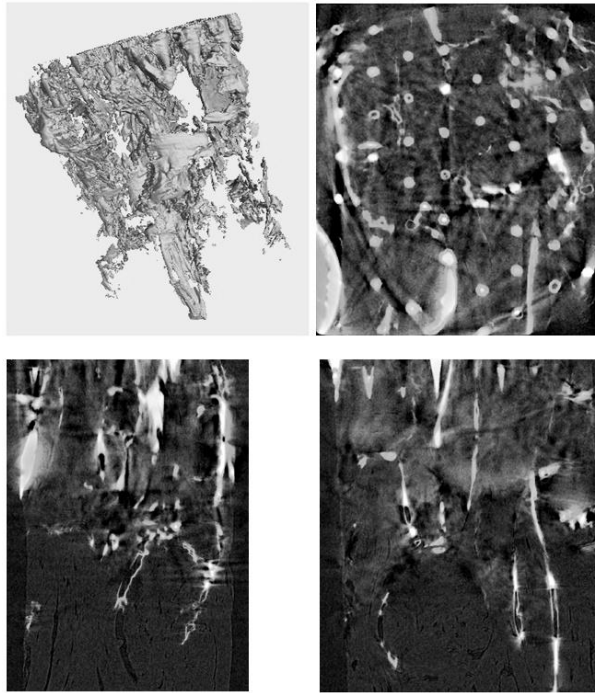


Figure 6 – Tomographic analysis of the Cu heat sink region of a DITS “bottom” sample: 3D reconstructed volume (top-left), axial (top-right), sagittal (bottom-left) and transversal (bottom-right) cross-section. Bright regions correspond to Cu and gray regions correspond to Ti. Scanning parameters: HV=95 kV, I=180 μ A, target: Mo, focus spot size: <1.5 μ m, voxel resolution: 2.75 μ m, cross-section width: 2 mm.

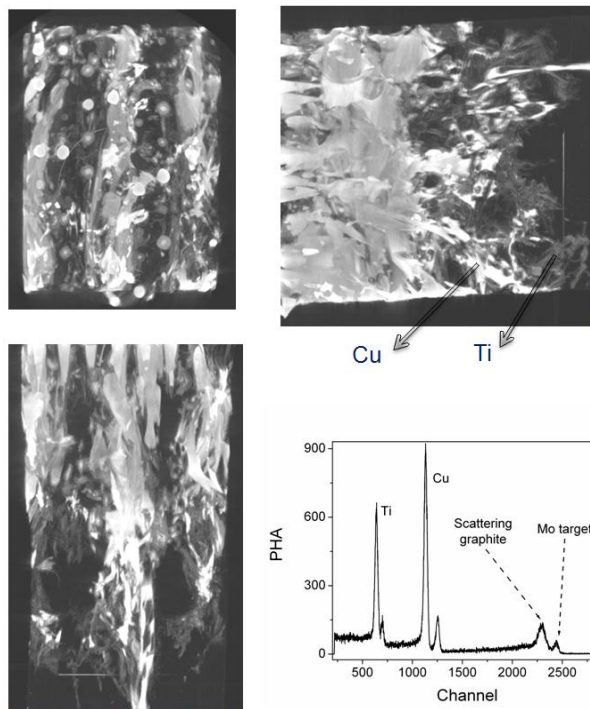


Figure 7 – Image fusion of axial (top-left), transversal (top-right) and sagittal (bottom-left) tomographic cross-sections. Bright regions correspond to Cu and gray regions correspond to Ti. X-ray fluorescence spectrum confirms the presence of Ti and Cu along the main fibres interspaces.

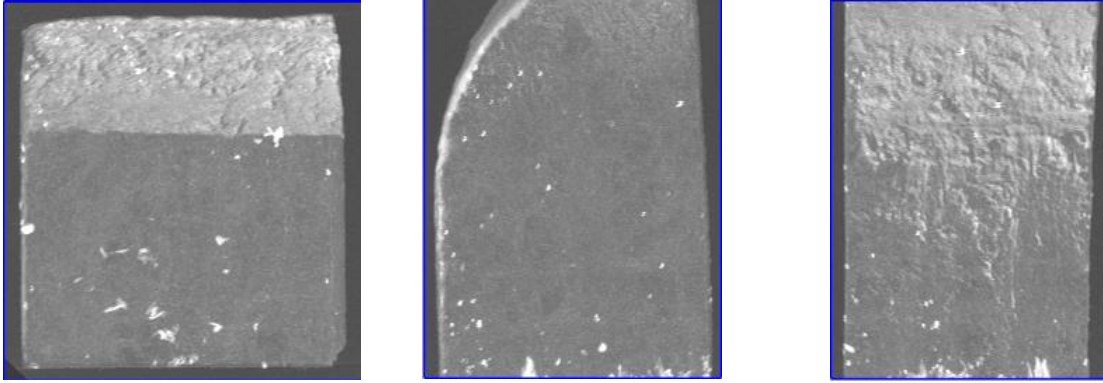


Figure 8 – Image fusion of axial (left), transversal (middle) and sagittal (right) tomographic cross-sections. Bright regions correspond to metallic deposit and gray regions correspond to CFC.

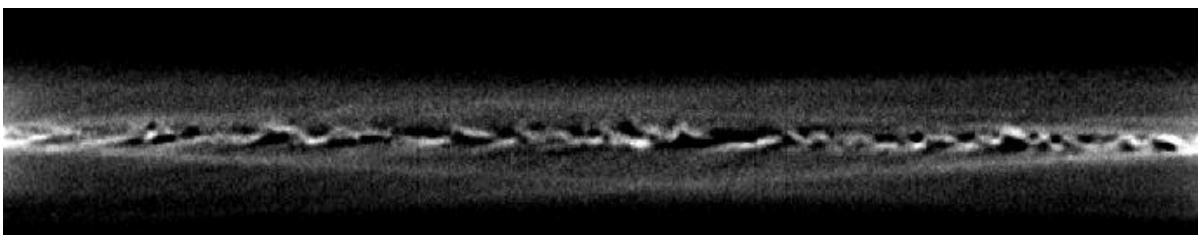
The thickness of the metallic deposit (coating) is around 20-25 microns. Its composition would be investigated within our Tomo-Analytic system.

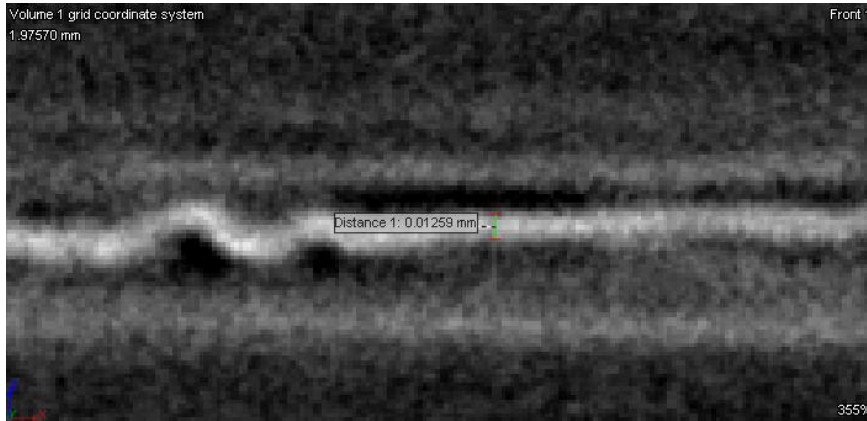
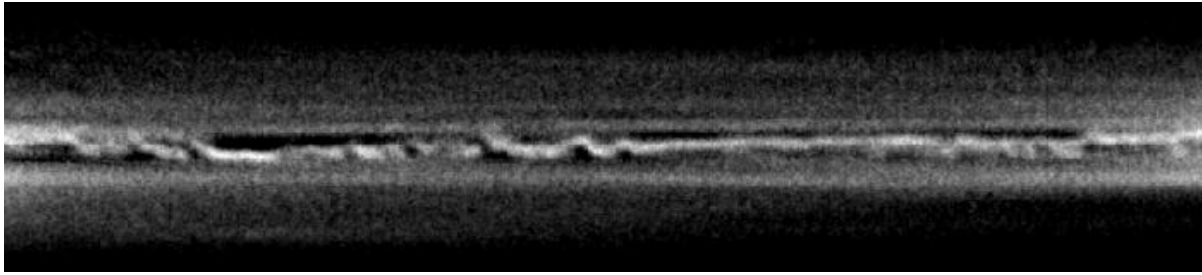
Finally we have analyzed the DMS780 CFC coated by tungsten realized within the ITER-like wall project [11]. The only scanning configuration which would permit such an analysis is described in the [12] Oblique-view cone-beam CT system, United States Patent 7139363, Inventors: M. Misawa and I. Tiseanu.

The sample cutting procedure is not trivial and it is still in development. Only the coating parallel to the fiber bundle direction was available for analysis. The main result obtained in the analysis is the accurate description of the coated surface and the correct evaluation of the coating thickness. The more ambitious goal of this study is to understand the influence of the coating layer on the local porosity of the CFC material.



Figure 9 – Tomographic analysis of the tungsten coated CFC region of ITER-like wall sample: 2D image of the tungsten layer (top-left) and two orthogonal views of the tungsten layer (second and third rows). Bright regions correspond to tungsten. The total thickness of the tungsten layer and the Mo buffer are evaluated at around 12 microns (bottom image).





3. Conclusion

High resolution cone beam micro-tomography was optimized for the analysis of CFC samples. An important result was the determination of the dependence of the porosity evaluation accuracy on the space resolution and the amount of tomography images noise. Following the optimization of both the measurement and reconstruction processes a spatial voxel resolution of 2.5 μm has been obtained. A procedure for the quantitative evaluation of the sample porosity factor has been introduced and tested. This procedure has been utilized on all CFC materials relevant for the fusion technology. It is proved that the tomographic analysis provides useful information about the pores connectivity and, in case of heat sink region of the DITS CFC PFC, the penetration of metallic structures along fibre interspaces. For the first time we have analyzed by 3D tomography the DMS780 CFC coated by tungsten realized within the ITER-like wall project. The characterization of the initial porosity of the new CFC ITER reference material NB41 has been carried out.

4. Acknowledgments

This work, supported by the European Communities under the contract of Association between EURATOM and MEdC, CEA, FZJ, was carried out under the framework of the European Fusion Development Agreement. The views and opinions expressed herein do not necessarily reflect those of the European Commission.

Relevant publication

Ion Tiseanu, Emanuelle Tsitrone, Arkadi Kreter, Teddy Craciunescu, Thierry Loarer, Bernard Pégourié, Timo Dittmar, *X-Ray Micro-Tomography Studies on Carbon Based Composite Materials for Porosity Network Characterization*

The works reported here have been presented at the 26th Symposium on Fusion Technology (SOFT), September 27 September – 01 October, 2010, in Porto, Portugal and are accepted for publication in Fusion Engineering and Design (FED).

References

- [1] A. Kreter, et al., Journal of Physics: Conference Series **100** 062024 (2008).
- [2] A.T. Peacock, et al., Phys. Scr. **T128** 23 (2007).
- [3] B. Pégourié et al. JNM **390-391** 550 (2009).
- [4] E. Tsitrone et al. NF **49** 075011 (2009).
- [5] P. Pelicon et al. "Deuterium mapping with micro-NRA using high energy focused He-3 beam for fuel retention studies in the walls of fusion reactors", to be published.
- [6] I. Tiseanu, et al., Fusion Eng. Des., 82 2608 (2007).
- [7] Tomo-Analytic, a combined 3D X-Ray micro-tomograph and micro-beam fluorescence system,
- [8] (<http://tomography.inflpr.ro>).
- [9] J. Sijbers et al., Phys. Med. Biol. 49 N247 (2004).
- [10] I. Tiseanu, et al., Fusion Eng. Des. 75–79 1055 (2005).
- [11] A. Grosman et al. JNM 337-339 821 (2005).
- [12] G F Matthews et al, Overview of the ITER-like wall project, Phys. Scr. 2007 137
- [13] M. Misawa, I. Tiseanu, Oblique View cone beam X-ray Tomography System, 10/379702(USA), 10903887.9(Germany), 0305013.5(United Kindom), 2003/03/06

**ANALIZA EROZIUNII STRATURILOR NANOCOMPOZITE PRIN
ABSORTIE/FLUORESCENTA DE RAZE X DE INALTA REZOLUTIE SPATIALA
(X-RAY MICROBEAM ABSORPTION/FLUORESCENCE METHOD AS A NON-INVASIVE
SOLUTION FOR INVESTIGATION OF THE EROSION OF W COATINGS ON
GRAPHITE/CFC)**

WP10-PWI-05-02-01/MEdC/BS/PS (BS_20B)

Ion Tiseanu, Teddy Craciunescu, Cosmin Dobrea, Adrian Sima

EURATOM-MEdC Association, Romania

National Institute for Lasers, Plasma and Radiation Physics, Bucharest, Romania

1. Introduction

Tungsten erosion, subsequent tungsten transport, and redeposition are of great interest, because a full tungsten divertor is foreseen to be used during the deuterium-tritium operational phase of ITER. The erosion of tungsten and carbon marker layers was extensively studied in the outer divertor of ASDEX Upgrade, and work is currently in progress to completely replace the existing JET CFC tiles with tungsten-coated tiles within the JET ITER-like wall project.

Global erosion, redeposition and transport of first-wall materials have been extensively studied in ASDEX Upgrade during the last seven years, using post-mortem surface analysis of tiles [1]. Specially prepared divertor or limiter tiles are used, which contain thin marker stripes for erosion/deposition measurements and are analyzed before and after exposure. Also regular tiles were analysed after exposure. Long-term samples are installed at the vessel walls or in remote areas without direct plasma contact. All samples are typically exposed during one discharge campaign, and they provide information about the campaign-integrated net material erosion/deposition pattern.

Due to the time consuming measurements and data evaluation, this technique allows to measure only a limited number of data points, typically along one line in poloidal direction. The need for a fast and nondestructive method, which allows the quantitative determination of the thickness of a tungsten coating on a carbon material on large areas, led us to evaluate a combined transmission/fluorescence X-ray (XRTF) technique. It is proved that this technique allows a good spatial resolution (several 10 μm), and it is fast enough to allow measurements for thousands of data points. Consequently 2-D erosion pattern on a whole divertor tile may be retrieved.

2. Methods

The method for erosion analysis was implemented using the Tomo-Analytic system (Figure 1), which we developed especially for fusion materials analysis [2].

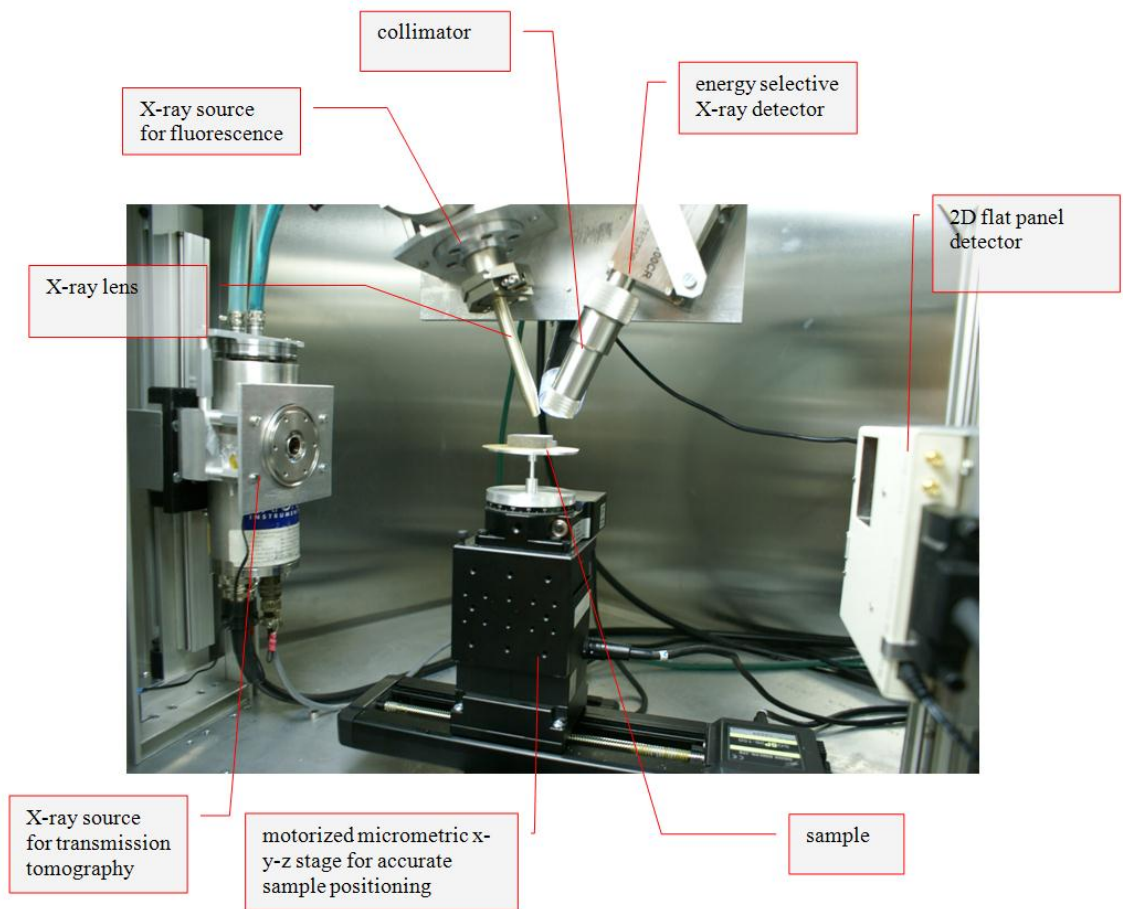


Figure 1 – Photo of the Tomo-Analytic instrument (<http://tomography.inflpr.ro>)

Tomo-Analytic is a combined X-ray fluorescence (XRF) and cone-beam tomography (3D-CT) system for the noninvasive 3-D morphology and composition mapping. The 3D-CT component is configured to take several hundred highly resolved ($48\ \mu\text{m}$) radiographic views of the object in order to build a 3-D model of its internal structure. 2-D slices through this volume can be viewed as images, or the 3-D volume may be rendered, sliced, and measured directly. For the NDT inspection of miniaturized samples the microtomography analysis is guaranteed for feature recognition better than $15\ \mu\text{m}$. 3-D tomographic reconstructions are obtained by a proprietary highly optimized computer code [3] based on a modified filtered back-projection algorithm. The X-ray-digital radiography and tomography analysis can provide information on: volumetric density variations, visualization of micro-cracks, voids, inclusions, network connectivity in porous materials, microstructure integrity of various components, accurate 3-D geometrical measurements.

The key element of the XRF component is polycapillary lens which provides a focal spot size in a range from few tens to a few hundreds of micrometers. A significant increase of X-ray intensity (up to three orders of magnitudes) is also obtained [4]. This guaranties higher detection sensitivity and shorter measurement time. The main limitation consists in the possibility to investigate relatively thin samples. The implementation of a confocal geometry realized with the attachment of a polycapillary conic collimator to the X-ray detector would further allow the extension of capabilities of the instrument towards fluorescence tomography (3-D composition mapping).

As the Tomo-Analytic system is a configurable and versatile tool, we can use different measuring methods for the characterization of the thickness uniformity of graphite/CFC with metallic coatings. In the X-ray transmission (XRT) configuration presented in Fig. 2, the X-ray lens has a direction perpendicular to the flat panel detector. The X-rays are detected after passing through the investigated sample, where they are

attenuated according to the composition and thickness of the materials. The optimal measurement configuration of the XRT geometry and the irradiation parameters were obtained by MCNP-5 Monte Carlo simulations [5].

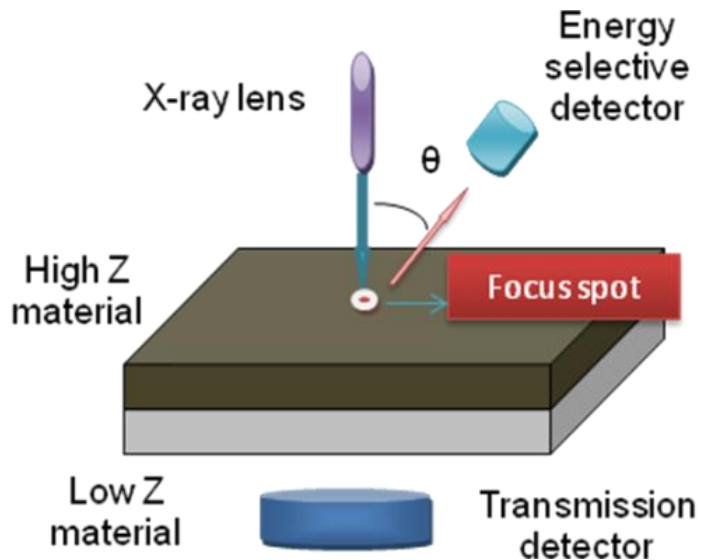


Figure 2 – Setup of the X-ray transmission/fluorescence module

The XRF component can be used in three different procedures for the determination of the coating thickness:

XRF1) One can convert the coating X-ray fluorescence peak intensities to elemental concentrations and/or film thicknesses. Until quite recently, using X-ray fluorescence to measure the thickness of coatings was relying on thickness standards to calibrate instruments. A new approach, called fundamental parameter analysis, uses the basic characteristics of the substances being irradiated and has brought significant improvements in accuracy and removed the requirement for complex sets of standards [4].

XRF2) The coating and the substrate material produce both X-ray fluorescence radiation, but the coating attenuates the substrate's radiation. As the degree of attenuation depends on the thickness a correlation can be derived between the secondary emissions and the coating thickness. Thereafter the thickness is calculated according to the following equation: $d = \ln(I_0/I) / (\mu + \mu_F / \cos(\theta))$, where I_0 and I are the incident and the substrate fluorescence radiation intensities, respectively, and μ , μ_F are the corresponding attenuation coefficients of the coating material. θ is the angle between the incident and the emitted X-ray beams.

XRF3) The X-ray back-scattered radiation by a substrate with low effective atomic number is attenuated by the coating material in direct correlation with the coating thickness. The coating thickness calculation is governed by a similar relationship: $d = \ln(I_0/I) / (\mu + \mu_C / \cos(\theta))$, where I_0 and I are the incident and back-scattered radiation intensities, respectively μ is the attenuation coefficient of the coating material for the incident energy and μ_C is the attenuation coefficient corresponding to the Compton peak energy. θ is the angle between the incident and the back-scattered X-ray beams.

3. Experiments and Results

ASDEX Upgrade fine grain graphite tiles were coated with tungsten of typical thicknesses (0÷1.5 μm). The coating uniformity analysis is performed using the X-ray transmission XRT and the X-ray fluorescence mapping by procedures XRF1 and XRF3.

A typical result of the XRT analysis is presented in Fig. 3. The X-ray transmission map can be used for the determination of the absolute value of the thickness of the W coating layer in terms of atoms/cm². Tungsten mass attenuation coefficients were generated with the XCOM program [6].

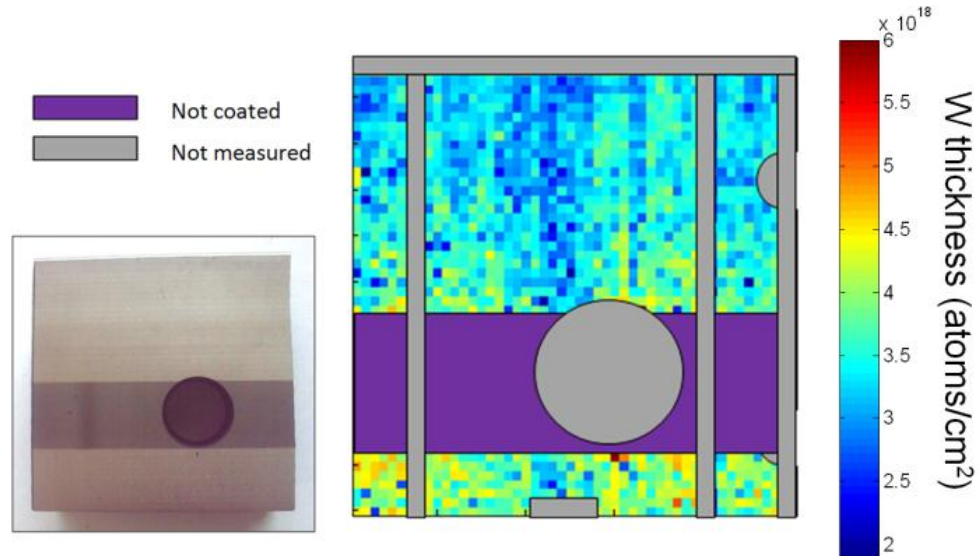


Figure 3 – W thickness determination by XRT. The sample (left) is presented together with the transmission map (right).

In order to compensate the influence of the graphite substrate, a non-coated reference sample must be used. A calibration curve relating the X-ray transmission factor and the graphite thickness is obtained. As the real tiles contain several cutting up profiles, the CAD model of the tile must be also taken into account. The X-ray transmission ensures fast and high resolution analysis. The images presented in Fig. 3 are obtained for a scanning time of approximately two hours on a 70 x70 pixels matrix. For each image pixel one has averaged the transmission values over an area of 1.0 mm² in order to reduce the effect of the coating/substrate roughness.

Fig 4 shows the X-ray fluorescence X-ray spectra of the ASDEX Upgrade W/Ni coated marker tiles.

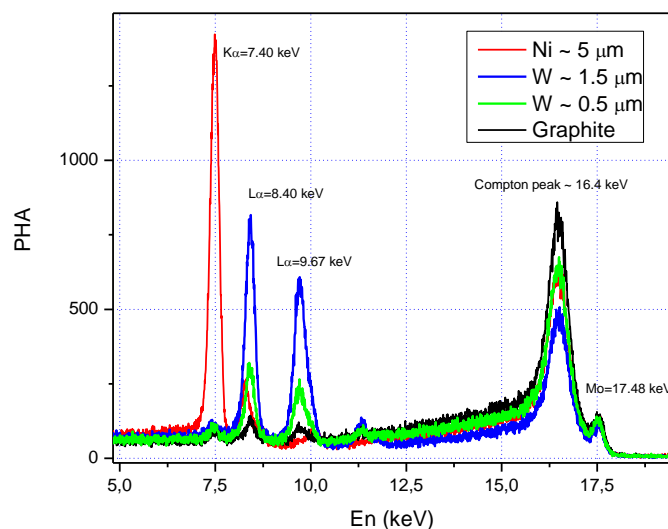


Figure 4 – X-ray fluorescence spectra in case of a W (0÷1.5 µm) and Ni (~ 5 µm) coated fine grain graphite sample.

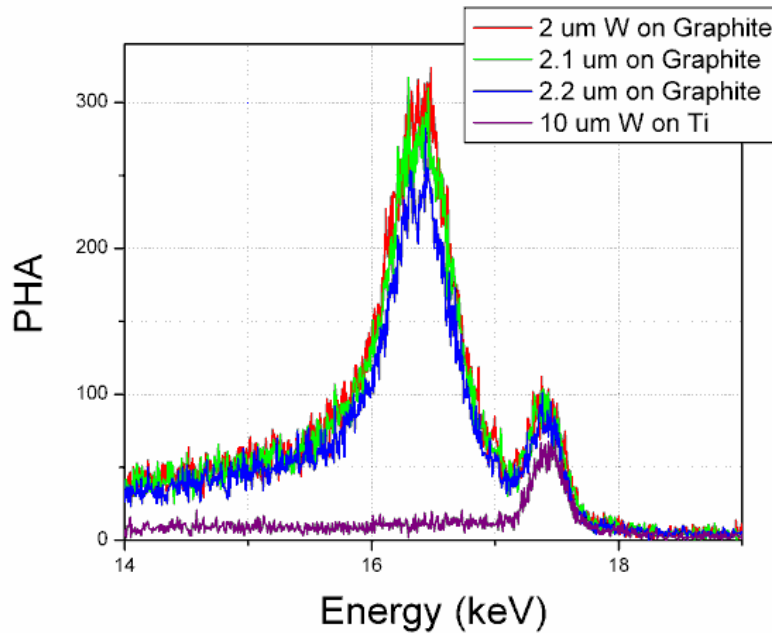


Figure 5 – Compton and elastic scattering intensities as function of tungsten coating thickness in case of microbeam back-scattering method (XRF3).

As can be seen in Fig. 4, the peak intensities of the tungsten characteristics lines L_{α} (8.40 keV) and L_{β} (9.67 keV) are very sensitive to the coating thickness. Hence the XRF1 procedure is recommended for relatively fast coating uniformity mapping in relative units. However this technique is limited to W layers not thicker than ~ 4 μm due to the high self-attenuation of the low energy of the W characteristic lines. When the coating process makes use of an intermediate layer (for example a Mo may be used as an interface layer between C substrate and the W coating layer [7]) the XRF2 technique can be used to determine the thickness of the coating layer. Thus, we can measure thicker W layers due to the higher energy of the Mo X-ray line ($K_{\alpha}=17.48$ keV).

The Compton peak intensities are also very sensitive to the coating thickness values (Fig. 4 & 5) and therefore the mapping of the coating thickness in absolute values is possible within the XRF3 procedure without using thickness standards. Using a Mo target X-ray source it is possible to measure W layer thicknesses up to 6-7 μm .

In case of tungsten coated CFC materials one has to take into account the influence of the substrate morphology. Fig. 6 shows the radiography of a NB31 ITER like reference CFC material and a microbeam backscattering profile. One can see a clear radiological contrast between the pitch-fibres (brighter parallel structures) and the pan-fibres composed of tiny fibres (needling) distributed somewhat randomly and going perpendicularly to the main pitch-fibre direction. The line profile shown in the right panel displays variations of the back-scattering intensity of up to 20%, which should be compensated for in the XRF3 procedure.

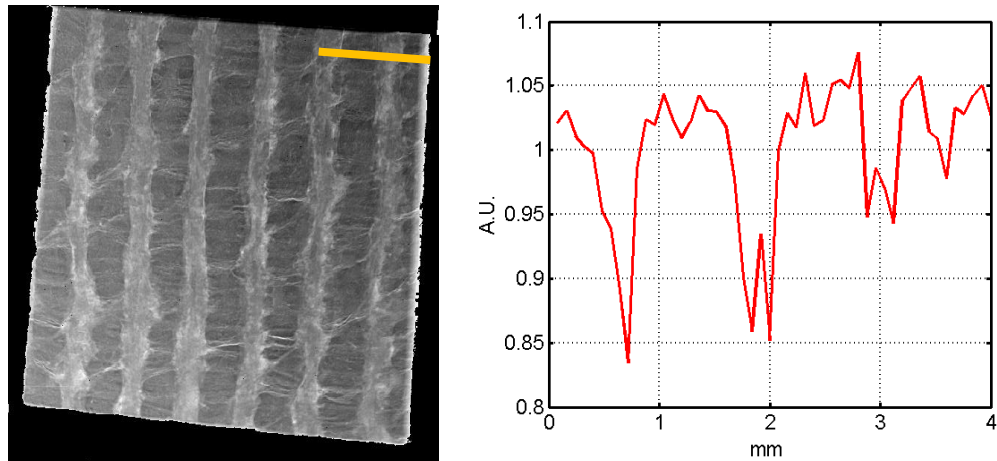


Figure 6 – High resolution radiography of NB31 ITER like CFC (left) correlated with the microbeam backscattering profile (right).

A 2-D map obtained using the combined XRF1/XRF3 techniques is presented in Fig. 7. In the pseudo-colour map red/blue corresponds to high/low intensities, respectively.

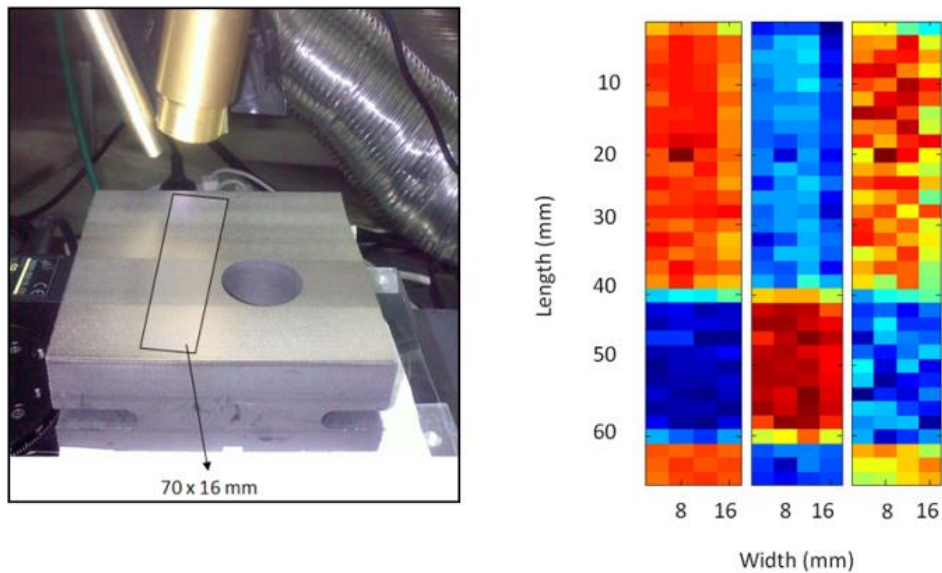


Figure 7 – Post-mortem analysis of a W coated fine grain graphite divertor tile: photo of the analyzed sample (left) showing the region of interest and pseudo-color map for W, Compton and elastic scattering.

Line profiles of the W/Ni coatings were measured with the purpose to assess the erosion/redeposition in the all-tungsten divertor of ASDEX Upgrade (Fig. 8-9). The Ni/W thickness absolute values could be derived and they are in good agreement with the measurements carried out in [1]. Fig. 9 shows the erosion profiles along the poloidal and toroidal directions as measured by the XRF3 technique applied to the corresponding Ni stripes. In all measurements it is possible to detect redeposition of Ni/W on non-coated graphite stripes.

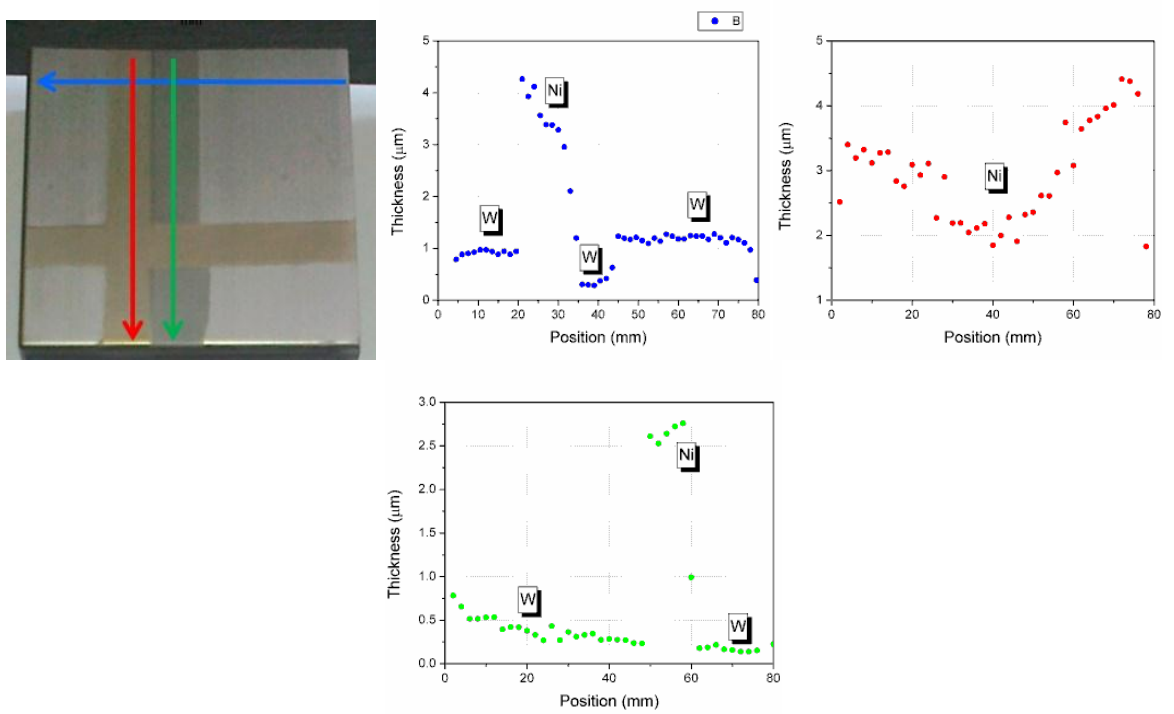


Figure 8 – Line profiles showing W/Ni erosion in the all-tungsten divertor of ASDEX Upgrade.

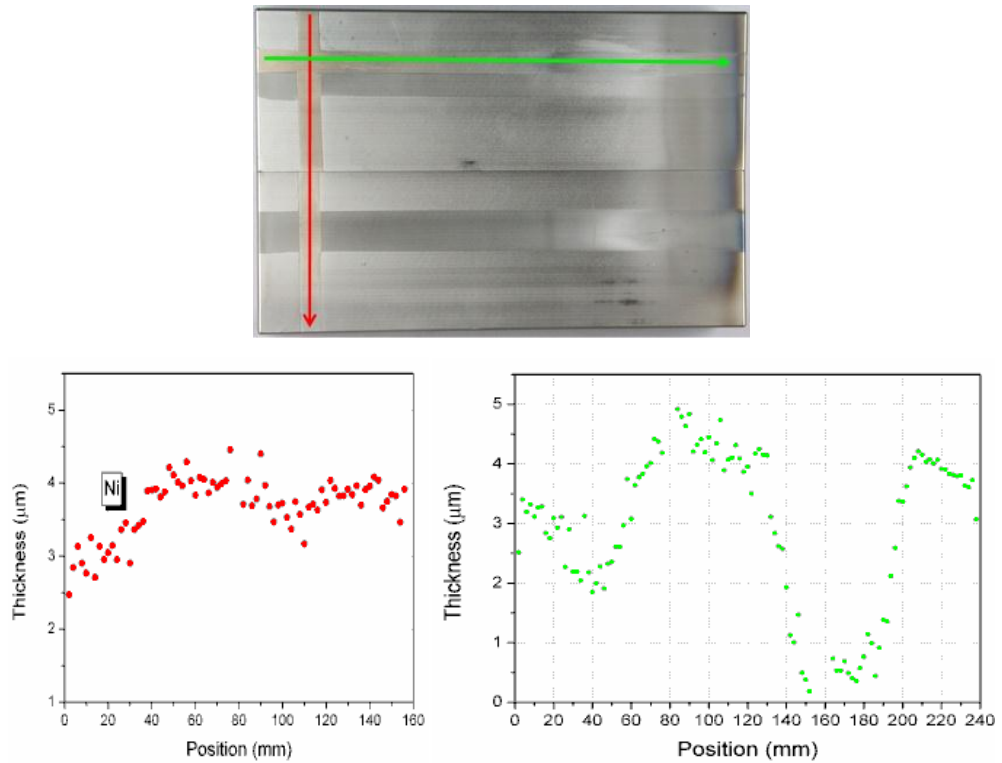


Figure 9 – The erosion profiles along poloidal (green) and toroidal (red) directions as measured by the XRF3 technique applied to the corresponding Ni stripes.

4. Conclusion

An instrument and associated measuring methods have been developed and qualified as a non-invasive solution for investigation of the erosion of W coatings on carbon materials substrates. The Tomo-Analytic instrument is a combined X-ray fluorescence (XRF) and cone-beam tomography (3D-CT) system for the non-invasive 3-D morphology and composition mapping.

The XRT component ensures fast and high resolution analysis of large areas of carbon materials coated with tungsten. However, the transmission method requires calibration in order to remove the influence of the fine graphite layer.

The main advantages of the XRF module are: i) high thickness resolution and material selectivity and ii) it permits calibration-free methods for the determination of the thickness of the coating layer. However the time needed for the XRF inspection of the sample is considerably larger in comparison to the XRT method. Therefore if a fine spatial resolution is required, the XRT method represents an appropriate alternative. The combined use of X-ray transmission and X-ray fluorescence methods represent a unique instrument for the post-mortem analysis of large area coatings. It can provide fast analysis, high spatial resolution and detection of deposited layers and intrusions. The combined method was successfully applied on W coated fine grain graphite tiles from the all-tungsten divertor of ASDEX Upgrade.

5. Acknowledgments

This work, supported by the European Communities under the contract of Association between EURATOM and MEdC, IPP and Tekes was carried out under the framework of the European Fusion Development Agreement. The views and opinions expressed herein do not necessarily reflect those of the European Commission.

Relevant publication

Ion Tiseanu, Matej Mayer, Teddy Craciunescu, Antti Hakola, Seppo Koivuranta, Jari Likonen, Cristian Ruset, Cosmin Dobrea, ASDEX Upgrade team, *X-ray microbeam transmission/fluorescence method for non-destructive characterization of tungsten coated carbon materials*

The works reported here have been presented at the Twelfth International Conference on Plasma Surface Engineering, September 13 - 17, 2010, in Garmisch-Partenkirchen, Germany and are accepted for publication in Surface and Coatings Technology (SCT).

References

- [1] M. Mayer, V. Rohde, K. Sugiyama, J.L. Chen, X. Gong, C. Hopf, J. Likonen, S. Lindig, R. Neu, G. Ramos, E. Vainonen-Ahlgren, A. Wiltner, and ASDEX Upgrade Team, *J. Nucl. Mater.* 390-391 (2009) 538.
- [2] I. Tiseanu, T. Craciunescu, C. Dobrea, A. Sima, *Proceeding of PRORA 2009 - Fachtagung Prozessnahe Röntgenanalytik*, Berlin, Germany, 2009.
- [3] I. Tiseanu, M. Simon, T. Craciunescu, B. N. Mandache, Volker Heinzl, E. Stratmanns, S. P. Simakov, D. Leichtle, *Fusion Engineering and Design*, 82 (2007) 2608–2614.
- [4] Beckhoff, B.; Kanngießler, B.; Langhoff, N.; Wedell, R.; Wolff, H. (Eds.), *Handbook of Practical X-Ray Fluorescence Analysis*, Springer, 2006, XXIV, ISBN: 978-3-540-28603-5, pp 89-190
- [5] MCNP-5 - Los Alamos National Laboratory, 2005. MCNP – A General Monte Carlo N-Particle Transport Code, Version 5, vols. I–II, LA-UR-03-1987 and LA-CP-03-0245
- [6] Berger MJ, Hubbell JH. XCOM: Photon Cross Section Database. Web Version 1.2. Available from: <http://physics.nist.gov/xcom>. National Institute of Standards and Technology, Gaithersburg: MD 20899, USA; August 1999.
- [7] C. Ruset, E. Grigore, H. Maier, R. Neu, X. Li, H. Dong, R. Mitteau, X. Courtois, *Physica Scripta*, T128, 171-174 (2007).

SCIENTIFIC AND TECHNICAL REPORT

Contract Number: 1-EU-8-BM-1-/1.03.2010

Project title: Transmission and Backscattering Mössbauer Spectroscopy Studies of the Short Range Order, Structure and Magnetic Properties in α -Fe and Binary Fe-Cr Model-Alloys.

Phase No. 2: Second round Mössbauer measurements. December 15th, 2010.

Room temperature transmission Mössbauer measurements on Fe-Cr powder alloys obtained by ball milling, after thermal treatments; Liquid helium temperature transmission Mössbauer measurements on Fe-Cr powder alloys obtained by ball milling; Backscattering Mössbauer spectroscopy studies by Conversion electron Mössbauer spectroscopy (CEMS) measurements and Conversion X-ray Mössbauer spectroscopy (CXMS) measurements on relevant samples; Data computing and analysis of short range order (SRO), local structure and magnetic properties, publication of relevant results.

CONTENTS

	Page
I. Title.....	1
II. Contents and general objectives.....	2
III-IV. Objectives of present report & Report abstract.....	3-4
V. Introduction	4-6
VI-VII. Experimental and Sample preparation bay ball milling.....	7-9
VIII. Results and discussion. A comparative fit: magnetic hyperfine fields distribution versus binomial model.....	9-25
VIII.1 (a, b). Structural consideration and calculations, SRO parameter.....	9-11
VIII.2 Mössbauer analyses of the spectra recorded at room and liquid helium temperature.....	12-17
VIII.3 Backscattering Mössbauer spectroscopy studies by Conversion electron Mössbauer spectroscopy (CEMS) measurements and Conversion X-ray Mössbauer spectroscopy (CXMS) measurements on relevant samples	17-21
VIII.4 Room temperature transmission Mössbauer measurements on Fe-Cr powder alloys obtained by ball milling, after thermal treatments	21-23
VIII.5 Data computing and analysis of short range order (SRO), local structure and magnetic properties, publication of relevant results and Conclusion.....	23-25
IX References	26

II. General objectives

This project aims to contribute to the achievement of the following one or more issues in Fe-Cr based alloys (potential candidates for blanket structures in fusion reactors) and α -Fe materials by means of Mössbauer spectroscopy: investigation of local structure and short range order, study of magnetic properties 'via' hyperfine magnetic fields in correlation with Cr concentration in the samples. The obtained results will be used for a more general and important issue: to realise if Mössbauer spectroscopy can be used to improve the technology for obtaining FeCr based alloys (in particular prepared via ball milling route) in view of applications for fusion reactors.

III. Objectives of present report

- Magnetic hyperfine interactions study and the assessment of the short range order parameter (SRO) in the FeCrY and FeCrTiY nanoscaled alloys, obtained by planetary ball milling, by means of transmission, conversion electron (CEMS) and conversion X-ray (CXMS) Mössbauer spectroscopy.
- Thermal annealing effect studies on the chromium distribution and low temperatures behaviour of the FeCrY and FeCrTiY alloys.

IV. Report abstract

FeCrY and FeCrTiY nanoscaled alloys, obtained by planetary ball milling, have been investigated by transmission, conversion electron and conversion X-ray Mössbauer spectroscopy to study the peculiarities of magnetic hyperfine structure and short range order parameter. In transmission geometry the measurements have been performed at room (RT) and liquid helium temperatures (LHT). Mössbauer spectra of the thermally treated (760 °C under vacuum) samples have been recorded also at room temperature. CEMS and CXMS measurements were performed at RT. Two fitting models were applied in the Mössbauer spectra computing for all recorded data: a hyperfine magnetic fields distribution (Hesse-Rübartsch model) and the binomial model. In the binomial fit model it is assumed that the Mössbauer areas of magnetic sublattices are proportional with the binomial probabilities for the substitution of Fe by Cr atoms in the bcc structure of α -Fe. For our samples, the average magnetic fields $\langle H \rangle$ values at iron nucleus given by the two models are very close indicating that both models are appropriate for the study of magnetic interaction in Fe-Cr based alloys. No phase transitions were evidenced between the room temperature and liquid helium temperature. For the FeCrY samples (without thermal treatment) the SRO values are close to zero, revealing a rather random distribution of Cr atoms in α -Fe structure. In the case of FeCrTiY nanoscaled sample, the SRO parameter becomes negative indicating an increase of Fe-Cr pairs in the system. For thermally treated samples (vacuum \sim 760 °C) the best fit with the experimental data in the binomial

model was obtained at a chromium concentration of ~ 9% instead of 14.1% (nominal content in the untreated samples). The values of $\langle H \rangle$ given by the distribution model for the treated samples support the same chromium concentration value. This finding, together with the positive SRO values, indicates a shortage in Fe-Cr pairs after thermal treatments and a possible chromium clustering process. Due to the very small crystallite size of the studied samples, the results by CEMS and CXMS measurements are similar with those obtained in transmission geometry. The surfaces effects – characteristic information given by these two methods, can't be evidenced, the particle size being much lower than the penetration depths of the conversion electrons and conversion X-rays.

One can infer that Mössbauer spectroscopy is a very appropriate method to study the magnetic hyperfine interactions and SRO parameter peculiarities in Fe-Cr based alloys. The Mössbauer spectroscopy is of particular interest when we need to obtain information about magnetic hyperfine interaction correlated with SRO parameter, reflecting the homogeneity of the samples, information that can be used to improve the production technology of Fe-Cr based materials for fusion reactors.

V. Introduction

Mössbauer effect measurements [1-2] are usually performed either by the transmission (TMS) or scattering method. In the transmission arrangement, γ -rays emitted from the source and passing through sample are used to observe the resonance absorption as a function of relative velocity between source and sample. Mössbauer spectra obtained by this method are absorption-type; the number of γ rays counted decreases at the velocity of resonance absorption. Nuclear and atomic processes following the nuclear resonance consist in the emission of various radiations: γ -rays, conversion electrons, X-rays and Auger electrons. This secondary radiation is employed to obtain an emission-type Mössbauer spectrum by the scattering method, in which the intensity of secondary radiations increases at the nuclear resonance velocity. Electrons emitted after the nuclear resonance absorption, i.e., conversion plus Auger electrons are called resonantly scattered electrons or resonance electrons.

Secondary nuclear and atomic processes after the nuclear resonance absorption in ^{57}Fe , the most popular in Mössbauer spectroscopy, are summarised as follows:

- **γ -ray transition:** *in the γ -ray transition, the nuclear state de-excites to the ground state, re-emitting γ ray which has the same energy as that of the incident γ ray.*
- **internal conversion process;** *in this process the nuclear state de-excites to the excited atomic state which has a hole in inner atomic shell, e.g., K, L, M or N shell. In this case, an electron is emitted instead of γ ray.*
- **X-ray transition;** *the excited atomic state produced by the internal conversion process, e.g. K-hole state, de-excites to a lower state with L-, M-, or N-hole by transferring an electron in one of the outer shells to the K hole. There are two competitive de-excitations for the atomic inner holes state, i.e., X-ray transition accompanying photon emission and Auger process accompanying electron emission.*
- **Auger process;** *in the Auger process, the atomic transition energy is converted to an electron in the other shell, which then goes to the continuum leaving another hole in the shell. In addition to the KLL Auger electron, KLM and KLN electrons are also available for the scattering method.*

Resonance electron and conversion X-ray emission associated with nuclear resonance of ^{57}Fe nucleus are illustrated in Figure 1.

The transmission method cannot be applied to the Mössbauer measurement for very thin or very thick samples; incident γ rays do not pass through too thick samples and the number of the resonance absorption becomes smaller in thinner samples. Since there is no need to reform the materials and no limit for the sizes and shapes in principle, the scattering method is often applied to the non-destructive test of samples, which are difficult to be reformed. The transmission method gives us the information as an average of whole thickness of sample. The information obtained by the scattering method is restricted to the layer to which the secondary radiation employed in the measurement can penetrate from the surface of sample. In the ^{57}Fe Mössbauer spectroscopy, the penetration depth of 14.4 keV γ ray and 6.4 keV is the order of 10 μm and that of 7.3 keV conversion electron and 5.6 keV Auger electron is the order of 10^3 Å; the maximum escape depth for the 7.3 keV conversion electron is 2500 Å and the surface region in which electrons are detectable without energy losses is 50 Å. For ^{57}Fe , the emission probability of resonance electrons is considerably higher than that of γ ray or X-ray. Mössbauer spectra are easily obtained by detecting resonance electrons rather than re-emitted γ ray or K X-ray.

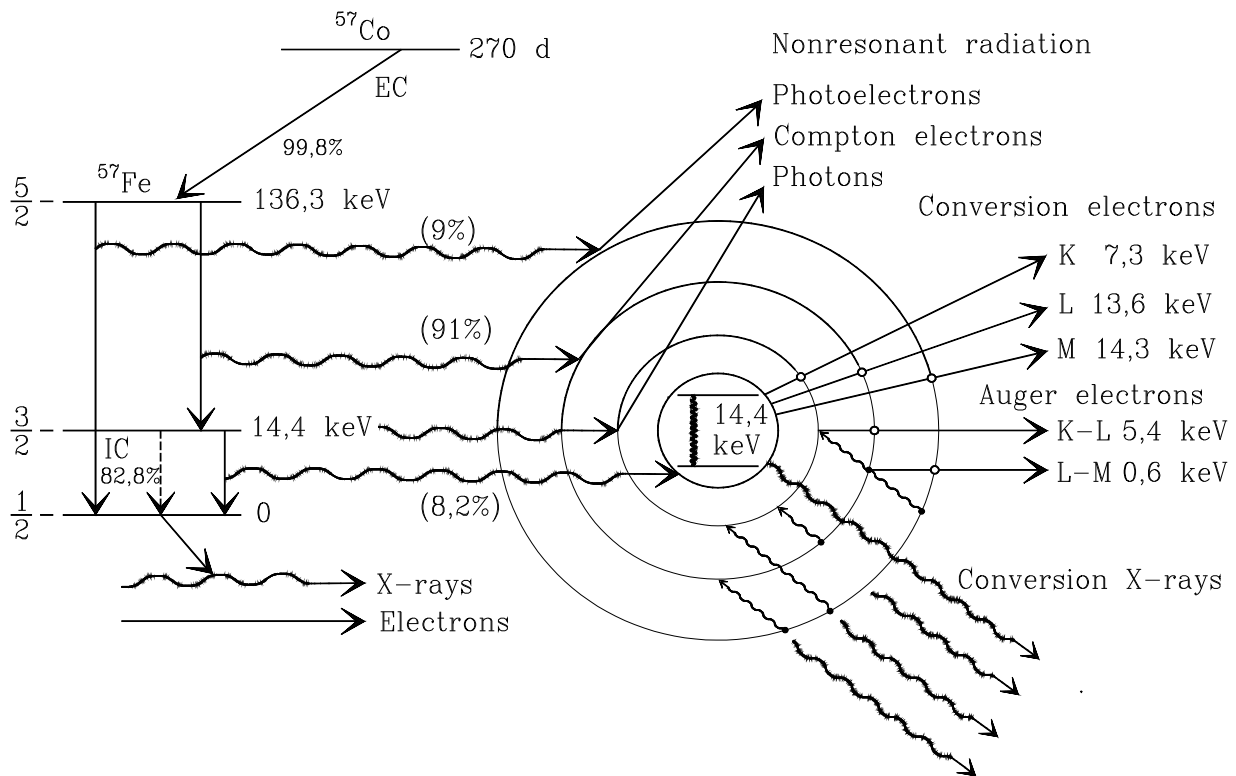


Figure 1: Resonance electron and conversion X-ray emission associated with nuclear gamma resonance of ^{57}Fe nucleus.

In agreement with the working plan of the contract (*Second round Mössbauer measurements; dead line: December 15th 2010*), this report will present:

- Room temperature transmission Mössbauer measurements on Fe-Cr powder alloys obtained by ball milling, after thermal treatments;
- Liquid helium temperature transmission Mössbauer measurements on Fe-Cr powder alloys obtained by ball milling;
- Backscattering Mössbauer spectroscopy studies by Conversion electron Mössbauer spectroscopy (CEMS) measurements and Conversion X-ray Mössbauer spectroscopy (CXMS) measurements on relevant samples;
- Data computing and analysis of short range order (SRO), local structure and magnetic properties, publication of relevant results.

A more detailed Mössbauer data fitting including a 'binomial model' is presented for all recorded spectra of the studied samples.

VI. Experimental

In transmission method, the Mössbauer spectra were recorded at room temperature by means of Promeda (Israel) type standard spectrometer with a WissEL (Germany) acquisition interface (Figure 2a). A 25 mCi Co/Rh source was used in a velocity range of ± 10 mm/s. Helium liquid temperature Mössbauer investigations were performed on a See Co (USA) close cycle cryostat (Figure 2b).



Figure 2. Laboratory Mössbauer spectrometers: a) Promeda spectrometer; b) See Co spectrometer.

In scattering procedure, the records were performed using the electron detection (CEMS) and X-ray detection (CXMS). The backscattering measurements were conducted at a high degree of accuracy with a new detector, gas-flow proportional detector [3]. This new detector is multi-purpose gas-flow proportional counter for surface Mössbauer spectroscopy. In figure 3a and 3b two images of this homemade detector are presented. The detector design is better than previously reported [4-6]. The main improvements obtained are: the height of the detection volume can be changed in large limits from 1 to 38 mm, the detection volume can be symmetrical or not in respect with anode plan, the anode changing is easily and different anode configuration can be used. It is suitable for studies with all Mössbauer isotopes which can be measured at room temperature: ^{57}Fe , ^{119}Sn and ^{151}Eu . By changing the volume detection and flow gas it is possible to make measurements by electron, X-ray or gamma ray detection. For electron detection a 99% He + 1% C₄H₁₀ mixture was used and for X-ray a 90% Ar + 10% CH₄ mixture. The gas flow rate can be set in the range of 50 – 1000 cm³/hour by a flow meter working at a

pressure of about 0.1 Mpa.



Figure 3a: Lateral view of the detector



Figure 3b: Top view of the detector

It is possible to set relatively low flow rates with sufficiently small deviations, so that no fluctuations in the amplifying factor appear. The access of the gas was designed such to avoid vibration of the anode, due to the flow rate and any gas leak. We used an economical radiation shielding for counter, consisting of a combination of lead, copper and steel disks. In order to absorb unfavourable X-rays from the sources, a plexyglass filter was placed in front of the shielding. All CEMS and CXMS spectra were recorded in perpendicular back-scattering geometry, i.e. with the incident γ -ray direction perpendicular to the sample plane.

VII. Sample preparation by planetary ball milling

Two samples of FeCr like alloys, FeCrY and FeCrTiY (courtesy of Prof. Jose Brito Correia – IST Portugal) were considered for Mössbauer investigations. The FeCr alloys were prepared by ball milling in argon atmosphere, at 400 rot/min for 18 hours, using planetary mill Retsch PM100MA with Stainless steel vials. The target composition was: 85.2%Fe-14.1%Cr-0.3%Y-0.3%Ti. One of the bunches milling charge was constituted by 17.16g of Fe, 2.82 g of Cr and 0.02g of Y; the other was constituted by: 17.05 g of Fe, 2.82 g of Cr, 0.06 Y and 0.07 g of Ti. The mean particle size for both obtained samples is ~ 10 nm.

VIII. Results and discussion. A comparative fit: magnetic hyperfine fields distribution versus binomial model.

VIII.a. Structural consideration and calculation

In Figure 4 a three dimensional structure around Mössbauer iron atom (in red colour) is represented up to the 4th metallic ions shells.

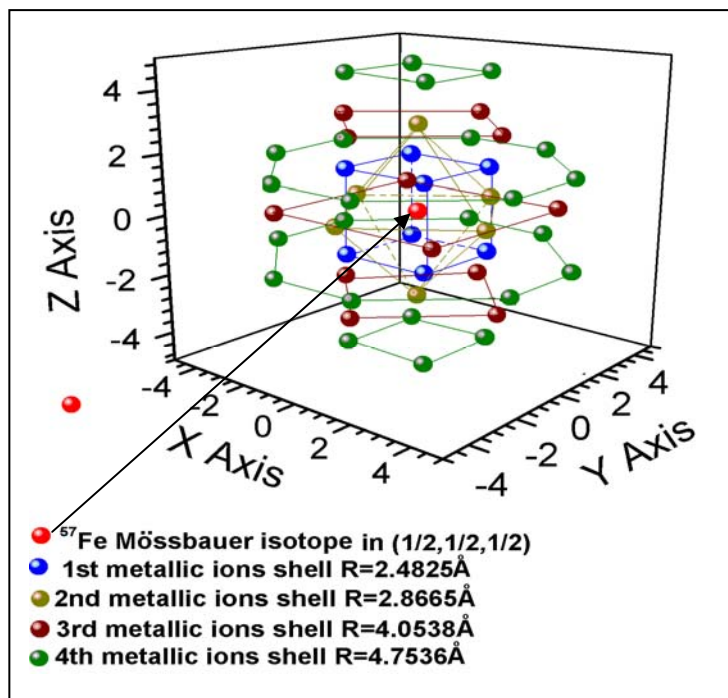


Figure 4. Local environment around ^{57}Fe Mössbauer isotope in $\alpha\text{-FeCr}$.

The first and the second metallic surroundings are *cubic* and respectively *octahedral*, containing 8 and respectively 6 neighbours. The third and the fourth metallic shells contain 12 and respectively 24 neighbours, arranged in parallel planes along Z axis. It has been reported that Fe atoms, which possess Cr atoms as the nearest neighbour, exhibit a smaller hyperfine field than that of pure Fe, and its reduction rate per Cr atom is about 3 T [7]. J.

Cie’slak & S.M. Dubiel [8] found a drop of 3.2 T for each Cr atom in the first coordination sphere and 2.2 T for the second one. The hyperfine magnetic field at the iron nucleus can be approximated by the formula,

$$H(m, n, c) = H(0,0,c) + m\Delta H_1 + n\Delta H_2; \quad (1)$$

where $\Delta H_1 = 3.2$ T and $\Delta H_2 = 2.2$ T and “c” stands for Cr concentration.

The contribution of the Cr in third and fourth coordination sphere is too low to give a relevant change in Mössbauer spectra. Consequently we can consider only two first coordination spheres when we account for the effects of Fe substitution by Cr in this alloy. If the substitution process is random, the probability to find ‘m’ Cr atoms in first coordination and ‘n’ Cr atoms in the second one is given by the combinatorial formula,

$$P(m, n; c) = \binom{8}{m} \binom{6}{n} c^{m+n} (1-c)^{14-m-n} \quad (2)$$

This formula of the binomial probability, $P(m, n; c)$ holds for Iron substitution by Chromium in the 1st and 2nd vicinity of iron in α -Fe structure. Probability calculations regarding the substitution of iron atoms by Cr atoms, versus Cr molar concentration x , (for the first two relevant coordination spheres around the central Mössbauer iron atom), are presented in figure 5(a, b).

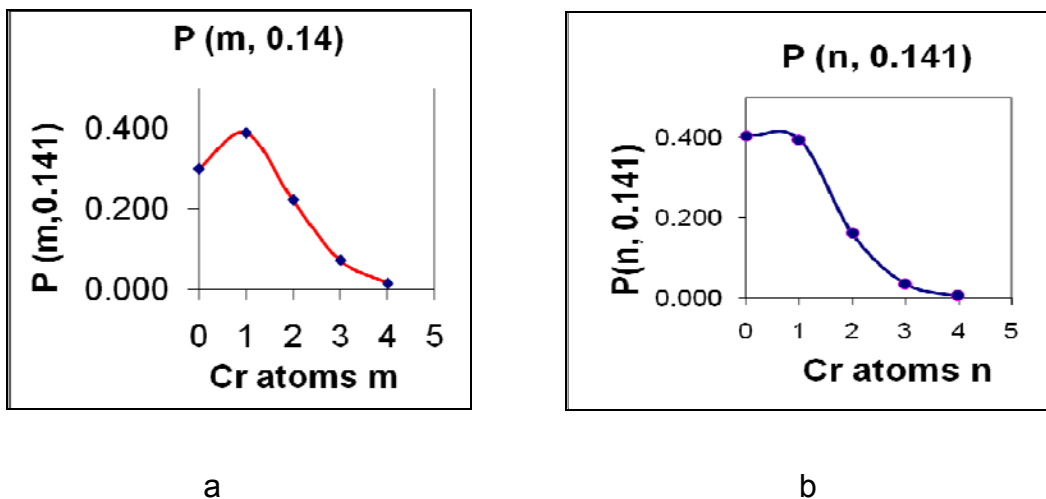


Figure 5. Binomial probabilities for iron substitution by Cr in the cubic (a) and respectively (octahedral) coordination spheres.

The calculated Mössbauer areas (proportional with the P (m, n, c)) corresponding to different (m, n) magnetic sublattices, @ c = 0.141 are presented in Figure 6.

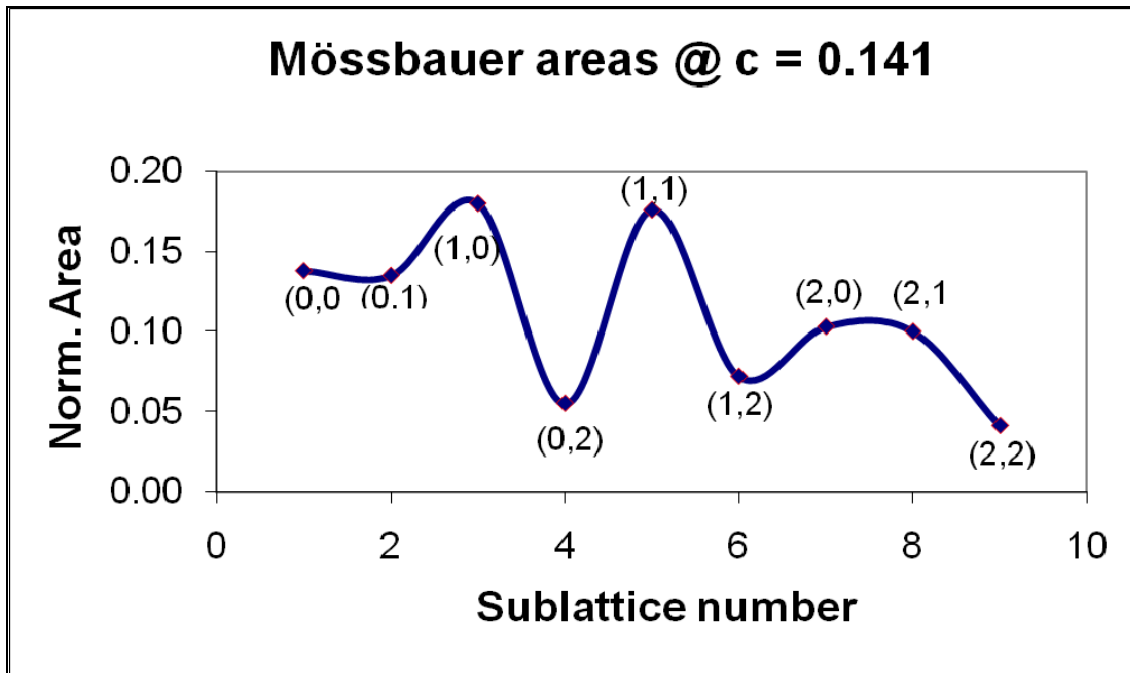


Figure 6. Normalised Mössbauer calculated areas @ c = 0.141 for different (m, n) pairs.

VIII b. Short range order parameter (SRO)

In order to characterise the situation where there is a deviation from the random distribution of substitutional element, a new parameter was introduced by Cowley [9]. For a binary XY alloy a “short range order parameter” (SRO) or “Cowley parameter” was defined as α_j :

$$\alpha_j = (1 - p_{Y(j)}) / c_Y; \quad (3)$$

where $p_{Y(j)}$ is the probability of finding Y atom as a j^{th} neighbour of an X atom, and ‘ c_Y ’ is the fraction of Y atoms in XY alloy.

$\alpha_j = 0$ perfect random distribution;

$\alpha_j < 0$ mutual arrangement of atoms is correlated (surplus of XY pairs-short range ordering)

$\alpha_j > 0$ clustering – shortage (short-range separation).

The following relation exists [10, 11] between the mean hyperfine magnetic field at the Iron nucleus $\langle H \rangle$ at concentration c of substituting element (Cr in our case) and α parameter:

$$\langle H \rangle = (1 + kc) \left[1 + c \sum_{i=1}^N z_i h_i (1 - \alpha_i) \right] \quad (4)$$

$\langle H \rangle$ is the average hyperfine magnetic field: $\langle H \rangle = \frac{\sum_{i=1}^N A_i H_i}{\sum_{i=1}^N A_i}$

where A_i are the Mössbauer normalised areas and N – number of magnetic sublattices.

$z_1 = 8$; $z_2 = 6$; are the coordination numbers, $h_i = \Delta H_i / H_{Fe}$; k = field magnification factor.

In the range of chromium concentration ~13 -14%, V.V. Ovchinnikov [10, 11] showed that

$$\alpha_1 \approx \alpha_2 = \alpha$$

Equation 4 becomes

$$\langle H \rangle = (1 + kc) \left[1 + c(1 - \alpha) \sum_{i=1}^N z_i h_i \right] \quad (5)$$

Based on equation (5) we calculated SRO parameters using the following values of h_1 and h_2 [12]: $h_1 = -0.082$; $h_2 = -0.074$.

VIII.2 Mössbauer analyses of the spectra recorded at room and liquid helium temperatures.

VIII.2a. Room temperature transmission Mössbauer spectra

Mössbauer analyses in transmission geometry at room and liquid helium temperature will be presented in this section. For all recorded spectra, a comparative fit with distribution (Hesse-Rübartsch [13]) and binomial model is presented. The room temperature Mössbauer spectra fitted in terms of the distribution model have been already presented in the first Report (in June 2010) of the Contract but for comparison with binomial model and the presentation clarity we shall display also these graphs.

In figures 7-13 the Mössbauer spectra of FeCrY and FeCrTiY at room temperature fitted with both distribution and binomial models are depicted. The continuous lines are the calculated spectra (or subspectra) for the best fit with the experimental data.

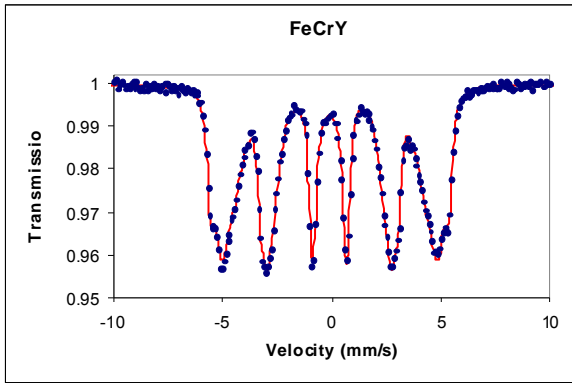


Fig. 7. RT Mössbauer spectrum. Hhf distribution fit.

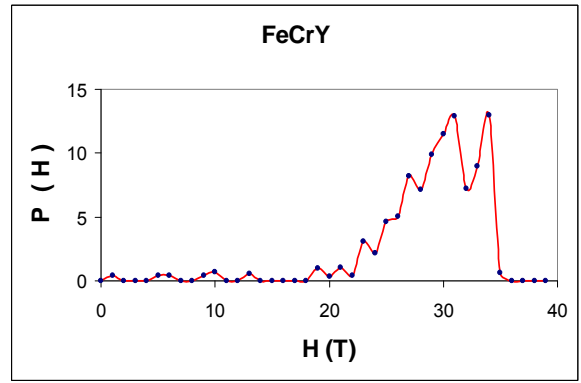


Fig. 8. RT distribution probabilities P(H)

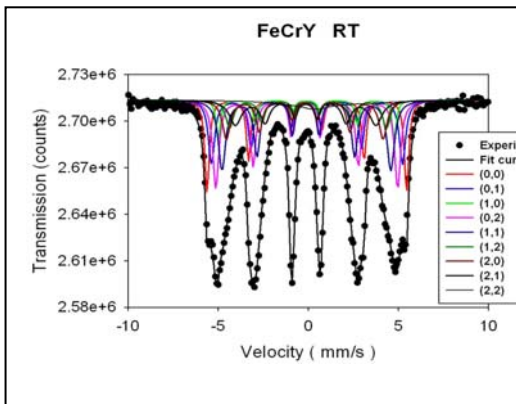


Fig 9. RT Mössbauer spectrum. Binomial fit.

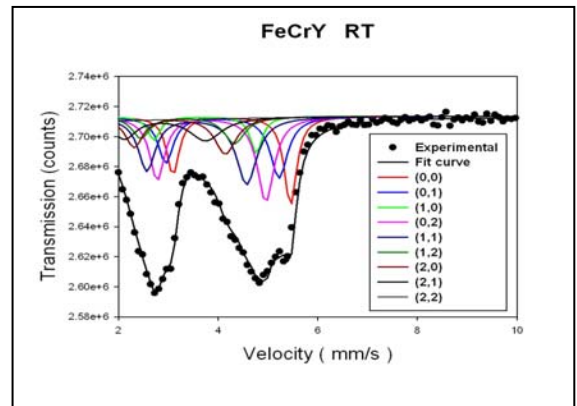


Fig 10. Fit detail from binomial model.

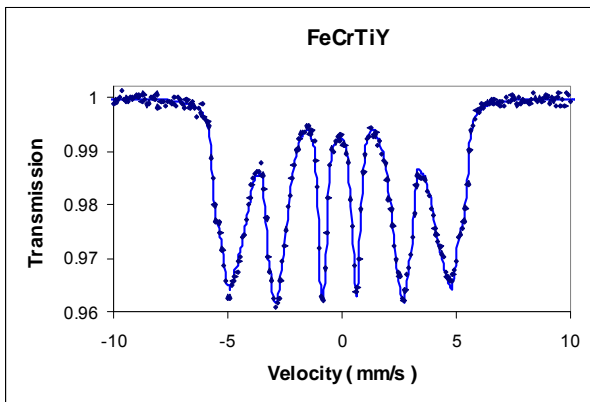


Figure 11. RT Mössbauer spectrum. Hhf distribution fit.

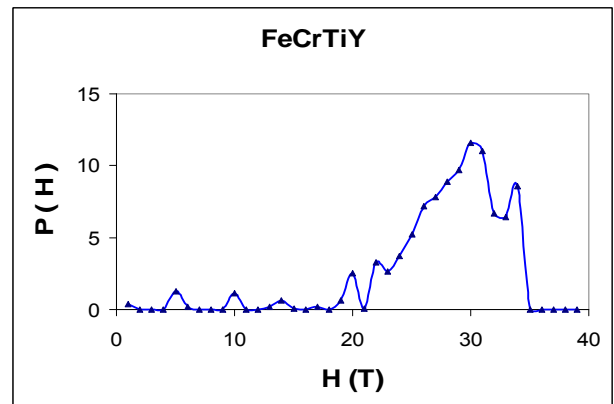


Figure 12. RT distribution probabilities P(H)

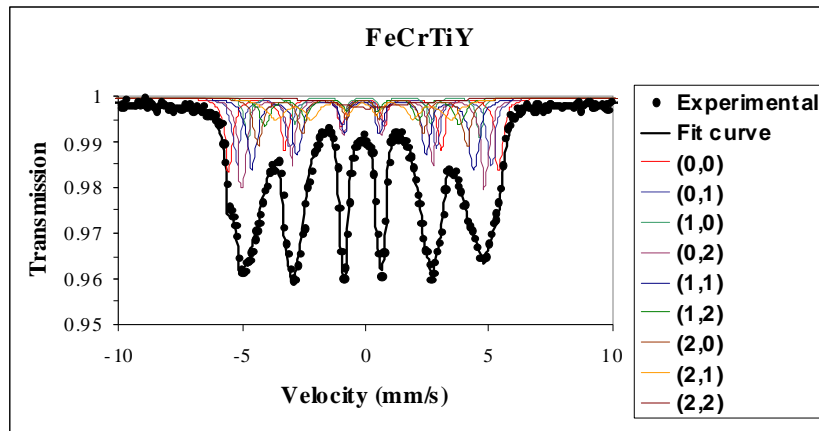


Figure 13. RT Mössbauer spectrum. Binomial fit.

The calculated binomial probabilities, Mössbauer areas, calculated magnetic fields (with eq. 1), experimental magnetic hyperfine fields H_{hf} , and average magnetic hyperfine fields $\langle H \rangle$ as resulted from the spectra fitting with binomial and distribution models for FeCrY and FeCrTiY nanoscaled alloys at chromium concentration $c = 0.141$ are presented in Table 1. One can remark the very close values resulted for the average magnetic fields $\langle H \rangle$ in the two fitting models: magnetic hyperfine distribution (Hesse-Rübartsch) and binomial fit.

Cr at (m,n)	$P_{cub}(m,c)$	$P_{orth}(n,c)$	$P_{co}(m,n,c)$	Mössbauer areas	Calculated H_{hf} (T)	FeCrY H_{hf} (T) Dist.	FeCrY $\langle H \rangle$ (T)	FeCrTiY H_{hf} (T) Dist.	FeCrTiY $\langle H \rangle$ (T)
0,0	29.92%	40.46%	12.11%	13.83%	33.30	34.01		33.72	
1,1	38.97%	39.52%	15.40%	17.60%	27.90	28.77		27.73	
2,2	22.20%	16.08%	3.57%	4.08%	22.50	10.9		9.47	
0,1			11.82%	13.51%	31.10	32.55		31.72	
1,0			15.77%	18.02%	30.10	31		30.3	
0,2			4.81%	5.50%	28.90	30.01		29	
2,0			8.98%	10.27%	26.90	26.72		26.05	
1,2			6.27%	7.20%	25.70	26.73		24.31	
2,1			8.77%	10.03%	24.70	23.97		21.82	
Binomial fit							28.92		27.88
Distrib. fit							28.91		27.85
Errors							± 0.05		± 0.05

Table 1. Binomial probabilities, Mössbauer areas, magnetic hyperfine fields H_{hf} , and average magnetic hyperfine fields $\langle H \rangle$ as resulted from the spectra fitting with binomial and distribution models for FeCrY and FeCrTiY nanoscaled alloys at chromium concentration $c = 0.141$.

In figure 14 the calculated (with eq.1) and the experimental hyperfine magnetic fields values are depicted versus magnetic Mössbauer sublattices, for the FeCrY and FeCrTiY at room temperature. A very good agreement between theory and experiment can be observed.

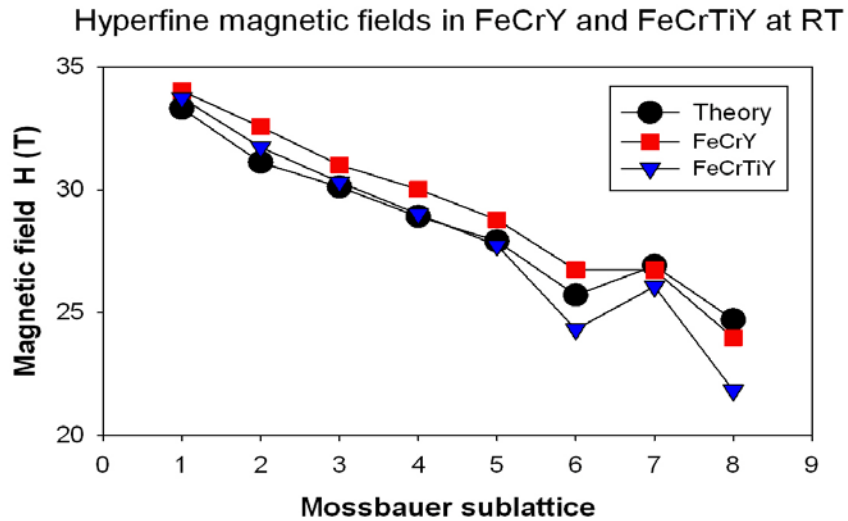


Figure 14. Magnetic hyperfine field as resulted from binomial fit versus Mössbauer sublattice in comparison with the calculated values in the case of FeCrY and FeCrTiY, at room temperature.

VIII.2b. Liquid helium temperature Mössbauer spectra

Using the “See Co” Mössbauer spectrometer with helium closed cycle cryostat the Mössbauer spectra of nanoscaled FeCrY and FeCrTiY were recorded at 4.7K. Figures (15 -20) display the spectra fitted in terms of distribution and binomial fit. The spectra are similar with the room temperature ones indicating that no phase transitions occur in this temperature range. The values of the average magnetic fields are 29.84T and 29.83T for FeCrY and respectively FeCrTiY in the binomial model and 29.55T and 29.53T for the same samples in distribution model. The values are superior to those at room temperature as expected but very close each ones irrespective to the fit model of Mössbauer spectra. All $\langle H \rangle$ values obtained from the performed Mössbauer measurements are presented in the Table 2 at the end of this report.

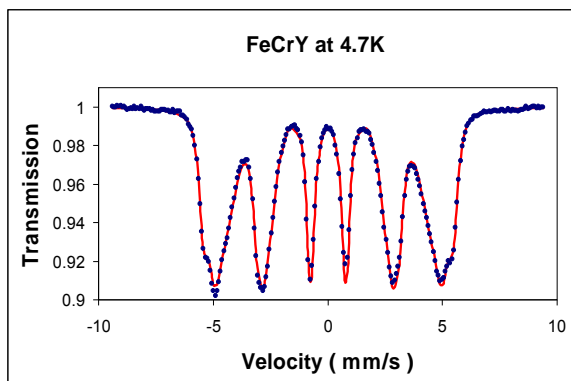


Figure 15. Mössbauer spectrum at 4.7K.

(Hhf distribution fit)

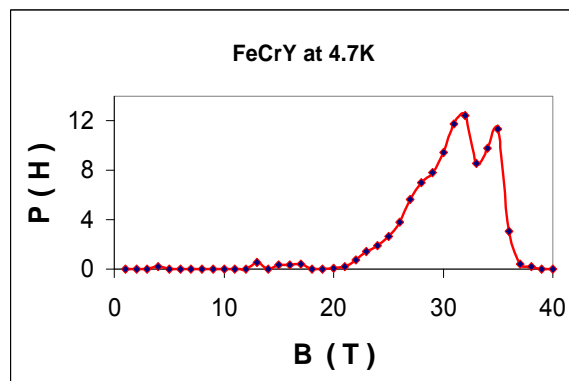


Figure 16. Distribution probabilities $P(H)$ at 4.7K

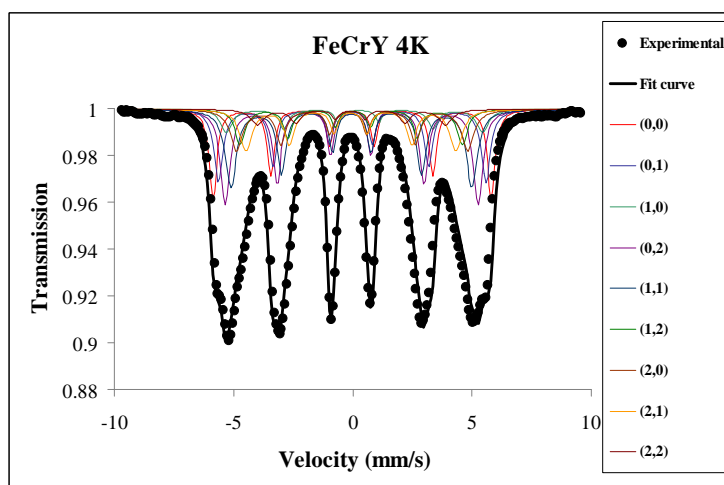


Figure 17. Mössbauer spectrum at 4.7K. Binomial fit.

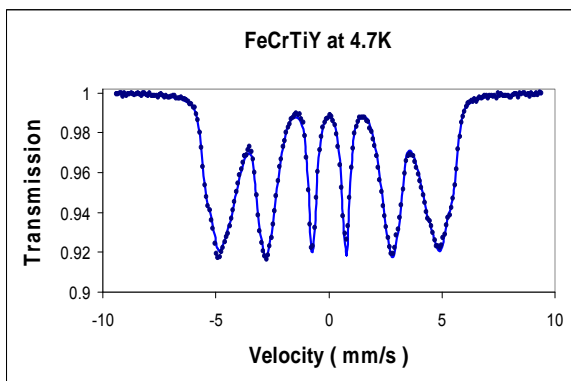


Figure 18. Mössbauer spectrum at 4.7K.

Hhf distribution fit.

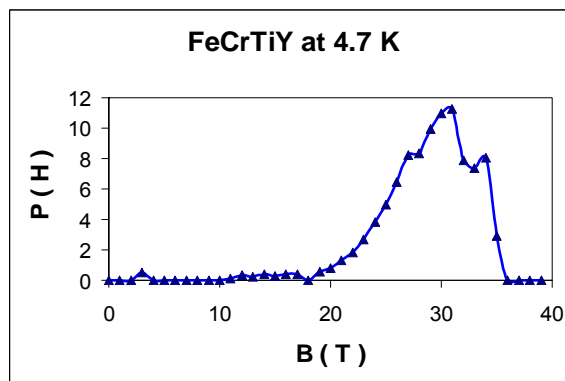


Figure 19. Distribution probabilities $P(H)$ at 4.7K.

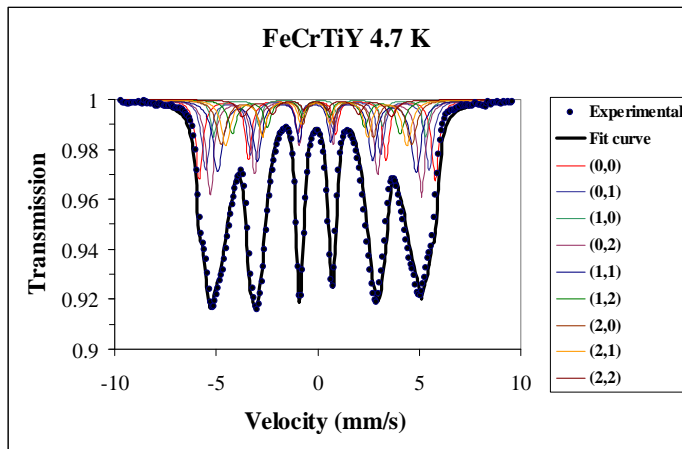


Figure 20. Mössbauer spectrum at 4.7K. Binomial fit.

VIII.3. Mössbauer spectroscopy studies by Conversion electron Mössbauer spectroscopy (CEMS) measurements and Conversion X-ray Mössbauer spectroscopy (CXMS) measurements.

VIII.3a. CEMS DATA

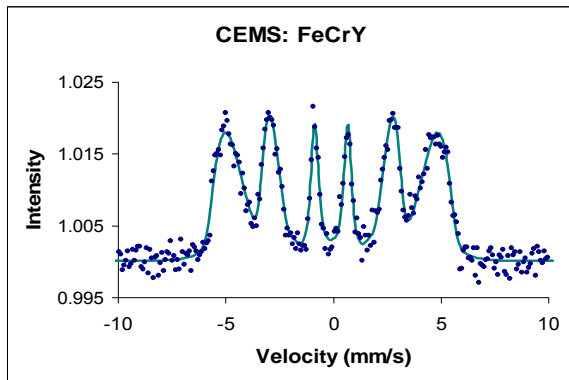


Figure 21. RT CEMS. Distribution fit.

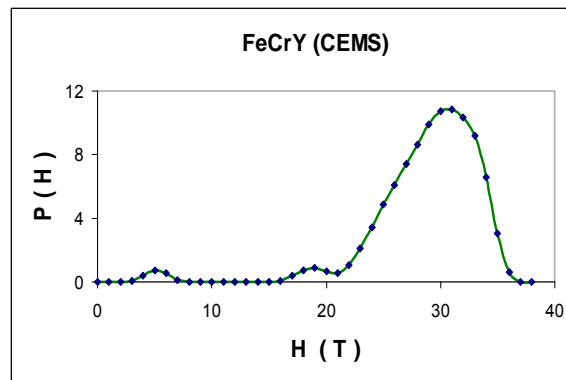


Figure 22. Distribution probabilities $P(H)$.

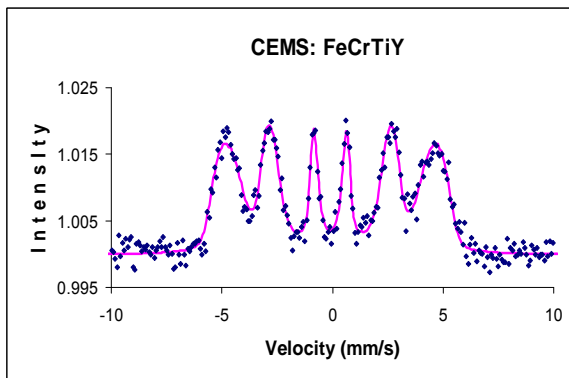


Figure 23. RT CEMS. Distribution fit.

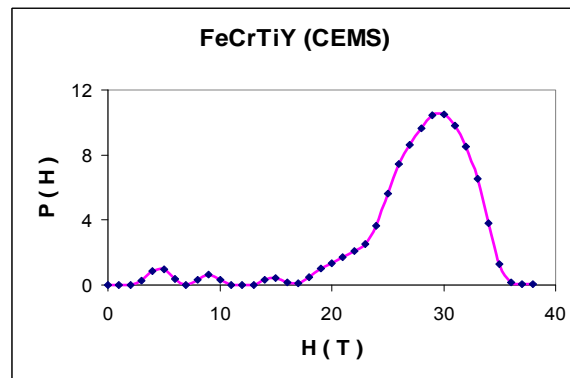


Figure 24. Distribution probabilities $P(H)$.

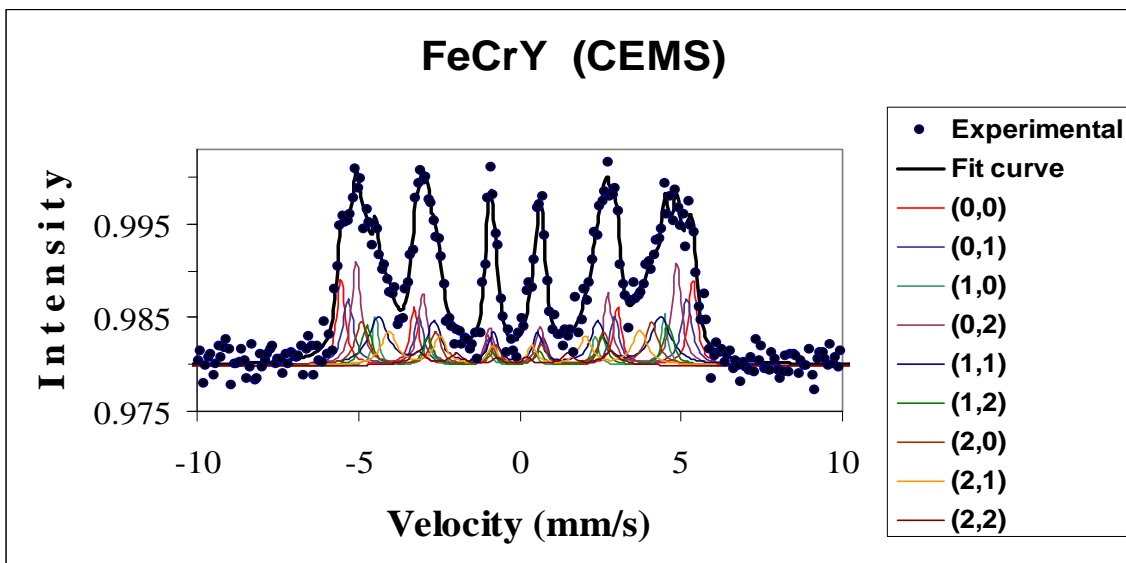


Figure 25. RT CEMS spectra fitted with binomial model.

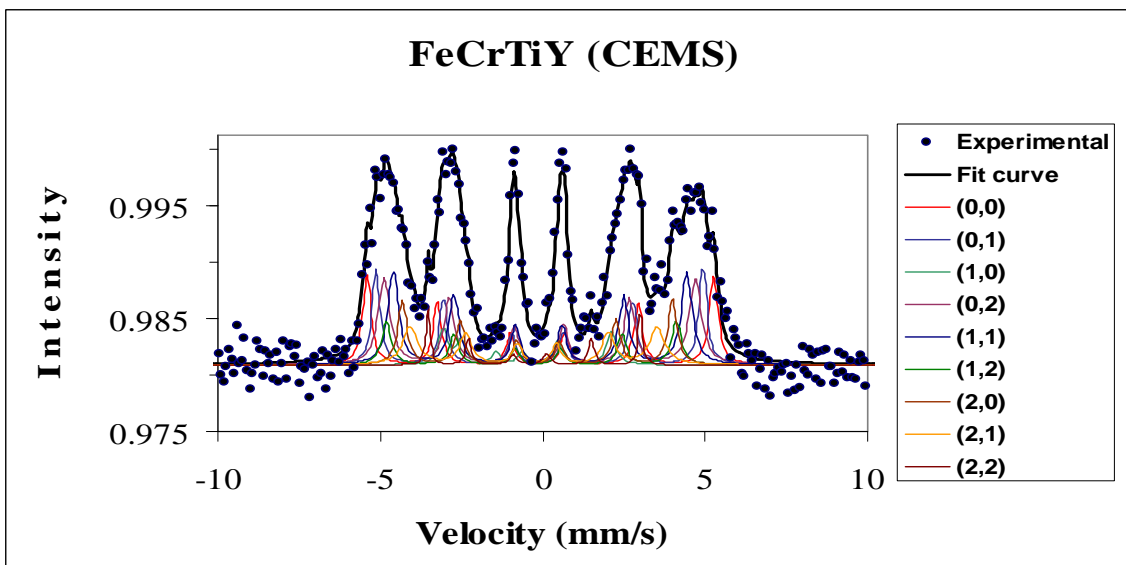


Figure 26. RT CEMS spectra fitted with binomial model.

The values of the average magnetic fields $\langle H \rangle$ are 29.01 T and 27.79 T for FeCrY and respectively FeCrTiY in the binomial model and 28.80 T and 27.51 T for the same samples in distribution model (see the general data Table 2). As in the case of transmission spectra results one can observe a little drop in the magnetic field values for titanium doped sample; this behaviour suggests that the titanium atoms are placed in the very near neighbouring of iron atoms in the structure leading to a more pronounced magnetic dilution. The $\langle H \rangle$ values given by CEMS spectra fitting are generally smaller than those in transmission, probably due to surface effects that are important in such cases.

VIII3b. (CXMS) DATA

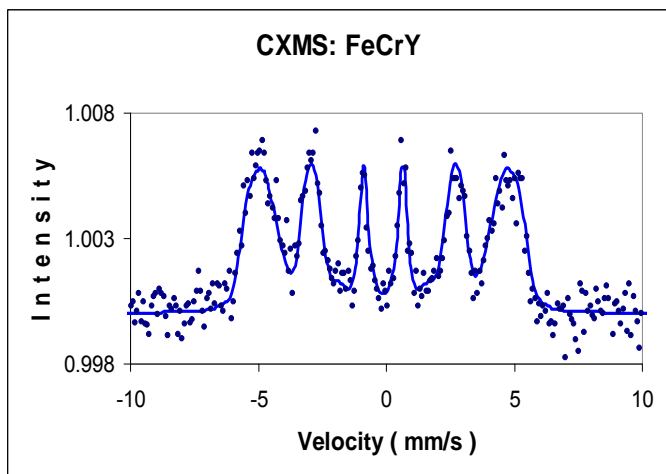


Figure 27. RT CXMS. Distribution fit.

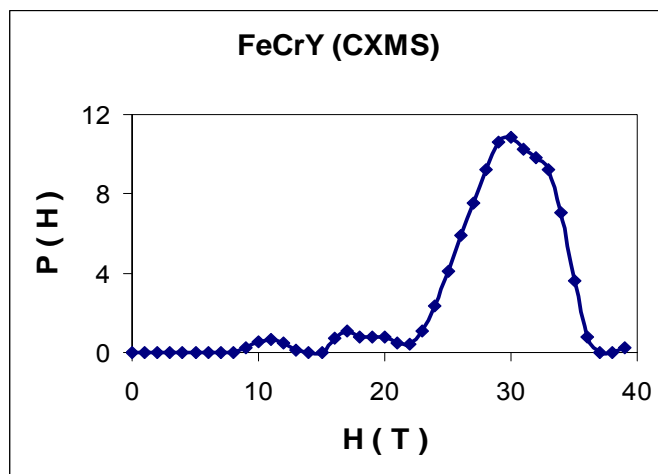


Figure 28. Distribution probabilities P(H).

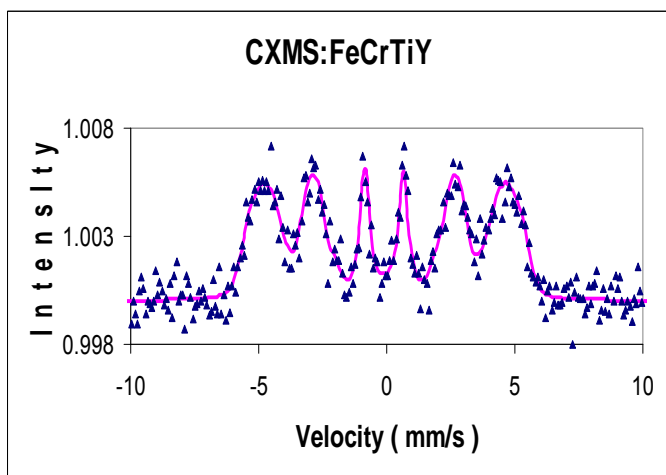


Figure 29. RT CXMS. Distribution fit.

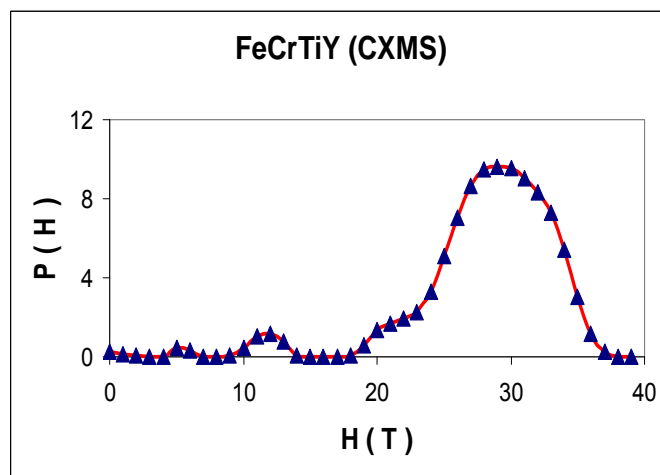


Figure 30. Distribution probabilities P(H).

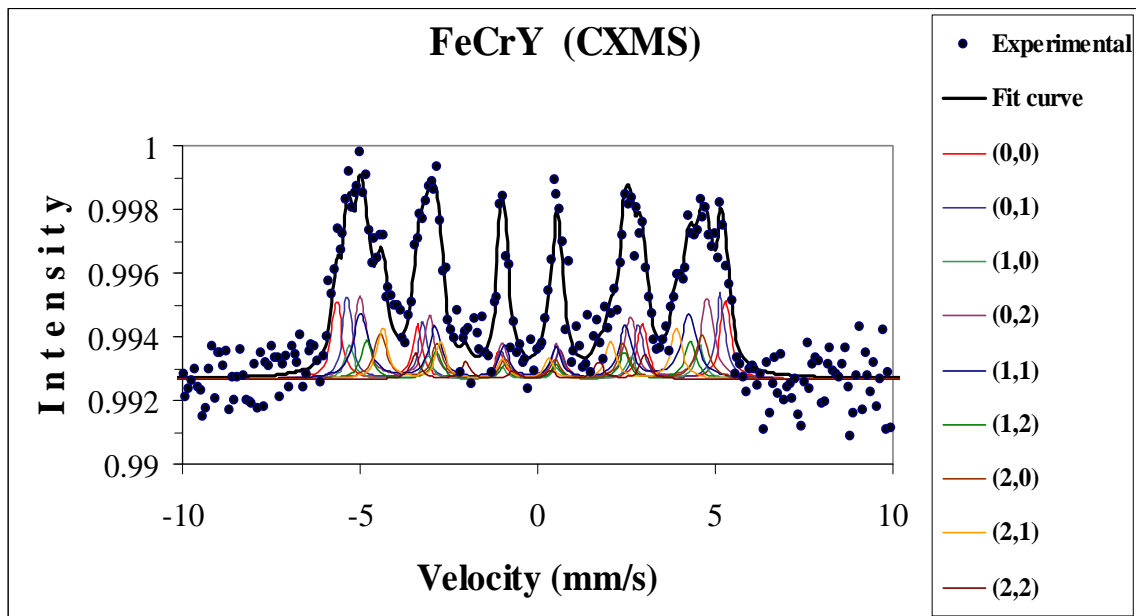


Figure 31. RT CXMS spectra fitted with binomial model.

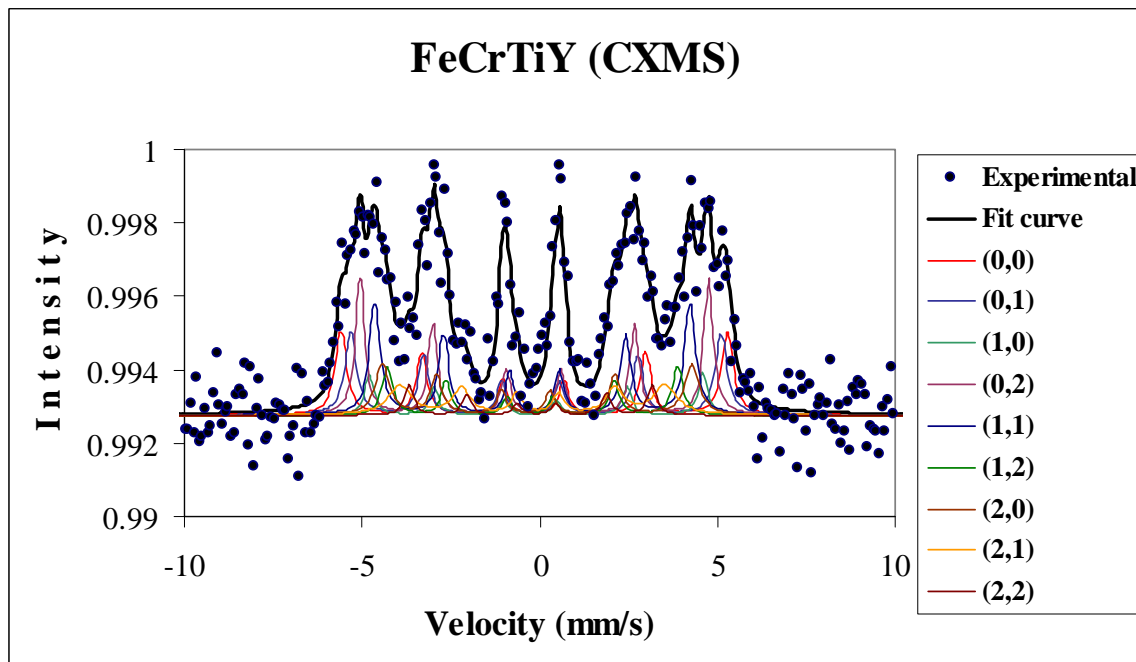


Figure 32. RT CXMS spectra fitted with binomial model.

The values of the average magnetic fields $\langle H \rangle$ given by the fit of CXMS spectra are 29.57T and 28.64 T for FeCrY and respectively FeCrTiY in the binomial model and 28.95 T and 27.99 T for the same samples in distribution model (Table 2). As in the case of transmission and CEMS results one can observe a little drop in the magnetic field values for titanium doped sample; the explanation has been already presented.

VIII. 4. Room temperature transmission Mössbauer measurements on Fe-Cr powder alloys obtained by ball milling, after thermal treatments.

FeCrY and FeCrTiY, nanoscaled samples, obtained by planetary milling were thermally treated at 760 °C for 2 hours in order to study the thermal effects on the structure and magnetic hyperfine interactions and SRO parameters. The treatments were performed under vacuum in order to avoid oxidations processes. The room temperature Mössbauer spectrum of the sample FeCrY after thermal treatment is depicted in figure 33. In comparison with the untreated spectra one can remark a very different shape of the Mössbauer spectra. The general shape suggests the presence of a magnetic field distribution in the sample. The fit with magnetic field distribution model gives the distribution presented in figures 33 and 34.

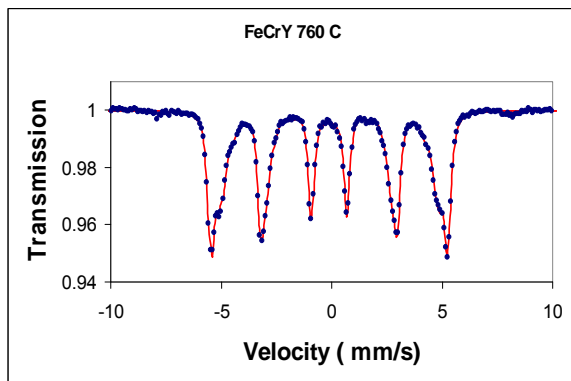


Figure 33. RT Mössbauer spectrum of the sample FeCrY treated at 760C. Distribution fit

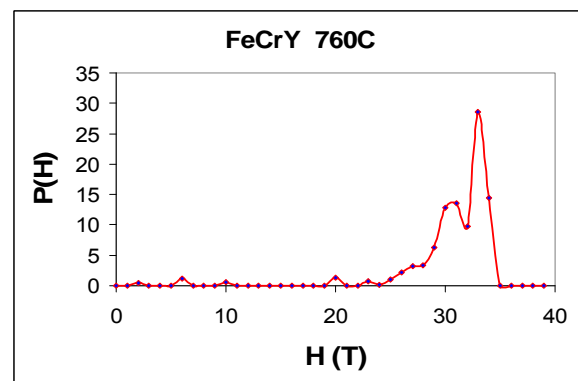


Figure 34. Distribution probabilities $P(H)$.

The fit with the binomial fit is presented in fig 35.

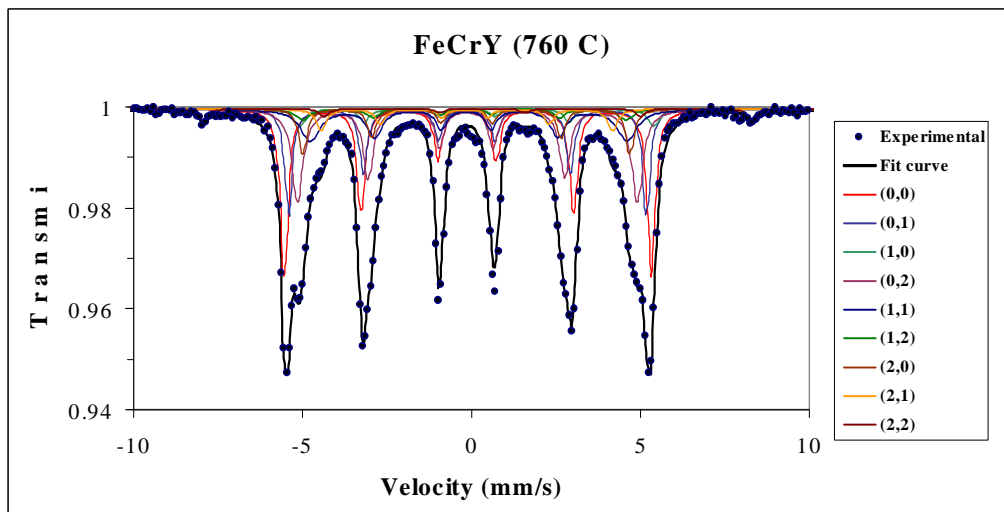


Figure 35. Binomial fit on Mössbauer spectra of the sample FeCrY after thermal treatment @760 C. The corresponding Mössbauer spectra of the FeCrTiY and the fit results are depicted in figures 36-38.

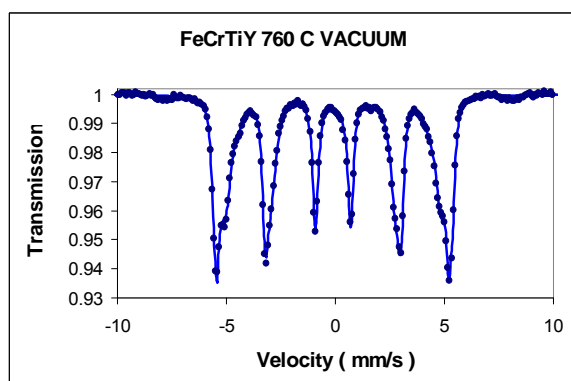


Figure 33. RT Mössbauer spectrum of the sample FeCrTiY treated at 760C. Distribution fit.

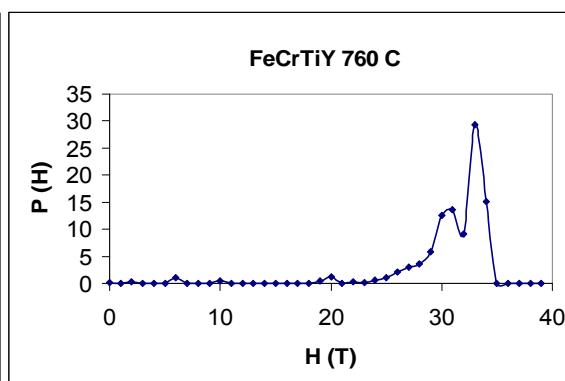


Figure 34. Distribution probabilities P(H).

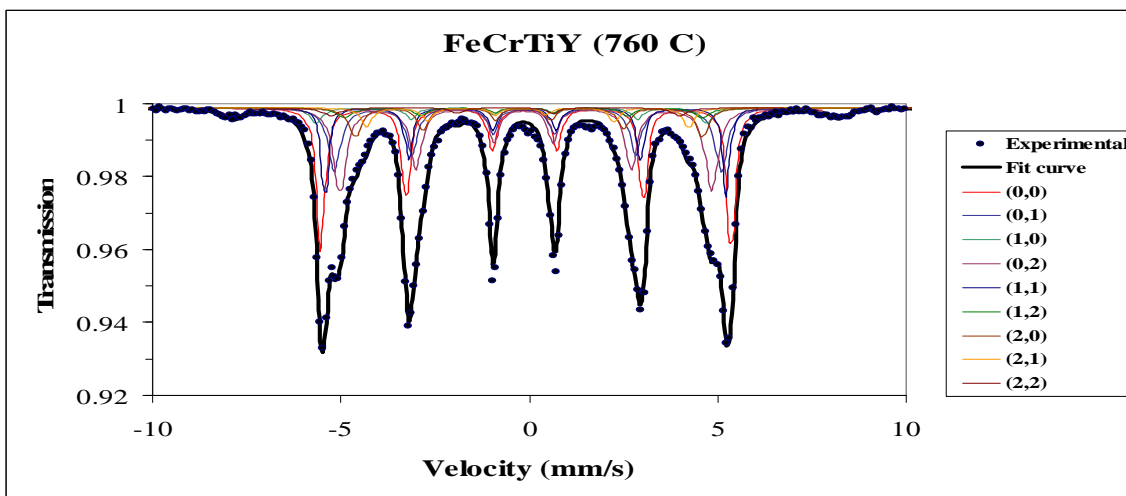


Figure 38. Binomial fit on Mössbauer spectra of the sample FeCrTiY after thermal treatment @760 °C.

In the binomial model approach the best fit with the experimental point (presented in Figures 35 and 38) was obtained considering the binomial probabilities calculated for a chromium concentration of ~ 9 % instead of 14.1 % as in the initial samples (after planetary ball milling). This behaviour indicates a reject of chromium atoms from the system, probably a clustering process. The values of the average magnetic fields $\langle H \rangle$ given by the fit of RT Mössbauer spectra of the thermally treated samples are 31.21 T and 31.31 T for FeCrY and respectively FeCrTiY in the binomial model and 30.63 T and 30.71 T for the same samples in distribution model (Table 2). All these values are more near the magnetic hyperfine field characteristic value of α -Fe ($H_{hf}(\text{Fe}) \sim 33.3$ T).

VIII.3 Data computing and analysis of short range order (SRO), local structure and magnetic properties, publication of relevant results, Conclusions

Based on the equation 1-5 discussed in the first part of this report, the SRO parameters were calculated for all performed Mössbauer measurement; the average magnetic fields $\langle H \rangle$ calculated with both *hyperfine magnetic field distribution and binomial* models were considered in the calculations. Table 2 summarises the calculated or resulted data from the Mössbauer spectra fitting of the investigated samples, FeCrY and FeCrTiY. For all recorded spectra, the values of the isomer shifts IS [14, 15] are also presented. The following main conclusions of this study can be written as follows:

- ◆ Average hyperfine magnetic fields $\langle H \rangle$ and isomer shifts (IS) values determined by the hyperfine magnetic fields distribution and binomial fit models are similar for Mössbauer transmission experiments; some differences can be observed in the case of CEMS/CXMS data due to a modest statistics associated with such kind of measurements;
- ◆ The theoretical evaluation of $H(m, n, c)$ (hyperfine magnetic fields) for different (m, n) sites is in good agreement with the experimental Mössbauer data;
- ◆ No phase transitions were evidenced between RT and liquid helium temperature;
- ◆ For the as resulted (ball milled) samples, the average magnetic fields values $\langle H \rangle$ are smaller in the case of FeCrTiY with respect to the FeCrY samples; the effect could be attributed to a magnetic dilution by Ti atoms placed not so far from Fe atoms in the alloy structure;
- ◆ SRO determination indicates generally a rather random distribution of Cr atoms (the obtained values around zero). The effect of Ti in the system seems to consist in an increase of the number of pairs, all SRO values being small and negatives;

◆ In the case of the thermally treated samples the best fit with binomial model was obtained at a **Cr concentration of ~ 9 %** suggesting a rejection process during heating. For both samples, FeCrY and FeCrTiY, the SRO parameters are positives, indicating a shortage in Fe-Cr pairs after thermal treatments;

Table 2. <H> average hyperfine magnetic field, SRO and mean Isomer shift values for the studied samples.

Sample	H(0,0) (kOe)	<H>		SRO		<IS>*	
		(kOe)	(kOe)	(α)	(α)	mm/s	mm/s
		Dist. fit	Binom. fit	Dist. fit	Binom. fit	Dist. fit	Binom. fit
FeCrY RT	340.1	289.1	289.1	0.05	0.04	-0.011	0.003
FeCrTiY RT	337.3	278.5	278.8	-0.11	-0.11	-0.011	0.001
FeCrY 4K	354.0	295.5	298.4	-0.05	0.00	0.022	0.043
FeCrTiY 4K	354.0	295.3	298.3	-0.05	-0.01	0.023	0.047
FeCrY CEMS	337.4	288.0	290.1	0.07	0.11	-0.096	-0.012
FeCrTiY CEMS	334.2	275.1	277.9	-0.12	-0.03	-0.095	-0.112
FeCrY CXMS	339.3	289.5	295.7	0.07	0.18	-0.110	-0.087
FeCrTiY CXMS	339.9	279.9	286.4	-0.12	-0.01	-0.085	-0.057
FeCrY 760 °C	336.6	306.3	312.1	0.12	0.29	-0.005	0.001
FeCrTiY 760 °C	337.4	307.1	313.1	0.12	0.30	-0.005	-0.016
Errors	±0.4	±0.4	±0.4	± 0.02	± 0.02	±0.005	±0.005

* Isomer shift (IS) is relative to α -Fe.

Based on the present study we can infer that Mössbauer spectroscopy is a very suitable method to study the magnetic hyperfine interactions and SRO parameter peculiarities in Fe-Cr based alloys. Due to the fact that Fe and Cr lattices are isostructural, the X-ray diffraction method is not very useful to study Fe-Cr based alloys. The Mössbauer spectroscopy is of particular interest when we need to obtain information about magnetic hyperfine interaction correlated with SRO parameter, information that can be used to improve the production technology of Fe-Cr based materials for fusion reactors.

Preliminary results concerning the room temperature transmission Mössbauer measurements have been presented at National Physics Conference, September 2010 Iasi Romania under the title:

Mössbauer Spectroscopy Investigations on FeCr Based Alloys for Fusion Reactors.

Another paper,

Mössbauer spectroscopy studies of hyperfine magnetic fields and short range order parameter in the Y and Ti doped Fe-Cr nanoscaled alloys obtained by ball milling is in preparation, and will be published under the agreement with EFDA authorities.

IX. References

1. R. L. Mössbauer, Z. Physik, **151**, 124 (1958).
2. A. G. Maddock, Mössbauer Spectroscopy: Principles and Applications of the Techniques, (Horwood Chemical Science Series), Horwood (1997).
3. I. Bibicu, G. Nicolescu, C. Cretu, Hyperfine Interactions, **192**, 85 (2009).
4. Y. Isozumi, D. I. Lee, I. Kadar, Nucl. Instrum. Methods, **120**, 23 (1974).
5. A. S. Kamzin, L. A. Grigoriev, Sov. Tech.-Phys. Lett., **16**, 616 (1990).
6. I. Bibicu, M. S. Rogalski, G. Nicolescu, Nucl. Instr. and Meth. in Phys. Res., **B 94**, 330 (1994).
7. S. M. Dubiel and J. Zukrowski, J. Magn. Magn. Mater. **23**, 214 (1981).
8. J. Cieślak, S.M. Dubiel, J. Alloys Comp., **387**, 36–43 (2005).
9. J.M. Cowley, Phys. Rev. **77**, 669-675(1950).
10. V.V. Ovchinnikov et al, Fiz. Met. Metalloved. **42** (1976) 310.
11. V.V. Ovchinnikov¹, B.Yu. Goloborodsky, N.V. Gushchina, V.A. Semionkin, E. Wiser, Appl. Phys. A **83**, 83–88 (2006)
12. G.K. Werthaim, V. Jaccarino, J.H. Wernik, D.N.E. Buchanan, Phys. Rev. Lett., **12**, 24 (1964).
13. J. Hesse and A. Rübartsch, J. Phys. E: Sci. Instruments **7**, 352-532 (1974).
14. N. N. Greenwood, T.C. Gibb, *Mössbauer spectroscopy*, Chapman and Hall Ltd. London (1971).
15. D. Barb, Efectul Mössbauer si Aplicatiile sale, Ed. Academiei Bucuresti 1972; *Grundlagen und Anwendungen der Mosbauer Spektroskopie*, Berlin 1980.

Dr. Lucian Diamandescu

National Institute of Physics, Bucharest, Romania

SECTIUNEA 1

RAPORTUL STIINTIFIC SI TEHNIC

FAZA DE EXECUTIE NR. 2.

CU TITLUL:

ANALIZA MICRO SI NANO-STRUCTURALA PRIN T.E.M., X-EDS, E.E.L.S., XRD SI SPECTROSCOPIE MOESSBAUER A MATERIALELOR REZULTATE IN FAZELE DE PROCESARE TEHNOLOGICA PENTRU OBTINEREA OTELURILOR FERITICE TIP O.D.S. (O.D.S.F.S.) SI A ALIAJELOR DE W TIP O.D.S.

- € **RST – raport stiintific si tehnic in extenso**
- € **PVAI – proces verbal de avizare interna**
- € **PVRLP – procese verbale de receptie a lucrarilor de la parteneri***
- € **PF – protocol de finalizare(numai pentru faza finala)**

*forma si continutul se stabilesc de catre conducatorul proiectului, tinand seama de cele continute in PVAI

REPORT on PROGRESS

**Stage of research performed in the frame of the
contract nr. 1EU-8 / 01.03.2010**

entitled

**MICRO AND NANO-STRUCTURAL ANALYSIS BY T.E.M., X-EDS,
E.E.L.S., XRD AND MOESSBAUER SPECTROSCOPY OF THE
PROCESSED MATERIALS IN VARIOUS TECHNOLOGICAL
STAGES OF O.D.S. FERRITIC STEELS (O.D.S.F.S.) AND O.D.S. W-
ALLOYS ELABORATION**

**concerning the following activities mentioned in the
EFDA WP10-MAT-ODSFS task agreement**

WP10-MAT-ODSFS-01-01/MEdC/BS

WP10-MAT-WWALLOY-01-01/MEdC/BS

**P.I. Dr. Corneliu Sarbu
project responsible**

**Natl. Inst. for Mater. Physics
Magurele-Bucharest, Romania**

December 2010

CONTENT

General and partial objectives	4
Abstract	5
Results of the research performed in the period June 30th – December 15th 2010	
The studied materials. The instrument of analysis	6
The microstructure of the pure W-alloy sample	7
The microstructure of the W-alloy+1vol%Y2O3 sample	8
The microstructure of the W-alloy+5vol%Y2O3 sample	14
Conclusions	21
Annex 1-RST	22

GENERAL OBJECTIVES

The reported research aims at matching the following general objective:

(i) Developing the present generation of micro and nano-structured ODS W-alloys by optimising a set of parameters governing the MIM (Metal Injection Moulding). The aim is to reproduce the main microstructure features identified as responsible for the high strength and the limited loss of fracture toughness after irradiation. The research is focused on the following chemical compositions: W-alloy +1vol%Y₂O₃, W-alloy+5vol%Y₂O₃ and W-alloy+5vol%Ta. The pureW-alloy is taken as a microstructure reference. The grain microstructure of the material produced by MIM, the presence of extended defects and the distribution of the nano-oxide or the nano-Ta particles inside the W grains are necessary technological informations to be known by our Dutch partner who is producing the ODS or Ta-strengthened W-alloys. The microstructure is expected to be characterized by using transmission electron microscopy (TEM) and related microanalysis (X-EDS) as a basic combination of investigation techniques. Other microanalysis techniques could be used in as much as they are appropriate.

PRESENT STAGE OBJECTIVES HAVING DECEMBER 15 2010 AS DEADLINE

According to the contract, the partial objectives assumed for the 2-nd round of analysis (deadline December 15, 2010) are:

- a) analysis of solid samples of pure-W and W-5vol%Ta, as supplied by our Dutch partner;
- b) analysis of solid samples of ODS-W with 1% and 5% Y₂O₃, as supplied by the Dutch partner;
- c) if necessary, the analysis of samples supplied with delay by our Portuguese partner will be extended beyond June 30, 2010; this situation can occur if the foreign partner doesn't succeed to supply in due time his samples for analysis;

We have to point out that, according to the contract, our work of analysis is highly dependent on the supply of samples by our foreign partners.

Because the Portuguese Association has decided in June 2010 to cease their research on the elaboration of ODS ferritic steels, we had to cease at mid 2010 the microanalysis of ODSFS and to dedicate our work to the exclusive investigation of the W-alloys strengthened with Ta and Y₂O₃. Because of the difficulties of getting the Ta-powder from their supplier, the Dutch partner was not able to supply us with any sample of the W-alloy+5vol%Ta and therefore its analysis was not done.

ABSTRACT

A couple of solid samples of ODS strengthened W-alloys having different compositions and a pure-W alloy sample as reference, all fabricated by MIM (Metal Injection Moulding), were investigated by TEM and X-EDS microanalysis, in order to determine their morphology and chemical composition at micro and nano-scale. Of main interest was the distribution of strengthening particles of Y₂O₃ inside the W matrix grains and the existence of any other extended defects in the materials.

The information we will supply to ODS W-alloys producer has technological importance for adapting the MIM process parameters.

We drew the general conclusion that

- (1) the strengthening Y₂O₃ particles are present in almost all W grains of both ODS compositions,
- (2) the presence of Ytria inclusions containing nanoparticles of W inside them was detected either as inclusions in the matrix W grains, or as self-consistent grains in both ODS materials,
- (3) the size distribution of ODS inclusions is large, from nanoparticles to microparticles and so is the size distribution of the Ytria particles containing W inside them, whereas the size of W matrix grains is large, of the order of several microns,
- (4) pores are present overall in both the investigated solid samples.

RESULTS OF THE RESEARCH PERFORMED IN THE PERIOD JUNE 30 – DECEMBER 15, 2010

The materials. The instrument of analysis

We have investigated 2 samples of ODS W-alloys:

1. W-alloy + 1vol%Y₂O₃
2. W-alloy + 5vol%Y₂O₃
3. and a reference sample of pure W-alloy.

All solid samples were fabricated by MIM and kindly supplied by the Dutch Association, namely by Dr. Darina Blagoeva from NRG Petten.

The instrument used for micro and nano-characterization was an analytical TEM electron microscope model JEM-200CX-TEMSCAN, able to generate an electron beam of maximum 200keV energy, in TEM and in SEM modes of operation. The analytical TEM is equipped with a SEM attachment, which is able to generate μ -beams (i.e. the electron beam can have a diameter of the order of several microns, which is not the case in the TEM operating mode) of electrons. The μ -beam can be focussed on very small features of the sample, allowing to perform “on-point” the X-EDS analysis.

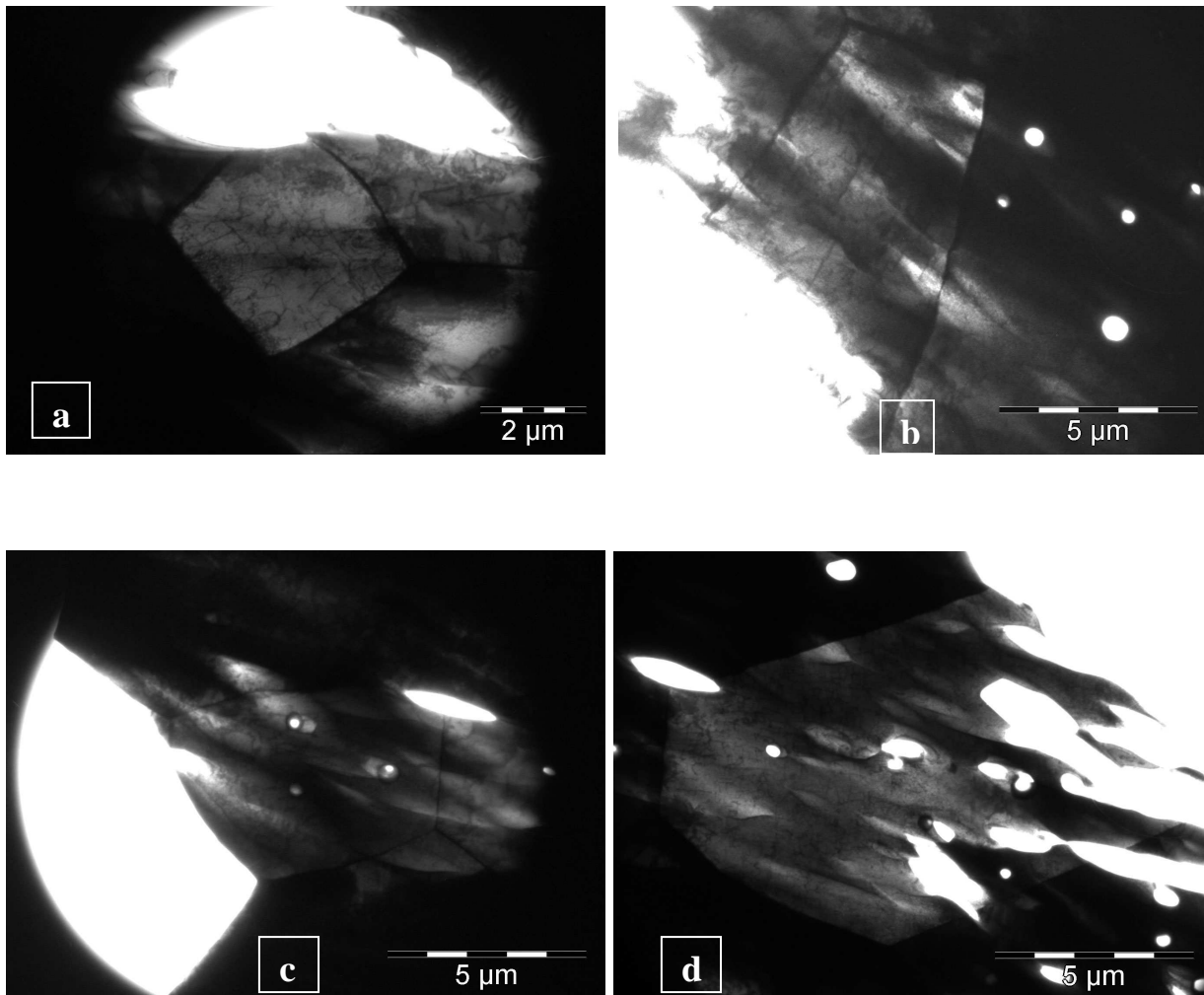
The microscope is equipped with an X-EDS spectrometer model EDS-2004 made by IXRF Systems Inc., 15715 Brookford Drive, Houston, Texas. It operates when the microscope works in both SEM and TEM modes, with an energy dispersion detector of Si(Li) mounted in high position, i.e. at a takeoff angle of 72 deg., which is very favorable in some instances because the sample has not to be tilted away from horizontal in order to acquire a good quality spectrum. In the SEM mode of operation the electron beam can be accelerated at 40, 80, 120, 160 and 200 kV, the beam diameter being that of a μ -beam. An important advantage offered by this instrument is that it can work in SEM mode at much higher accelerating voltages than in dedicated SEM microscopes. These highly focussed energetic beams can penetrate and generate X-rays from very deep levels inside the sample material.

The samples were prepared for TEM by the standard method of ion beam milling.

The microstructure of the pure W-alloy sample

The main observations made on the microstructure of this material are summarized in the series of images presented in Fig.-1 (a to d).

FIGURE-1



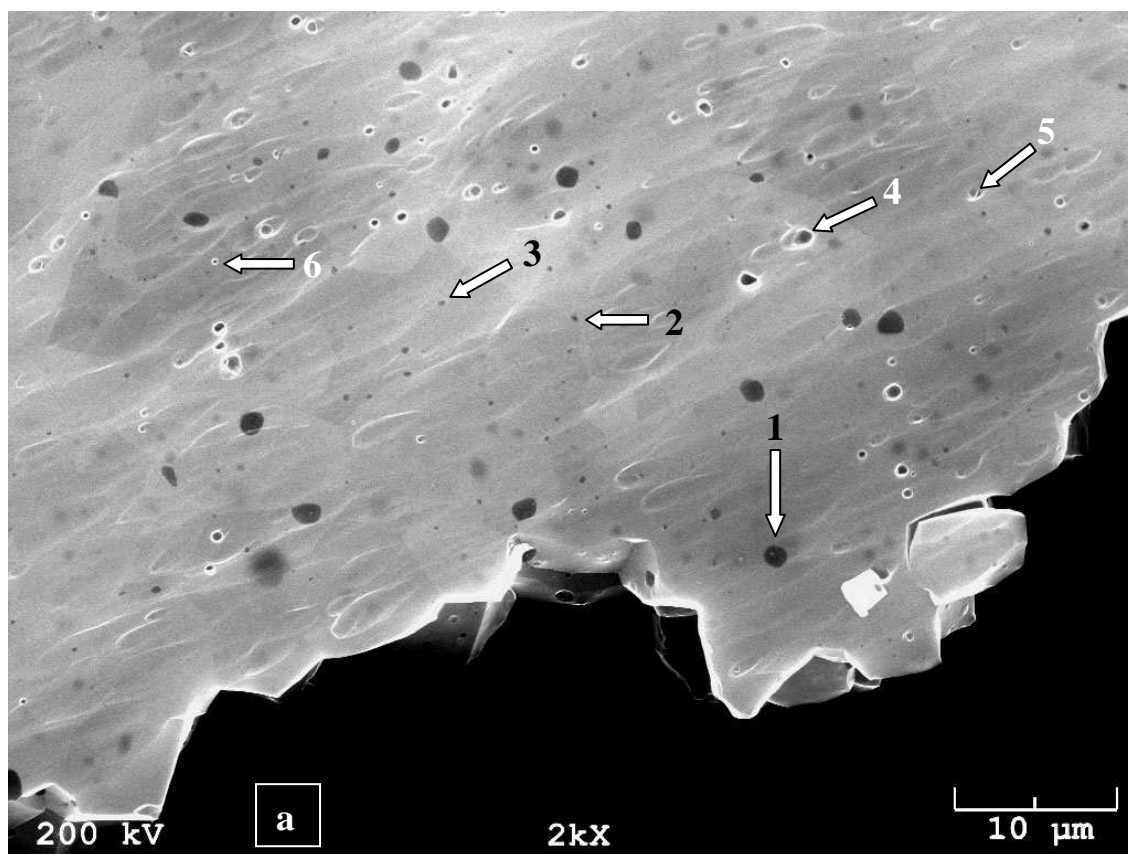
The W grain dimensions are of the order of several μm . The small round holes observed in images (b), (c) and (d) should be due to the preexisting pores in the material. In image (a) there is no pore.

It was difficult to find more observable entire grains, because of the slightly unsatisfactory quality of sample thinning. We will continue to improve the technique of ion beam milling of our W samples.

The microstructure of the W-alloy + 1vol%Y₂O₃ sample

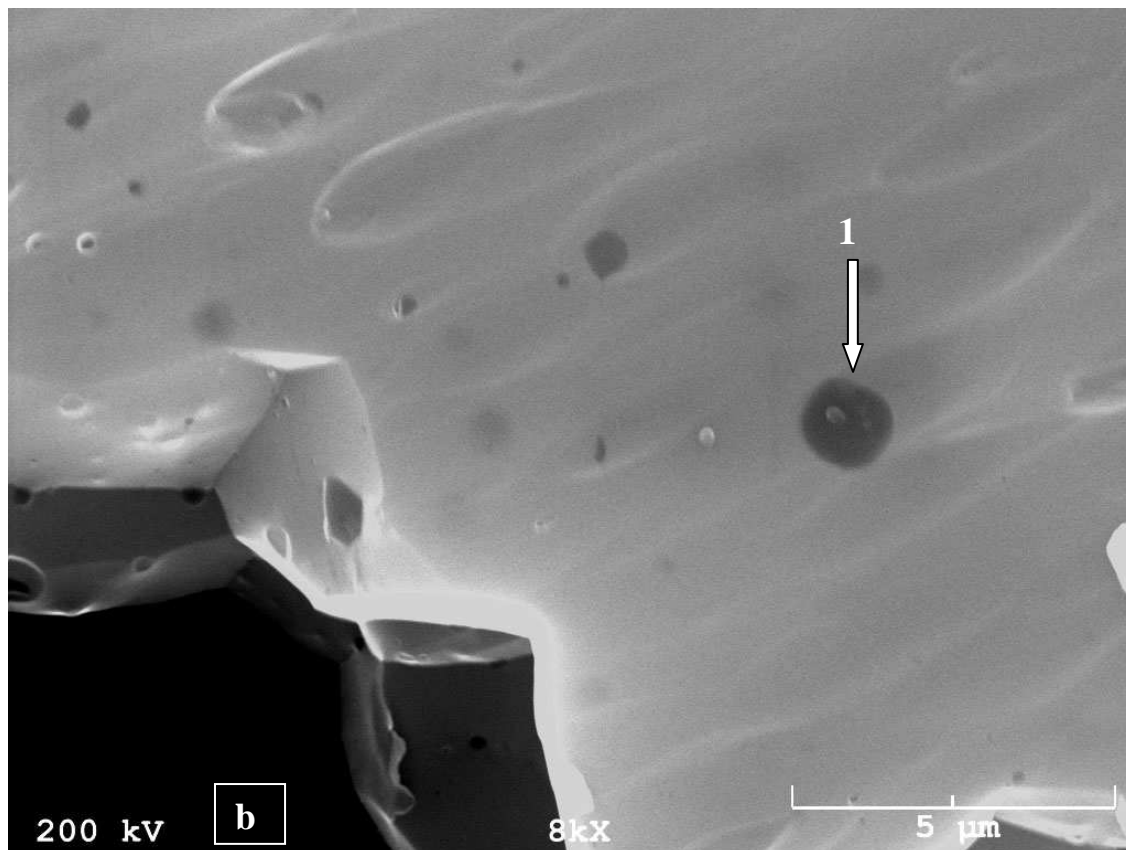
The main features observed by SEM and X-EDS in this sample are shown in Fig.-2, a and b (morphology observations) and following X-EDS spectra.

FIGURE-2



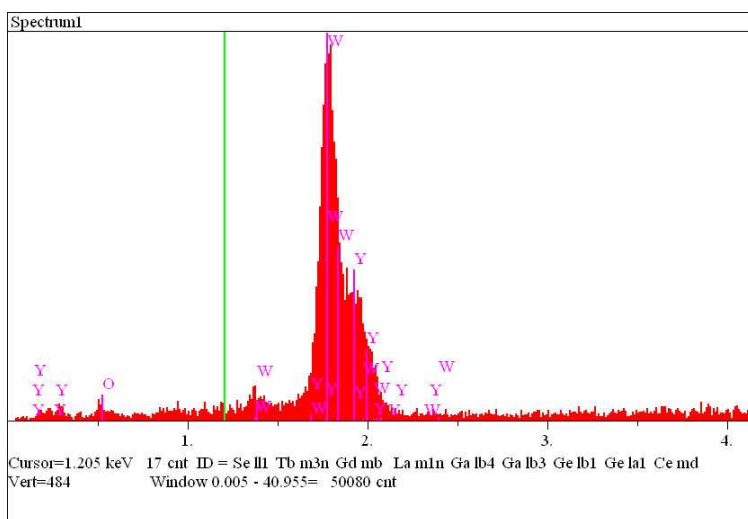
In both figures, 2(a) and 2(b) there are to be observed two kinds of features:
 (1) dark spots, as are those marked – as an example – by 1, 2, 3; these are inclusions containing Y, as was settled by X-EDS analysis of the dark spot #1 in Fig.-2(a); the results of this analysis is given below;
 (2) holes, as those marked by 4, 5, 6; these are pores in the material;

The bulk distribution of pores can be better observed in Fig.-2(b) from below, where the dark spot #1 is better visible. This dark spot is marked also by the contamination grown inside the dark spot area during the on-point analysis by X-EDS.



The X-EDS analysis performed by directing the 40kV electron μ -beam on the dark spot #1 generate the spectrum shown in Fig.-3.

FIGURE-3



The quantification done with this spectrum, by applying the ZAF correction gives the following result:

Y(La): 75.888 ± 4.201 wt%

W(La): 24.412 ± 0.791 wt%

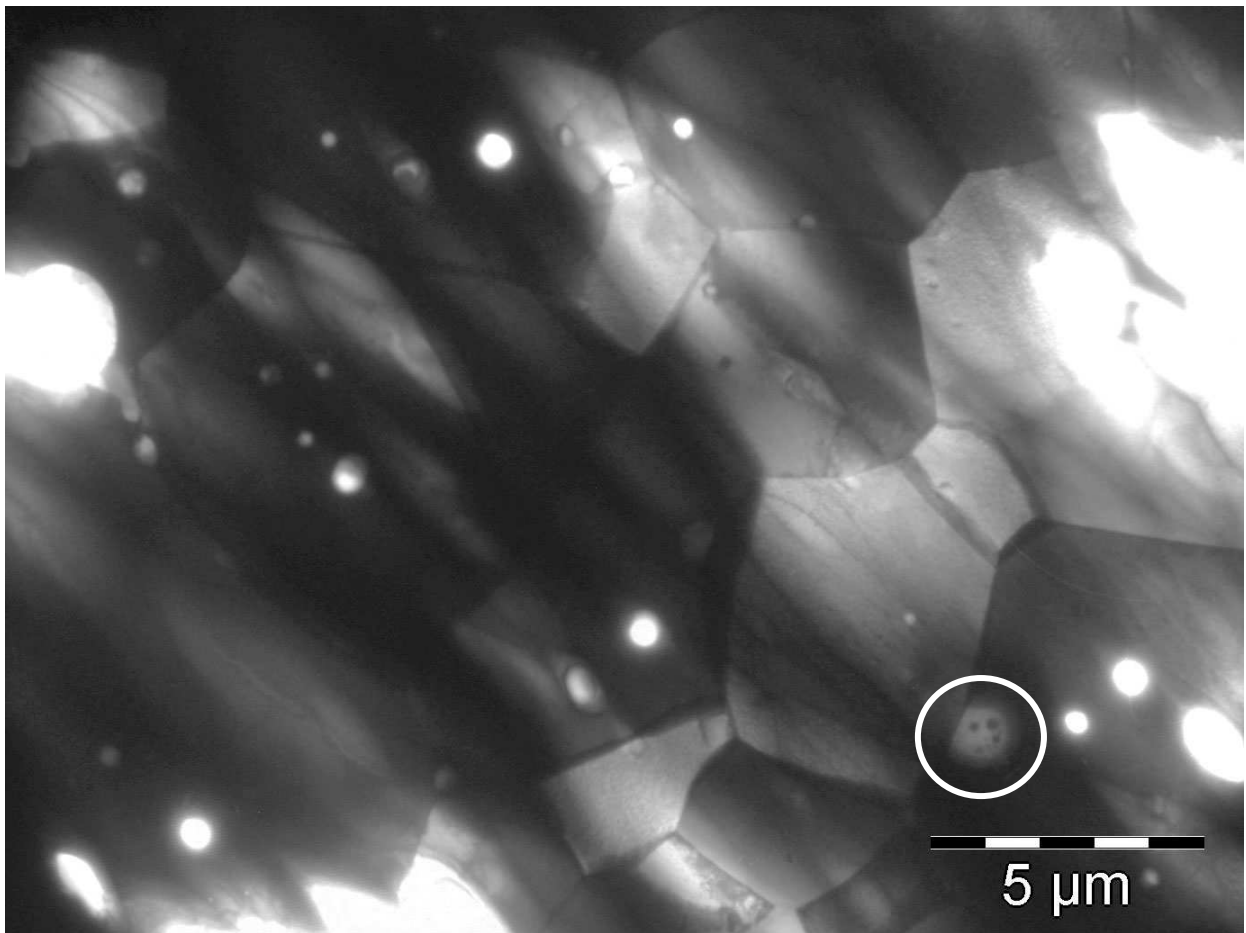
the Oxygen peak being not quantifiable.

When the same analysis is done on the material outside the dark spot #1, the spectrum shows only the presence of W.

We performed X-EDS analysis on many dark spots of the same kind and found similar results. This is the evidence of the fact that the dark spots are originating in Yttria inclusions in the W grains.

Because in Fig.-2 it is hardly visible how the Yttria containing inclusions are distributed among the W grains, we show in Fig.-4 a TEM image in which the W matrix grains are clearly distinguishable.

FIGURE-4

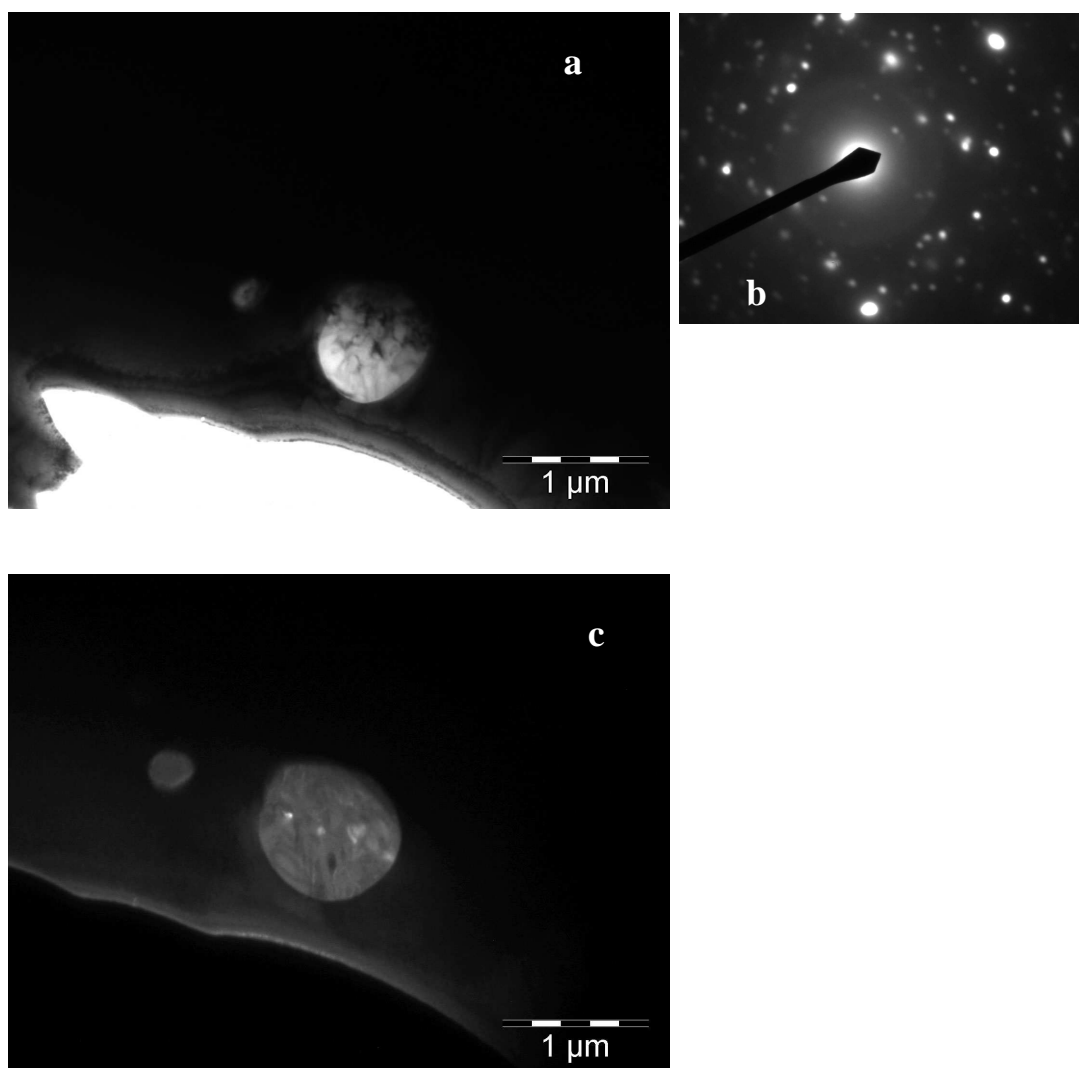


The small round holes observed here are most probably the intersections of pre-existing pores with the thinned sample surface, whereas the small round features looking different than the holes are Yttria inclusions. It was checked by X-EDS analysis of several inclusions that they are always containing Y, whereas in their neighborhood it can be detected only the presence of W.

A seldom observed feature of the W-alloy + 1vol%Y₂O₃ material is the one marked by the white circle in Fig.-4. Its characteristic appearance is (a) high transparency to the electron beam and (b) the presence of very small black inclusions inside this highly transparent material. It can be observed either as a small grain, or as an inclusion inside a W grain. In W-alloy + 5vol%Y₂O₃ such a feature is much more frequently observed.

In order to get an indication of the composition of this kind of feature we have analysed an inclusion showing a similar contrast. The inclusion is shown in Fig.-5(a), along with its SAED pattern in Fig.-5(b) and a dark-field (DF) image of it (Fig.-5c).

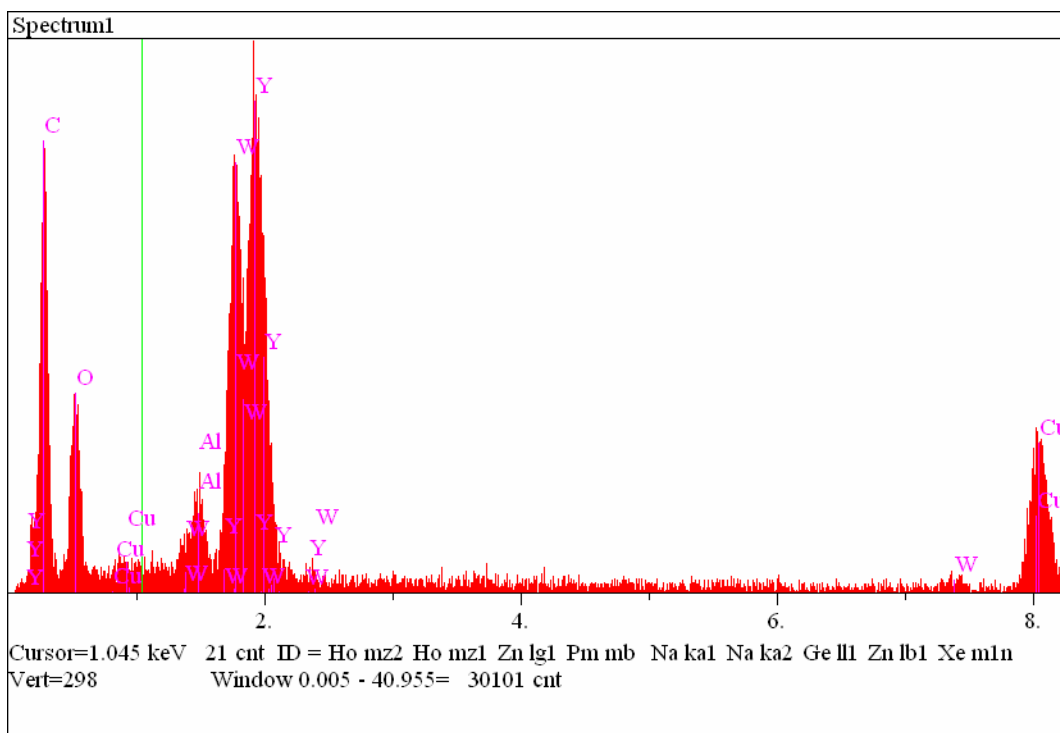
FIGURE-5



The SAED, taken almost exclusively from the inclusion's material, indicates that the content of inclusion is crystalline and consists of several phases. The DF image shows the presence of small crystalline inclusions inside the particle.

By means of the XEDS analysis performed with a μ -beam of electrons directed to the big transparent inclusion shown in Fig.-5 we get the spectrum shown in Fig.-6.

FIGURE-6



The XEDS spectrum quantification indicates the following composition (based on the thin-film approximation, as the inclusion is highly transparent to the electrons):

Y(La): $47,719 \pm 1,902$ wt%
O(Ka): $17,799 \pm 1,232$ wt%
W(La): $34,482 \pm 1,902$ wt%

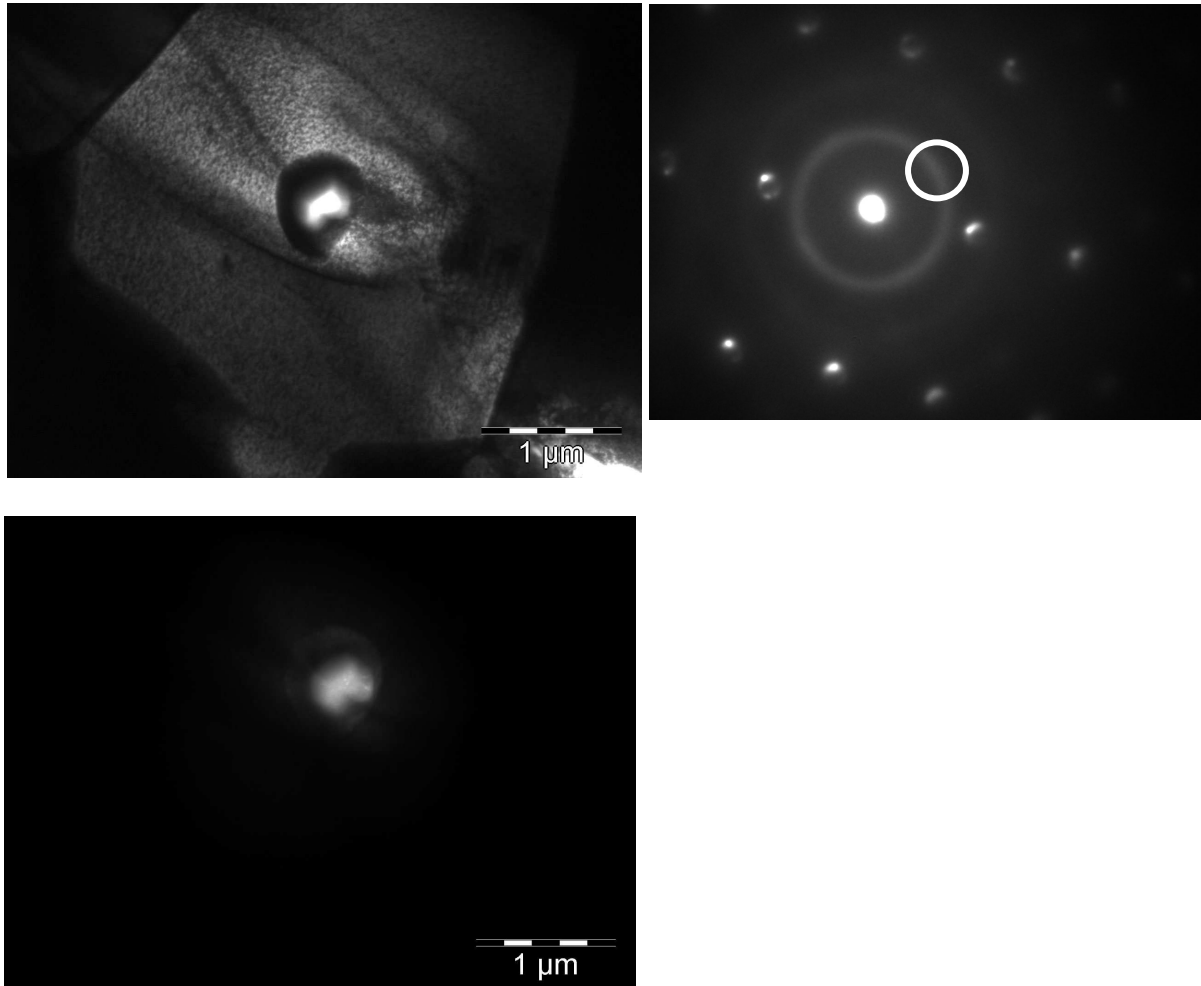
This is an indication that the inclusion contains mainly Yttria, in which there are embedded very small W micro-crystals.

This kind of feature is much more frequently observed in the W-alloy + 5vol% Y₂O₃ and we will show in the frame of the presentation of this material the results of a more detailed X-EDS analysis.

Another observation we made concerning the microstructure of W-alloy + 1vol% Y₂O₃ is that there are inclusions in it containing an amorphous material.

This is shown in Fig.-7, where the dark-field (DF) image taken with the smallest objective lens aperture put on the diffuse ring present in the SAED pattern confirms the presence of an amorphous material inside an inclusion located in a W matrix grain. It was not possible to perform an X-EDS analysis of this amorphous material, so we cannot be sure that it contains Y or anything else.

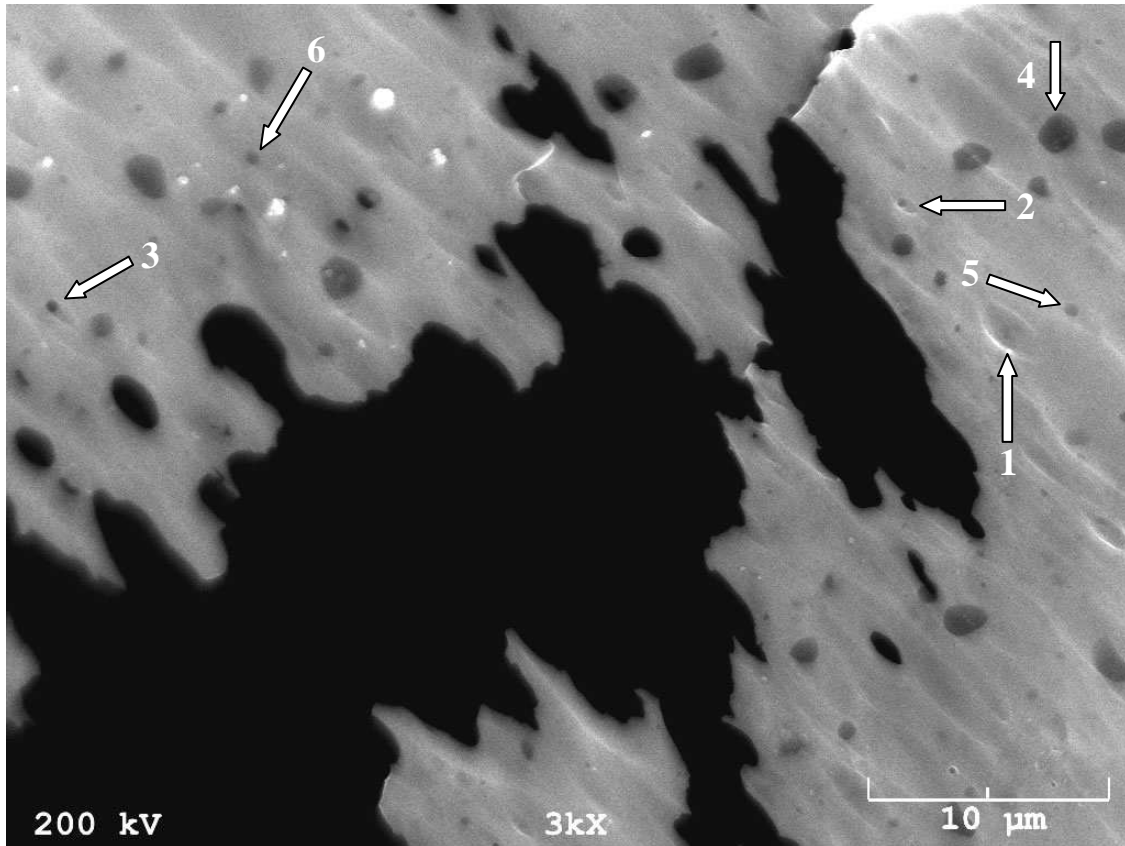
FIGURE-7



The microstructure of the W-alloy + 5vol%Y₂O₃ sample

From Fig.-8 it can be seen that the general aspect of the sample looks similar to that shown in Fig.-2.

FIGURE-8

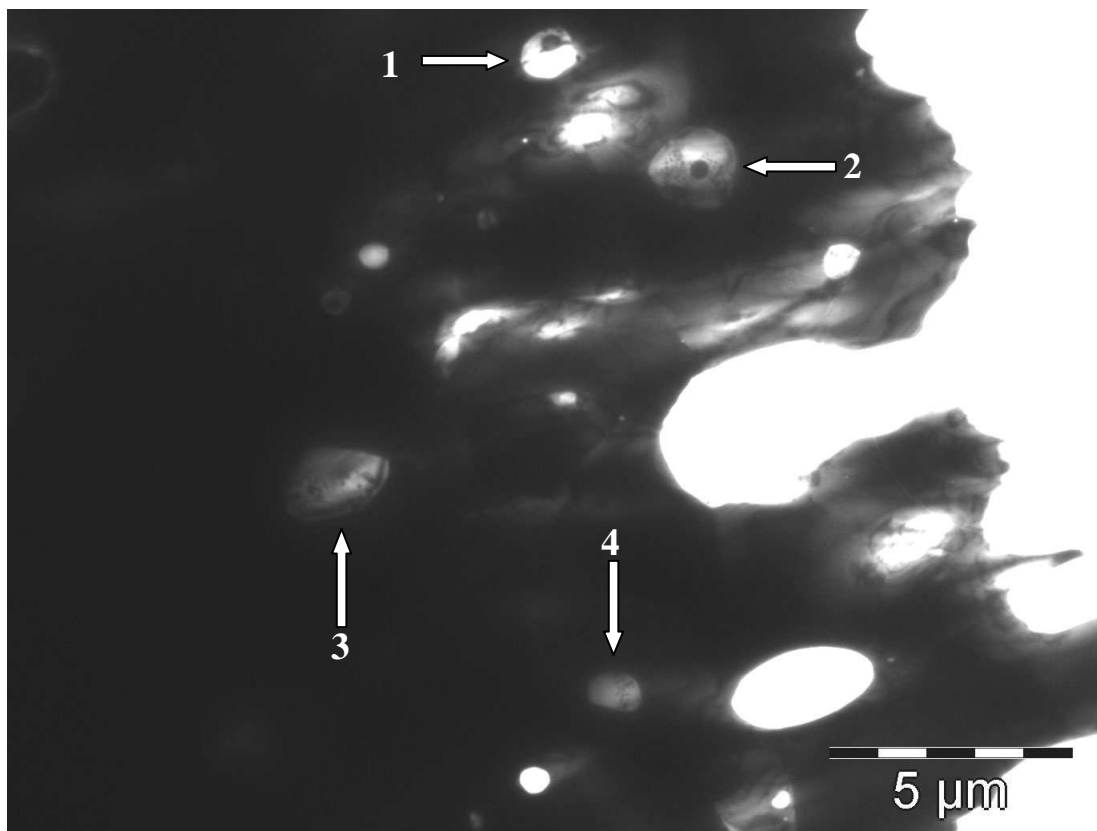


In this figure are to be observed:

- (1) holes, labeled with 1, 2, 3; these should be pre-existing pores in the material;
- (2) dark areas/spots, labeled with 4, 5, 6; these should be inclusions containing Yttria

A feature that cannot be observed in this image, but is very characteristic to the sample, can be clearly seen only in the TEM images like the one shown in Fig.-9 below.

FIGURE-9



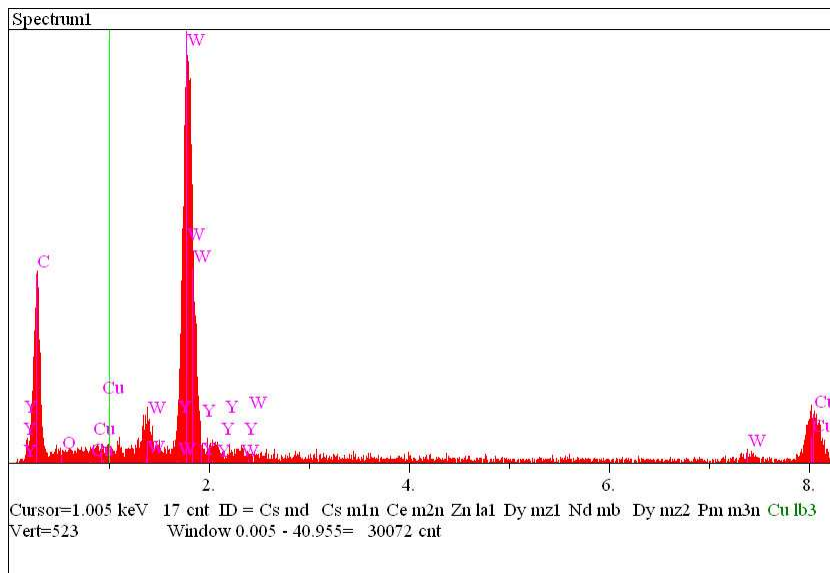
In Fig.-9 can be seen a feature similar to that seldom observed in sample W-alloy + 1vol%Y₂O₃ (see above Fig.-4: the feature marked by a circle and Fig.-5) but which is present everywhere in sample W-alloy + 5vol%Y₂O₃. This feature appears either as an inclusion showing light contrast and containing a single black dot inside (see marks 1 and 2 in Fig.-9), or as an inclusion containing many very fine particles appearing as black dots (see mark-3 in Fig.-9), or as a light inclusion with no black dot inside (see mark 4 in Fig.-9).

The X-EDS microanalysis, performed at 200kV (in order to be sure that the μ -beam of electrons is transmitted through the light inclusion (this is important for the choice of the kind of correction to be chosen for elements quantitation) in such a way that the μ -beam is analyzing only one point (the sample drift will affect that “point” by slightly shifting the e-beam during spectrum acquisition) of the transparent inclusion will reveal that the black dots are W inclusions into the large transparent Yttria inclusions. Some of the results from the many analyses performed by us are shown below.

The X-EDS analysis of inclusion labeled 1 in Fig.-9 was performed both on the visible black dot and on the transparent remaining material observed on the rim

of the hole. The spectrum acquired from the black dot is shown in Fig.-10, together with the elements content quantification.

FIGURE-10



The quantification of the elements content of the black dot gives the following result:

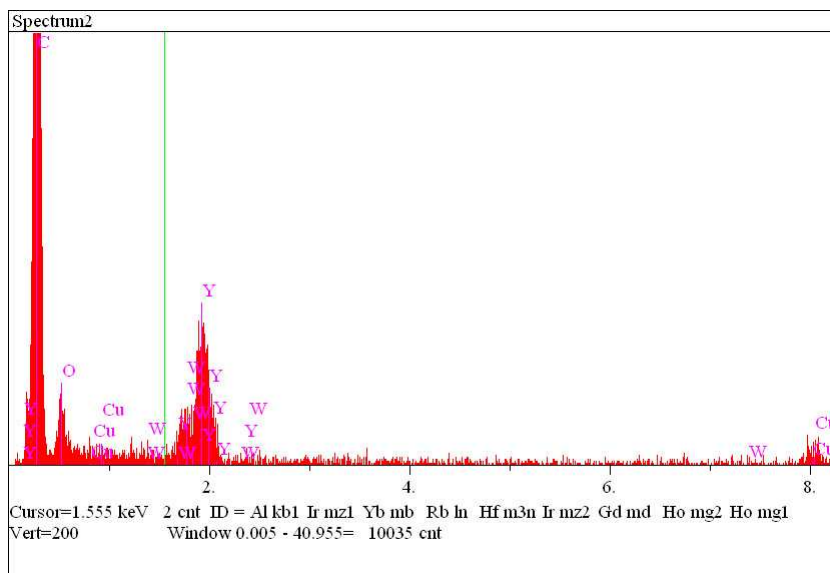
Y(La): 0.935 ± 0.329 wt%

W(La): 98.296 ± 3.972 wt%

O(Ka): 0.769 ± 0.317 wt%

The spectrum acquired from the thin remaining material next to the black dot is shown in Fig.-11, along with the elements content quantification.

FIGURE-11



The quantification of the elements content of the thin material around the hole in inclusion #1 gives the following result:

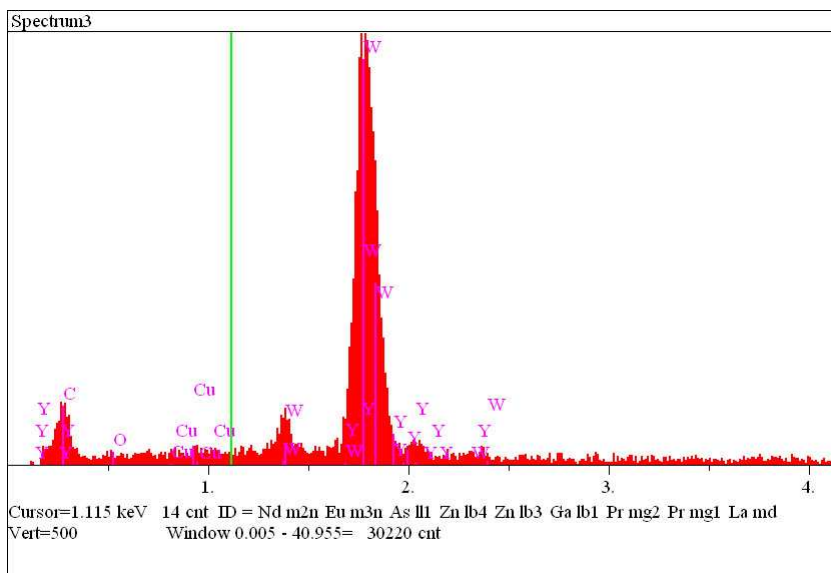
Y(La): 65.416 ± 5.233 wt%

W(La): 10.758 ± 2.497 wt%

O(Ka): 23.826 ± 3.351 wt%

A similar X-EDS analysis performed on the inclusion labeled 2 in Fig.-9 gives the following results: when the black dot is analysed, the acquired spectrum is that shown in Fig.-12, whereas when analysis is done on points outside the black dot, next to it, the acquired spectra are those shown in Fig.-13, 14, 15, 16.

FIGURE-12



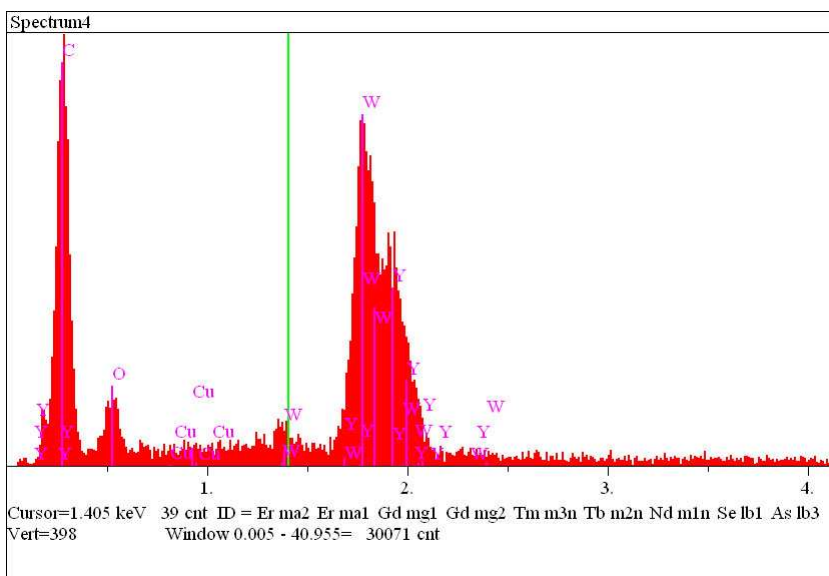
The quantification of the elements content of the black dot present in inclusion #2 gives the following result:

Y(La): 27.421 ± 7.143 wt%

W(La): 72.579 ± 2.719 wt%

O(Ka): 0.000 ± 0.000 wt%

FIGURE-13



Quantification of the elements content measured on a point P2 outside the black central one and close to it

Y(La): 37.987 ± 1.874 wt%

W(La): 50.620 ± 2.545 wt%

O(Ka): 11.393 ± 1.089 wt%

FIGURE-14

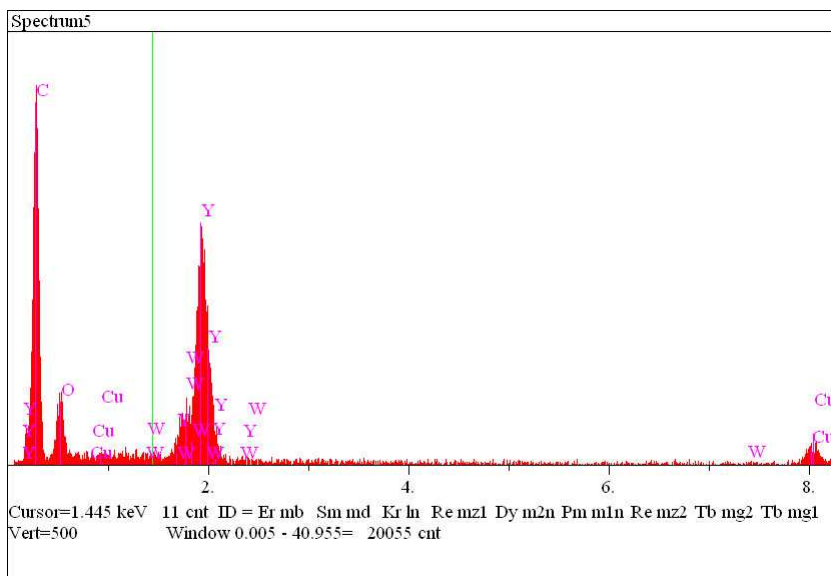


FIGURE-15

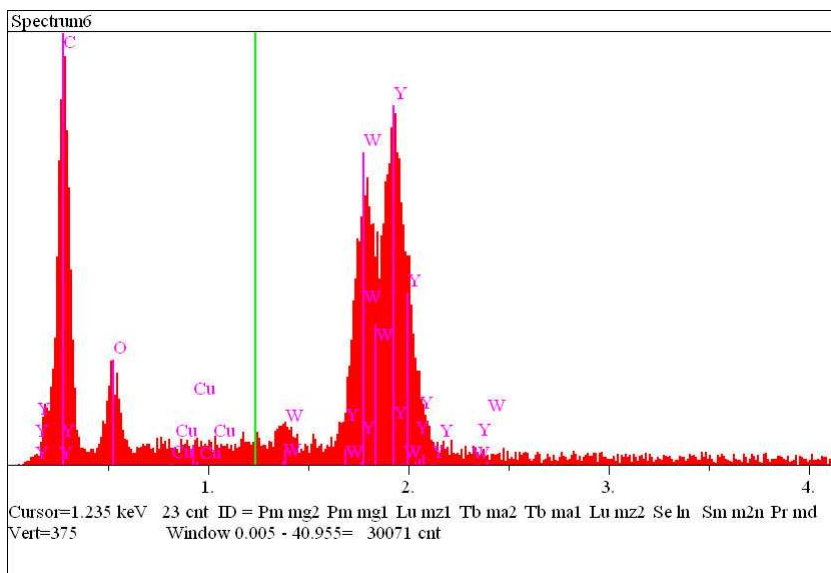
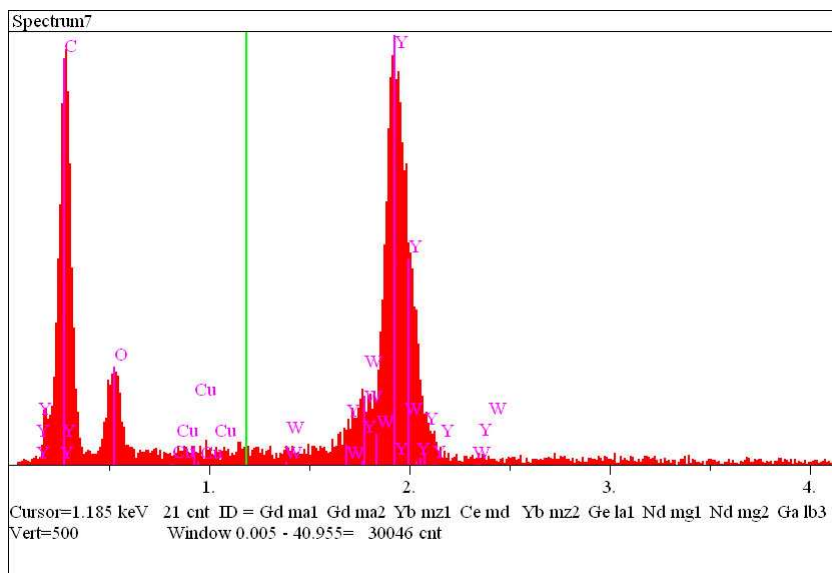


FIGURE-16



Quantification of the elements content measured on another point P5 outside the black central one and close to it

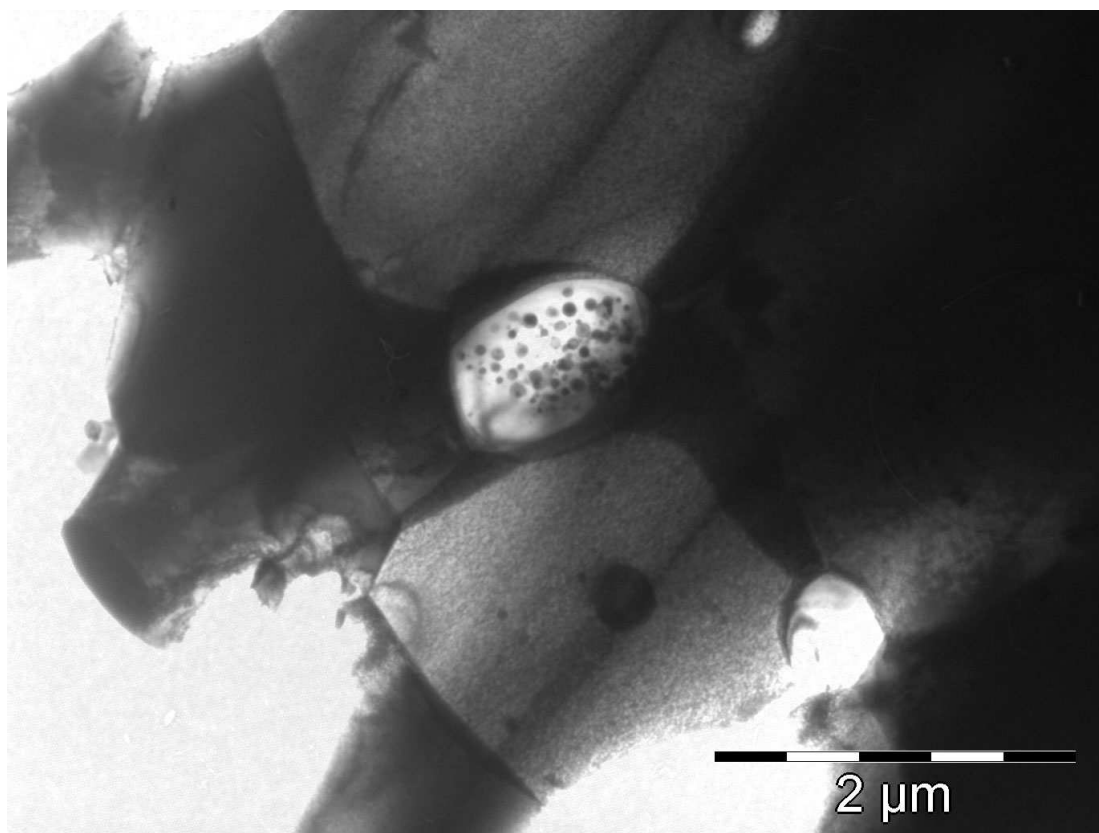
Y(La): 77.265 ± 2.344 wt%

W(La): 6.313 ± 0.788 wt%

O(Ka): 16.423 ± 1.146 wt%

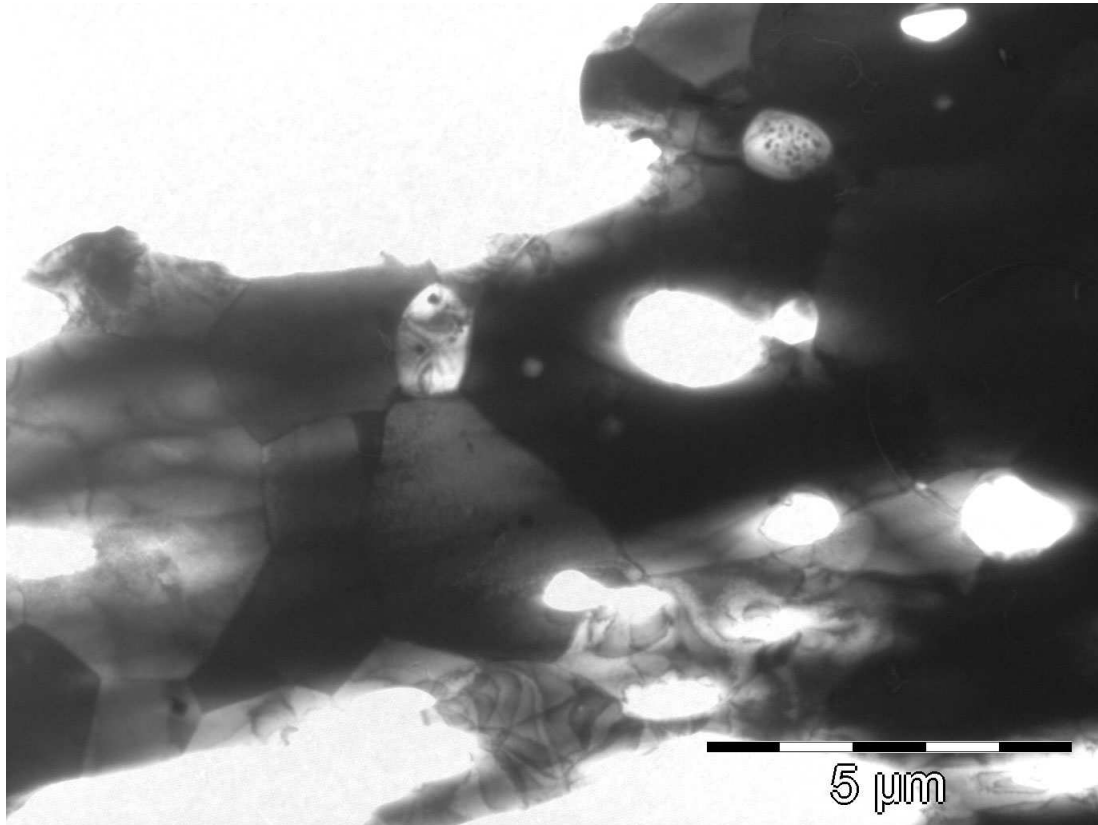
In Fig.-17 it is shown a similar Ytria grain which contains a lot of very small W spherical inclusions. Its relationship to the W matrix grains is clearly visible, showing that the inclusion plays the role of a regular grain of the matrix.

FIGURE-17



The next Fig.-18 shows another Ytria containing W, similar to that shown in Fig.-17 and being located as if it were a regular grain of the W matrix.

FIGURE-18



In our opinion the presence of this kind of grains everywhere inside the material should be considered the main characteristic of the W-alloy + 5vol%Y₂O₃. Their influence on the mechanical properties of the material could be considerable.

CONCLUSIONS

In all three W-alloys reported here, i.e. pure-W-alloy, W-alloy + 1vol% Y₂O₃ and W-alloy + 5vol% Y₂O₃, fabricated by MIM, pores are present everywhere.

In the two ODS W-alloys the strengthening oxide particles are almost uniformly spread inside the material volume, mainly as inclusions in the W grains. W grains containing more than one oxide inclusion are observed everywhere.

In both ODS W-alloys it was put into evidence the existence of a population of large inclusions made of Ytria, most of them containing small spherical particles of W inside. These inclusions are playing both the role of regular grains of the W alloy and of inclusions inside the volume of the regular W-alloy grains. In what concerns the mechanical properties of the ODS W-alloys, we suppose that the existence of those special Ytria grains can play an important role.

Project:

FUNCTIONAL GRADIENT W-STEEL MATERIALS BY UNCONVENTIONAL CO-SINTERING ROUTES

< MAT-WWAlloys-01-01 >

Second stage: July-December 2010:

Process optimization for different W-steel FGM

Report content

- Main lines of the project and scientific content
- Second stage main lines
- Summary of the work performed
- Main scientific and technical results
- Conclusions and future steps
- References
- Summary of the report (Romanian)

Main lines of the project and scientific content

The development of the DEMO fusion reactor is a priority of the EU. In this frame the construction of the reactor structure is a complex and fast evolving domain. This includes joining, machining, fabrication process development, and mock-up testing on the basis of the current He cooled divertor design. Thus identification of fabrication related material issues and implications for tungsten materials development are important. In general, W is going to be used as armor material while Eurofer is going to be used as structural material, with the expectation that ODS steels will replace Eurofer in various parts of the structure in the future. Development of functional gradient materials (FGM) for the transition from W to Eurofer steel, using co-sintering of property gradient alloys with low or reduced activity is a key issue in this work.

The main goal for this year is to realize W-steel FGM. Thus different proportions of W-steel powders should be mixed (and/or mechanical alloyed) by ball milling. About 40 samples with 4 to 10 layers of these powders will be sintered by different routes using unconventional sintering like spark plasma, hot press or microwave. The composition and microstructure of the materials will be evaluated and optimized.

Second stage main lines

In the second stage the sintering process was optimized for different W-steel FGM and the properties of the resulting materials will be analyzed and compared to the requirements of the DEMO design.

Summary of the work performed

In the first stage the process parameters and preparation routes for W-Fe FGM have been obtained experimentally resulting in solid and mechanical consistent samples. We have investigated the influence of layer thickness and compositions as well as the role of different sintering temperatures and pressures. Important results were obtained concerning the effects of different thermal and electrical conductivities of W and Fe in SPS process, the oxygen influence on sintering process and the diffusion of Fe and W in final materials.

In this stage we have optimized the process for W and steel. For these FGM we have produced cylindrical samples with 10 mm diameters and 1-8 mm heights. The samples were realized by spark plasma sintering (SPS) starting with mixtures of steel and W powders in various atomic proportions, placed in up to 9 different layers with thickness from 0.1 to 3 mm. The samples have been sintered at temperatures between 1100 and 1300 C with applied pressures between 60 and 80 MPa in Ar.

We have also tested and obtained concluding proofs concerning the possibility to join steel plates (steel to steel) and W plates (W to W) using the SPS equipment. This is an important step toward future developments since it might be necessary to join FGMs with EFDA designed structural materials at temperatures different (lower) to those required for FGM consolidation.

Finally, we also successfully tested the hot press procedures to consolidate W fibers composites realized by the IPP Garching.

Main scientific and technical results

Sintering of W-steel FGMs

Powder mixtures of W and steel have been obtained by ball milling (in Ar) of the initial powder and have been placed in up to 9 different layers in graphite molds. The materials have been sintered at 1100, 1200 and 1300 C in Ar by SPS. The pressure was applied incremental up 80 MPa. The experiments were carried out aiming to solve 3 main points in the material optimization.

The first point of interest is to determine the optimal temperature for sintering the FGM. Since steel and W have different electrical conductivities, the current going along the sample will increase the temperature depending on the layer particular composition, while the process temperature is determined only at one edge of the sample. Thus it is possible either to melt the steel rich part if there the temperature is higher than expected or to have a poor sintering of the W rich side if there the temperature is lower than expected. We have determined that a process temperature of 1300 C read at the steel rich side of the sample is optimal to achieve a good consolidation in the whole sample without melting the steel. A result of the process is illustrated in figure 1, which shows a SEM picture of the interface between steel 100% and steel 80%-W20% layers.

The second point of interest is related to the porosity of the material. The first tests performed on W-Fe FGM in the first stage have shown that applying the pressure at low temperature and heating the sample afterwards results in a small amount of porosity (about 10%) which decreases when the sintering temperature increases. However, applying pressure during heating further reduces the porosity with final results around 97% densification of the samples.

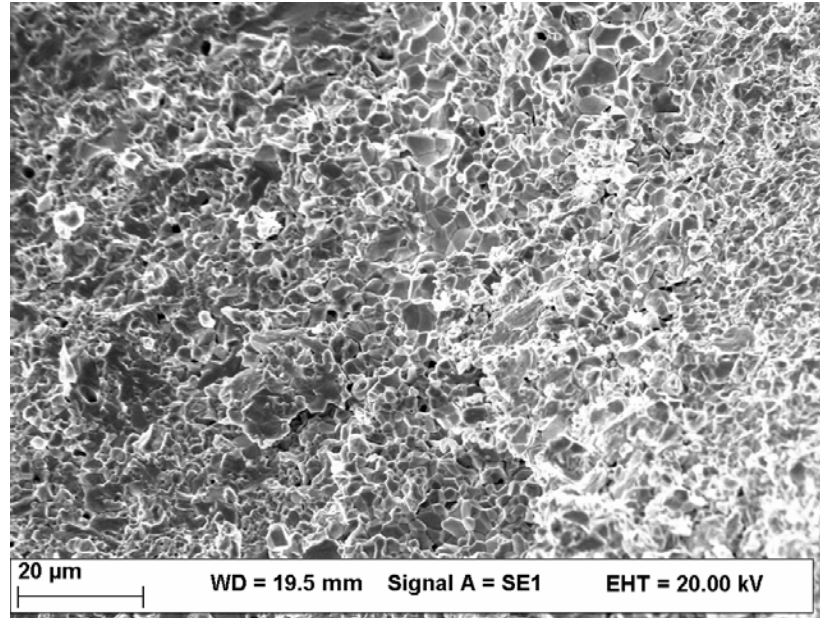


Fig. 1. SEM picture of the interface between steel 100% and steel 80%-W20% layers of a FGM sintered at 1300 C in Ar and pressure up to 75 MPa.

The third main point of interest in the process optimization concerns the realization of a material to a true compositional and morphological gradient in the final material. This can be achieved by increasing the number of layers while decreasing their thickness and taking into account the different diffusion rates of the constituents. Of course, one should keep in mind that a very high number of layers complicates the preparation procedure, especially at industrial scale. Figure 2 compares the morphology of interfaces between layers with different compositions. According to our experimental results, an optimum might be obtained for 8 mm thick sample with 9 layers with composition W:steel of 10:0, 9:1, 8:2, 7:3, 6:4, 4:6, 2:8, 1:9, 0:10 and almost constant increasing of layer thickness toward steel reach end.

Joining steel to steel and W to W plates

Using our SPS equipment we have joined several steel and W plates. The procedure implied connecting plates from the same material (standard industrial steel, or W, or ODS-Germany), applying low pressure (less than 20 MPa) and heating at 400 C/min up to a material dependent maximum, then cooling down to about 75% of this temperature and maintaining it for about 5 minutes. These tests are an important step

toward future developments since it might be necessary to join FGMs with EFDA designed structural materials at temperatures different (lower) to those required for FGM consolidation.

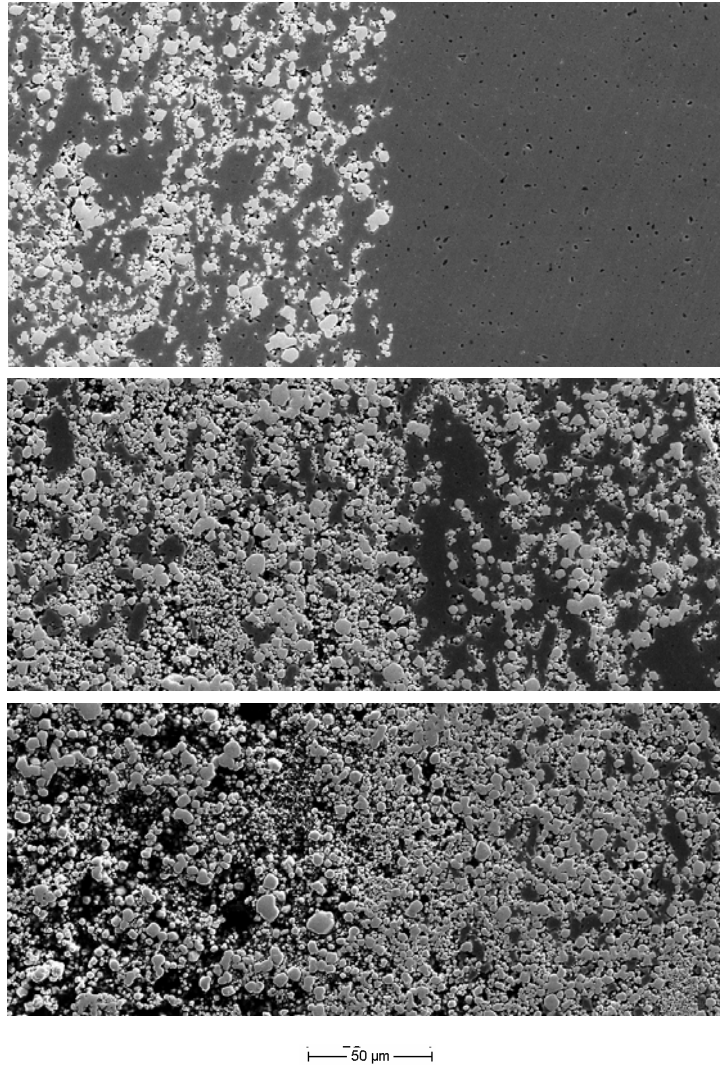


Fig. 2. Comparison of interfaces between layers with different W-steel compositions:
Top W 50% (atomic %) with steel,
Middle: W 75% with W 50%,
Bottom: -.W 70% with W 60%.

Hot pressing fibrous W

In the frame of EFDA cooperation we have also used our equipments to consolidate W fibers composites realized by the IPP Garching. The composites consisted in W fibers, with a W oxide layer and an outer W layer deposited by CVD. The samples have been slowly heated and then slowly pressed up to about 60 MPa. We have obtained a densification of about 10-15%. An optical microscope picture of the consolidated sample is depicted in Figure 3.

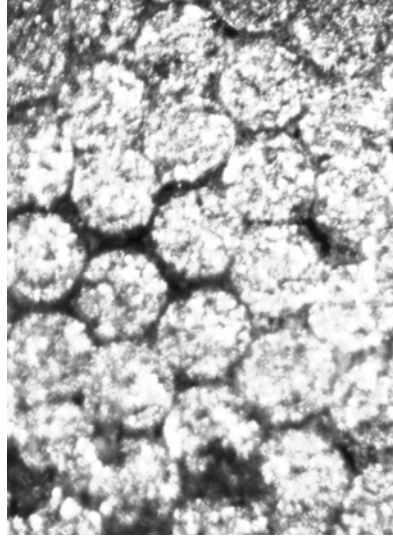


Fig. 3. W fibers (IPP Garching) consolidated by hot pressing at 1450 C.

Conclusions and future steps

The investigation of process parameters and preparation routes for W-steel FGM performed in this stage has led to process optimization. We have produced cylindrical samples with 10 mm diameter and up to 8 mm height by SPS realized from up to 9 different layers. Optimal temperature, pressure and layers composition have been determined. We have also tested and obtained concluding proofs concerning the possibility to join plates (steel to steel, ODS to ODS and W to W) using the SPS equipment. as an important step toward future developments of materials for DEMO. As a next step we propose to optimize the procedure for a direct joint between W-steel FGM and W and (ODSFS) steel using spark plasma and microwave furnaces.

The present results will contribute to the development of material science and advanced materials for DEMO. The information and know-how obtained will be a start point for further work concerning property gradient joint between W-Eurofer by unconventional co-sintering.

References

- R.M. German, Z.A. Munir. Metallurgical Transactions A, **7A** (1976) 1873.
- G. Prahbu, A. Chakraborty, B. Sarma, Int Journal of Refractory Metals & Hard Metals; **27** (2009) 545.
- S. Grasso, Y. Sakka, G Maizza, Sci. Technol. Adv. Mater. **10** (2009) 053001.
- Y. Kawakami, F. Tamai, T. Otsu, K. Takashima, M. Otsu, Solid State Phenomena; **127** (2007) 179.
- H. Wang, Z. Zak Fang, Kyu Sup Hwang, H. Zhang, D. Siddle, Int Journal of Refractory Metals & Hard Metals; **28** (2010) 312.

Report of research activities

Activity 6

In situ TEM observation of dynamics of screw&edge dislocations and He bubbles in alpha-Fe and binary Fe-Cr model-alloys subjected to ion irradiation versus temperature

WP10 MAT-REMEV-06-01/MEdC/BS

I. Preliminary report: first stage

Reporting period: **01 March 2010 to 30 June 2010**

Thematic of the first stage

- 1. Preparation and testing of the specimen preparation for in situ-TEM studies on a-Fe and Fe-Cr samples**

Introduction

As is clearly mentioned in the „ Strategic objectives for fusion materials modelling and experimental validation (2010-2015) (EFDA-D-2D4B78) [1], the lattice defects and especially the extended defects play a fundamental role in the evolution of the microstructure and plasticity processes during irradiation and heating of metallic materials.

High-chromium low activation ferritic-martensitic steels are considered to have the thermal and mechanical properties needed by structural materials in fusion reactors. First step to understand the irradiation defect formation and mobility in steels, in order to compare with the modelling calculations is the study of test pure metals and alloys as a-Fe and Fe-Cr.

The study of the Fe-Cr system is important to understand the precipitates formation which triggers hardening and embrittlement of ferritic/martensitic steels under fission reactor conditions.

In situ TEM study is an important tool for the study of the structural evolution of materials during heating or cooling, especially for the dislocation lattice dynamics observations. The methods for observations of defects and their dynamics in crystalline materials have been developed parallel with the development of the conventional TEM techniques [2-4]. Many of the problems which are important for the EFDA materials are known from similar studies performed for conventional nuclear reactor materials. In the present days, new method are applied for collection of experimental data using TEM technique [5-8]. One of the problems , which become again important for new structural studies, is the gas bubbles formation during irradiation phenomena and dynamics of the irradiation defects in such materials.

Our goal is to perform experimental in situ TEM studies on samples prepared in a frame of the MAT-REMEV project and also on samples prepared in our institute especially in the case of pure α -Fe and pure Fe-Cr alloys.

In situ TEM observations will be performed by variation of the sample temperature between RT and 900°C or from -200°C (LN) to RT , using conventional TEM Bragg contrast method. Preparation of the TEM specimens will be performed by electro-polishing or ion milling process.

Objectives proposed to be fulfilled in the first stage of the study are :

- In situ TEM observations of the dislocations dynamics in α -Fe and binary Fe-Cr alloys model samples by variation of the specimen temperature during TEM observations.
- Presenting and demonstrating our possibilities to collect interesting structural data which can be correlated with the structural modelling works performed in the frame of the MAT-REMEV project.

Experimental

Samples preparation

First step in the Fe and the Fe-Cr alloy sample preparation was performed by ark melting preparation of about 2 grams of Fe (9% Cr) alloy sample. The starting materials was pure (99.995%) Fe rod with 5 mm diameter (from Alfa Aesar) and Cr grains (99,99% from Alfa Aesar)

The samples used in this study were prepared by rapid solidification of the liquid metal in argon atmosphere using a melt spinning method and the following steps. A bulk sample of several grams is introduced in a vertical positioned quartz tube with a capillary at his bottom end. The sample inside the quartz tube is heated in radiofrequency till the melting. The temperature of the melt metal is measured by a pyrometric system. In our case, for the Fe and Fe-Cr alloy preparation, the capillary diameter is 0.5 mm, the heating of the liquid metal is at 1600°C.

Than the metal is melted, a meniscus is formed at the end of the bottom capillary. A low pressure of argon gas (0.28 atm) is applied at the upper end of the quartz tube. The melted metal is evacuated in a laminar way on the surface of the cold copper wheel which is rotated whit high speed. (2000 rot/min) All the system is inside a stainless steel vacuum chamber, which is filled with 1 atm. Pure Ar gas. The melted metal will be rapidly solidified. In the case of iron sample, we obtain ribbon of about 30 to 40 microns in thickness, about 1 mm large and several (5-10) centimetres of uniform length. The surfaces of the metal ribbon are different in morphology, as can be seen in figure1.

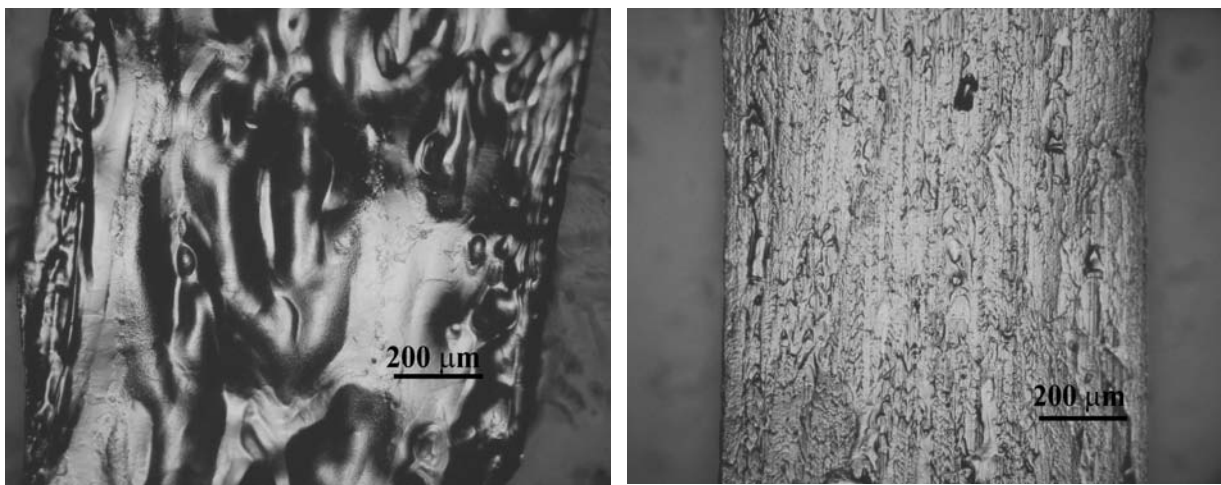


Figure 1. Optical images of the pure Fe ribbon produced by spin melting method. The free surface of the ribbon is smooth but with big variation of relief (right). The ribbon surface in contact with the cold wheel is shown in the left image.

For melt-spinning sample preparation, was used a Buehler Melt Spinner SC version system, designed for laboratory applications, up to approx. 10 g per run. The image of the apparatus and the sample morphology are exposed in Figure 2.

The copper spinning wheel has 200 mm diameter can be rotated with 2000-3000 rot/min. RF power generator is 6kW in a frequency range of 20-150kHz . Spinning wheel have tangential velocity from 3 to 30 m/s. High vacuum chamber can be operated with inert gas at max 1 bar or under vacuum ($<10^{-5}$ mbar). The temperature measurements of the melting area are performed by a pyrometric system.



Figure 2. Melt spinning apparatus used for sample preparation.

Instrumentation

We dispose of a JEOL 200 CX analytical transmission electron microscope provided with equipments and accessories as : SIS-Olympus Keen View - 20 CCD camera for TEM image recording and processing via the iTEM software platform, IXRF EDS 2004 system for the chemical composition analysis, double-tilt specimen holder, single-tilt heating holder, single-tilt straining holder and single-tilt cooling holder.

In terms of TEM specimen preparation, we dispose of the necessary know-how and of a large variety of techniques and equipment allowing us to approach a whole lot of samples, from powders to metallic samples and thin films (plan view and cross-section): crushing, slicing with wire-saw, grinding and polishing for solid samples (Kent and MTI polishing machines), ion milling (Gatan PIPS and Gatan Duo Mill installations), electrochemical thinning (Struers machine).

For this study, the TEM specimen were prepared from small pieces of ribbons which were ion thinned in the Gatan PIPS device.

Results

General view of the samples.

The both examined samples, Fe and Fe-Cr alloy, are similar in their inside morphology regarding the size of the grains and the densities of the defects and subgrainboundaries. A typical image is presented in figure 3.

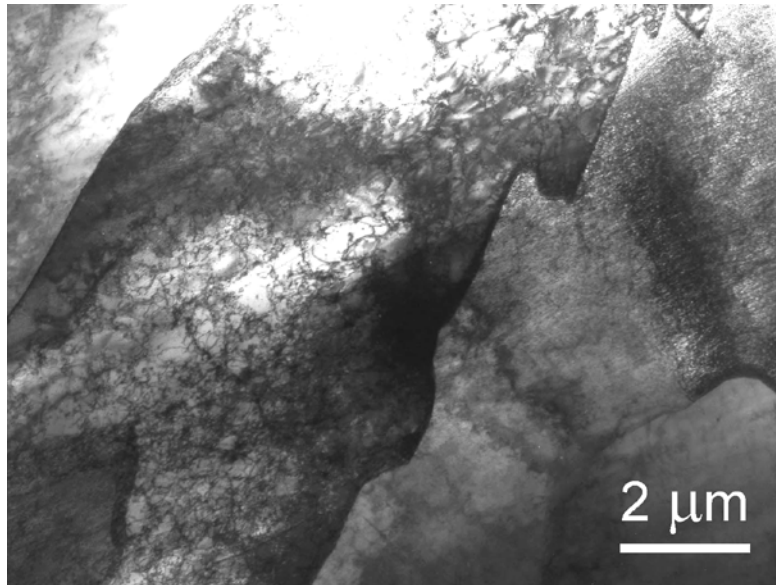


Figure 3. Low magnification image of the thin area in the Fe-Cr specimen

A closer look of the specimen structure reveal the presence of a quite high density of bubbles as can be observed in figure 4. The bubbles are related with the presence of a complicate net of dislocations.

The sizes of these bubbles are mainly between 20 and 30 nm in diameter, but bubbles of 50 or 60 nm are also present. The size distribution for the pure Fe sample is presented in figure 6. The sample annealed at 600°C in vacuum (better than 10^{-5} mBarr) for 30 minutes, show a alignment of the bubbles and an apparently reduced size of the bubbles.(see figure 5)

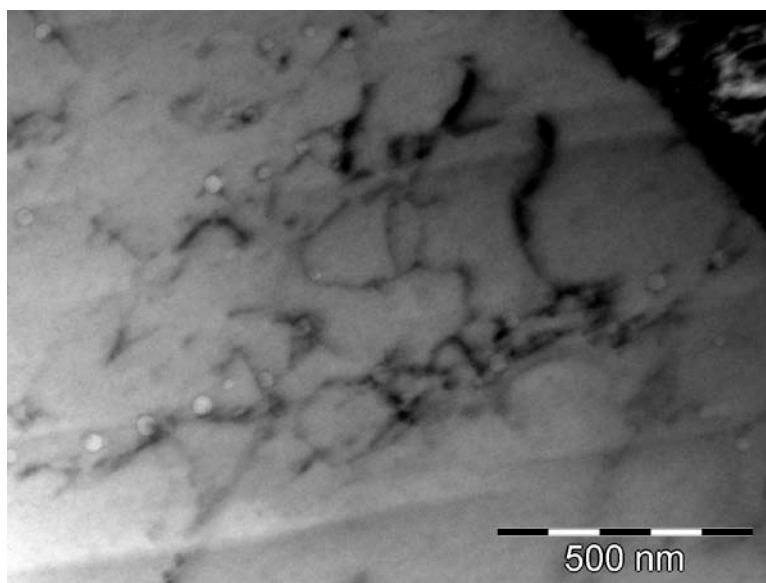


Figure 4. TEM image of the bubbles and the dislocations in the as prepared Fe(Cr 9%) alloy sample

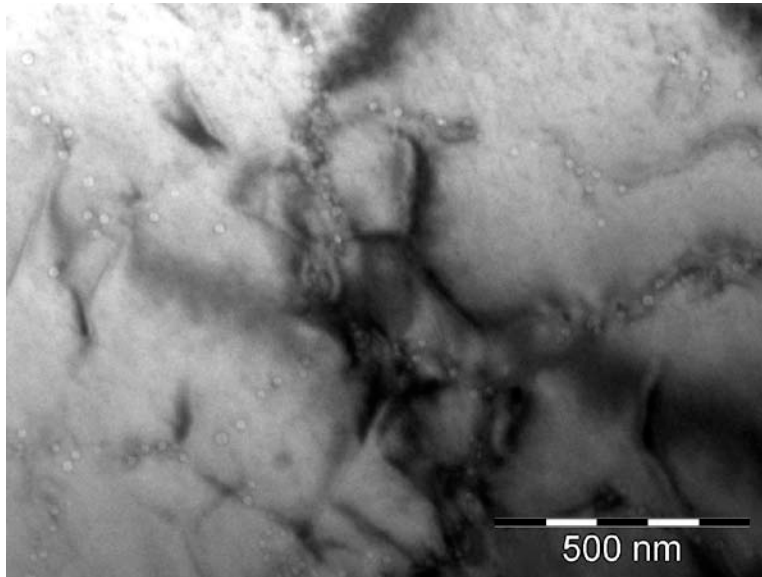


Figure 5. Alignment of the bubbles in the Fe samples which was heated at 600°C for 30 minutes before the ion thinning process. The bubbles net form a cell morphology.

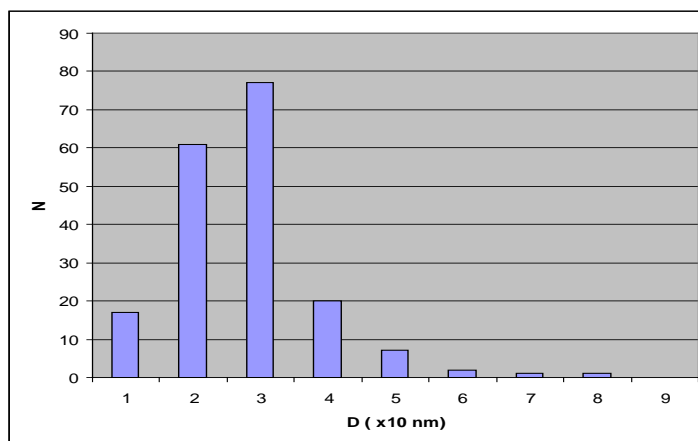


Figure 6. Distribution of the argon bubble size in the a- Fe sample. The size of the bubble remain constant during the temperature growth of the sample in the in situ experiments. The average size is 27.5 nm.

These observed bobbles are generally connected by dislocations, which can be easy put in contrast. Most of them have the same Burgers vectors because the contrast vanishes for majority of these dislocations, by the tilt of the specimen.

The origin of these bubbles is subject of discussions. Generally, similar bubbles are not observed in amorphous and nanostructures allow which are commonly produced by the melt spinning technique. In the case of Fe and Fe-Cr samples, the metal crystallize with high speed on the cold rotating wheel and the size of the crystalline grains are of the order of several (or more) microns. This high speed crystallization process produced a high supersaturation of vacancies, which will precipitated to form voids in the lattice. However, these voids are filled with gas (in our case argon gas) because without gas the voids collapse to form small dislocation loops. The dislocation network, which are combined with the presence of the gas bubbles, are born in the

same process of crystallization. There are very few long dislocation lines, most of them are short and curved.

The identification of the Burgers vectors of some of the dislocation segments in this net, show the presence of strange Burgers vectors [4] as is exemplified in the figure 7.

The but of this in situ TEM study was to observe and record the movement of dislocations in the Fe and Fe-Cr samples. This was performed using the video CCD camera which was set for acquisition of 25 frame per second, during heating of the sample. One example is exposed in the following images.

Video recordings were performed in several places in the both pure Fe and Fe(9%Cr) alloy specimens. The heating holder was heated from RT to 400°C and then to 500°C or 600°C.

The dislocation movements was observed practically only in the Fe specimens. The similar experiments performed in the Fe-Cr specimens, show that in this case the dislocations segments are much more difficult to displace.

In fact, the dislocation movement observed by us are composed in a successive small jump in the dislocation from one place to another, kipping the position in some pinning points.

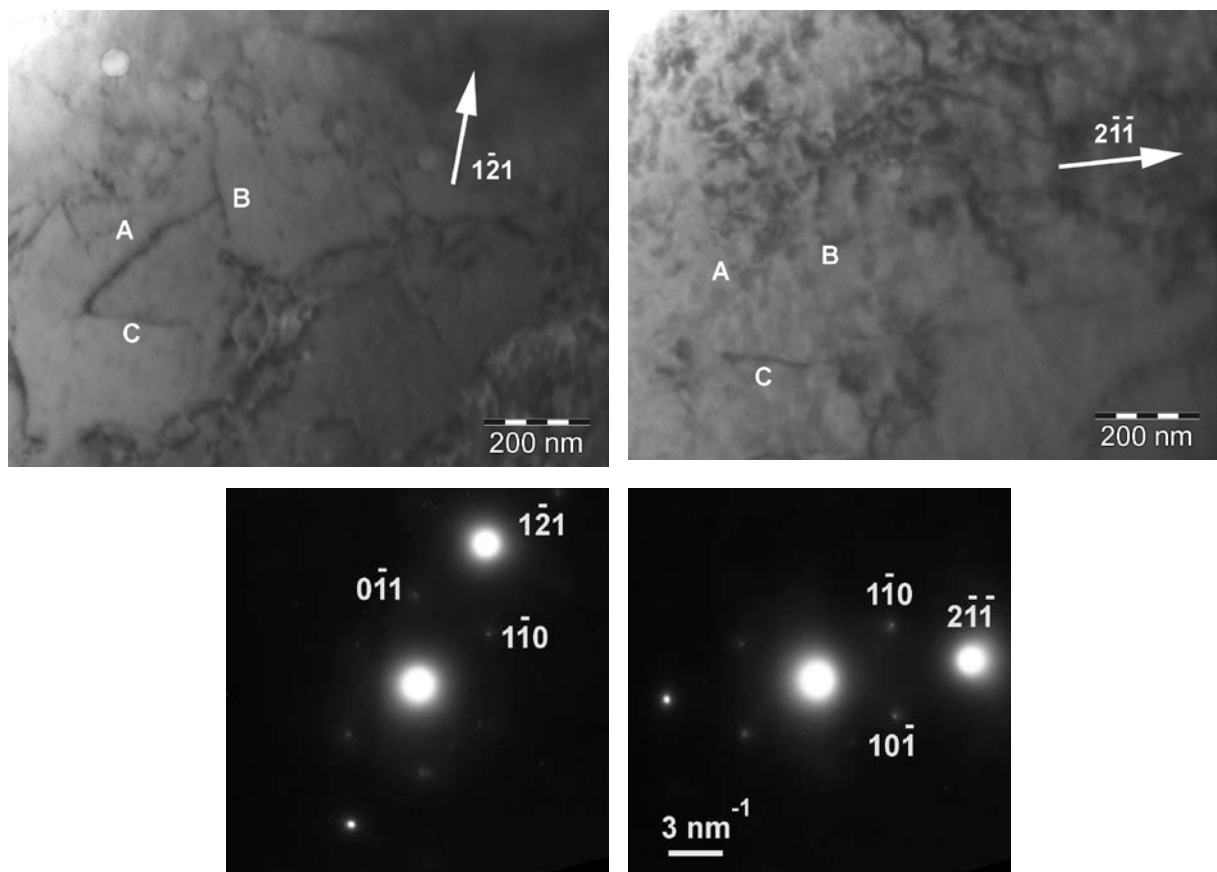


Figure 7. Burges vectors determinations by change of the operating reflection of the Bragg contrast. The crystalline grain is near the $\langle 111 \rangle$ zone axis orientation. In this case the result is compatible with the folowing vectors:

$$\text{dislocation A : } \mathbf{b} = \frac{1}{8} \begin{bmatrix} 0 \\ 1 \\ 1 \end{bmatrix} \quad ; \quad \text{dislocation B : } \mathbf{b} = \frac{1}{8} \begin{bmatrix} 0 \\ 1 \\ 1 \end{bmatrix} \quad ; \quad \text{dislocation C : } \mathbf{b} = \frac{1}{4} \begin{bmatrix} 2 \\ 1 \\ 1 \end{bmatrix}$$

In figure7 presents an example of dissociation of a perfect dislocation into 3 partials on a {110} plane according to relation [1] :

$$\frac{1}{2}[111] \rightarrow \frac{1}{8}[110] + \frac{1}{4}[112] + \frac{1}{8}[110]$$

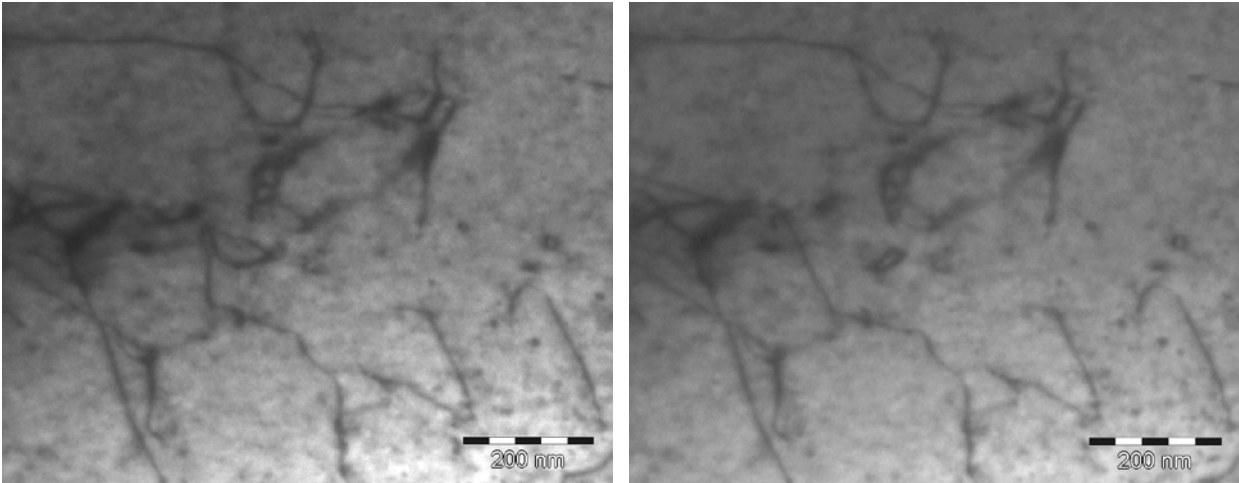


Figure 8. Two images from a sequence after the dislocation movement. (right –frame1, before movement ; left- frame 2, after movement)

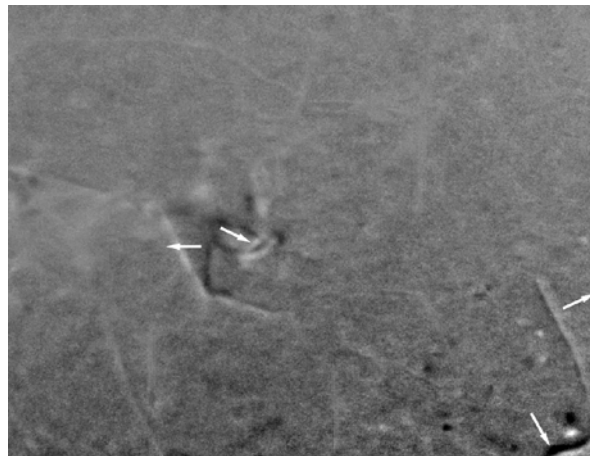


Figure 9. Digital image (frame 1 – frame 2), showing the places where the segments of the dislocation net change the position. (method from references [5,6])

No movements of dislocation connected with the bubbles were observed in both kind of samples, even at higher temperature. Also, no movement of bubbles position was observed. In our experiments, the heating over 500°C temperature produces oxidation of the sample by formation of a polycrystalline FeO phase oxide. Higher temperature can be reach for pure iron specimens in a better vacuum or using carbon layers caps. In such case the temperature of about 800oC can by obtained without oxidation, but with the price of carbon alloying of the sample. The iron bcc-fcc phase transformation can be observed in this way.

Conclusions

- Pure Fe and Fe(9%Cr) model alloy were produced in a form of thin ribbon by using the melt spinning process.
- The models samples were prepared for TEM using the ion thinning method and introduced in the microscope using the heating holder.
- The observations were performed in the range of RT - 400°C and 600°C. Over this temperature, a rapid oxidation of the specimen was observed.
- The model Fe and Fe-Cr alloy samples are crystallized with quite large grains from their fabrication moment. Their inside structure show the presence of a net of complicate dislocation and the presence of a quite high density of gas bubbles with an average diameter of about 30nm.
- The majority of the gas bubbles are interconnected by dislocation lines. These dislocation lines are not mobile during in situ observations.
- The movement of dislocation segments during heating was observed only in Fe specimens.

References

- [1]. J.L.Boutard, M.J.Caturla, S.L.Dudarev, F.Willaime, Strategic objectives for fusion materials modelling and experimental validation (2010-2015) EFDA-D-2D4B78 , Fusion Materials Topical Group, March 2009
- [2]. S.Amelinckx, The direct observations of dislocations, Academic Press, New York, London, 1964
- [3]. P.B.Hirsch, A.Howie, R.B.Nicholson, D.W.Pashley, M.J.Whelan, Electron Microscopy of thin crystals, Butterworths, London, 1965
- [4]. D. Hull, Introduction to dislocations, Pergamon Press, Second Edition ,1975
J.W.Edington, Practical eletron microscopy in materials science, ed. Van Nostrand Reinhold company, New York, 1976
- [5]. D.Caillard „Kinetics of dislocations in pure Fe. Part I. In situ straining experiments at room temperature, Acta Materialia 58(2010) 3493-3503
- [6]. D.Caillard „Kinetics of dislocations in pure Fe. Part II.. In situ straining experiments at low temperature, Acta Materialia 58(2010) 3504-3515
- [7]. A.Arakawa, M.Hatanaka, E.Kuramoto, K.Ono, H.Mori, Changes in the Burgers vector of perfect dislocation loops without contact with the external dislocations, Physical Review Letters, PRL 96, 125506-1 (2006)
- [8]. A.Ramar. P.Spating, R.Schaublin, Analysis of high temperature deformation mechanism in ODS EUROFER97 alloy, Journal of Nuclear Materials 382,(2008) 210-216

II. Report of the second stage

Reporting period: **30 June 2010 to 20 November 2010**

Thematic of the second stage

- 1. TEM study of the He nano-bubbles in pure iron spin melting rubbers**
- 2. Low energy He ions irradiations of pure iron TEM specimens**

Principal Investigator: V.S.Teodorescu

MEdC

National Institute for Materials Physics, Bucharest-Magurele, ROMANIA

Introduction

In the first preliminary report of activities we have reported the presence of Ar gas bubbles in the iron ribbons produced by melt spinning method. By changing the Ar gas with He gas, we have produced iron ribbons with He bubbles in the same apparatus. Helium atoms diffuse very easily in the iron matrix [1] and the density and the size of the helium bubbles appearing in the iron ribbons depends strongly on the crystallization speed and the cooling rate. There are very few data about the cooling rate of the melt spinning process and much less about the crystallization speed; these data must be estimated for each material.

Our work was focused on analyses of the morphology of the dislocations and the helium bubbles in the pure iron ribbons obtained by melt spinning method and the study of their evolution with thermal treatment, in situ and ex situ in the electron microscope by TEM.

Experimental

The ribbons were produced at different rotation speeds of the spinning wheel, using pure (99.995%) Fe bar pieces (from Alpha Aesar). The ribbons are extracted in 1 atm He atmosphere, using an evacuation pressure of 1.3 atm. The Fe samples are heated by induction in a quartz tube in He atmosphere. The liquid Fe temperature is around 1650°C and the meniscus of the liquid can be extracted. A continuous ribbon is formed in the case of 2000 rot/min for a liquid extraction He pressure of 1.3 atm. In this case the surface of the wheel has a radial speed of about 20 m/s. The ribbon remains in contact with the Cu wheel for about 4 – 5 cm, and leaves the wheel surface with a speed equal to the radial wheel speed having a temperature around 700-800 °C, estimated by measurements obtained by using an optical pyrometer.

The Fe liquid column, coming out from the quartz tube nozzle, is spread laterally at the contact with the wheel surface and the ribbon width is about 1.1 mm. The surfaces of the ribbons are not flat. The surface formed at the contact with the wheel surface is quite flat with a high density of small holes or defects morphologically similar to fissures. At this surface, the liquid in contact with the RT copper of the wheel has a cooling rate of about 10^9 - 10^{10} K/s. The solidification and the crystallization is very fast. However, in the ribbon thickness, this cooling rate is lower, and is estimated to be around 10^7 K/s. Figure 1 shows schematically the data related to the ribbon formation in the melt spinning process.

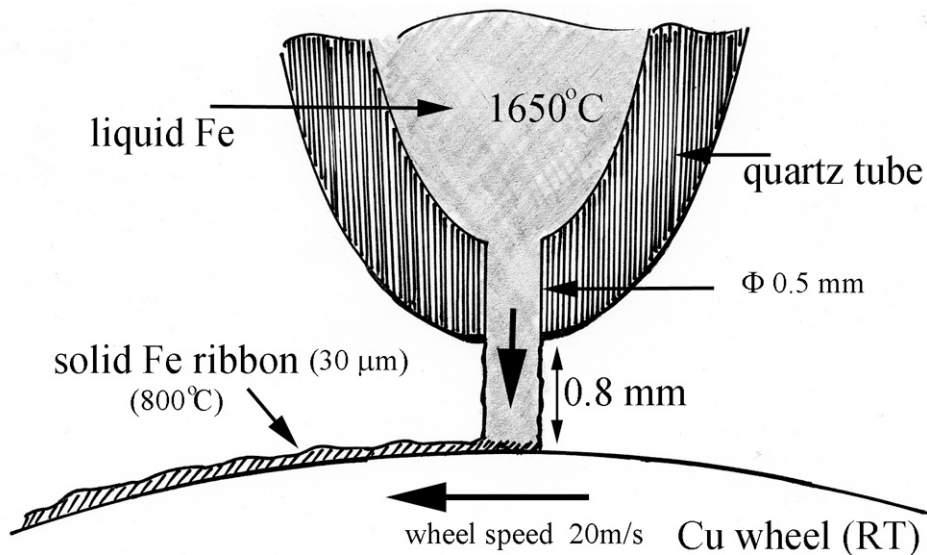


Figure 1. Schematics which shows data of the melt spinning process. The continuum ribbon is obtained if the mass of the liquid evacuated by the nozzle is equal with the mass of the solid ribbons evacuated by the cold copper wheel. This leads to a correlation between the extraction gas pressure and the rotation speed of the cold wheel.

The free surface of the ribbon is much smooth but with quite large relief formed by hills and valleys. Practically is difficult to say what is the ribbon thickness, and our estimation is with an error of about $\pm 5 \mu\text{m}$.

The crystalline grains of the pure iron ribbons are very large, compared with some other metals and allows produced by same method. This means that the solidification speed for iron is very fast. The X ray measurements of the ribbons shows only the bcc phase and a very weak [100] texture which is observed also in the case of TEM observations. (see figure 2)

On the other hand, the local thickness of the ribbons is related with the solidification speed of the iron grain which probably depends of the local crystalline orientation. As the transparent areas in the TEM specimens are positioned manly in the valley of the ribbon, probably the speed of solidification/crystallization with the [100] direction perpendicular to the wheel surface is maximum as number of nucleus but the grow rate in the same direction is a minimum one.

For the same gas extraction pressure, the ribbon thickness depends quite linear by the value of the wheel rotation speed, as revealed by the graphics in figure 3. The rotation speed is related with the cooling rate of the liquid in the ribbon. However, the cooling rate decrease much faster than the wheel rotation. The thickness of the ribbon has a minimum at about 25 mm , which probably depends of the crystallization dynamics features which is not dependent by the wheel speed.

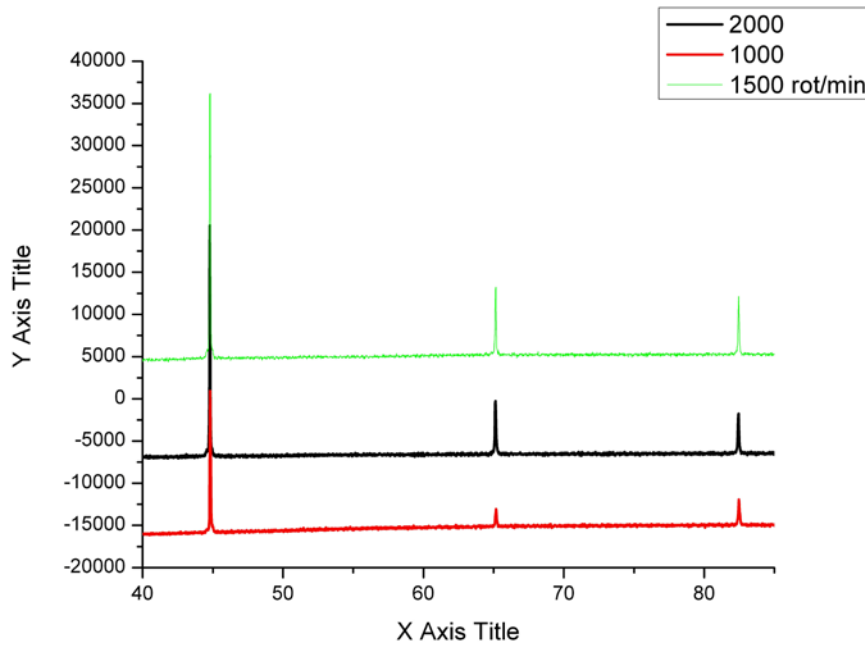


Figure 2. XRD spectra of the Fe ribbons after annealing at 1000°C, showing the presence of bcc phase and a weak [100] texture.

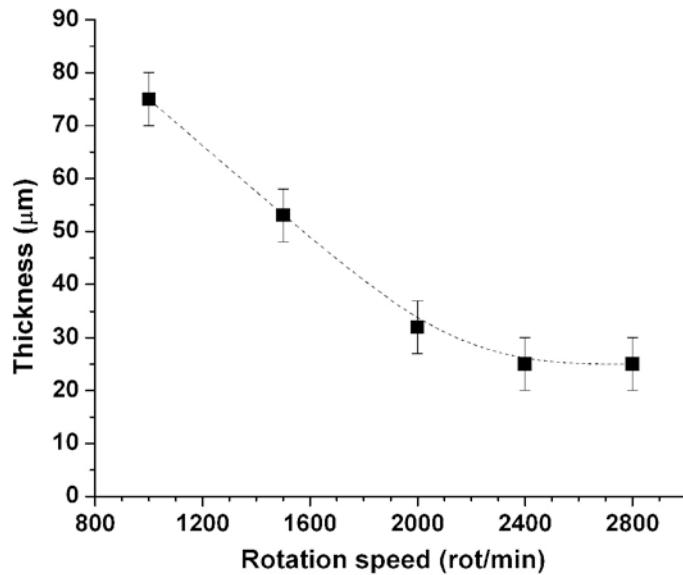


Figure 3. Variation of the thickness of the ribbons extracted using a 1.3 atm of extraction He gas pressure. Only ribbon extracted with 2000rot/min is a really continuum ribbon, the rest are fragmented.

In our first report of the presence of gas bubbles inside the iron ribbons produced by melt spinning, the working gas in the melt spinning apparatus was argon, which is also the normal gas

used for such experiments. Our first TEM specimen preparation from the produced ribbons was performed by using the Gatan PIPS device, which use also argon for the ion guns. It was clear that the bubbles are filled with argon, but not clear than these bubbles were formed.

By using helium instead of argon in the melt-spinning apparatus, the bubbles will be filled with helium. In order to be sure that the bubbles are formed during the cooling process of the ribbons and not during the ion milling process, the TEM specimen were prepared first by electropolishing. In this method, performed at $-2\text{ }^{\circ}\text{C}$ and 20V in a solution of 10% perchloric acid in ethanol, no atoms diffusion is activated in the ribbon, which maintains the initial structure formed by cooling.

However, the results obtained by TEM observation of specimens from the same ribbon sample prepared by ion milling and electropolishing, were very similar and the average size of the He bubbles also. Practically, this demonstrates that the gas bubbles are formed during the cooling stage of the ribbon and the gas insight the bubbles is the gas used in the melt-spinning apparatus.

TEM examinations of the He bubbles in the pure Fe ribbons.

The TEM image Figure 4. presents the He bubbles observed in a ribbons produced at a rotation speed of 2000 rot/min, the continuum one. The images were obtained using low contrast of the matrix, near the $[100]$ orientation. The size distribution is shown in Figure 5.

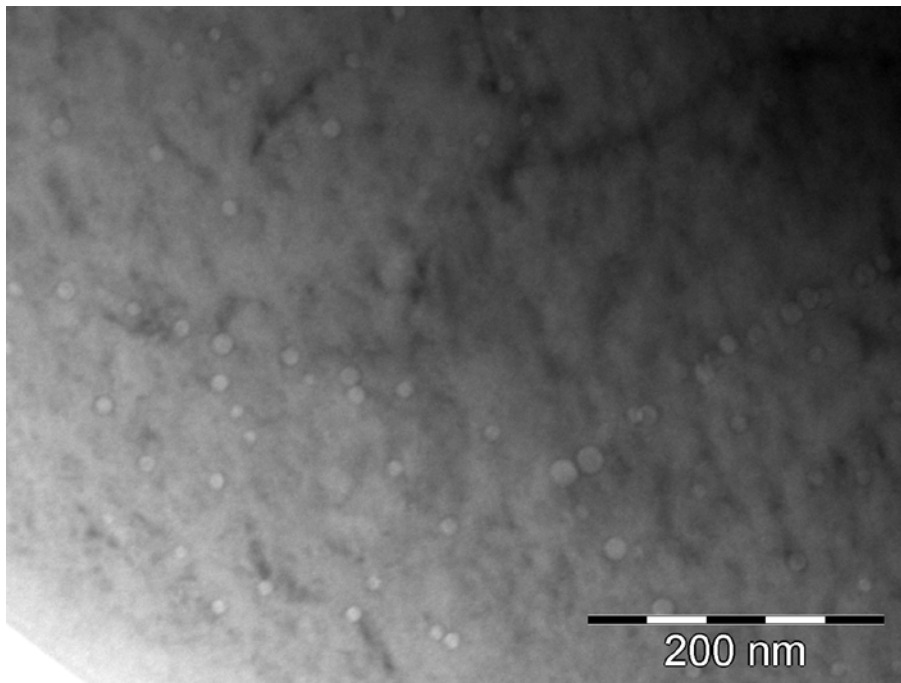


Figure 4 . He gas bubbles in the pure iron sample. The sample orientation is near $[100]$ zone axis.

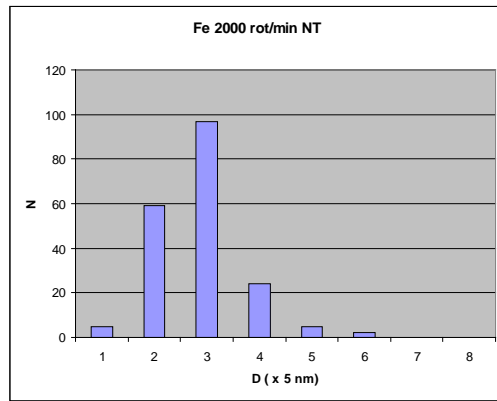


Figure 5. Size distribution of the He bubbles observed in the ribbon produces at 2000rot/min. The size range is between 10 and 30 nm, and the average about 14 nm.

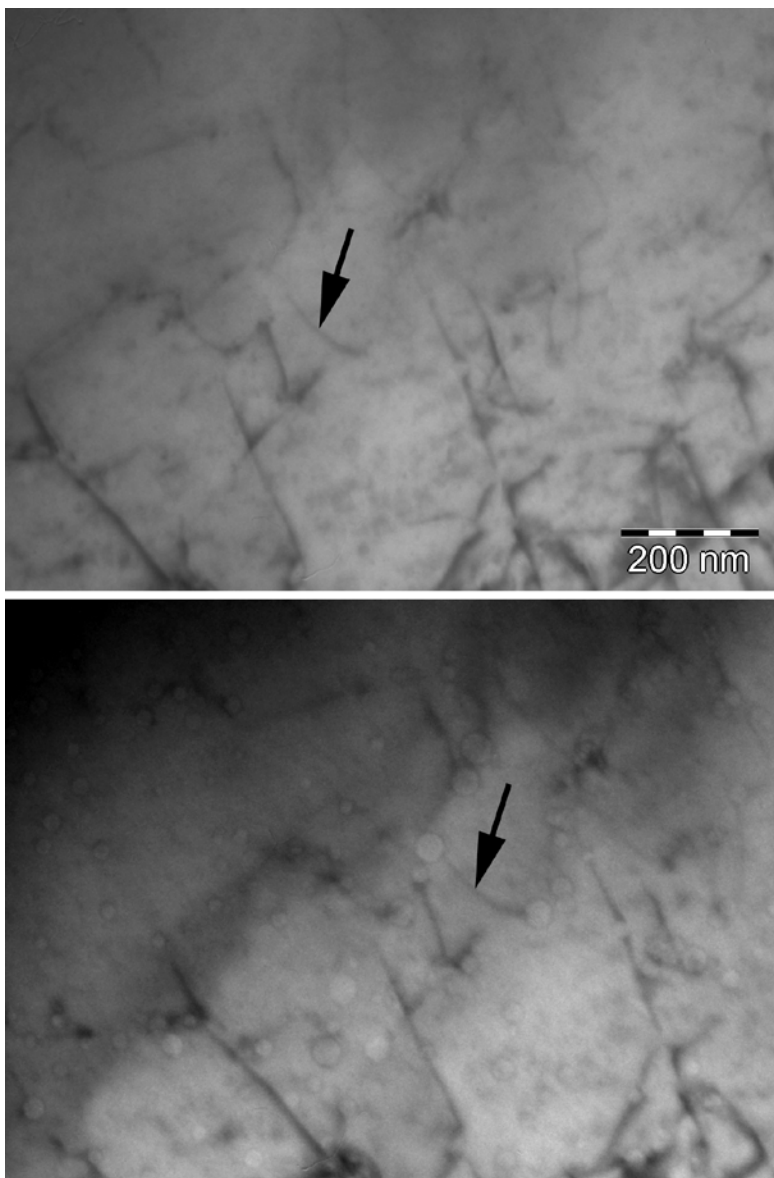


Figure 6. Images of the same area of the sample, the difference is only in focus of the microscope. It is clear that the majority of the dislocation lines connect at least two bubbles.

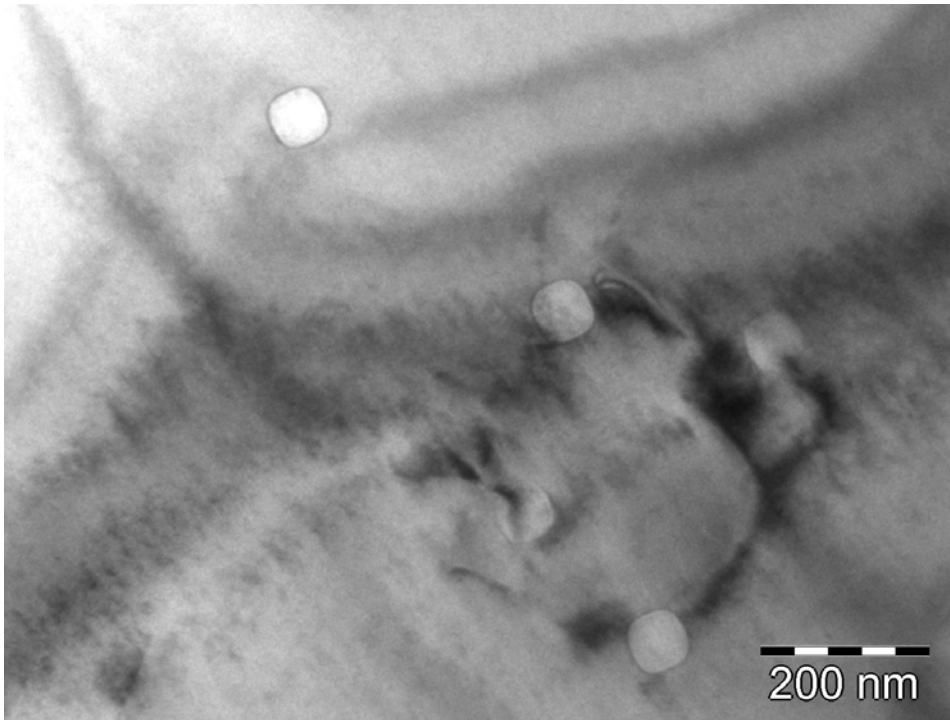


Figure 7 TEM image of the He bubbles in the ribbon extracted with 1000rot/min. The average size of the bubbles is 52 nm, and the shape is faceted. Dislocation lines connect some of these bubbles.

The gas bubbles observed in all the examined ribbons are connected with a network of dislocations (see figures 6 and 7). The dislocations between the bubbles are not straight line, and generally show angular change of direction, probably connected with some pinning points, with a non identified nature.

The majority of the TEM observations were performed in transparent areas with an orientation near the [100] zone axis. All the ribbons show a weak [100] texture and the probability to obtain a thin area in such areas is the more probable.

The in situ TEM observations of the specimens prepared from the ribbons by heating till 500°C in the microscope, do not lead to any clear modification in the bubbles morphology. No moving dislocations were observed. By heating at higher temperature, the specimen oxide rapidly and the observation become not concluding.

He bubbles observed in the annealed ribbons.

The ribbons were also examined by TEM after an annealing at 1000°C for 5 minutes in vacuum. Two reasons lead us to this experiment. First one is to see that happened with the dislocations and the bubbles at higher temperatures, because the TEM prepared from the as produced ribbons cannot be heated more than 500°C without destroying the transparent area. The second reason is connected with the bcc>>fcc phase transition of the iron which take place 910°C.

We have expected that this transition will induced strong modifications in the sample morphology. However, the TEM observations of the ribbons after annealing at 1000°C do not show qualitative modifications for the sample having bubbles. Figure 8 and 9 show the morphology and the size of the bubbles after annealing of the ribbon produced with 2000 rot/min. By annealing, the average size of the bubbles increases from 14 nm to 34 nm, and the density of dislocation look to be lower.

Strong modifications appear in the sample produced with higher rotation speed. Before annealing, practically no bubbles were observed. After annealing, large spherical bubbles appear, connected with a complicate network of dislocations, as can be seen in figure 10.

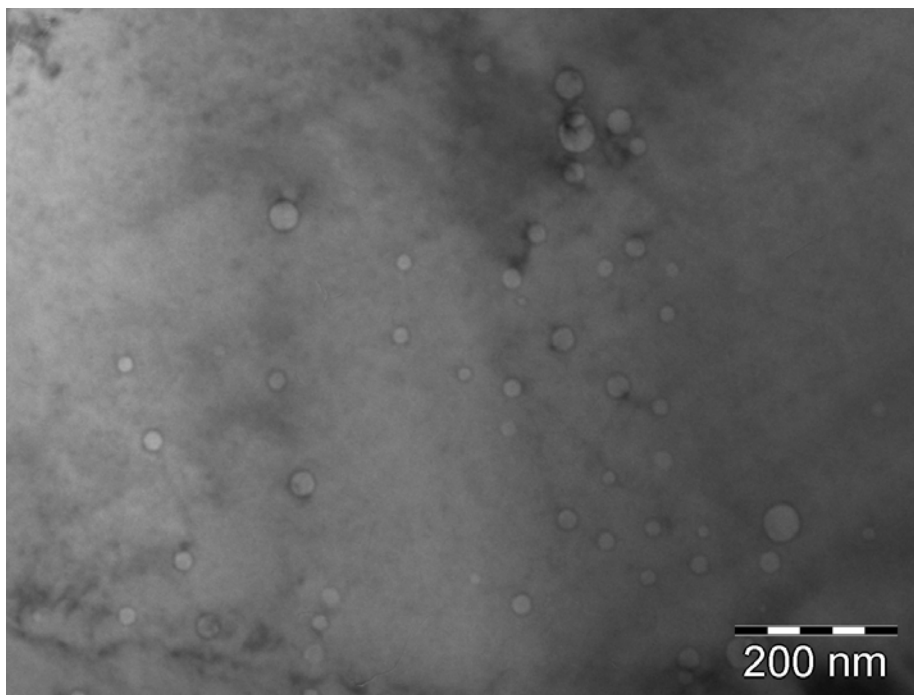


Figure 8 He gas bubbles in the sample I after the thermal annealing at 1000°C. The bubbles bigger than 50 nm have the tendency to become faceted. The sample is observed closed to the {100} direction.

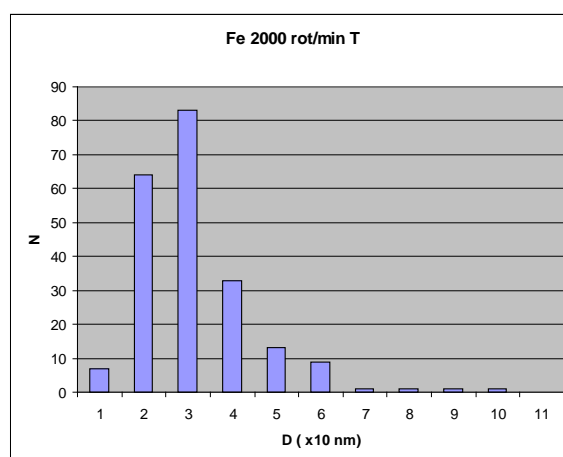


Figure 9 . Size distribution of the He bubbles in the sample I after thermal annealing. The majority of the bubbles are between 20 and 60 nm in size, but some bigger like 100nm can be rarely observed. Average diameter is 34 nm.

Table 1 show synthetically the results obtained from the TEM study analyses of the helium bubbles in the iron ribbons.

The He bubbles become observable if the rotation speed of the wheel is less than 2400rot/min. These mean that there are a maximum value of the cooling rate witch is a threshold value for the bubbles nucleation and grow. If the cooling rate is higher, the He diffusion is stopped and the He bubble cannot be formed. However, the He is presents in the iron lattice and the annealing allow the nucleation and grow of large bubbles (200 nm is size). The TEM contrast of such bubbles (see figure 10) is quite strange and probably a closer look of such defects must be performed in near future.

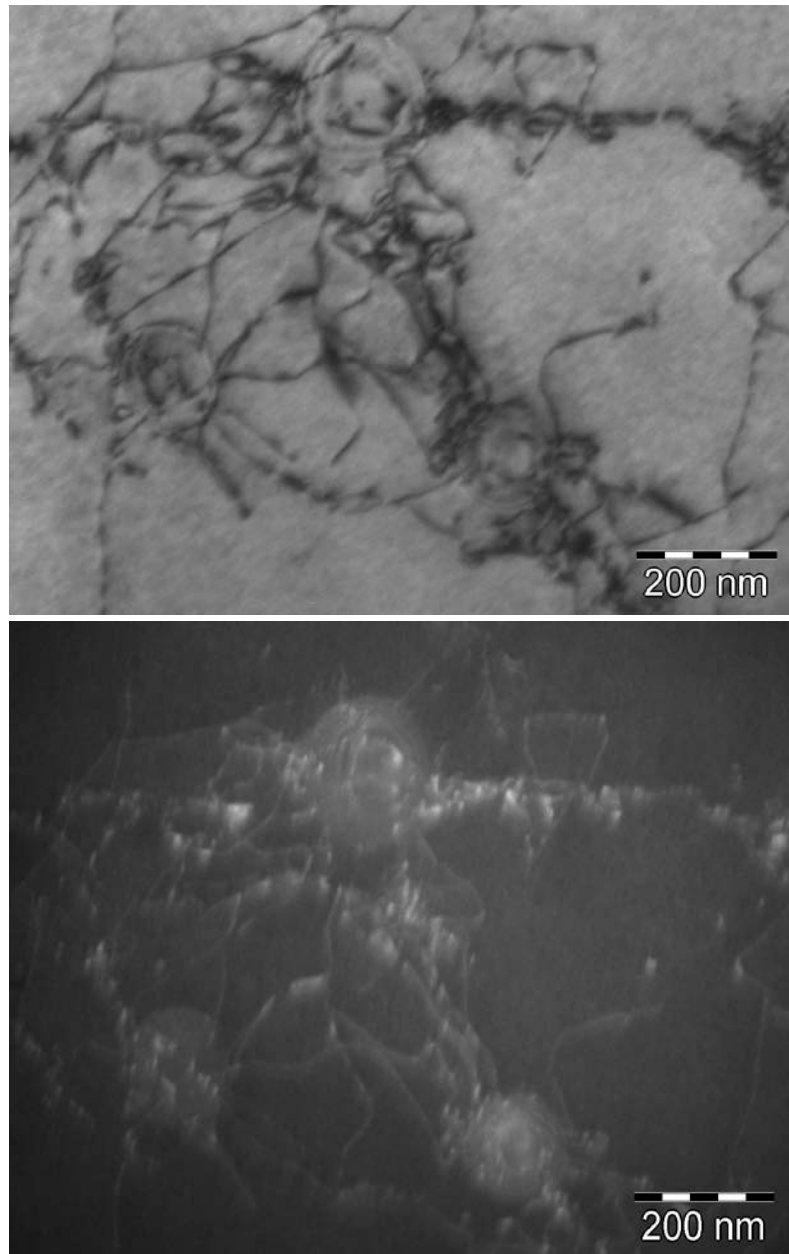


Figure 10. TEM images (bright field –top- and dark field – bottom-) of helium bubbles in the ribbon produced with 2400 rot/min after annealing at 1000°C.

It is also clear that the density of the bubbles is connected with the initial nucleation density. If the cooling rate allows the bubbles formation, the density is high and the average size is small.

The rapid cooling of the ribbons allow us to suppose that the bcc structure of the solidified iron (high temperature bcc delta phase) transform directly in the alpha bcc phase, meaning that the transition $bcc(\delta) \gg fcc(\gamma) \gg bcc(\alpha)$ cannot happened. In this case, a high supersaturation of vacancies appears in the cooling/solidification/ crystallization process. This supersaturation of vacancies must form voids which traps also the helium gas atoms from the iron lattice. Otherwise the empty voids will collapse in dislocation loops.

This means that the helium bubbles in the as produced ribbons are not in equilibrium and can be faceted (like voids) if their size is bigger that 50 nm.

Another effect observed in the ribbons is the alignment of the helium bubbles along dislocation lines. This effect is probably due to the mechanism of bubbles formation, in which dislocation line can act as pipe lines for easy diffusion of the helium atoms in the iron matrix. This effect can also explain the presence of the interconnection between the dislocation network and the bubbles.

Table1. Results on the He bubbles in the pure Fe ribbons

Sample	I	II	III	IV	V
Wheel speed Rot/min	1000	1500	2000	2400	2800
Ribbon thickness (+/- 5 μm)	75	55	35	25	25
Average size of the He bubbles in the Fe ribbon (nm)	52	25	14	Practically no observed He bubbles	Practically no observed He bubbles
Average size of the He bubbles in the Fe ribbon after annealing at 1000°C (nm)	200	-	34	200	-

References

1. Atomistic studies of helium defects properties in bcc iron: comparison of He-Fe potentials, D.M.Stewart, Yu.N.Osetsky, R.E.Stoller, S.I.Golubov, T.Seletskaiia, P.J.Kamenski, *Phylosophical magazine*, 90(7-8)935-944(2010)

Main conclusions of the work

Thin Fe ribbon were produced by melt spinning method using helium as working gas, starting with pure iron bar (99.995% Alfa Aesar) material. The TEM specimens were prepared for using the ion thinning method (Gatan PIPS) and electropolishing method (Struers) using perchloric acid (10%) in alcohol etilic at low temperature (-2 °C).

The TEM observations, performed at RT, have show the presence of helium bubbles. The differences in the bubbles size distribution observed in the ion thinning and electropolishing specimens are not significant, meaning that the bubbles are not formed during the ion thinning process.

The structure of the pure Fe ribbons was studied also at RT, but after annealing at 1000 °C in vacuum. The vacuum annealing was performed in order to transform the iron structure into the FCC (gamma iron) The size distribution of the He nano-bubbles was measured for a large range of ribbons produced in different conditions of the rotation speed of the spinning wheel.

The majority of the gas bubbles are interconnected by dislocation lines. These dislocation lines are not mobile during TEM observations or in situ TEM heating observations.

The alignment of the bubbles along the dislocation lines suggests that the bubbles nucleation and grow process is assisted by the presence of dislocations, which act like pipe lines for easy diffusion of helium atoms in the iron matrix

Low energy He ions irradiations of pure iron TEM specimens

The iron TEM specimens were prepared by mechanical thinning and electro-polishing starting from a 5 mm pure iron rod from Alfa Aesar (99.995%). As the structure of the rod has small grains, the TEM specimens were prepared also from samples which were annealed in vacuum at 1050°C for 5 minutes and slowly cooled down in about 30 minutes. After this treatment, the TEM specimens prepared from these annealed samples show larger grains with a low density of dislocations, clean surfaces and straight edges.

A TEM image of dislocations is exposed in figure 1

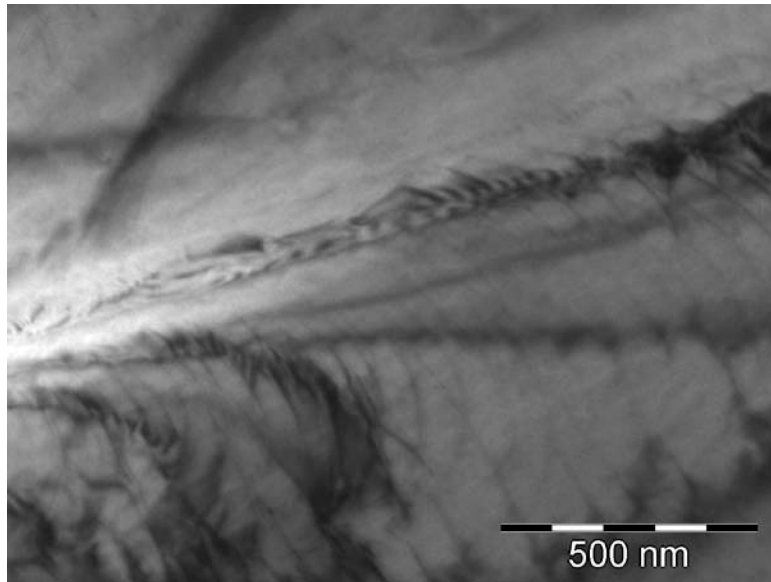


Figure 1. Pile up of dislocations in a grain near a source in pure iron specimen.

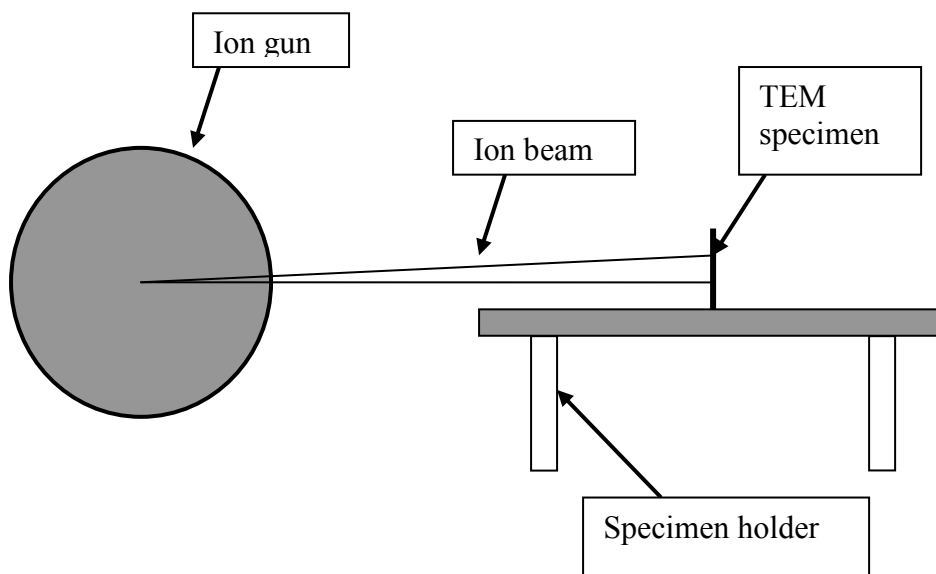


Figure 2. The He ions irradiation geometry in the Gatan Duo Mill apparatus

The He ions irradiations were performed using a modified Gatan Duo Miil apparatus working with helium gas. The specimen holder was modified to allow perpendicular irradiation. The already observed TEM specimen of pure iron annealed sample was placed in the Gatan apparatus and irradiated one side with 10keV ions with a total fluence of about 10^{16} ions/cm² in about 1000 seconds. The ion fluence was estimated using the specimen current data and the expected geometry of the irradiation geometry.

A sketch of the irradiation geometry is presented in figure 2.

The irradiated TEM specimen was observed just after irradiation. No structural modifications were observed in the bulk of the specimen. No He bubbles formation was observed in the specimen. However, the images are covered with a noisy contrast coming from the specimen surface. A focus variation of the TEM image is shown in figure 3 revealing this contrast feature.

This surface contrast reveals the nano-relief formation on the irradiated specimen surface. This relief is also revealed by the modification of the straight edges which become very accidented and with some nano-holes as exposed in figure 4.

The ion irradiation were performed in a quite short time (about 1000 seconds), but the specimen was already oxidized. The estimated oxygen partial pressure in the Gatan is about 10^{-7} torr, which limit the total irradiation time, even in the condition that a part of the oxide is sputtered by the ions.

The SEM observations of the TEM specimen on both irradiated and nonirradiated faces do not show clear differences. However, the AFM examination reveals significant differences. Figures 5 and 6 show the AFM images of the irradiated and the non-irradiated faces of the TEM specimen. The non irradiated surface show a relief with quite large oscillations extended of about one micrometer wavelength. In the case of the irradiated surface, this relief becomes much more dense, having oscillation extended of about 50 nm. The amplitude of this dense relief is about 10 nm. This relief formed by a succession of random distribution of round nano-hills and nano-valley in the source of the noisy contrast observed in TEM (see figure 4).

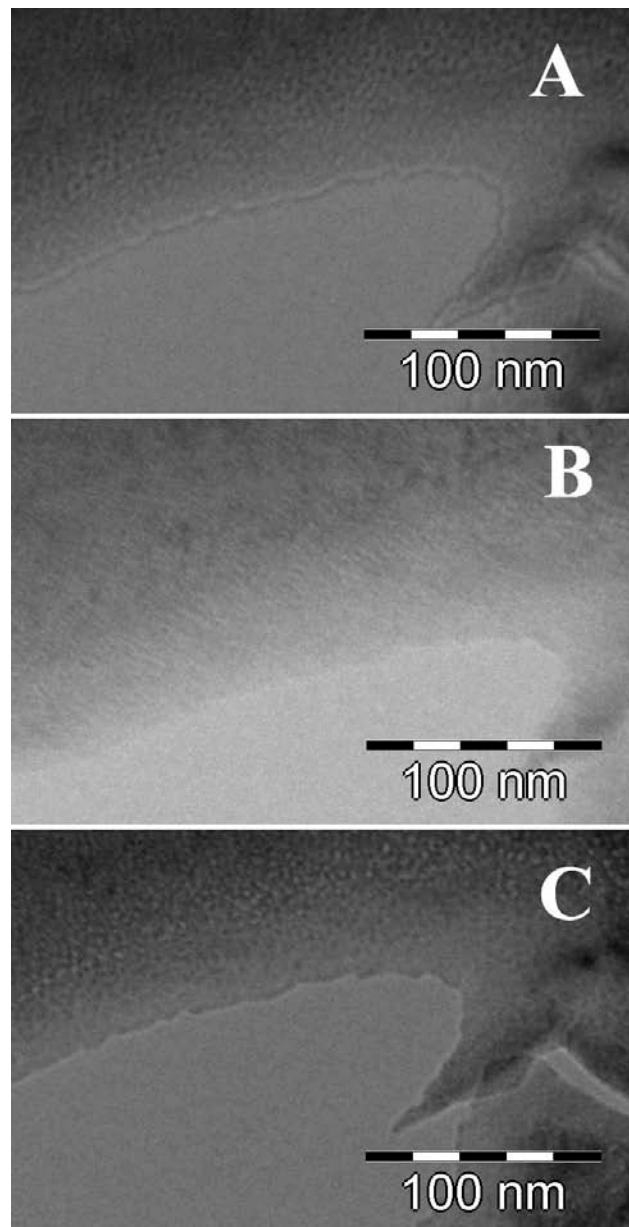


Figure 3. TEM images of the pure iron irradiated specimen in different focus positions: A – over focus, B- focus , C - under focus

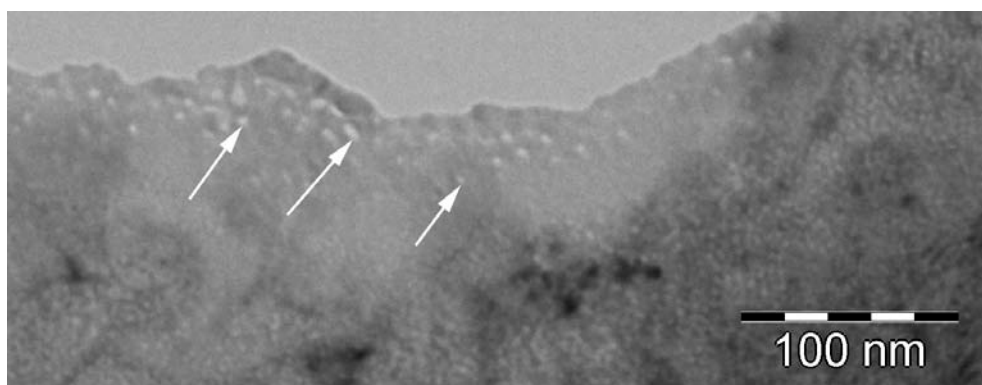


Figure 4. The modified edges of the TEM specimen after ion irradiation.

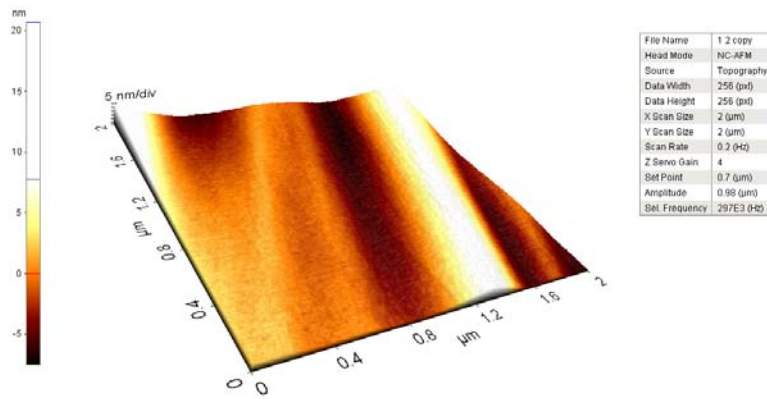


Figure 5 . AFM image of the non-irradiated surface of the TEM specimen.

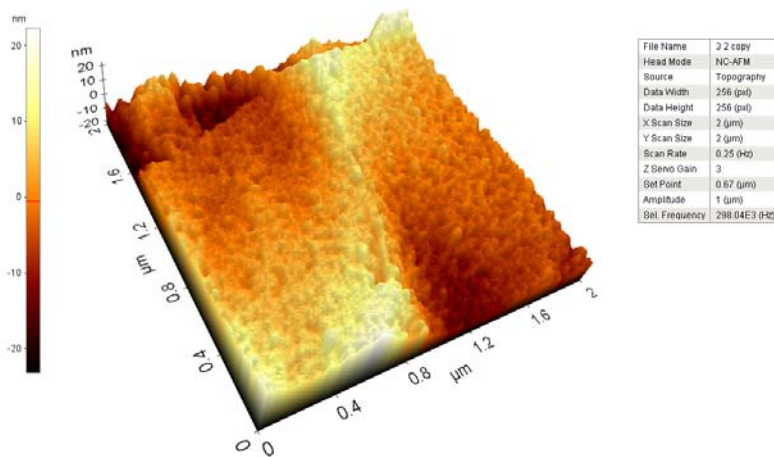


Figure 6 . AFM images of the irradiated surface of the TEM specimen.

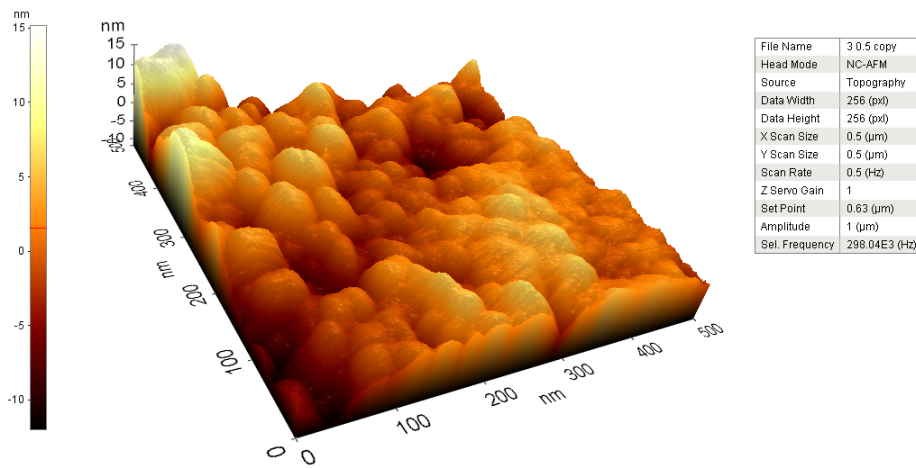


Figure 7 . Detail of the AFM image of the irradiated surface of the TEM specimen.

Conclusions

The low energy irradiation of the pure iron specimens with 10keV He ions do not induces He bubbles formation in the bulk of the specimen. No modifications of the bulk structure of the TEM specimen were observed. As expected the ion irradiation induce surface modifications, which are partially due to the sputtering effect. The surface relief becomes very dens with random oscillations in the range of 50 nm wavelengths and amplitude of about 10 nm as revealed by AFM observations.

METODE DE CURGERE OPTICA PENTRU PROCESAREA IMAGINILOR FURNIZATE DE CAMERA VIDEO KL8 DE LA JET

OPTIC FLOW METHODS FOR IMAGE PROCESSING OF THE DATA FROM VIDEO CAMERA KL8 AT JET

Etapă 2 - Validation of the optic flow method for experiments relevant to the study of fusion plasmas: pellets, filaments, MARFes.

Teddy CRACIUNESCU, Ion TISEANU

EURATOM-MEdC Association, National Institute for Lasers Plasma and Radiation Physics, Bucharest, Romania

Introduction

A wide angle view fast visible camera (Photron APX) was recently installed in the Joint European Torus JET [1]. The camera is viewing the full poloidal cross-section of the vacuum vessel and is covering a toroidal extent of $\sim 90^\circ$. The wide angle view is appropriate for the study of pellet ablation, large scale instabilities and plasma wall interactions. Since the high confinement mode of operation (H-mode) is the standard operating regime envisaged for ITER, Edge Localised Mode instabilities (ELM) [2] are of particular importance considering the power loads they can induce on the plasma facing components. Recently it has been proven that the view of the fast visible camera is able to provide useful information about ELMs [3]. Investigations of pellet ELM triggering, as a method to mitigate the ELM-caused heat load on plasma facing components, have been also recently performed on JET by means of the fast visible camera [4]. The fast visible camera observations may support also the validation of existing theories concerning ELM energy transport [5] and the study of filamentary structures observed during the development of the ELM instabilities [6].

Important quantitative information can be obtained by applying image processing techniques to the data provided by the fast visible camera. Specifically, the sequences of ordered images allow the estimation of motion as instantaneous image velocities or discrete image displacements, the so-called *optical flow*. The estimation of motion information from image sequences is a key problem in computer vision. The objective of the analysis consists of finding the vector field, which describes how the image is changing with time (see e.g. Refs. 7-8 for good overviews on this subject). This provides important information about the spatial arrangement of the objects viewed and the rate of change of this arrangement. Discontinuities in the optical flow can help in segmenting images into regions that correspond to different objects. Optical flow can be used also for object detection and tracking, as well as movement detection.

The aim of this project is to prove that optical flow can be successfully applied to study different fusion plasma relevant issues, including plasma wall interactions, using images

from the fast visible camera. It is demonstrated that the optical flow approach is able to offer unique information concerning different plasma physical phenomena.

During the first part of the year 2010 an algorithm based on the optical flow method, combining the advantages of local methods (robust under noise) and global techniques (which yield dense flow fields), was developed for JET fast visible camera image processing. The method incorporates a multi-resolution coarse-to-fine procedure in order to be able to work with large displacements between consecutive frames. Occlusion detection is also implemented. The method was extensively tested on synthetic images the method and proved to give good results for images with characteristics similar to the images provided by the JET fast-visible camera. It means that images can be affected by saturation, discontinuous movement, reshaping of image objects, low grey-level in-depth resolution.

During the time interval July-December 2010, the work on this project continued with the validation of the developed method on experimental data and also with application to the study of various issues relevant to the study of fusion plasmas: pellets, filaments, MARFEs.

Experiments and Results

The validation of the developed optical flow method was performed using experimental data to determine the speed of pellets. In the case of the JET pulse #76168, the pellet was emitted with a speed of 215 ± 12 m/s and it started to be recorded by the video camera as a visible object at $t=20.011246$. At least at the beginning, for ~ 40 frames, the pellet is flying approximately on a straight line in the direction in which it was injected. This is indicated by the approximately fixed position of its reflection on the vacuum vessel components. Two frames from this sequence are presented in Fig. 1. As the direction of injection is known, together with the geometry of the experiment (see Fig. 2) it is possible to correlate the apparent speed of the pellet in the 2D images with its real speed in the 3D space. Later in the sequence, the radiation emitted by the pellet cloud determines an increased illumination of the scene (see again Fig. 2) which enables the identification of known objects in the scene such as the ICRH antenna. The presence of a known object in the image permits the conversion of length units from pixels to meters. The advantage of using the ICRH antenna for this conversion is that it is located in the centre of the camera field of view, in the neighbourhood of the position from which the pellet is emitted. The distance AB in Fig. 2 has 92 pixels which correspond to 1.4 m.

The optical flow has been calculated for different pairs of images selected from the part of the sequence that corresponds to the time interval when the pellet is flying approximately along a straight line. A representative result is presented in Fig. 1. It has been calculated using as input the images shown in the same figure. Two distinct shapes can be observed: one corresponds to the pellet and the other to the pellet mirror-image on the vacuum

vessel which is also an object in the image. In principle, the flow field component corresponding to the mirror-image would not exist if the pellet was moving on a straight line. A slight deviation from this assumption, combined with the variation of the size of the bright area corresponding to the pellet (and consequently of its mirror-image) are responsible for the presence of this component. However its magnitude can be neglected as compared to the component corresponding to the pellet. Therefore the assumptions used for the pellet speed calculations are still valid.

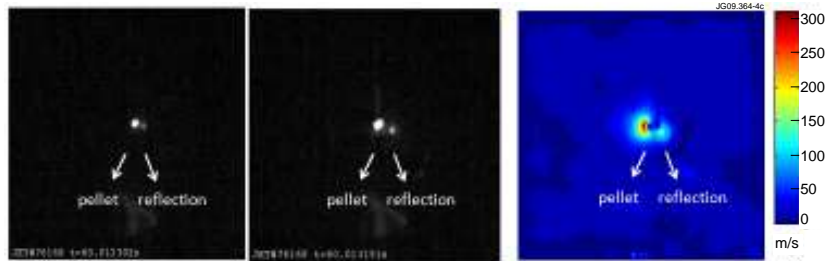


Figure 1 - Frames from the image sequence showing the pellet flying (left) - images are represented on 256 gray-levels – and corresponding optical flow (right).

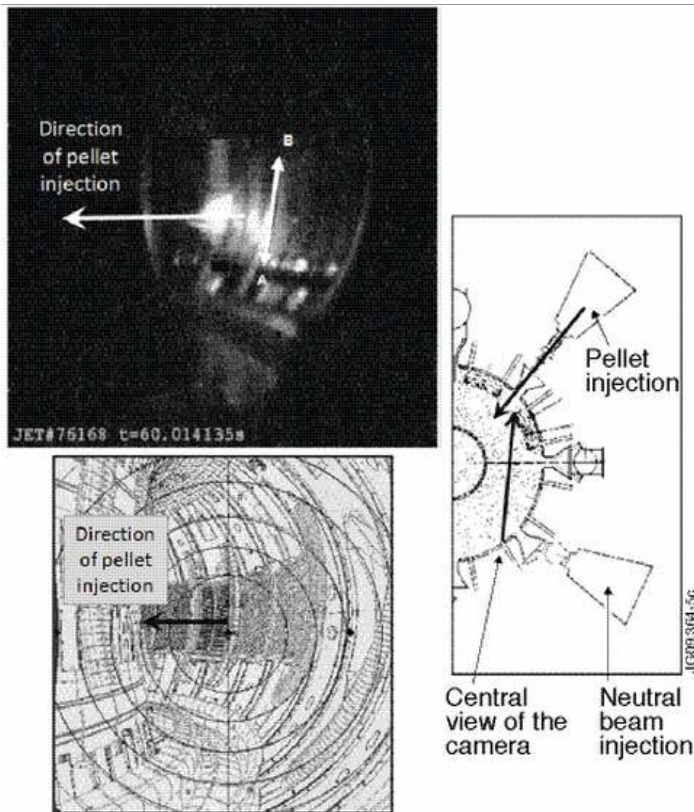


Figure 2 - Geometry of the experiment. A 3D view is obtained thanks to the illumination produced by the pellet (left-top); the direction of injection of the pellet is shown. The 3D information from the image can be correlated with geometrical information and with the camera view (left-bottom). The top view (right) permits the determination of the angle between the central view of the camera and the direction of injection of the pellet. The 3D view permits the identification of components with known geometry as the ICRH antenna (segment AB).

Image segmentation has been used to isolate the component corresponding to the pellet movement. The speed has been determined as the average speed of the pixels of the flow field component corresponding to the pellet, and it has the value ~ 270 m/s. The $\sim 25\%$ error, relative to the speed of injection, arises from the uncertainty in measuring the distance AB in Fig. 2, the approximation related to the calculation of the projection of the pellet speed on the plane corresponding to the camera images, and also, as already mentioned, to the slight change of the size of the bright area corresponding to the pellet and a slight deviation from the assumption that the pellet is moving on a straight line. This result demonstrates the capability of the optical flow method to provide a reasonable estimate the speed of moving objects in the plasma.

After validation the optical flow method was applied to the study of various issues relevant to the study of fusion plasmas like e.g. filaments and MARFES.

An interesting application of the optical flow method is the determination of the speed of plasma filaments. Plasma filaments are coherent structures characterized by enhanced visible radiation relative to the background plasma. Their motion is convective rather than diffusive, and they may differ from the background plasma in temperature and composition. Typically they are aligned with the magnetic field. The propagation is important to the overall dynamics in a variety of plasmas. In recent years, clear evidence of the ELM as a filamentary propagating structure has been shown. The interaction of ELM plasma filaments, with the tokamak first wall (divertor and limiter tiles) is one of the critical issues for ITER due to the deposited heat loads [9]. In several cases, the ELM filaments could be tracked along the surface of the outer limiters. Field-aligned plasma filaments are visible in the fast camera images as bright spots on the outboard poloidal limiters. A representative example is presented in Fig. 3. Images are recorded for JET pulse #69903. The time separating consecutive frames is $33 \mu\text{s}$ and the integration time is $20 \mu\text{s}$.

The application of the optical flow method is illustrated in Fig. 3, where the modulus of the velocity field and the error images are presented for a short sequence of three images. No pattern related to the moving filament can be observed in the error image, so the corresponding optical flow is accurately estimated. The low intensity structure of the error image is determined by several resizing and smoothing operations performed during the multi-resolution coarse-to-fine procedure. Using image segmentation techniques the region of interest corresponding to the moving filament has been extracted and used for speed calculations. The width of the poloidal limiter (185 mm), which corresponds to 14 pixels, has been used to convert pixels in length units. The optical flow calculations have been performed for a sequence of 10 images for which the basic assumptions of the method are fulfilled: no new objects appear in the image and objects reshaping can be neglected. The calculations have used as inputs both pairs of consecutive images and disparate images in the sequence. The calculated speed of the filament is 985 ± 81 m/s.

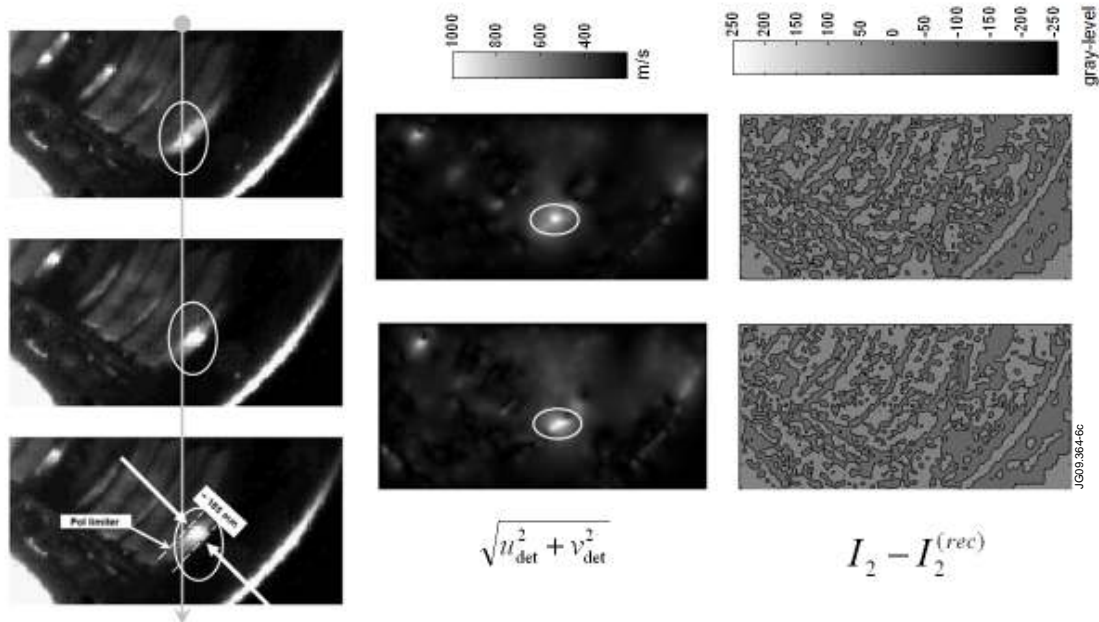


Figure 3 – Image sequence showing ELM filaments moving up along the poloidal limiters (left), modulus of the optical flow field (middle) and error images (right). The moving filament for used for speed calculation is marked with a circle.

The optical flow method has been applied also to determine the speed of MARFEs. MARFE is the acronym for “multi-faceted asymmetric radiation from the edge” and normally develops in fusion devices close to the density limit. MARFEs are considered the result of thermal instabilities excited under critical conditions through different mechanisms: impurity radiation, recycling of neutral particles, anomalous transport of charged particles and energy (see e.g. Ref. 10).

MARFEs appear as toroidally symmetric rings of enhanced radiation and usually occur on the high field side of the torus. A typical example is presented in Fig. 4, for the JET pulse #70050.

The time interval between two consecutive frames is 31 μ s. The optical flow has been calculated for this sequence and the horizontal u_{calc} and vertical v_{calc} components, together with the modulus $\sqrt{u_{calc}^2 + v_{calc}^2}$, are presented also in Fig. 4. Image segmentation has been used to isolate the vector field corresponding to the MARFE and the speed has been calculated again as the average of the speed of the corresponding pixels. For pixels to meters conversion we have used the distance shown in Fig. 5 which is twice the minor radius of the torus.

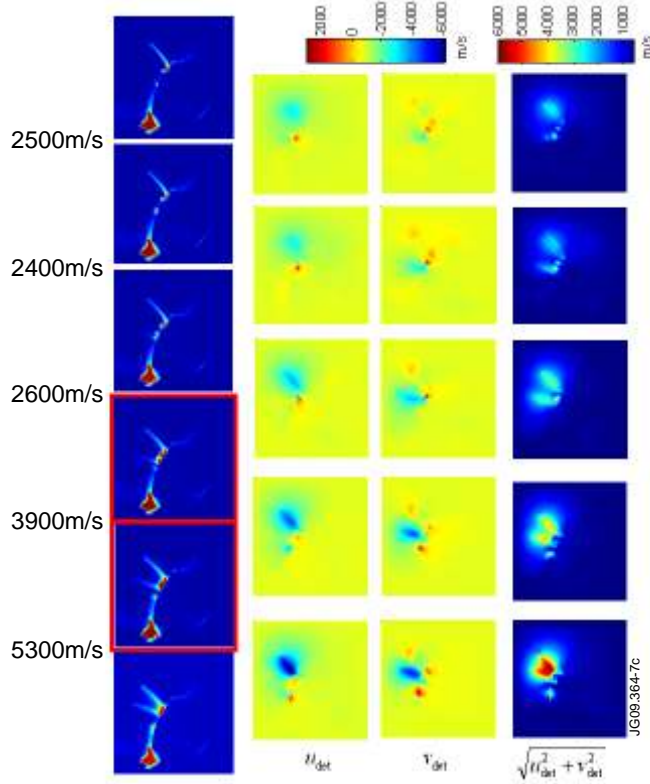


Figure 4 – MARFE image sequence (first column) and optical flow calculation: horizontal component (second second column), vertical component (third column) and modulus (last column).

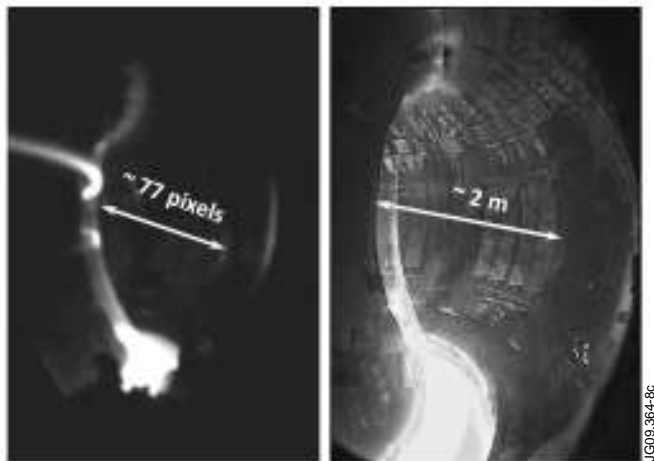


Figure 5 – Images used for the conversion of pixels to length units. The left image is from the MARFE sequence. The right one, taken from a different experiment, offers a better view of the details due to enhanced illumination.

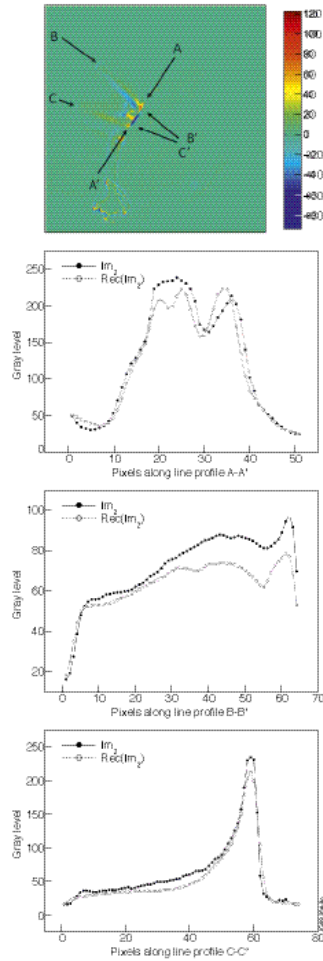


Figure 6 – Optical flow method applied to MARFEs. First row: the error image corresponding to the optical flow calculation for the fourth and fifth images in Fig.4; three lines AA', BB' and CC' are defined in order to calculate line profiles and to compare the second image I_2 with its reconstruction $I_2^{(rec)}$. Second to fourth row: line profiles along the directions AA', BB' and CC' for second image I_2 (filled circles) and reconstruction of second image $I_2^{(rec)}$ (empty circles).

The error image corresponding to the optical flow between fourth and fifth images (marked with red border in Fig. 4) is presented in Fig. 6 (first row). In order to obtain a more complete picture about the accuracy of the calculated optical flow, three line profiles have been evaluated for the second image I_2 and its reconstruction $I_2^{(rec)}$ obtained from the first image I_1 and the calculated optical flow. The results are presented also in Fig. 6 (second to fourth row). The line profiles demonstrate that shapes are reconstructed accurately for all the three line profiles. Line profiles BB' and CC' are interesting from the point of view of MARFE speed calculation. In case of CC' the reconstructed profile matches, with a negligible error, the real one. In case of BB' the shape is correctly reconstructed but a deviation of $\sim 25\%$ arises in the second part of the profile. This indicates that if the speed is to be calculated with higher accuracy, it is necessary to avoid this region or to use only the velocity field corresponding to CC'.

Conclusion

The validation of the developed optical flow method was performed using experimental data. After validation the optical flow method was applied to the study of various issues relevant to the study of fusion plasmas like e.g. filaments and MARFes. The method proved to achieve good results in case of experimental images provided by the JET fast-visible camera which can be affected by saturation, discontinuous movement, reshaping of image objects, low grey-level in-depth resolution. For objects moving close to known structures of the tokamak vacuum vessel, the velocity in the real 3D space has been inferred from the 2D image analysis. The optical flow method is a unique tool able to cope with several different plasma physical phenomena and to provide useful information for modelling.

The results were published (see Refs. 10-11).

The work on this project will continue with the customization and adaptation of the optical flow method for the control of pellet extrusion speed based on the image sequences provided by a CCD camera viewing the ice at the exit of the nozzles of the extrusion cryostat. The method has to be adapted to the characteristics of camera. Also, in order to allow image processing of a large amount of data (more than 3000 frames for single JET pulse) an effort will be dedicated to optimization. Particular attention will have to be devoted to the extraction of useful information in real time – a very difficult task because of the extremely high computational and frame rate requirements.

Acknowledgement

The reported work includes contributions from Vasile Zoita (EURATOM-MEdC Association) and also from the following people outside the EUATOM-MEdC Association: Andrea Murari (Consorzio RFX, Associazione ENEA-Euratom per la Fusione, Padova, Italy), Arturo Alonso (Laboratorio Nacional de Fusion, EURATOM-CIEMAT, Madrid, Spain), Peter Lang (Association EURATOM-IPP, Max-Planck-Institut für Plasmaphysik, Garching, Germany) and Gabor Kocsis (RMKI-KFKI EURATOM Association, Budapest, Hungary).

References

- [1] J. A. Alonso, P. Andrew, A. Neto, J. L. de Pablos, E. de la Cal, H. Fernandes, J. Gafert, P. Heesterman, C. Hidalgo, G. Kocsis, A. Manzanares, A. Murari, G. Petravich, L. Rios, C. Silva, P.D. Thomas, Fast visible camera installation and operation in JET, 34th EPS Conference on Plasma Phys. Warsaw, 2 - 6 July 2007 ECA Vol.31F, P-2.124 (2007).
- [2] A. Kirk, H. R. Wilson, G. F. Counsell, R. Akers, E. Arends, S. C. Cowley, J. Dowling, B. Lloyd, M. Price, and M. Walsh, Spatial and Temporal Structure of Edge-Localized Modes, Phys. Rev. Lett. 92(2004)245002.

- [3] J.A. Alonso, P. Andrew, A. Neto, J.L. de Pablos, E. de la Cal, H. Fernandes, W. Fundamenski, C. Hidalgo, G. Kocsis, A. Murari, G. Petravich, R.A. Pitts, L. Rios, C. Silva, Fast visible imaging of ELM-wall interactions on JET, *Journal of Nuclear Materials*, 390-391(2009)797-800.
- [4] G. Kocsis, J.A. Alonso, B. Alper, G. Arnoux, G. Cseh, J. Figueiredo, D. Frigione, L. Garzotti, J. Hobirk, S. Kalvin, M. Lampert, P.T. Lang, G. Petravich, T. Szepesi, R. Wenninger, Pellet cloud distribution and dynamics for different plasma scenarios in ASDEX Upgrade and JET, 36th EPS Conf. on Plasma Physics, Sofia, Bulgaria 2009, *Europhysics Conference Abstracts*, Vol. 33E, P-1.151, 2009
- [5] R Wilson, S C Cowley, A Kirk, P B Snyder, Magneto-hydrodynamic stability of the H-mode transport barrier as a model for edge localized modes: an overview, *Phys. Rev. Lett.* 92 (24) (2004) 245002.
- [6] W Fundamenski, R A Pitts, A model of ELM filament energy evolution due to parallel losses, *Plasma Phys. Control. Fusion* 48 (2006) 109–156.
- [7] J. L. Barron, D. J. Fleet and S. S. Beauchemin, Performance of optical flow techniques, *International Journal of Computer Vision*, 12-1(1994)43-47.
- [8] D. J. Fleet and Y. Weiss. Optical flow estimation. In *Mathematical models for Computer Vision: The Handbook*. N. Paragios, Y. Chen, and O. Faugeras (eds.), Springer, 2005.
- [9] G Federici, A. Loarte G. Strohmayer, Assessment of erosion of the ITER divertor targets during type I ELMs, *Plasma Phys. Control. Fusion* 45(2003)1523-1547.
- [10] B. Lipschultz, B. LaBombard, E.S. Marmor, M.M. Pickrell, J.L. Terry, R. Waterson, S.M. Wolfe, MARFE: An Edge Plasma Phenomenon, *Nucl. Fusion* 24 (1984) 977.
- [11] T. Craciunescu, A. Murari, A. Alonso, P.T. Lang, G. Kocsis, I. Tiseanu, V. Zoita, "Application of Optical Flow Method for Imaging Diagnostic in JET", *J. Nucl. Mater.*, 400-3: 205-212, 2010.
- [12] A. Murari, J. Vega, T. Craciunescu, S. Gonzalez, S. Palazzo, G. Vagliasindi, D. Mazon, M. Gelfusa, J. F. Delmond, A. de Maack, Latest Developments in Image Processing Methods and Technologies for Magnetic Confinement Nuclear Fusion, submitted to *IEEE Intelligent Systems (EFDA-JET preprint EFD-P(10)03*.

**National Research and Development Institute for Cryogenics and Isotopic Technologies
National Institute for Laser, Plasma and Radiation Physics**

SCIENTIFIC REPORT
To the Contract 1EU/08/08.2008
JULY-DECEMBER 2010

Project BS-7: Upgrade of the JET Gamma-Ray Diagnostics
Project leader: M. Curuia
EFDA-JET Task Agreement: JW6-TA-EP2-GRC-04

Specific Objective

Upgrade of the JET gamma-ray cameras – neutron attenuators (code KN3-NA)

*Marian Curuia⁽¹⁾, Mihai Anghel⁽¹⁾, Teddy Craciunescu⁽²⁾, Mihaela Gherendi⁽²⁾, Sorin Soare⁽¹⁾,
Vasile Zoita⁽²⁾*

⁽¹⁾ National Institute for Cryogenics and Isotopic Technologies, Rm. Valcea

⁽²⁾ National Institute for Laser, Plasma and Radiation Physics, Magurele, Bucharest

December 2010 milestones:

- A. Report on the installation at JET of the KN3-NA Assembly
- B. Report on the radiation tests on the neutron attenuator prototype

CONTENTS

Summary

A. Installation at JET of the KN3-NA Assembly

A.1. Introduction

A.2. Horizontal camera neutron attenuator

A.3 Vertical camera neutron attenuator

B. Radiation tests on the neutron attenuator prototype

B.1 Introduction

B.2 Methods

B.3 Experiments and results

B.4 Conclusions

B.5 Acknowledgement

Reference

Annex 1

Summary

After five months of in house tests the KN3-NA assembly was delivered to JET and the installation process has been started.

The short version of the Vertical Camera Neutron attenuator casing (VC-NA) is presently installed following a 180° horizontal rotation due to a manufacture and design error. Some checks (the position of internal reinforcements) are still needed before confirming that it is acceptable for physics purposes. This attenuator casing is compatible with 5 bar internal water pressure. The long version of the VC-NA needs to be manufactured again following issues related to the positioning of the internal reinforcement. It is expected that only design modifications will be needed before going into manufacture. For the Horizontal Camera Neutron Attenuator casing (HC-NA), internal reinforcements have to be added, to the present drawings to withstand the latest proposed supplied water pressure (3 bars). A new design will be proposed in January 2011, and then a new TCD-I will be issued. The delivery of the new casing is planned for mid-May 2011. In parallel it was proposed to use the present HC-NA “prototype” to proceed with the installation and tests of the HC-NA system in general and to swap between the prototype and the final HC-NA once the latter is available. No operation on plasma is foreseen with the prototype. The manufacture of the new long version of the VC-NA and the new HC-NA will be done within the present project budget with a redistribution of resources.

Radiation tests on vertical camera neutron attenuator prototype have been done using Plasma Focus Installation PF1000 as neutron source. The attenuation factor was measured and proved to be in agreement with the attenuation factors considered to be attainable within the project constraints as estimated by neutron transport calculations.

A. Installation at JET of the KN3-NA Assembly

A.1. Introduction

The operation of the neutron KN3 attenuators assembly was tested before delivery to JET. The in-house tests were carried out on a test stand specifically designed for this purpose. The in-house tests addressed all the functions of the neutron attenuators assembly except for the radiation functions.

In July the KN3-NA Assembly was delivered to JET and the commissioning process has been started.

During the commissioning process a careful on site inspection has been carried out when manufacturing errors and serious design flaws has been revealed. An important source of errors was the changing of water supply system. During the Scheme Design Phase the attenuators were proposed to be filled with static water. Meanwhile this solution has been changed, due to sampling issues, into to pressurized water supply and not all drawings have been updated to the new situation.

The manufacturing errors were generated by high pressure water supply that claims a strong internal and external reinforcement structure that could have a considerable influence over the neutron and gamma ray measurements. All these issues have been discussed during two meetings held at JET with the responsible persons. As results of these meetings, a new solution for attenuators water supply has been identified, meaning the reducing of demineralised water

from 5 bar to 0.5 bar. Taking into account this new solution for water supply new horizontal and vertical (long version) attenuators will be redesigned and reconstructed (cost redistribution within the Art. 6.3 Order 13A).

A.2. Horizontal camera neutron attenuator

Horizontal Camera Neutron Attenuator casing (HC-NA) were designed to work as a simple pure water tank and internal reinforcements have to be added, to the present drawings to withstand the latest proposed supplied water pressure (3 bars). A new design will be proposed in January, and then a new TCD-I will be issued. More details regarding the design of the HC-NA casing are presented in the Memorandum on horizontal camera neutron attenuator casing, annex 1.

A.3. Vertical camera neutron attenuator

The current status of the Vertical Camera Neutron Attenuator (VC-NA) short version VC-NA (S) is the following:

- The VC-NA (S) with internal reinforcements is already installed at its location on JET
- Attenuator casing was installed with a 180 deg rotation (to solve a flaw in the mechanical design: positioning of the water supply pipes in the detector line of site when attenuator is in Parking position).
- The installed VC-NA (S) is to be checked in order to confirm that the internal plates are outside the detector Field-of-View (FoV), fig. 1.
- MCNP calculation to evaluate the effect of the internal plates on the gamma-ray field at the position of the gamma-ray detectors (the CsI(Tl) detectors) is proposed to be done.

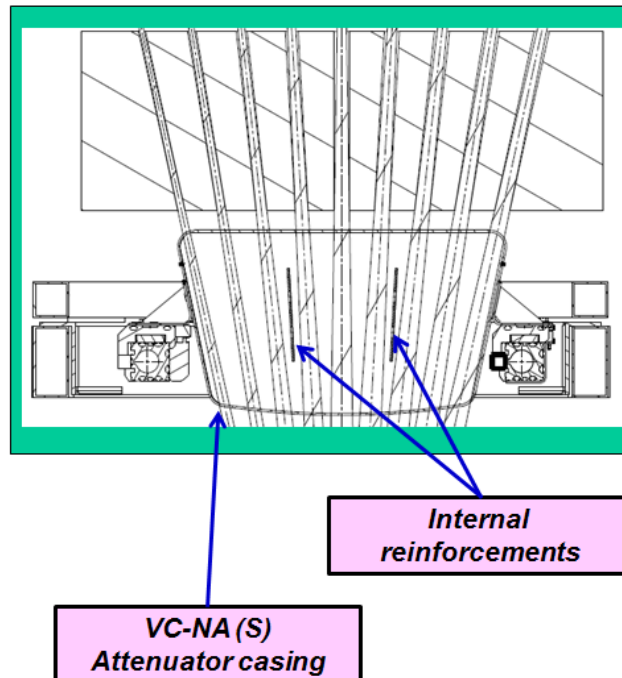


Figure 1 Internal reinforcement for VC-NA (S)

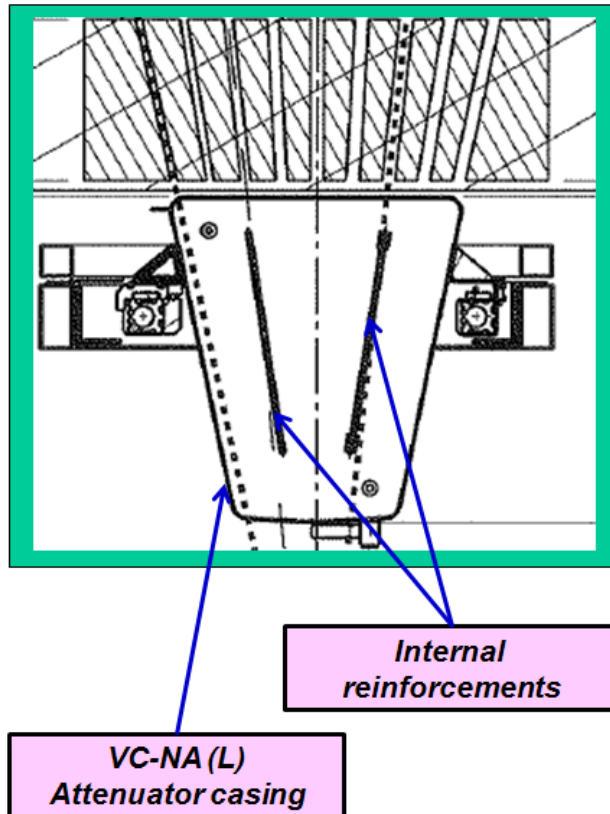


Figure 2 Internal reinforcements for VC-NA (L)

Vertical Camera Neutron Attenuator (VC-NA) long version VC-NA (L), fig. 2

- The constructed VC-NA casing has internal plates which intersect the FoV of two gamma-ray detectors.
- A new casing, without internal plates, is to be constructed for VC-NA (DT)
- The detailed design drawings have been updated (MEdC Association) with a minimum of changes with respect to the initial (static water fill) design.
- The drawings are now updated to accommodate with the CATIA SmarTeam JET program design

B. Radiation tests on the neutron attenuator prototype.

B.1. Introduction

The JET KN3 gamma-ray cameras diagnostics system has already provided valuable information on the fast ion evolution in JET plasmas. Gamma-ray diagnostics at JET (gamma-ray spectrometry [1] and imaging [2]) have provided some of the most interesting results in experiments such as those of the TTE campaign [3]. The applicability of gamma-ray imaging diagnostics to high power deuterium pulses and to deuterium-tritium discharges is strongly dependent of the fulfilment of rather strict requirements for the control of the neutron and gamma-ray radiation fields. Therefore a coherent set of upgrades was therefore considered indispensable to extend the JET gamma-ray diagnostic capabilities and to improve the measurements in order to better support the experimental programme. One of these objectives consists in the design, construction and testing of neutrons attenuators for the vertical and horizontal cameras of the KN3 gamma-ray imaging diagnostics. This diagnostics upgrade should make possible gamma-ray imaging measurements in high power deuterium JET pulses, and eventually in deuterium-tritium discharges.

Design solutions based on water neutron attenuators have been developed for the KN3 Gamma-Ray Cameras (the KN3-NA diagnostics upgrade) [4]. At the present moment all the components of the KN3-NA assembly have been manufactured and tested on a test stand which is an exact replica of the KN3 horizontal camera neutron attenuator assembly and partially replicates the installation configuration for the KN3 vertical attenuator installation configuration. Mechanical, electrical, pneumatic and hydraulic tests were performed.

The next step for the validation of the KN3-NA system consisted in radiation tests. These tests were performed by using a prototype neutron attenuator on the PF-1000 plasma-focus device at Institute of Plasma and Laser Microfusion (IPPLM), Warsaw and the results are reported here.

B.2. Methods

Neutron-photon transport calculations have shown that the radiation distribution inside the KN3 neutron attenuators is strongly influenced by the surrounding structures [11]. Thus it would be very difficult (if not impossible) to measure independently the neutron attenuation factors with the attenuators at their final location on JET, using the KN3 detectors. It was therefore proposed to construct an independent setup in order to get experimental information on the neutron field. This setup includes the use of other detectors than those of the KN3 diagnostics. The experiments have to be compared with MCNP calculations. A key point is represented by the attenuation factor. The experiments should prove that the value of the attenuation factor is in agreement with the value estimated to be attainable within the project constraints [12] (see Table 1).

Initially it was planned to perform the tests on the JET site, using a point neutron source (Cf-252), placed at the focal points of the KN3 cameras and one additional side position (see Fig. 1). This configuration allows for the measurement of integrated neutron flux and also of neutron energy distribution behind the attenuators.

Table 1 – The the attenuation factors estimated to be attainable within the project constraints

Neutron attenuator	Material	Neutron energy	
		2.45 MeV	14.1 MeV
KN3-HC-NA	H ₂ O	10 ²	15
KN3-VC-NA (Long)	H ₂ O	10 ⁴	10 ²
KN3-VC-NA (Short)	H ₂ O	10 ²	15

However due to the specific operations schedule during JET shutdown it was not possible to allow enough time for the experiments. Therefore, the test experiment plan was changed and a new location was proposed at the Institute of Plasma Physics and Laser Microfusion, Warsaw, Poland. The neutron source is provided by the Plasma-Focus PF1000 device. This is the largest dense magnetised plasma facility in the world and in the same time, the main plasma installation of the International Centre for Dense Magnetised Centre. The main electromagnetic parameters are given in Table 2. Other characteristic information is provided in Fig. 2.

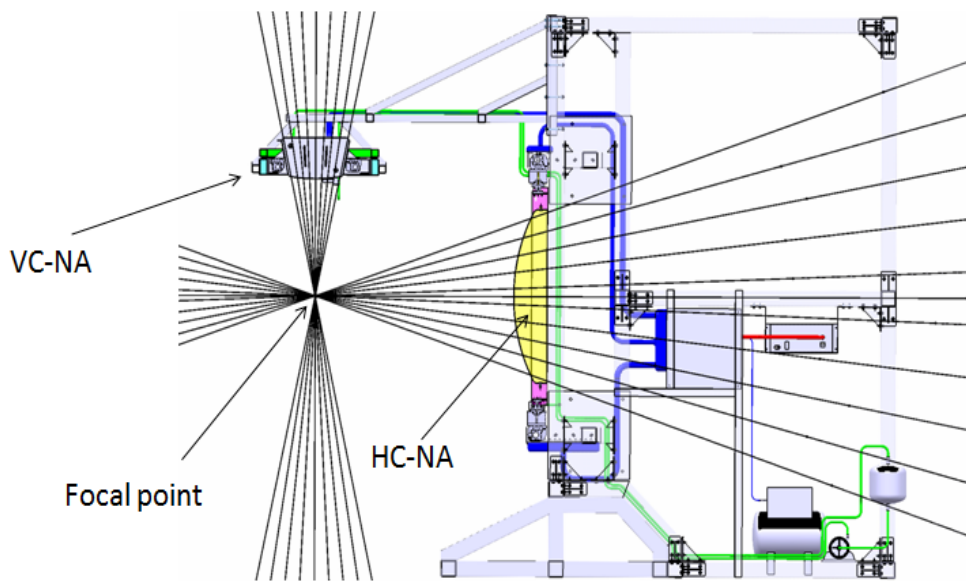


Figure 1 - Initial test configuration

Table 2 - Main electromagnetic parameters of PF-1000 [5]

Capacitor bank charging voltage:	20-40 kV
Capacitor bank stored energy:	266 - 1064 kJ
Current rise-time:	6 μ s
Peak current:	1.3 - 2.5 MA

In order to measure the transfer function of attenuator, the neutron field was measured using super-heated fluid detectors, SHFD's (also known as "bubble detectors") [10]. SHFD are suspensions of metastable droplets which readily vaporize into bubbles when they are nucleated by radiation interactions. The active detecting medium is in the form of microscopic (20-50 μ m) droplets suspended within an elastic polymer. The phenomenon of neutron detection by a SHFD is a mixture of nuclear interactions (neutron collisions with nuclei of the active medium), thermodynamic behavior of the detecting medium (the super-heated fluid), and the mechanical response of the elastic polymer. If sufficient energy is transferred from the colliding neutron to the nucleus of one of the elements in the composition of the active medium, the recoil nucleus will initiate the generation of a vapor embryo of sub-micron dimensions. Under proper conditions (that depend on the thermodynamics of the active medium) the vapor embryo will lead to the vaporization of the super-heated droplet with the subsequent expansion into a macroscopic (0.2 – 0.5 mm) bubble. The SHFD's have a threshold-type energy response with the threshold energy depending on droplet composition, detector operating temperature, detector operating pressure. For a standard bubble detector like the BD-PND-type, the energy response is approximately flat within the range 0.3-10 MeV.

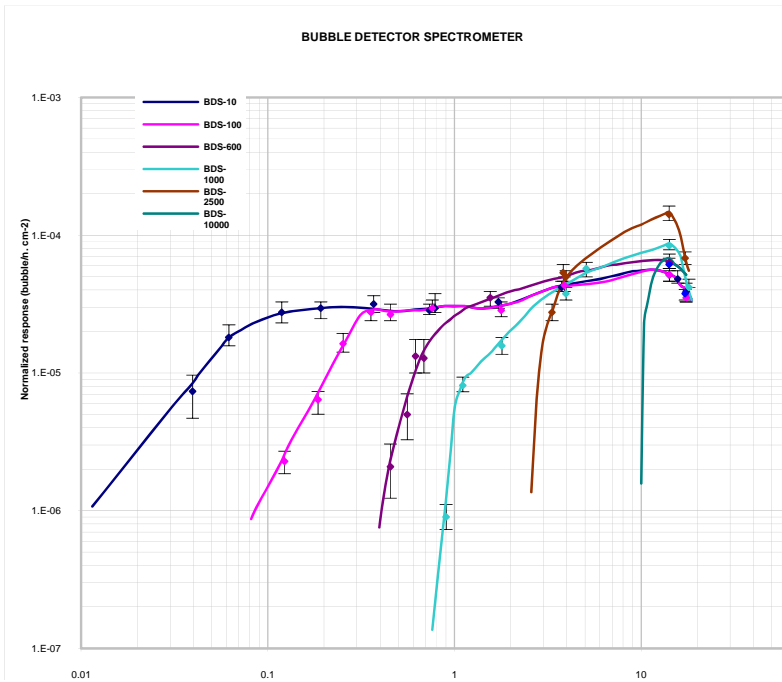
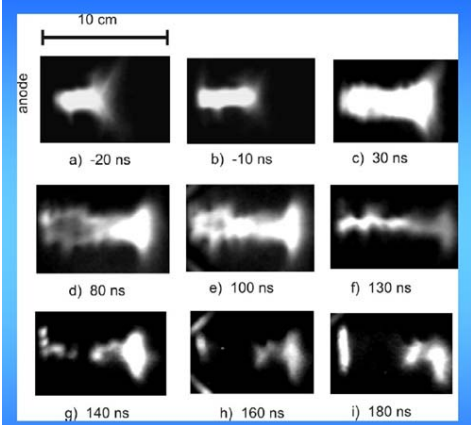
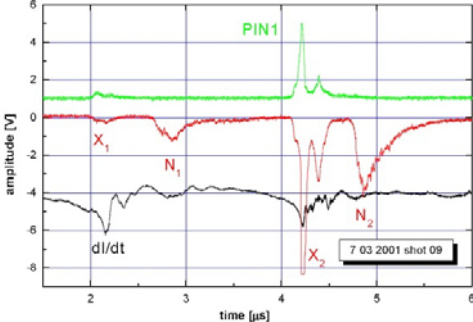
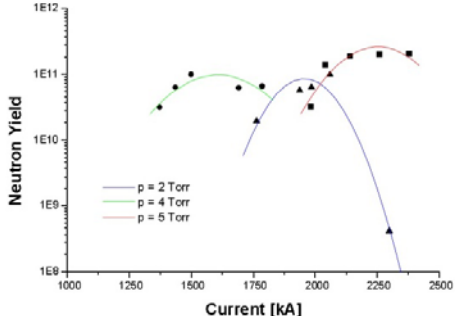


Figure 2 – BDS neutron energy response

Using detectors with different energy thresholds, a bubble detector spectrometer (BDS) is obtained. The BDS covers a broad energy range (0.01 – 20 MeV) and provides six energy thresholds in that range (Fig. 2). Therefore the SHFD detectors were used for measuring the neutron fluence and also to determine the neutron energy distribution.

Table 2 – PF-1000 description.

	<p>PF equivalent discharge circuit [6]</p>
--	--

	<p>XUV frames [6] - exposure time 2 ns, window 200-300 eV+above 600 ev</p> <p>a-c: pinch \varnothing 1-2 cm d: first expansion e-f: second pinch g-i: explosion, dense structure without zipped-effect dense spherical structure</p>
	<p>PF-1000 typical shot:</p> <p>Soft X-ray signal (green) and dI/dt discharge (black) for shot 0703-09. Hard X-ray and neutron signal - 15 m downstream (red).</p>
	<p>Neutron yield (end-on) as a function of the maximum discharge current [7].</p>

As the experiments provide a large amount of experimental data, it was necessary to develop a software package in order to ensure an automatic counting of the bubbles in each detector with enough precision and allowing fast data processing. The software implements a sequence of image processing techniques which are briefly presented here. First an automatic threshold is performed in order to isolate in the image the bubble structure.

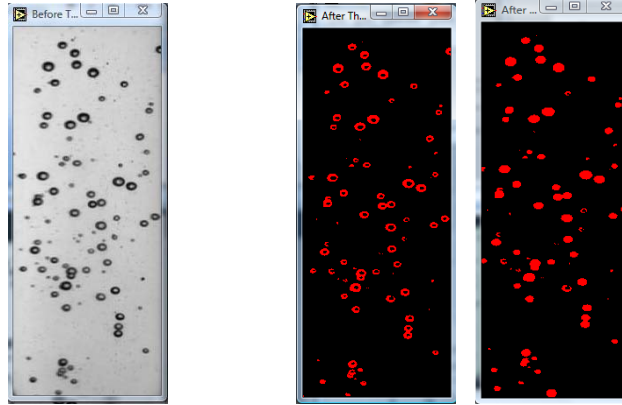


Figure 3 – Illustration of the image processing sequence for bubble detector counting: recorded image of bubbles (left), image after thresholding and opening-dilation process (middle) and image after filling holes and smooth right angles (right).

The automatic threshold is performed by the clustering method. This technique sorts the histogram of the image within a discrete number of classes corresponding to the number of phases perceived in an image. The gray values are determined, and a barycenter is determined for each class. This process repeats until it is obtained a value that represents the centre of mass for each phase or class. Very small particles, which do not correspond to neutron detection, are removed by using an image opening function followed by dilation. This operation does not significantly alter the area and shape of particles because erosion and dilation are dual transformations, in which borders removed by the erosion process are restored during dilation. Filling holes and smooth right angles along the edges of particles is performed prior to evaluate particle parameters. Pixels are added to the image in a neighbourhood that matches a template specified by the structuring element. A 4-connectivity structure element proved to be an optimum choice for this kind of images. The Heywood circularity factor [8-9] is used in order in order to classify the particles in the image.

The Heywood factor is defined as the ratio of a particle perimeter to the perimeter of the circle with the same area. The closer the shape of a particle is to a disk, the closer the Heywood circularity factor to 1. For our images we found that a value in the range [0.94-1.06] will ensure a correct detection of the particles. An illustration of the results of the image processing sequence is given in Fig. 3. The image processing sequence was implemented using IMAQ Vision for Labview software package (<http://www.ni.com/vision/>) – see Fig. 4.

3. Experiments and results

The experiments were performed using the prototype version of the KN3-VC-NA (Short) attenuator. The main goal of the experiments consisted in determining the fast neutron attenuation factor (mean neutron energy about 2.5 MeV).

The experiments were performed with the assumption that the neutron source can be approximated with a point source, i.e., its dimensions are much smaller than the distance source-detector. The PF1000 neutron source was considered to have a cylinder shape (2 cm diameter, 5 cm length) and the direction of the point source is perpendicular to the detectors (see Fig. 5 – left).

Preliminary experiments were performed during May 2010 and were dedicated to the characterization of neutron field specific to the PF-1000 device. During extensive experiments neutron spectra were recorded, using the detectors with different energy thresholds (BDS bubble detector spectrometer). The experimental configuration is presented in Fig. 5 - right. The attenuator and detectors are placed on the discharge chamber axis, in the down-stream direction.

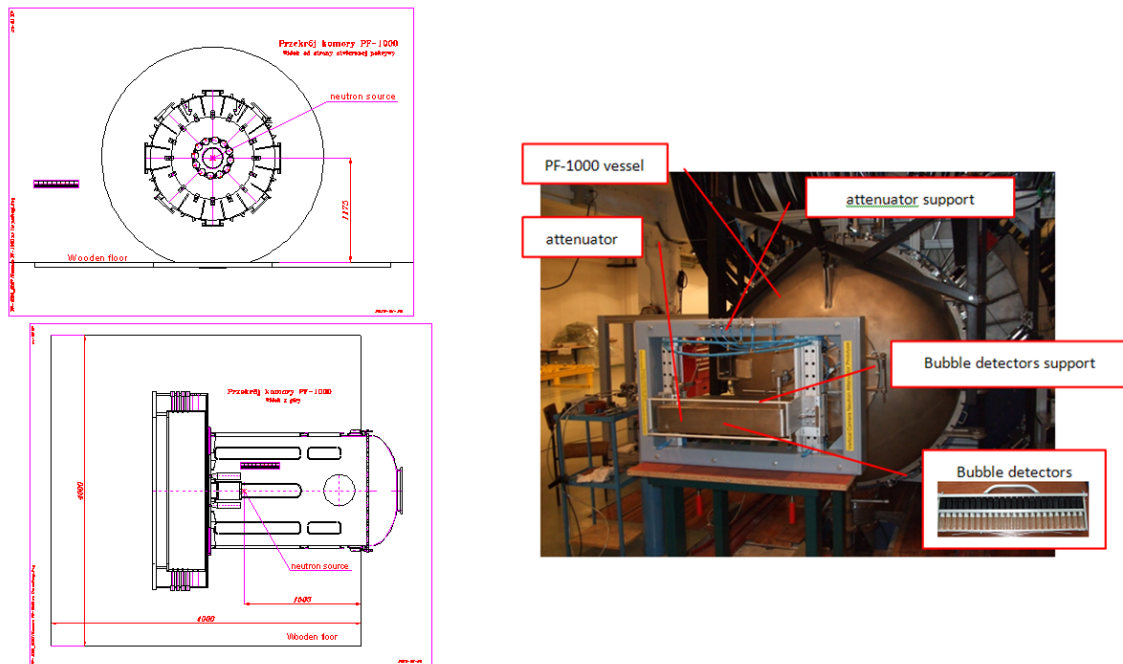


Figure 5 – Experimental configuration #1

The experimental results revealed that even without the attenuator, the energy distribution has a strong component in the low energy range ($E < 0.1$ MeV) (Fig. 6). It was assessed that the main reason for this component are the surrounding structures. (Fig. 7). The low-energy neutron field would have a strong influence on measurements concerning the attenuation factor.

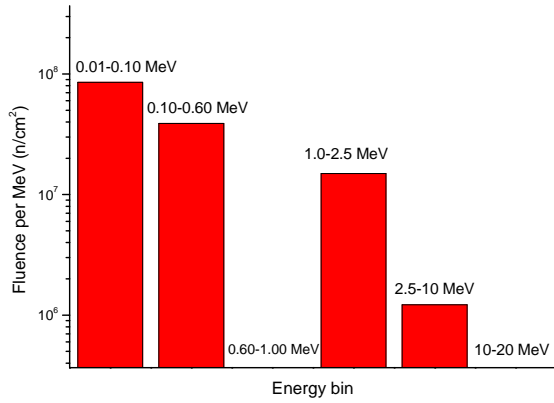


Figure 6 - Neutron spectra showing a significant component in the low energy range ($E < 0.1$ MeV) due to neutron scattering induced by surrounding structures.

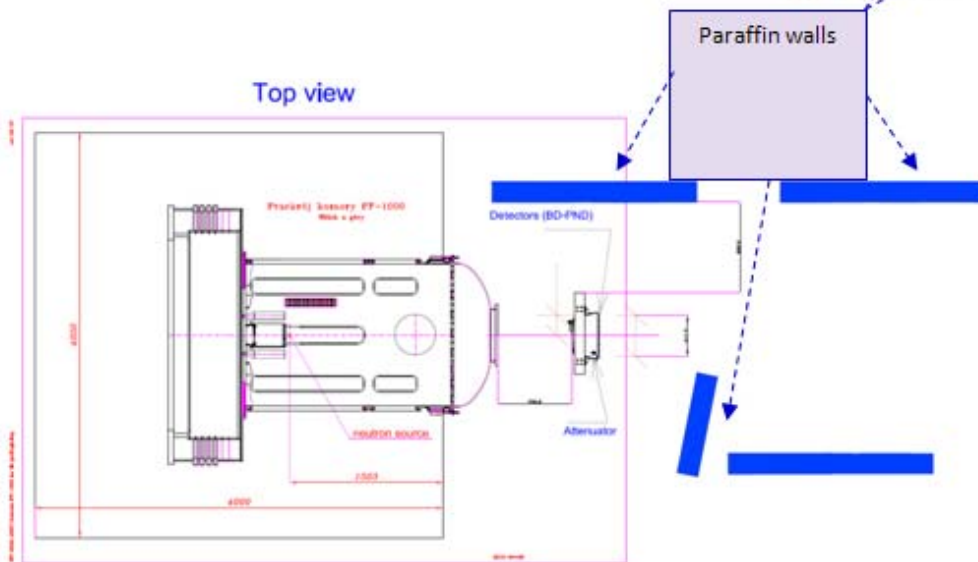


Figure 7 – Surrounding structures that determines neutron scattering.

Therefore further experiments were performed during the second half of the year 2010 in order to find an optimum experimental setup and to determine the transfer function of the attenuator.

A new measuring location was used: the attenuator and detectors are placed on the discharge chamber axis, in the up-stream direction. The location was chosen in order to minimize the influence of the neutron scattering surrounding structures. Additionally the detectors were placed inside a paraffin collimator in order to provide additional shielding from neutron scattering structures (Fig. 8). This detector-attenuator-source configuration is also a better simulation of the KN3 neutron profile monitor (central channel).

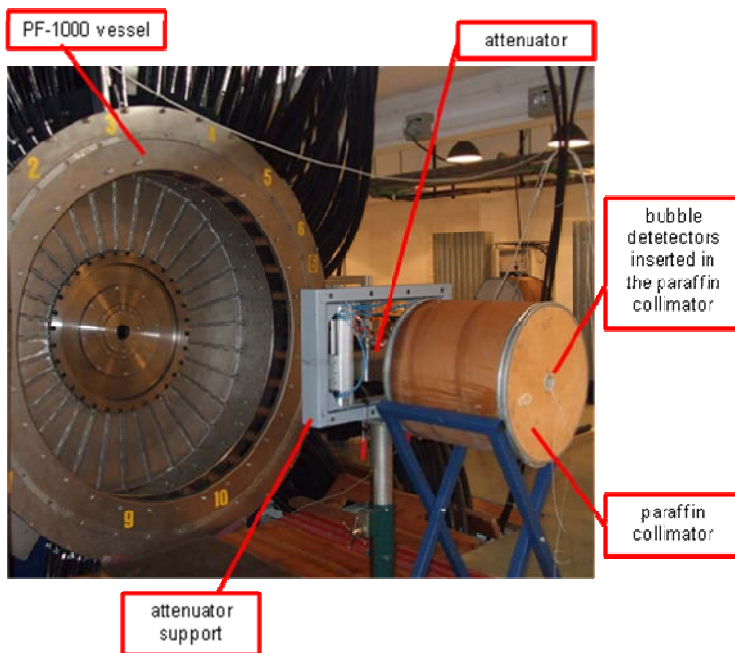


Figure 8 – Experimental configuration #2

In order to test this configuration neutron spectra were recorded, using detectors with the energy thresholds listed in Table 3 (BDS, bubble detector spectrometer). It is worth mentioning that for these experiments a new set of spectrometric detectors (BDS), with increased efficiency (especially for the energy thresholds above 1 MeV) were purchased and used.

Table 3 – BDS energy thresholds/energy bins

BDS spectrometer for energy distribution recording - energy thresholds/energy bins (MeV):	BDS energy bins used for attenuation factor determination (MeV)
<ul style="list-style-type: none"> • 0.01-0.10 • 0.10-0.60 • 0.60-1.00 • 1.00-2.50 • 2.50-10.00 	<ul style="list-style-type: none"> • 1.00-2.5 • 2.50-10.00

The energy distribution obtained with the new BDS (before introducing the attenuator between the detectors and the neutron source) is illustrated in Fig. 9. The energy distribution was recorded in multiple shots which cumulates a total neutron production of $4.80 \cdot 10^{11}$.

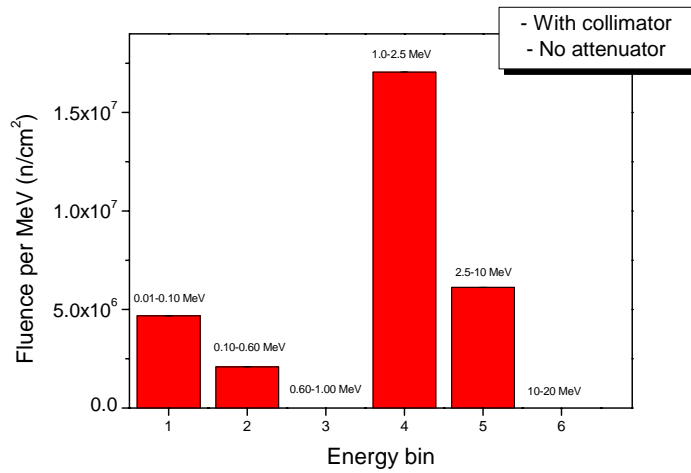


Figure 9 - Neutron energy distribution obtained using an experimental configuration #2 (no attenuator).

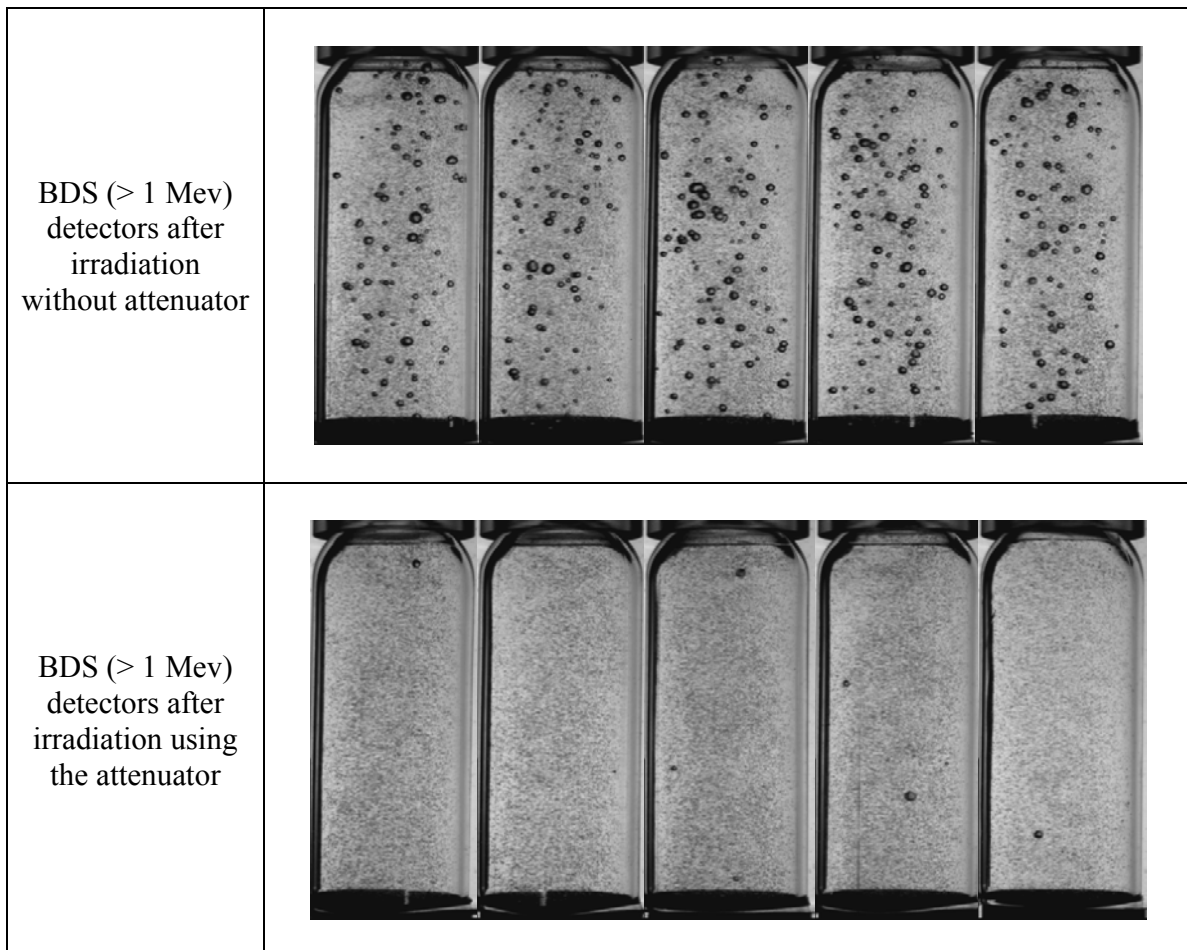


Figure 10 – Representative detector exposure for attenuation factor determination.

As it can be observed the distribution has a small component in the low energy range ($E < 0.1$ MeV). This component is due to the neutrons moderated by the paraffin collimator and scattered into the detector region.

The attenuation factor was determined by recording the detector response, with and without attenuator, in the energy range above 1 MeV. A representative result is presented in Fig. 10. The detectors were exposed to multiple shots in order to ensure a good statistic. The total neutron production was 0.81×10^{12} for the measurements without attenuator and 1.03×10^{12} for the measurements with attenuator, respectively. The detector responses were normalised both with respect to the neutron production characteristic during their exposure and to their sensitivity. The detector response function was used for detector response deconvolution. The evaluation of the attenuation factor is summarized in Table 4.

Table 4 – Attenuation factor evaluation.

Geometry	Total neutron production	Corrected no of bubbles	Attenuation factor
Without attenuator	$0.807 \cdot 10^{12}$	88 ± 1.43	112 ± 31
With attenuator	$1.032 \cdot 10^{12}$	0.79 ± 0.43	

The evaluated attenuation factor proved to be in agreement with the attenuation factors considered to be attainable within the project constraints ($\sim 10^2$). /X/

B.4. Conclusion

Radiation tests for the validation of KN3-NA attenuators were performed. The experiments were performed by using the PF-1000 plasma-focus device at Institute of Plasma and Laser Microfusion IPPLM Warsaw. They used the prototype version of the KN3-VC-NA (Short) attenuator. After extensive preliminary experiments a measurement arrangement characterized by a negligible scattering background was implemented. Neutron energy distribution measurements confirmed the efficiency of this setup. The attenuation factor was measured and proved to be in agreement with the attenuation factors considered to be attainable within the project constraints as estimated by neutron transport calculations. The results presented here may be considered as the first step in the commissioning procedure for the JET KN3-NA diagnostics upgrade.

Acknowledgement

The reported work presented at the part B includes contributions of the following people from EUATOM-IPPLM Association (Poland): Marek Scholz, Marian Paduch, Sławomir Jednorog and Rafal Prokopowicz.

References

- [1] V.G. Kiptily, F.E. Cecil, O.N. Jarvis, M.J. Mantsinen, S.E. Sharapov, L. Bertalot, S. Conroy, L.C. Ingesson, T. Johnson, K.D. Lawson, S. Popovichev, *γ -ray diagnostics of energetic ions in JET*, Nucl. Fusion 42(2002)999.
- [2] O.N. Jarvis, J Adams, P.J.A. Howarth, F.B. Marcus, E. Righi, G.J. Sadler, D.F.H. Start, P. Van Belle, C.D. Warrick, N. Watkins, *Gamma ray emission profile measurements from JET ICRF-heated discharges*, Nucl. Fusion, 36(1996) 1513.
- [3] V. G. Kiptily, Yu. F. Baranov, R. Barnsley, L. Bertalot, N. C. Hawkes, A. Murari, S. Popovichev, S. E. Sharapov, D. Stork, V. Yavorskij, *First Gamma-Ray Measurements of Fusion Alpha Particles in JET Trace Tritium Experiments*, Phys. Rev. Lett. 93(2004)115001.
- [4] V. Zoita, M. Anghel, T. Craciunescu, M. Curuia, T. Edlington, M. Gherendi, V. Kiptily, K. Kneupner, I. Lengar, A. Murari, A. Pantea, P. Prior, S. Soare, S. Sanders, B. Syme, I. Tiseanu. *Design of the JET upgraded gamma-ray cameras*. Fus. Eng. Des. 84(2009)2052.
- [5] H. Schmidt et al., "Review of Recent Experiments with the Megajoule PF-1000 Plasma Focus Device", Physica Scripta. Vol. 66, 168, 2002.
- [6] M. Scholz et al., "Recent Results of MJ Plasma-Focus Experiment". 6th Dense Z-Pinch Symposium, Oxford, 2005.
- [7] P. Kubas, "Fast deuterons and neutrons in Plasma Focus discharge", 34th EPS Conference on Plasma Phys. Warsaw, Vol.31F, P-1.017 (2007).
- [8] H. Heywood, Particle shape coefficients, Journal of the Imperial College Chemical Society, 8(1954)15.
- [9] R M Carter, Y Yan, Measurement of particle shape using digital imaging techniques, Journal of Physics: Conference S
- [10] M. Gherendi, V. Kiptily, V. Zoita, S. Conroy, T. Edlington, D. Falie, A Murari, A. Pantea, S. Popovichev, M. Santala, S. Soare, "Super-heated fluid detectors for neutron measurements at JET", J. Optoelectronics Advanced Mat., 10 (2008) 2092-2094.
- [11] I. Lengar and V. Zoita, "Neutron beam distribution for the KN3 attenuators; application for the horizontal and the long vertical attenuator", JET EP2 GRC project report, November 2008.
- [12] I. Lengar, "Modelling of the neutron beam distribution for the KN3 attenuators; neutron-induced gamma-rays in the attenuator", JET EP2 GRC project report, April 2008.

Annex 1

Memorandum on the horizontal camera neutron attenuator

1. Review

The GRC Neutron Attenuators (GRC-NA) were designed to work as a simple pure water tanks at an internal pressure of 1.1 bar absolute. The only loads they had to sustain were those generated by the magnetic field and by their own weight; these loads were evaluated at 200Nm on vertical axis for the Horizontal Camera Neutron Attenuator, as shown in the GRC KN3 NA Scheme Design report.

The material used for the Horizontal Camera Neutron Attenuator was INCONEL 600 sheet 5mm thick.

At a later stage, due to sampling issues, it was suggested to connect both the water tanks to the JET cooling water system that works at a pressure of 5 bars.

2. Manufacturing (testing) requirements

The Horizontal Camera Neutron Attenuator is an all welded structure made of INCONEL 600 sheet 3mm thick and should pass the following tests:

- penetrating liquids
- pressure 7.5 bar
- He leak

3. Functional requirements (no physics)

Four designs were developed complying with the following requirements:

- available space (when rotating by 90 deg.) to the Horizontal Camera concrete wall
- as little as possible material in the water tank
- avoid interference with the field of view of the detectors

4. FEA evaluated designs

The four designs were evaluated by FEA means; the primary design target was a low level of stress in the region of interest (lower than the yield strength of the material, 283MPa). A secondary design target was to minimise the quantity of material within the water tank and to avoid obstructing the fields of view of the gamma-ray cameras detectors.

All designs were based on:

- INCONEL 600 sheet 3mm thick
- 20mm diam. rod SS316
- an all welded structure

4.1 First Design: no reinforcement

The first design evaluated by FEA was a container with no reinforcements, internal or external. The results show that this structure is not suitable for an internal pressure of 750000Pa. The material used was INCONEL 600 with Modulus of elasticity 207GPa, Yield strength 283MPa, Ultimate tensile strength 655MPa, density 8340kg/m³. The FEA results show a lateral displacement of cca. 13mm and the maximum von Mises stress between 0.7 and 0.9GPa much higher than the yield strength of the material.

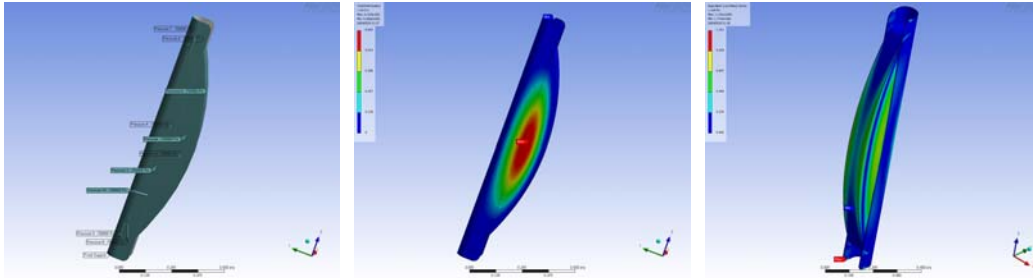


Figure 1 Loading scenario; displacement & von Mises stress

4.2 Second Design: internal reinforcement

To the same structure, as that from section 4.1, four internal fins were added and placed between the fields of view of the Horizontal Camera. The same material properties and loading scenarios were used.

The results show a lateral displacement of cca. 3mm and von Mises stress of 243MPa which is too close to the value of the yield strength of the material. An additional drawback was a larger quantity of material inside the water tank.

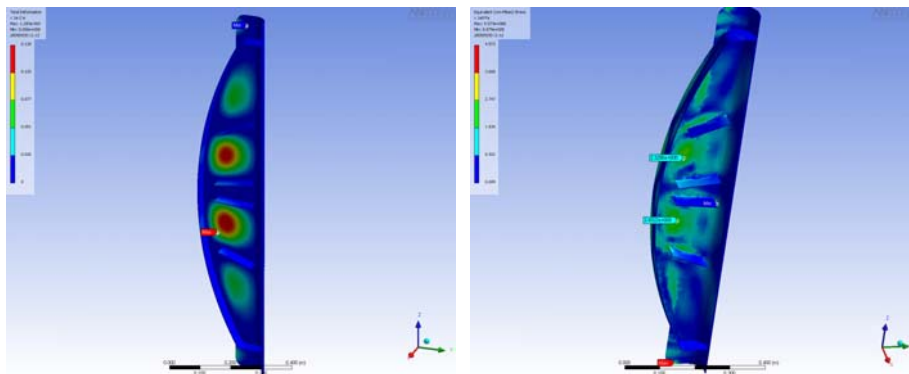


Figure 2 Loading scenario; displacement & von Mises stress

4.3 Third Design: external reinforcement

To the same structure, as that from section 4.1, each of the lateral faces was reinforced by a channel section, welded on the widest region, with the following dimensions: 750 x 20 x 3mm INCONEL 600. A string of five holes, diam. 20mm, were cut into channel section and later welded (square weld, 2mm) onto the lateral water tank faces to increase the contact surface.

The loading scenario and material properties are similar to those from the previous designs (internal pressure 750000Pa, moment on vertical axis of 200NM, standard Earth gravity). The results show a lateral displacement of 2.4mm, von Mises stress of 314MPa higher than the yield strength of the material.

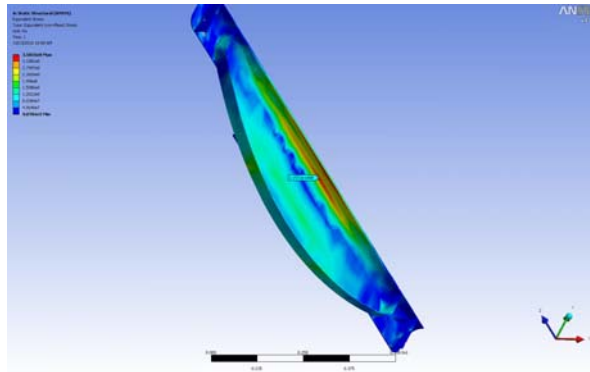


Figure 3 von Mises stress; back of the structure on the internal face von Mises stress level over a considerable are is 315 MPa

The safety factor lay below 1 on a large area in the rounded internal region to the back of the water tank.

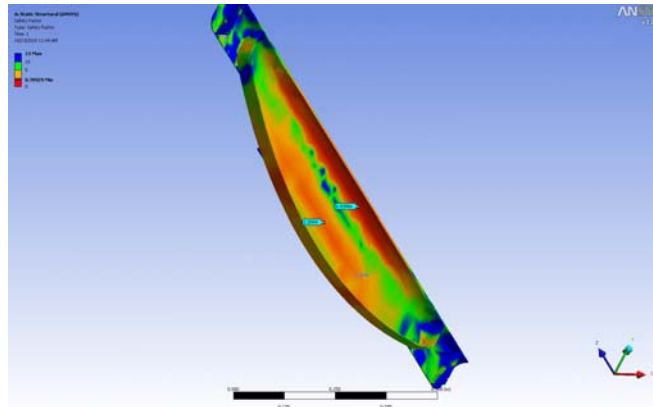


Figure 4 Safety factor; less than 1 back of the structure on the internal

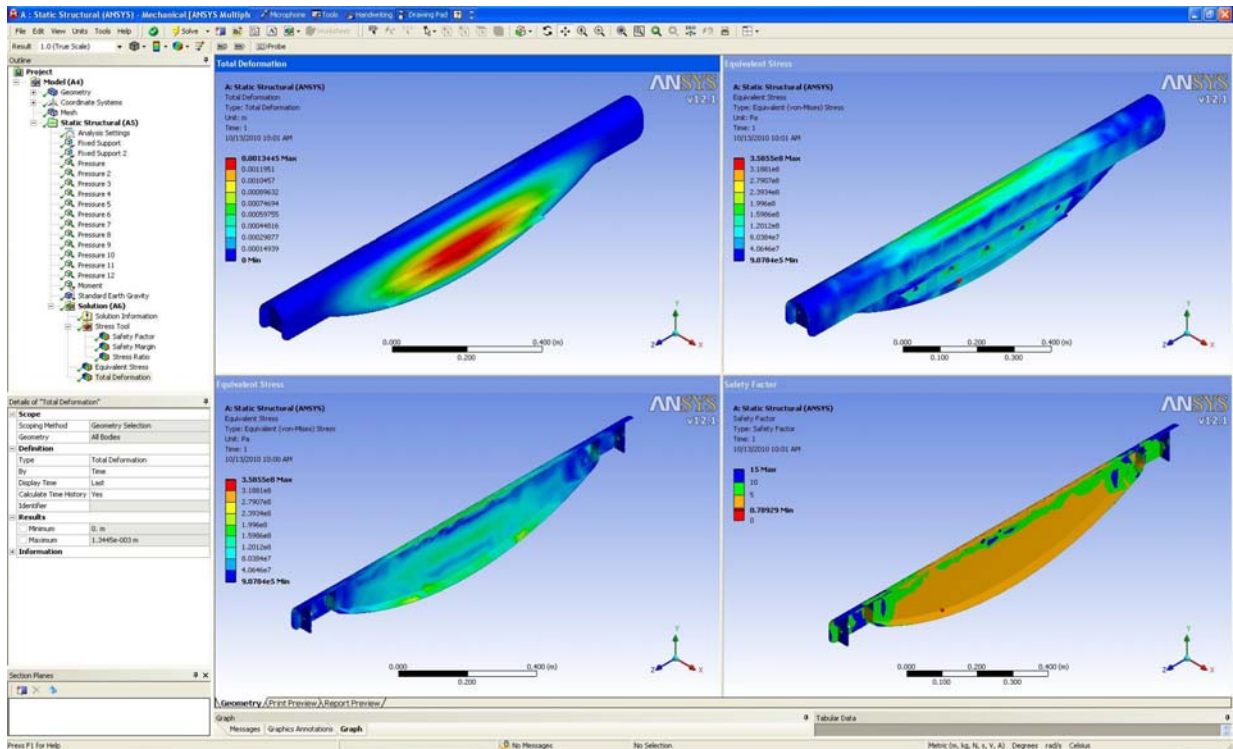


Figure 5 Summary of the results; displacement & von Mises stress full model and vertical sections

4.4 Fourth Design: internal and external reinforcement

The previous design, from section 4.3, had to be strengthened internally because the channel sections could not be extended due to available space restrictions. The loading scenario and the material properties are similar to those already used.

The results show a lateral displacement of maximum 0.3mm, von Mises stress of 140MPa and a safety factor of minimum 1.26.

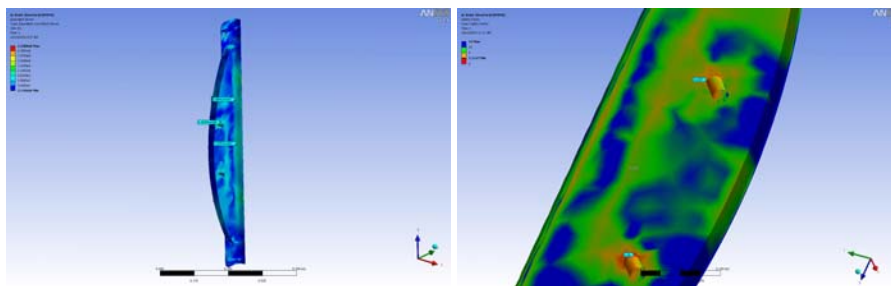


Figure 6 von Mises stress (140MPa) and safety factor

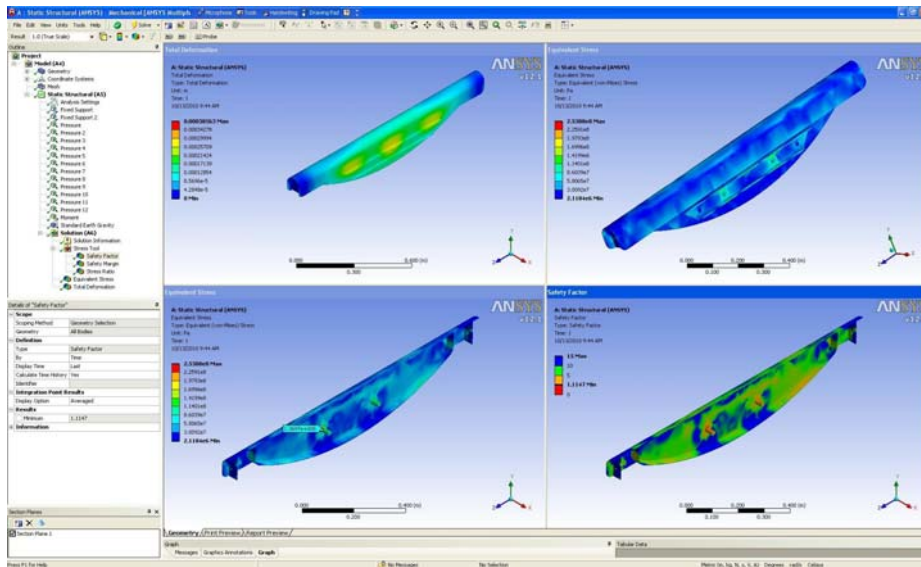


Figure 7 Summary of the results; displacement & von Mises stress full model and vertical sections

5. Current design (Internal & external reinforcements)

The last design (section 4.4) was developed before the manufacture process. The manufactured structure:

- clears the Horizontal Camera concrete face by 7mm when rotated by 90 deg.
- introduces the least quantity of material into the water tank. The design with four internal fins introduced a volume of material of 111cm³ compared to 50cm³ of the design with internal and external reinforcements
- the internal reinforcements do not obstruct the horizontal gamma-ray camera detectors fields of view. The internal rods clear the detectors field of view by 13mm, fig.8.
- does not cause turbulence due to the low flow (pure water inlet/outlet diameters are 6mm)
- passed all tests (test certificates): 7.5 bars pressure, He leak test and penetrating liquids test.

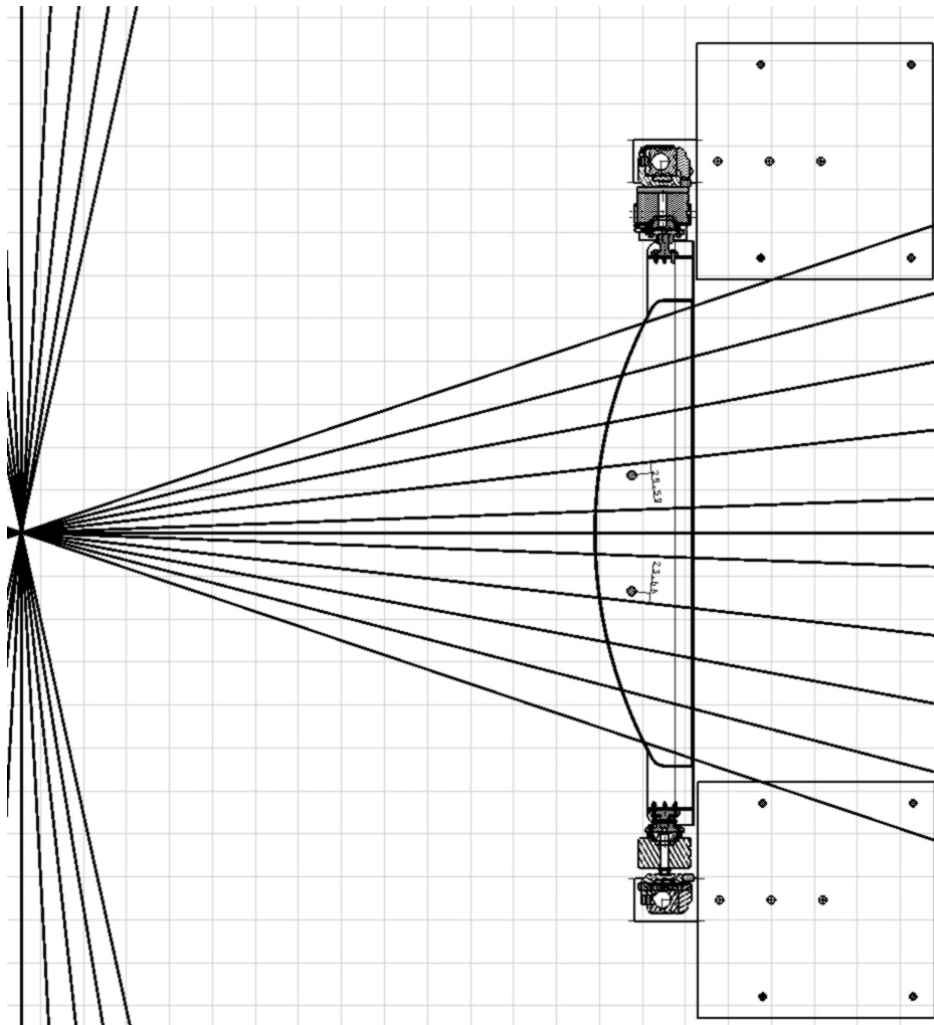


Figure 8 distance between the internal reinforcements and the horizontal gamma-ray camera detectors field of view

Manufacturing details:

- Assembly drawing, figure 9
- Components drawings: internal & external reinforcement, neutron attenuator lateral faces, figure 10 a, b, c.

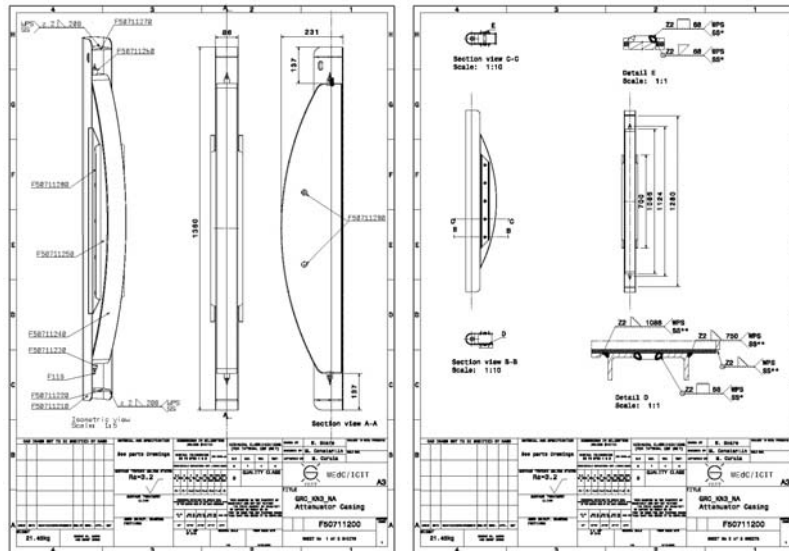


Figure 9 Neutron attenuators assembly drawing

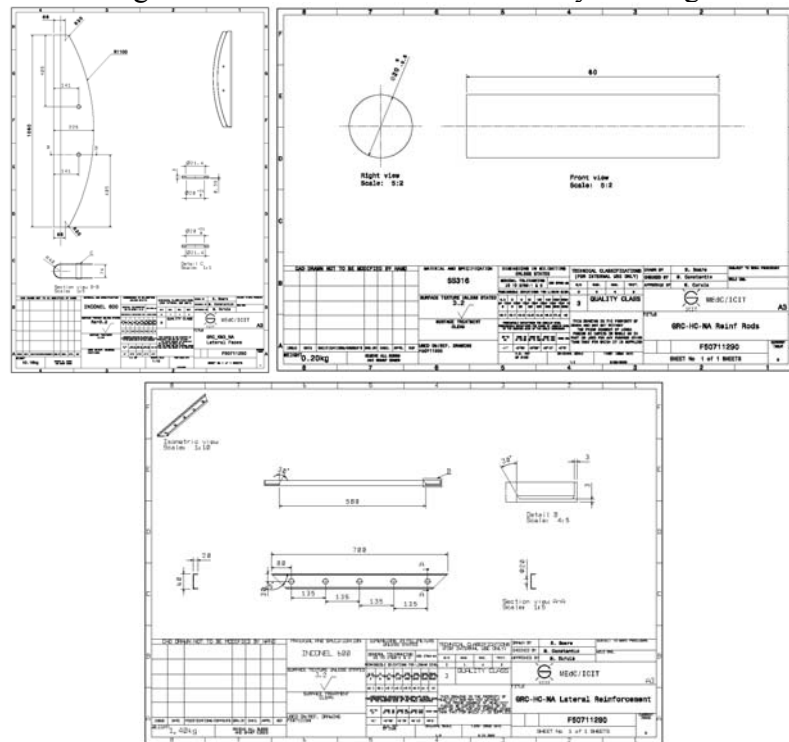


Figure 10 Components drawings

6. Conclusions

- Table 1 summarises the four evaluated designs.

Design No.	Max. Displacement (mm)	Max. Von Mises stress (MPa)	Minimum Safety Factor	Volume of Material in water tank (cm ³)

4.1 No Reinforcement	13	700 to 900	-	-
4.2 Internal Fins	3	243	-	111
4.3 External Channel Sections	2.4	314	0.9	-
4.4 Internal & External reinforcement	0.3	140	1.26	50

The last evaluated design, section 4.4:

- introduces the least material into the water tank
- does not obstruct the detectors field of view
- fits into the space box (when rotated by 90 deg. Clears the horizontal camera concrete face)
- passed all quality tests

EURATOM – MEdC ASSOCIATION
National Institute for Laser, Plasma and Radiation Physics

Title of the project:
“Plasma Wall Interaction –
Providing W coated CFC samples for fuel retention measurements”
EFDA Task Agreement Code: WP10-PWI-01-01-01/MEdC/BS

Interim Report for the period 01.07.2010 – 15.12.2010
(only MEdC tasks)

Authors: C.Ruset, E.Grigore, I.Munteanu, N.Budica

Head of the EURATOM-MEdC Research Unit,
Dr. Florin Spineanu

Project officer,
Dr. C. Ruset

Bucharest 2010

CONTENT

1. General objective of the project	3
2. Specific objectives for the period July – December 2010	3
3. Results and discussion	3
4. Conclusions	5

1. General objective of the project

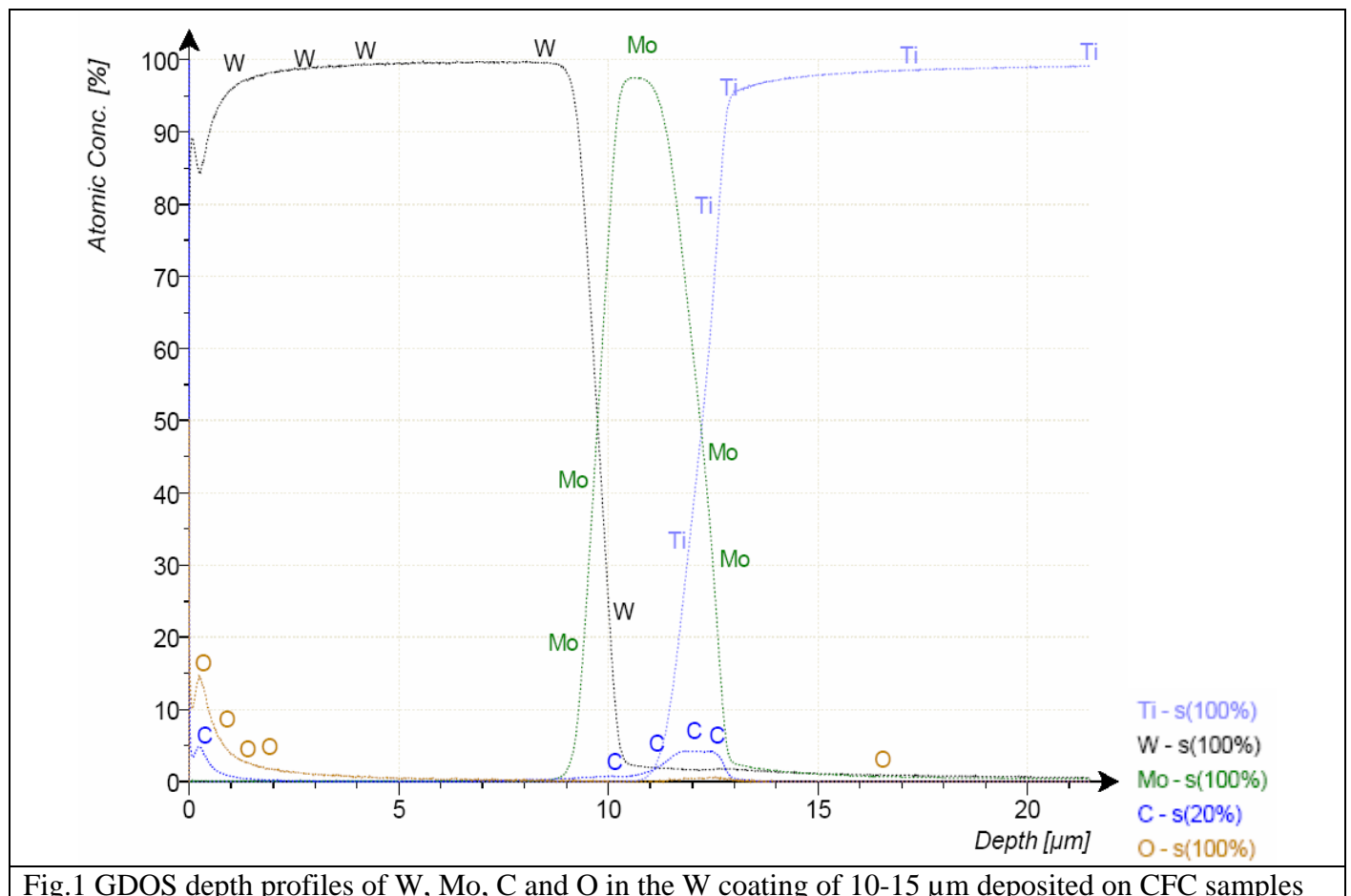
In the framework of the ITER-like Wall project approx. 2,000 CFC tiles from the new JET wall are coated with W layers of 10-15 μm and 20-25 μm using Combined Magnetron Sputtering and Ion Implantation (CMSII) technology. The change from carbon to metallic wall is expected to result into a significant decrease of the fuel retention. The W coatings deposited by CMSII technique are very dense, pore-free and have a nano-crystalline structure. The fuel retention was never measured on this type of coatings. Since a significant proportion of the ITER-like wall consists of W coatings it was defined as objective for the present project determination of the fuel retention for this type of coatings.

2. Specific objectives for the period July – December 2010

Specific objective for MEdC in the period July – December 2010 was to analyze the W coatings produced on CFC samples for fuel retention measurements.

3. Results and discussion

A number of 16 samples with approx. dimensions 59 x 10 x 5 mm and a special geometry have been manufactured from CFC material. Six samples were coated with a W layer of 10-15 μm and other six with 20-25 μm . A Mo interlayer of 2-3 μm was introduced at the CFC interface in both cases with the aim to improve the coating adhesion. In each coating run four Ti witness samples were placed in different positions in order to check coating uniformity. These samples are also used to measure the coating impurities especially carbon and oxygen. The concentration depth profiles for the coating constituents as they have been measured by Glow Discharge Optical Spectrometry (GDOS) are shown for the two types of coatings in Figs. 1 and 2.



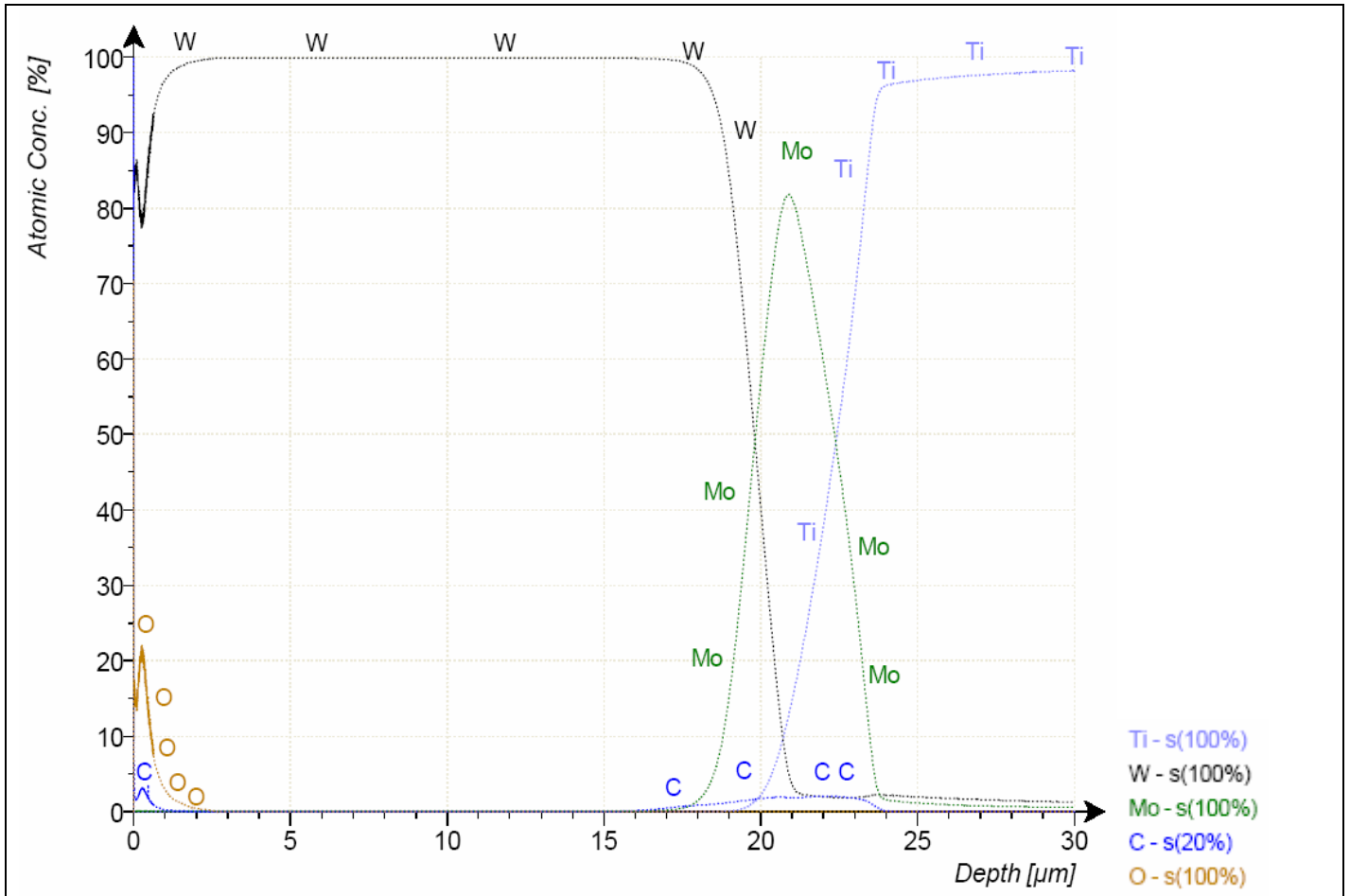


Fig.2 GDOS depth profiles of W, Mo, C and O in the W coating of 20-25 μm deposited on CFC samples

Small amounts of carbon and oxygen were detected at the surface of the samples due to the contamination produced when samples were exposed to the atmosphere after coating. A small amount of C (<1 at.%) was also detected at the Ti-Mo interface. This carbon was deposited on Ti samples from CFC tiles during the sputter-cleaning process.

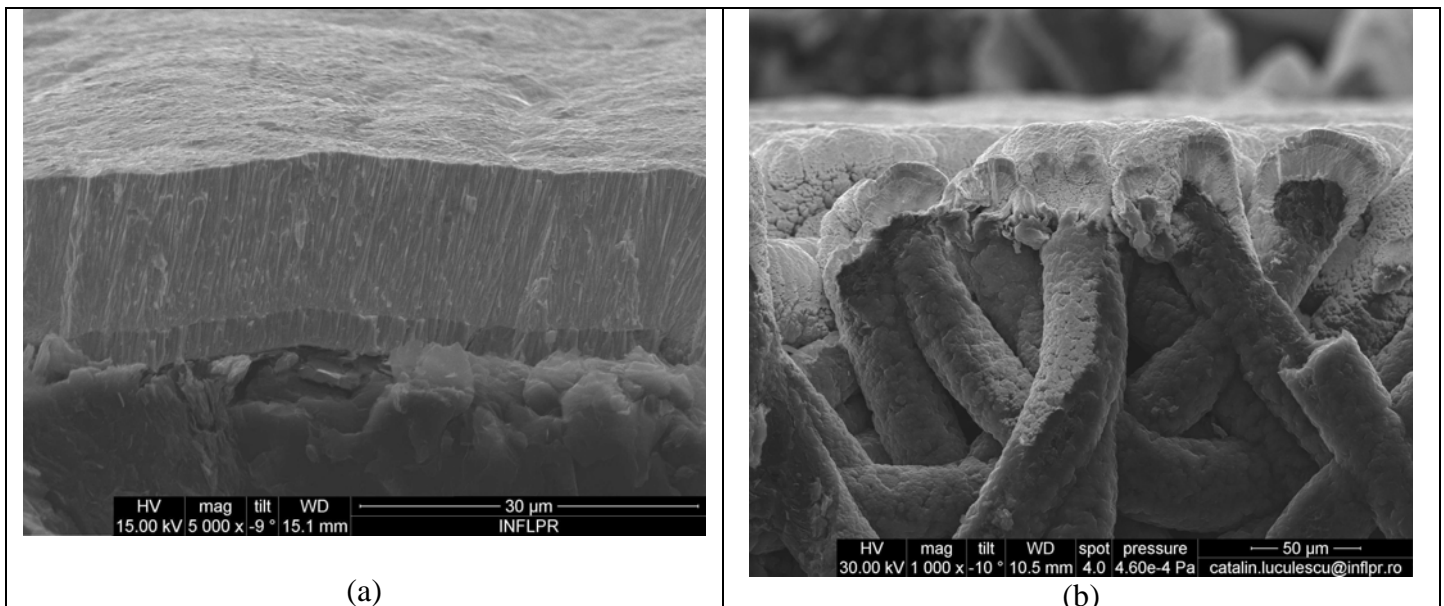


Fig.3 SEM images of the W coating deposited on CFC in graphite area (a) and fibers area (b)

It is expected that the fuel retention of the W coated CFC tiles to be affected by the structure of the CFC layer. SEM analyses of the W coating have been carried out in the graphite area and in carbon fibers area. The results are shown in Fig. 3. It can be seen that the coating is very compact, pore free and from this point of view the penetration of the fuel should be reduced. On the other hand, the CFC material is very porous. W coating closes small pores, but large pores with dimensions of tens of microns remain open to the atmosphere. This can be seen in Fig.3b. Consequently, the fuel can penetrate through these pores and remain trapped below the coating.

4. Conclusion

- Analyses of the deuterium retention were carried out at FZJ, but the final results are not available yet.
- This milestone of MEdC Association was accomplished.

EURATOM – MEdC ASSOCIATION
National Institute for Laser, Plasma and Radiation Physics

Title of the project:
**“Manufacturing and testing of W-coated CFC tiles for
installation in JET for the ITER-like Wall project”**

EFDA Task Agreement Code: JW6-TA-EP2-ILC-06

Interim Report for the period 01.07.2010 – 15.12.2010
(only MEdC tasks)

Authors: C.Ruset, E.Grigore, I.Munteanu, N.Budica, D.Nendrean

Head of the EURATOM-MEdC Research Unit,
Dr. Florin Spineanu

Project officer,
Dr. C. Ruset

Bucharest 2010

CONTENT

1. General objective of the project	3
2. Specific objectives for the period July – December 2010	3
3. Results and discussion	3
4. Dissemination of results	3
5. Conclusions	4

5

1. General objective of the project

As it was stated in the previous reports, the main objective of the project is W coating of particular tiles for the main chamber and divertor tiles for the new JET wall. In total there are approx. 1,800 tiles which have to be coated with layers of 10-15 μm and 20-25 μm .

2. Specific objectives for the period July – December 2010

The W coating activity in the second semester of 2010 was focused on the Main Chamber tiles and LBSRP divertor tiles. At the technical meeting which occurred at JET on 25.03.2010 it was decided that a lot of 62 divertor tiles had to be coated as spares. A priority list containing 288 remaining tiles to be W coated with 10-15 μm and 20-25 μm at that moment was issued. Priorities were organized on 6 levels. Finalization of the quality documentation for all the tiles delivered to JET was another objective for the reporting period. The final deliver date for the coated tiles was delayed from September to November 2010.

3. Results and discussion

The priority list induced some difficulties in the W coating production because the jiggling devices have to be changed frequently and this reduces the productivity.

During the reporting period a number of 162 tiles of which 66 for the main chamber and 96 for divertor have been coated and delivered to JET in 3 consignments. A particular attention was paid to the scintillator cup, a component with a special axial geometry, which had to be coated as uniform as possible. This component is shown in Fig.1. A special jiggling device with the axis at 35° with respect to the chamber axis was designed and manufactured. Before coating the real CFC scintillator cup, an identical prototype made of fine grain graphite was coated. On this prototype a number of 6 Ti witness samples were positioned in different locations with the aim to check the coating uniformity. After coating, it was found out that the coating thickness was in the range of 7.7 – 12.5 μm . The real CFC scintillator cup was coated with the same device but the process duration was increased so the final coating to be in the range of 10 – 16 μm . It should be noticed that the CFC for the scintillator cup (A035) was different from DUNLOP CFC used for the other components. The W coating deposited on this material was successfully tested at high heat flux (HHF) in GLADIS at IPP Garching before coating the scintillator cup.

The CFC material was not only anisotropic, but in some cases the appearance of its structure for particular areas was clearly different of the other areas. In these cases small blisters (1-5 mm) along one or two fibers were detected at visual inspection after coating. The weakness of the coating in those areas was proved by HHF tests.

The quality documentation was finalized for the last 6 consignments (No. 4 to No.9). This documentation included: quality plans, certificates of conformity, inspection release notes, deviation permits, list of tiles versus coating thickness and certificates of cleaning the tiles for each consignment. As annexes to the quality plans the inspection reports and GDOS profiles were issued for each coating run. This documentation was discussed, signed and delivered in a technical meeting at JET which occurred on 8.12.2010.

Approximately 10% of the coated tiles were sent to IPP Garching for high heat flux tests in GLADIS. No other defects were detected except those already revealed at the visual inspection.

4. Dissemination of results

- Participation at the Symposium on Fusion Technology, SOFT 2010 in Porto, Portugal in the period 27.09-01.10.2010. A paper entitled “Development of W coatings for fusion applications”, authors: C. Ruset, E. Grigore, H. Maier, R. Neu, H. Greuner, M. Mayer, G. Matthews was presented in a poster session. It is accepted for publication in Fusion Engineering and Design journal.



(a)



(b)

Fig.1 Scintillator cup on the jigging device (a) and coated (b)

5. Conclusions

- 1) „ITER like Wall” project is very important for both ITER and JET. It will provide information about the plasma-wall interaction under these particular conditions, about the transport of the wall particules through the plasma and about the capacity of these materials to sustain the real thermal loads they are subjected at.
- 2) EURATOM MEdC Association brings a significant contribution to the project by coating with W (10-15 μm and 20-25 μm) all the tiles which had to be coated. This means about 1,800 tiles of different shapes and dimensions. All the tiles including spears were coated and delivered to JET together with the quality documentation. All the deliverables and milestones were accomplished. The final report will be issued by 17.01.2011. The project is finished.

CONTENT

1. Project Objectives.....	2
2. Objectives of Step 2	2
3. Summary of the performed work in Step 2	2
4. Scientific description	3
CONCLUSIONS.....	6

1. Project Objectives

The aim of this project is to study the behaviour of materials with relevance for the construction of fusion reactors (Tokamaks). Tritium and deuterium retention and release (detrutiation) will be investigated with emphases on the potential safety and environmental benefits of fusion power production. The experimental method to be used in this material research project is the most sensitive analyzing method known today, called Accelerator Mass Spectrometry (AMS). Its sensitivity is 10^{-15} for the isotope/element ratio and measures, one by one, every atom produced from the material to be analyzed. With its level of high analysing sensitivity AMS is the only experimental method capable to determine with very good efficiency the Tritium concentration.

Conventional ion beam techniques such as Rutherford backscattering (RBS), Nuclear reaction Analyses (NRA) and elastic recoil detection analyze (ERDA) can hardly measure Tritium.

AMS, due its functioning way, is able to scan the concentration of the isotope (T, D, etc) in the depth of the investigated material and deliver the depth profile of the concentration. By this measurement, of the depth profile of the implanted Tritium and Deuterium into the bulk of materials, AMS determines also the energy of the incident particles (incident energy- penetration depth relation). Therefore it can be applied as an efficient diagnose tool for the fusion experiments in Tokamaks. Diagnose and analyse are produced off-line, at the end of discharging campaigns in the Tokomak. Small cuts (10 x 10 x 4 mm) from the plasma facing components (PFC) are enough for an AMS analyse. It was proven that AMS suitable addresses material research topics declared as crucial issues by the European Development Agreement (EFDA) like: "Analyzes of selected plasma components (PFC) , material samples to support transport studies and in situ detrutiation activities" and " Development of in-situ diagnostic for the characterisation of deposited layers and/or coatings.

These kind of experimental material research are today of an imperative need since the construction of the first test fusion reactor ITER was started 2009 at Cadarache in the south of France. The reactor is expected to start operating in 2018 and many issues of research are still open in material behavior at high plasma temperatures and exposed to intense fluxes of ionized particles.

The general project objectives are as follows:

- Selection and preparation of samples from the divertor tiles of JET.
- Preparation of standards (adequate for the samples from JET).
- AMS analyzing experiments to determine the Tritium concentration Dept Profiling in divertor tiles form JET
- Complete distribution of Tritium retention in the divertor tiles from JET
- Data interpretation and conclusions.

2. Objectives of Step 2

The objective of actual stage is completion of depth profiles of the T content in the JET 2007 divertor tiles.

3. Summary of the performed work in Step 2

AMS sample were cutted form the divertor tiles from. Samples form capganes from 2007 were prepared for measurement by AMS. AMS analyzing experiments to determine the Tritium concentration Dept Profiling in divertor tiles form JET was performed.

The depth scanning is done by sputtering with accelerated ^{133}Cs ions on the sample surface at its location in the ion source. Measuring continuously the produced rare ions of Tritium one will register in the detector different beam currents according to the concentration at the depth of scattering.

Following samples were measured : 3 samples from tile 2IWG1A , 1 sample from tile 2IWG3A, 2 samples from tile 2BNG6D, 3 samples from tile 2ONG7A and 2 samples from tile 2ONG8A.

4. Scientific description

Divertor tiles from the Divertor 2007 were measured by AMS. Samples were cut from the divertor tiles were measured for the T content by the AMS depth profiling method.

The depth profiling was performed with an increased sputter speed in order to explore larger depth into the sample bulk. Following samples were measured : 3 samples from tile 2IWG1A , 1 sample from tile 2IWG3A, 2 samples from tile 2BNG6D, 3 samples from tile 2ONG7A and 2 samples from tile 2ONG8A.

The measured values indicate a different distribution of the Tritium over the divertor ensemble as compared to the divertor from 2004.

A major difficulty of the experiment was the very small size of the delivered samples by JET. In Photo no.1 are presented few of these samples. For depth profiling a scanning of the produced crater into the bulk of the sample has to be measured in order to calibrate the AMS measurement from the time scale to depth. Since the samples were in size very , very small, the base line of the optic profilometer was nearly impossible to be established. Therefore, the carter profilometry has many fluctuations and uncertainties.



Photo no.1: Some of the measured samples in this experiment.

Fig.1 presents some of the measured sample craters produced by sputtering with the ^{133}Cs in the AMS ion source.

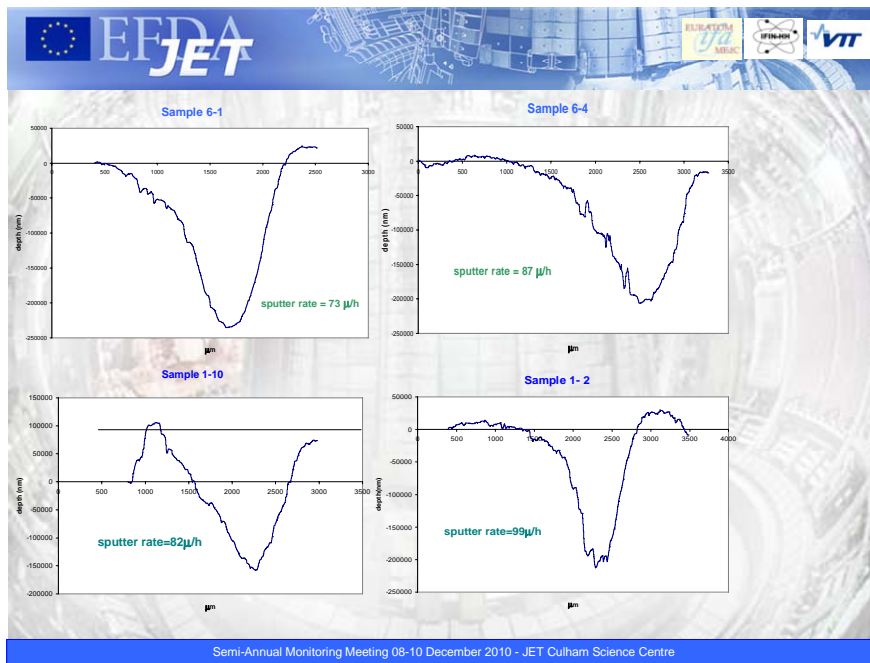


Fig. 1

The depth distributions for T content are shown in the fig.2 and fig.3. All data were background corrected and were calibrated with the last standard sample available in our laboratory.

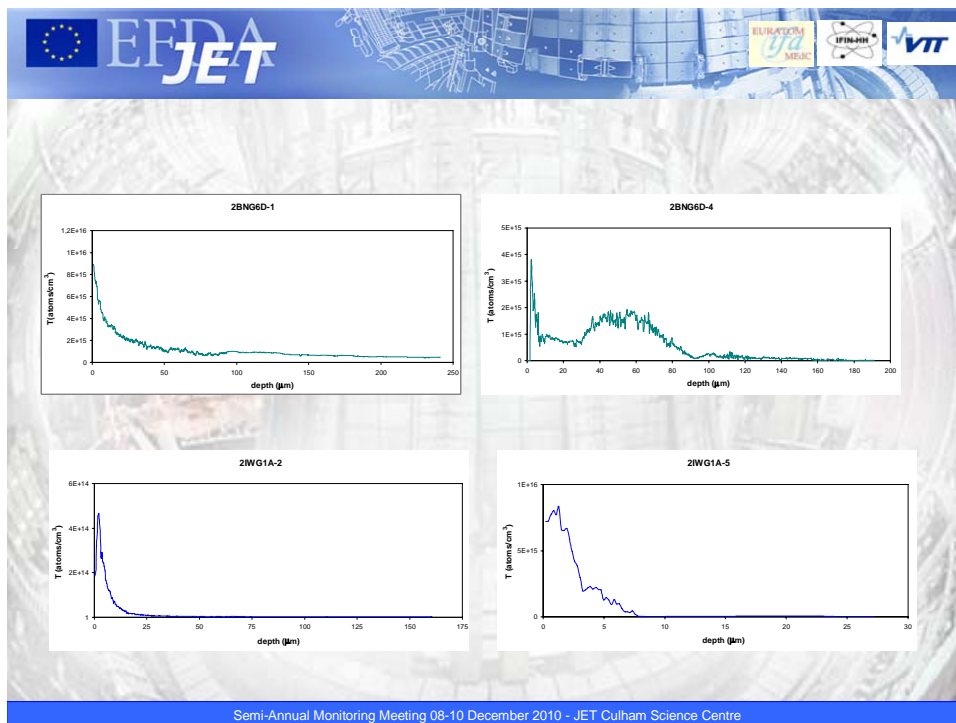


Fig 2

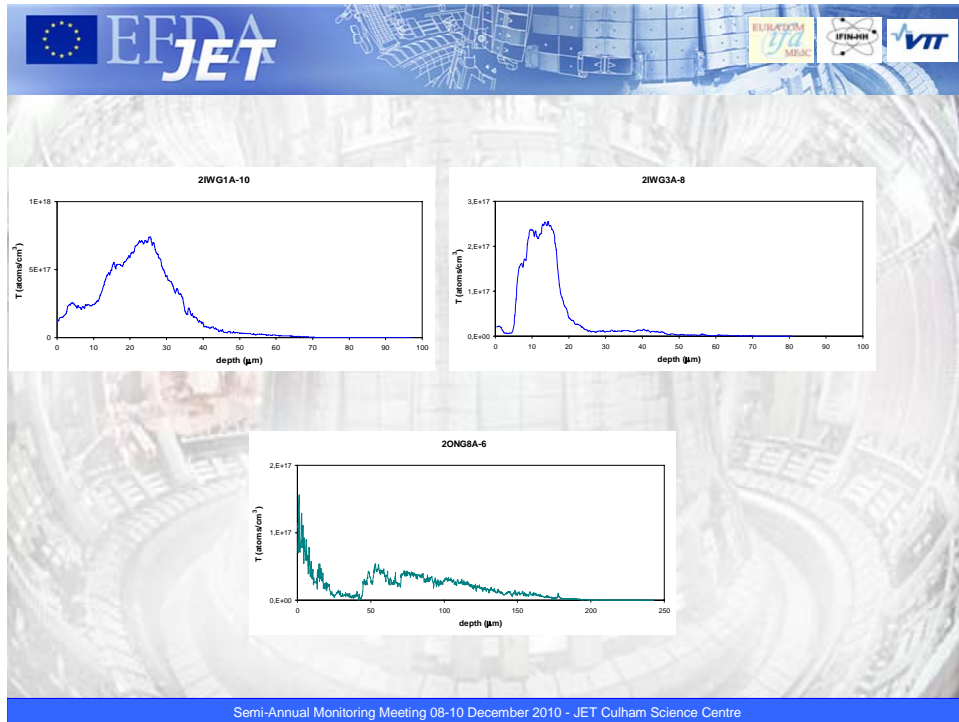


Fig 3

As can be seen sputter rates were in average 90µm/h and the explored depth were larger than 60 µm. From these depth distributions by integrating over the entire exported depth we obtain the T inventory expressed in atoms/cm².

These values are presented in fig.4 according to their locations in the divertor 2007.

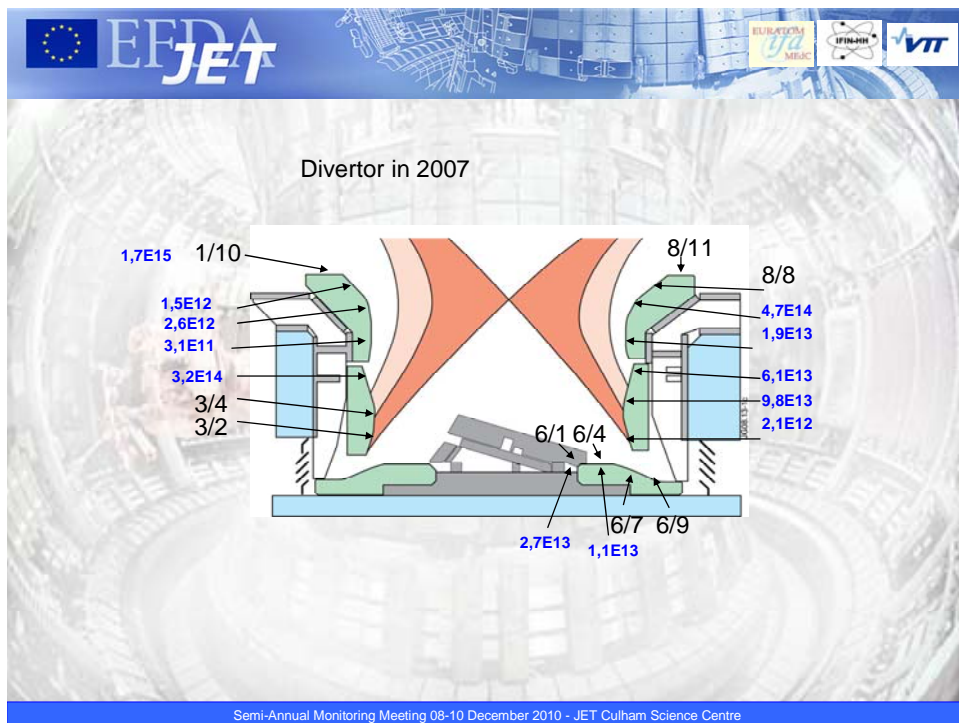


Fig.4 The T integrated depth distributions for T retention in the divertor tiles.

The distribution function of all these results over the entire Divertor 2007 and compared to the distributions obtained for the divertor 204 are given in fig.5

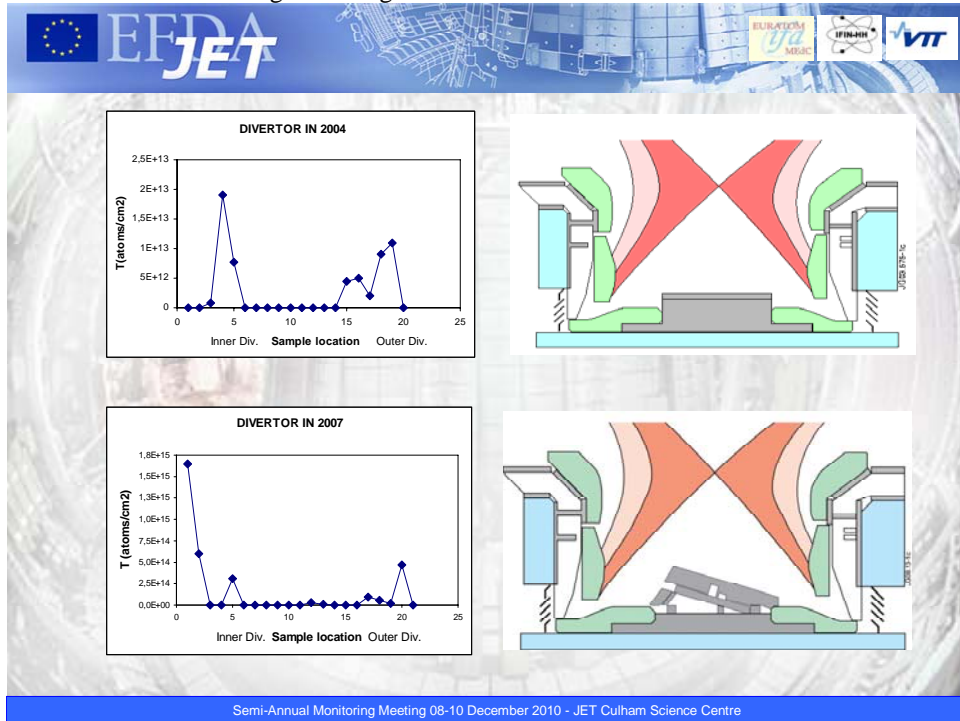


Fig.5 The T retention in divertor tiles from the 2004 and 2007 divertor configurations. It is evident that an important quantity of T is retained in the tile 2IWG1A-10

CONCLUSIONS

This report presents the scientific work performed for the first TASK of the project entitled: Tritium depth profile measurements of JET divertor tiles.

The performed tasks were the preparation of standard samples and preparation of samples from the divertor tiles of JET. Both tasks were fully accomplished. A two-piece set of standard samples for measuring T concentration depth profiling were chemical prepared, calibrated and tested experimentally. The entire AMS system is now ready to start in the next step the measuring the T concentration in protection tiles from JET.

Periodic Report of MEdC/ICIT Trainee in Training Network

“Tritium Technologies for the Fusion Fuel Cycle”

- Annual Report 2010 -

MEdC/ICIT Trainee in TRI-TOFFY network - Work package No. 5, Experimental Pilot Plant for Tritium and Deuterium Separation, such planned:

TRAINING PERIOD COMPLETED



- **Introductory/accompanying training at ICIT**
(duration: 5 months in total)

This scheduled objective has been already achieved in accordance with the Individual Development Plan and communicated into the last report to MEdC/EUROATOM

- **Introductory/accompanying training at KIT**
(duration: 45 days in total)

This scheduled objective has been already achieved in accordance with the Individual Development Plan.

- **Research training at ICIT**
(duration: 17 months)

This scheduled objective has been already achieved in accordance with the Individual Development Plan and in the last report 11 months of first training period in ICIT have been communicated. In this report the last training period in ICIT of 6 months will be communicated.

TOTAL: 22 months ICIT + 45 days KIT

Activity Report for Research training at ICIT

- THE ACTIVITY OF THE LAST TRAINING PERIOD AT ICIT RAMNICU VALCEA (FOR 6 MONTHS)

1. Study of equipment associated with low-temperature systems used in cryogenic facilities

2. Experimental activities

2.1 Participation to calibration tests of quadrupole mass spectrometer

2.2 Further experimental investigation regarding the influence of hydrogen isotopes over the use of active charcoal packing in tritium extraction and short term storage systems

3. Design activities

4. Presentations sustained and papers published

5. Bibliography and references

1. Study of equipment associated with low-temperature systems used in cryogenic facilities

ICSI Ramnicu Valcea extends the research capacity in the field of tritium and deuterium extraction and storage with the purpose of decontaminating tritiated heavy water resulted from CANDU allowing the recovered tritium to be used for fusion reactors. The “CRYO-HY” structural funds project implemented at ICIT Ramnicu Valcea will have a great impact factor over all the technology development in the cryogenic research domain in the European Union. The purpose of an 14.5 million euro technology and construction investment is to develop the biggest European low-temperatures laboratory for cryogenic fluids and also to increase the processing power of the actual “*Experimental Pilot Plant for Deuterium and Tritium Separation*”, also called Tritium Removal Facility (TRF) available at ICIT Ramnicu Valcea for the ITER future demands. Having an opportunity to use my knowledge regarded to the cryogenic distillation systems functionality and equipment assembly, accumulated in the “TRY-TOFFY” training till now, I’ve been direct implicated in activities regarding the upgrading of the refrigeration unit in this structural funds project “CRYO-HY” at ICIT Ramnicu Valcea. The new refrigerating system that will be acquisitioned is based on the cryogenic helium cycle with a power of 1000 W at 20 K, and is designed to provide various operating modes of cryogenic distillation at different flows. Helium gas provided by the refrigerator feeds the condensers of the

distillation columns, having the main role of condensing the vapours which run in counter flow with the liquid in the columns for cryogenic distillation.

The new refrigeration system, based on Helium cycle will be installed in the existing Hydrogen separation experimental pilot building and the related compressor will be positioned in a special designed light-room with natural ventilation.

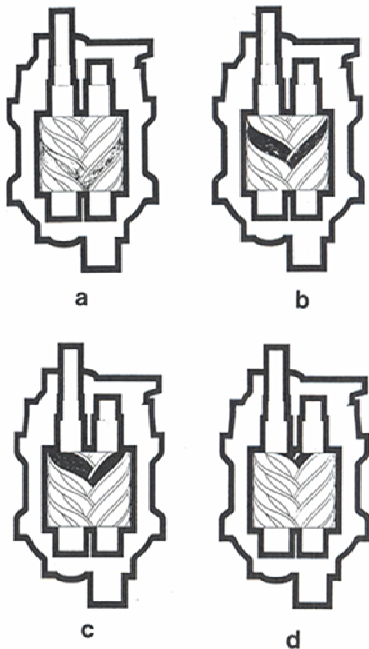


Figure 1: Linde L5 Helium liquefaction system in Low-temperature Lab of ICIT Ramnicu Valcea

The proposed investment will triple the refrigeration power of the cryogenic distillation facility, which will allow for development of experiments in conditions that are close to those in the future fusion reactors.

Having as data base support an older version of a Linde L5 type liquefaction system at ICIT Ramnicu Valcea, I've understood that the key factor of a smooth functioning of the cryogenic cascade is the cooling unit used. Having as documentation of the Linde L5 description of the components, thermodynamic scheme, the scheme of interconnection of the elements characteristic parameters operating mode, and some of the results in conducted experiments, I've made an analysis, regarding: the functional optimizing and structural characteristics of the helium cryogenic plant, cryogenic facility with real behavior of Helium, actual operation of the cryogenic helium plant, liquefaction plant and rolling through adiabatic relaxation - reduce irreversibility of the working processes of cryogenic helium installations.

Liquid helium production plant, Linde type L5 is fully automated and operate in the purification and liquefaction of evaporated helium gas storage system. It is using a single step screw compressor in the process of liquefying. The compressor the repress approximately 10g / s helium at a pressure between 10 ÷ 12 bar and a temperature of about 300K. Basic equipment of Linde L5 (figure 1) consists of: liquefying equipment, transfer lines, storage vessels, auto air purifier, compressor oil separation unit, oil absorber, electronic control unit. As conclusion of study, one of the most important equipment used in refrigeration unit configuration beside the liquefactor, that has a major impact over the optimized functionality of the refrigeration system is the compressor. Compression accounts for most of the energy requirements in refrigeration and liquefaction of gases in cryogenics facilities. I've identified this equipment importance and



Step-by-step view of the compression process within a screw compressor

Figure 2: Screw compressor compression

also be removed prior to the point-of-use. The process of compression is follows this path:

- gas enters at the suction side and moves through the threads as the screws rotate
- clearances between the threads decrease and compress the gas
- the gas exits at the end of the screws compressed

The effectiveness of this mechanism is dependent on precisely fitting clearances between the helical rotors and the chamber for sealing of the compression cavities. The rotary screw compressor has low leakage levels and low parasitic losses comparative with other types of compressors (example roots-type compressor). The work involvement in the “CRYO-HY” project was an opportunity for me to better understand the functionality and assembly importance of equipments used in cryogenic facilities, improving and verifying in this way the actual knowledge gain in the “TRY-TOFFY” training till now.

2. Experimental activities

2.1 Participation to calibration tests of quadrupole mass spectrometer

Cryogenic Pilot Plant of ICSI Rm. Valcea is an experimental plant for separating tritium and deuterium from tritiated heavy water by LPCE-CD method (Liquid Phase Catalytic Exchange – Cryogenic Distillation).

One of the key tasks in characterizing the separation performance of hydrogen isotopes by cryogenic distillation is the ability to measure with high accuracy the concentrations of molecular species of hydrogen isotopes.

I've based my study on it to get familiar with the types of compressor used in equipment associated with low-

level temperatures. In our new refrigeration unit, the

compressors used will be screw compressors (figure 2), because of the high quality of compression and low energy and maintenance cost. A rotary screw compressors use two helical screws, known as rotors, to compress the gas. Because we have special demand of quality compression and purity of the gas will use dry running rotary screw compressor. In an oil-free compressor, the air is compressed entirely through the action of the screws, without the assistance of an oil seal. They usually have lower maximum discharge pressure capability as a result. However, multi-stage oil-free compressors, where the air is compressed by several sets of screws, can achieve pressures of over 150 psig, and output volume of over 2000 cubic feet (56.634 cubic meters) per minute (measured at 60 °C and atmospheric pressure). However, this does not preclude the need for filtration as hydrocarbons and other contaminants ingested from the ambient air must

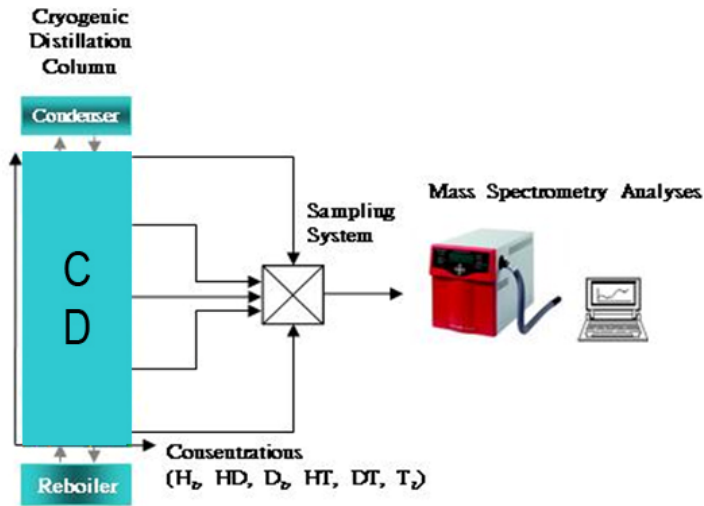


Figure 3: Measurement system

uses. These include identifying unknown compounds, determining the isotopic composition of elements in a molecule, and determining the structure of a compound by observing its fragmentation. Other uses include quantifying the amount of a compound in a sample or studying the fundamentals of gas phase ion chemistry (the chemistry of ions and neutrals in a vacuum). In future experimental campaigns in the cryogenic pilot plant for tritium and deuterium separation a GSD 320 quadrupole mass spectrometer will be used to determine the concentration profiles of hydrogen isotopes species along a cryogenic distillation column (figure 3).

Mass spectrometry (MS) is an analytical technique that measures the mass-to-charge ratio of charged particles. It is used for determining masses of particles, for determining the elemental composition of a sample or molecule, and for elucidating the chemical structures of molecules, such as peptides and other chemical compounds. The MS principle consists of ionizing chemical compounds to generate charged molecules or molecule fragments and measurement of their mass-to-charge ratios. The technique has both qualitative and quantitative

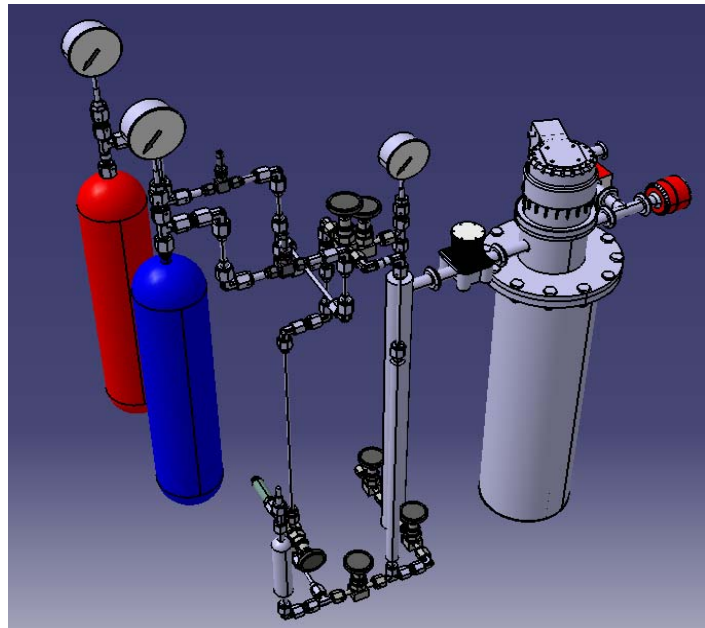


Figure 4: Proposed 3D model of Experimental Rig for GSD320

I've become familiar with this measurement technic and realised that the major issues of mass spectrometric analysis of hydrogen isotopes mixtures are the isobaric interferences due to ionic species that are produced inside the ion source by dissociation of molecules or by reactions between ions and neutral molecules.

The mass spectrometric performed analysis of the gas mixtures of hydrogen isotopic species H_2 , HD and D_2 have involved the measuring of the mass-2, -3 and -4 ion current signals generated by H_2^+ , HD^+ and D_2^+ ions, but these currents are affected by isobaric interferences.

Unfortunately, the used GSD 320 mass spectrometer has a lower resolving power than required for the separation between these close masses. So that, algorithms for determining these interferences and for correcting the main mass ion currents are necessary.



Figure 5: Experimental Rig for GSD320

A first approach of this issue was made by using mixtures of hydrogen & argon, deuterium & argon, and hydrogen & deuterium, at a constant pressure at the inlet of mass spectrometer (and, consequently, at a constant pressure inside the analytic of the mass spectrometer). A 3D design of a experimental rig was required to understand better the set-up for the calibration experiment for the GSD 320 (figure).

The quadrupole mass spectrometer had no feature for controlling the total pressure inside the analytic chamber and this could be kept at a constant value only by trying to maintain, all the time, a constant pressure at the inlet of mass spectrometer. Having in this way a issue regarding the difficulty in sampling of the gas from several points on the cryogenic separation column at the same (and constant) pressure, to

investigate another approach that consists of determining the isobaric interferences at variable pressure was a necessity. That has been resolved with the experimental rig (figure 5) constructed based on the proposed 3D model (figure 4).

2.2 Further experimental investigation regarding the influence of hydrogen isotopes over the use of active charcoal packing in tritium extraction and short term storage systems

I continued my research regarding active charcoal packing absorption capability of hydrogen isotopes at low temperature between 85K – 77K. because of my key task in the training program in this period at ICIT Ramnicu Valcea to design and implement a tritium extraction system in the TRF, I've had the opportunity of a better view of the equipment and the safety issues involving working with tritium. Having a study of the results obtain in the first experiments at ITER with the cryopumps, the best pumping condition were achieved using packing of active charcoal. Because of the accessible pore size at cryogenic temperatures, the active charcoal in the experiment made on the cryopumps relived that is a perfect packing for short term absorption of the hydrogen isotopes. After designing a 3D model of a absorption rate test bench in CATIA V5, I had the opportunity to participate to the physical assembly of capability of absorption of hydrogen isotopes and the tests with the activated charcoal as main probe for minimum absorption rate determination.

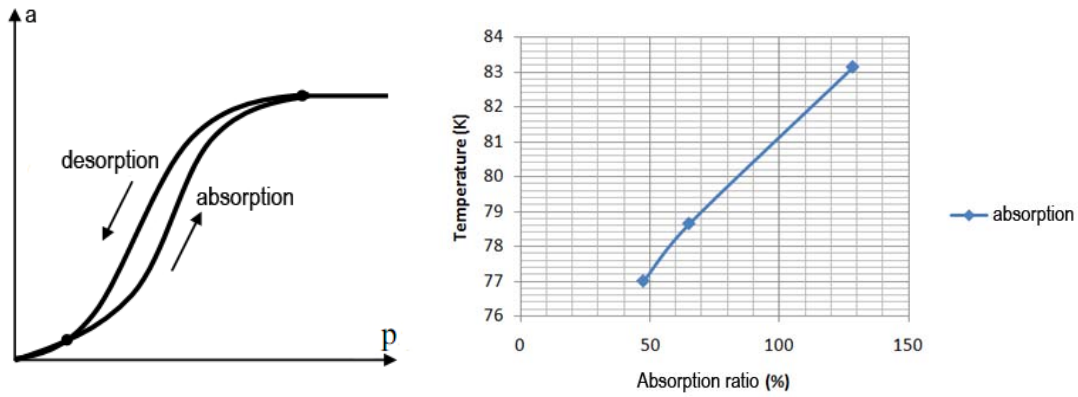


Figure6: Absorption ratio diagram depending on temperature

After the experiments I've observed a slow decreasing of the absorption efficiency and a irreversible hydrogen sorption that takes place at charcoal exposure in the H₂ or D₂ gas at 77 K (figure 6). This result demonstrated that active charcoal packing has the capability of hydrogen isotope storage, but in special condition. Based on this i had to define the position of the new extraction system in the TRF configuration (figure 7).

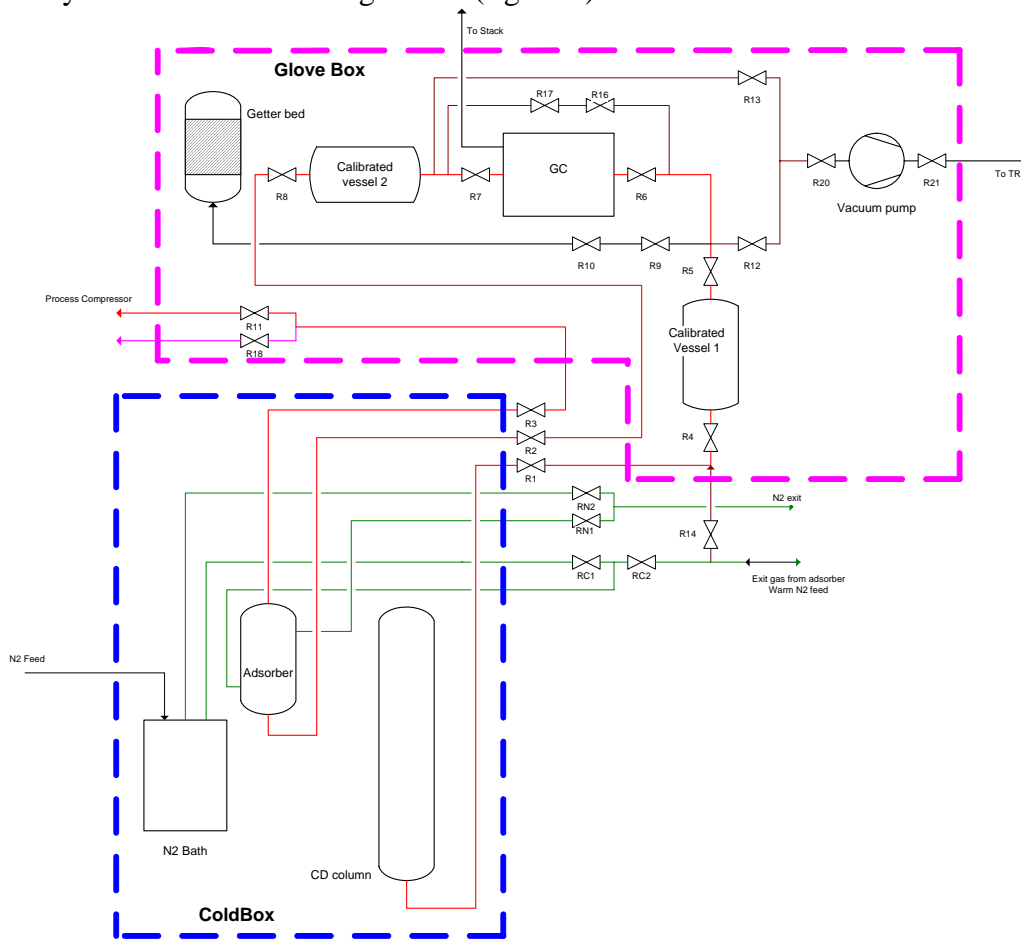


Figure 7: Tritium extraction and measurement system defined positioning

Tritium extraction system based on active charcoal packing can be an economical and technological suited choice because, of the large availability of charcoal, the enormous specific surface for absorption and simple design of the extraction system. On the other hand the major

problem are related to the big space occupied by the system, the very short-term storage option for tritium storage and the need of good heating-cooling system for absorption-desorption cycle.

3. Design activities:

I had the opportunity to use my CATIA skills to design also the 3D layout of the actual Cryogenic Distillation system of the TRF at ICIT Ramnicu Valcea. The need of the 3D layout comes with the new upgrade of the refrigeration unit. Because of the complex structure (figure 8) of the CD module of the TRF, several simulation will be made to find a way to safely deploy all the new equipment and also to preview a configuration of the system. The realization of this layout meant the study of all documents regarding to the Experimental Pilot Plant construction and equipment configuration and gave me the opportunity to better understand the importance of optimum location of refrigeration unit in CD system assembly and efficient functionality.

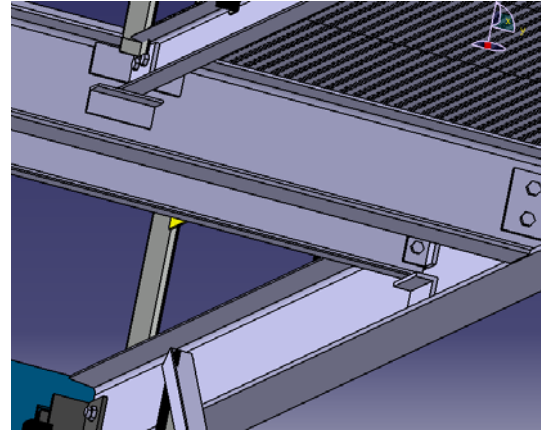


Figure 8: Structure view of 3D layout

Another topic of the program spent at ICIT Ramnicu Valcea was also to improve the characteristics and production of the hydrophobic catalysts used in the isotopic separation process in TRF. Using CATIA I've design and proposed a model of an automated catalyst manufacturing devices,

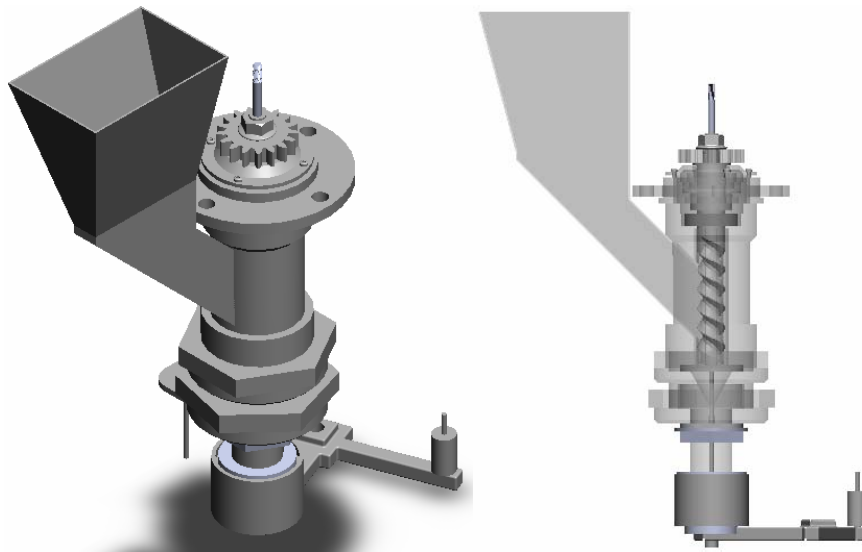


Figure 9: Automated catalyst manufacturing device

that was realized taking in consideration all the data gathered from the experiments regarding the fabrication and sinterization process of catalysts. This new “briquette” catalyst manufacturing installation is based on screw drill dosing component determining the some of the physical standard characteristics of the hydrophobic catalyst before entering the sinterization phase.

4. Presentations sustained and papers published

I had the opportunity to participate to this events:

1. Title of the presentation: “Tritium Technologies for the Fusion Fuel Cycle”
Location: Iasi at “Association days of EURATOM/MEdC ROMANIA”, 6th Edition, 2010
Sustained at: 02.06.2010
2. Title of the presentation: “Experimental H₂ and D₂ extraction rig with active charcoal packing”
Location: Ramnicu Valcea at “The 16th National Conference with International Participation *“PROGRESS IN CRYOGENICS AND ISOTOPES SEPARATION”*”
Location: Calimanesti-Caciulata, Valcea, Romania
Sustained at: 15.10.2010
3. Title of the presentation: “4th Periodic Report” in the framework of TRI-TOFFY network
Location: CEA Cadarache, France
Fuel Cycle / TRI-TOFFY network meeting
Sustained at: 15.11.2010

➤ So far I had the opportunity to publish this papers:

1. **I. Spiridon**, S. Brad, I. Stefanescu, „Experimental H₂ and D₂ extraction rig with active charcoal packing”, proceedings of Progress in Cryogenics And Isotopes Separation, 2010;

5. Bibliography and references

1. Romulus George Ana, Ion Cristescu, Lothar Dörr, Robert Michling, Stefan Welte, Werner Wurster – “Design and experimental activities in view of Water Detritiation–Isotopic Separation Systems combination in TRENTA facility”, Fusion Engineering and Design, 2009
2. Barron, Randall F. – ‘Monographs on Cryogenics 3 – Cryogenic Systems 2th edition’, Oxford University Press, 1985
3. Cristescu, Ion, a.o. - Detailed Design of Water Detritiation system for JET
4. ***, - ‘Selected Properties of Hydrogen (Engineering Design Data) – National Bureau of Standards’, Monograph 168

RST in extenso

TT19 5.1b

TITLE : PRODUCTION OF BERYLLIUM COATINGS FOR BERYLLIUM TILE MARKERS FOR THE ITER-LIKE WALL PROJECT

ETAPA II: (Decembrie 2010)

Ni and Be coatings on marker tiles provided by JET

Abstract

The aim of the project represents the coating with 2 μm Ni films followed by coatings of 8 μm Be films on marker tiles made of full beryllium blocks, using the thermionic vacuum arc method (TVA). The marker tiles will be installed on the first wall of the JET device in Culham, UK in order to determine the erosion grade of the wall after the experimental fusion campaigns.

At the beginning of the year 2010 were received a lot of 23 marker tiles in order to be coated. At NILPRP, Elementary Processes in Plasma and Applications group was organized the production flux in order to perform the coatings in the best conditions. The form and the dimensions of the marker tiles were analyzed carefully in order to design and manufacture the jiggings devices to ensure a uniform coating. The Ni and Be coatings were realized during 6 production runs, fulfilling the quality and production documentation. Were performed thickness and adherence measurements on the witness samples deposited in the same deposition runs as the marker tiles. Were carried out the documentations concerning the transfer of beryllium marker tiles and was obtained the needed authorization delivered by the Romanian Authority which control the activities in connection with the use of nuclear materials. The lot of 23 marker tiles was delivered to the JET, Culham and we received the confirmation that the tiles arrived in good conditions. Total number of marker tiles sent to JET: 45

Marker coatings using thermionic vacuum arc method

Due to the requirement to coat uniformly larger surfaces, a new thermionic vacuum arc (TVA) setup was developed. It uses cylindrical symmetry evaporating TVA guns for both beryllium and nickel, as seen in Fig. 1. The beryllium has been evaporated without a special crucible, being heated by the TVA electron beam at the upper surface. The bottom part of the anode was cooled by a water cooled stainless steel holder. The evaporation of this kind of anode reduces to zero the contamination of the growing layer. The deposition rates were of 3 - 7 nm/s for Be and 1 - 1.5nm/s for Ni. Nickel was evaporated using a TiB_2 crucible. The ions generated inside the plasma have been accelerated using a bias voltage source having a value of -700V and 10-15 mA current.

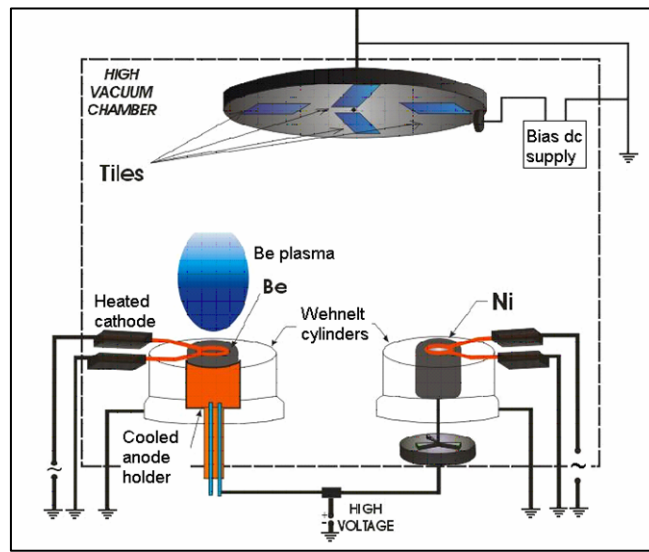


Fig. 1 Beryllium and Nickel coating TVA setup

The activities for the qualification of the thermionic vacuum arc method in order to produce beryllium heavy metal started in 2008, producing Be/Ni test-samples. Parallelepiped shaped test samples made of stainless steel were coated with a Ni layer of $2\pm 0.5\mu\text{m}$ and then a Be layer of 7-9 μm .

In this purpose there have been adapted the coating equipment resulting in redesigning and manufacturing of the revolving oven for substrates' heating during coating. It was redesigned and manufactured within "Elementary Processes in Plasma and Applications" laboratory. For the revolving system trimming and for markers' efficient coating there has been made a stainless

steel plate with clipping devices for simultaneous coatings of 3 “marker” plates of 60mm x 100mm x 30mm, each of them containing 60 stainless steel elements replaceable with Beryllium elements, brought by the JET (Culham) collaborators for TVA deposition method qualification.

Production runs

The parameters used in the sequential deposition of Ni ($2 \pm 0.5 \mu\text{m}$) and Be (6-9 μm) processes were recorded and Technological records, produced for the every run. An example of the coating processes parameters is presented below:

Nickel Coating

- Cathode filament heating: Vac, 50A
- Oven pressure (target $<5 \times 10^{-5}$ torr): start 5.5×10^{-6} torr, end 4.8×10^{-6} torr
- Tile surface temperature: start 253 °C, end 398 °C
- DC discharge Supply: Vdc = +1500V, Idc= 1.33A
- DC bias Supply : Vdc = -700V , Idc= 15mA
- Ni coating time: 40 min
- Thickness reading on QMB: 1.719~2 μm

Beryllium Coating

- Cathode filament heating: Vac, 53.4 A
- Oven pressure (target $<5 \times 10^{-5}$ torr): start 3.8×10^{-6} torr, end 3.6×10^{-6} torr
- Tile surface temperature: start 370 °C, end 380 °C
- DC discharge Supply : Vdc= 1350 V, Idc= 870 mA
- DC bias Supply : Vdc = - 700 V, Idc= 10 mA
- Length of time for Be coating time: 40 min
- Thickness reading on QMB: 6.110~7.5 μm (equivalent with 8.1 – 8.5 7.5 μm)

An example of two marker tiles **F70100061** and **F70100107** before and after coatings are shown in Fig. 2 and 3.

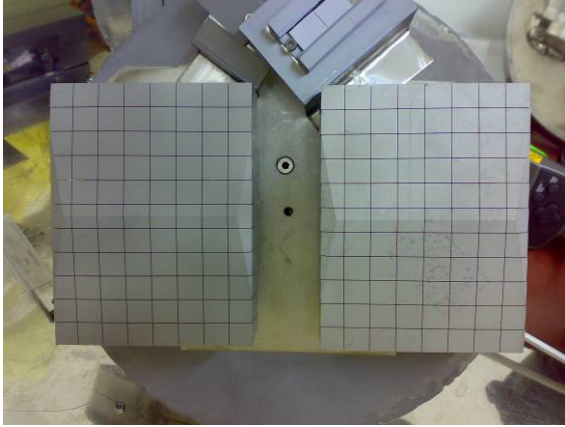


Fig. 2 Photograph of two marker tiles before deposition (IMG_2288)

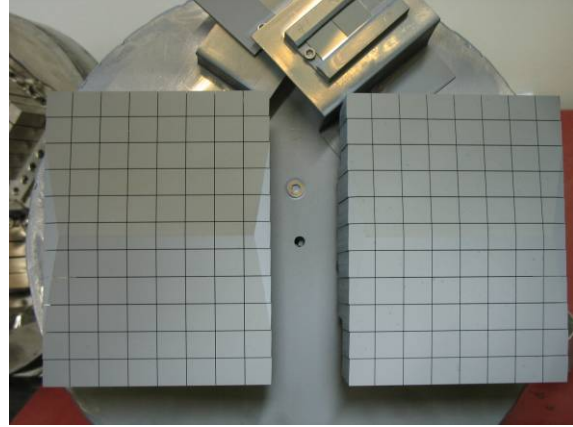


Fig. 3 Photograph of two marker tiles after Ni/Be deposition (IMG_3623)

PRODUCTION-Run 1

This way, the 22 beryllium tiles were coated with 2-3 μm Ni and 7-9 μm Be. The scratch adherence tests inferred the good adhesion of the coated layers. Thickness measurements were performed by JET staff (Paul Coad and Anna Widdowson) using IBA technique. An example of the film thickness distribution along the middle of the marker tile (F70100060) surface is presented in Fig. 4

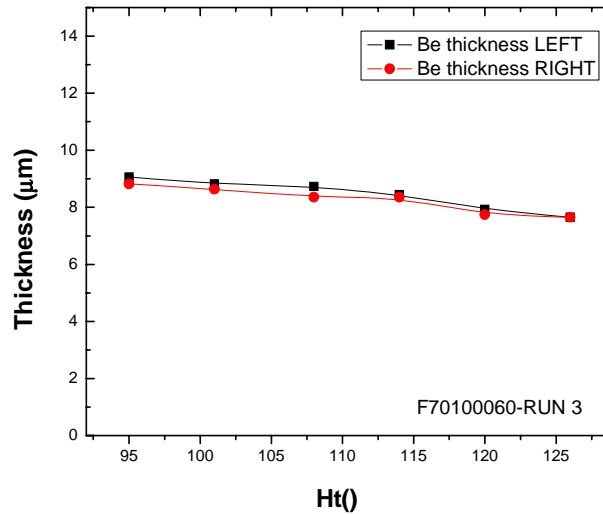


Fig. 4 Thickness measurement of the Be layer of the marker tile F70100060

After the coatings, the marker tiles were double heat sealed, packed in carton crates and put together in a wooden box. The plastic bag surfaces, carton crates and wooden box were smeared in order to characterize the beryllium contamination. After receiving the negative smear tests tiles were sent to JET site by a carrier company managed by JET –CCFE.

In 2010 a lot of 23 beryllium marker tiles were coated with Ni and Be using the same parameters of the thermionic vacuum arc method.

An example of an efficient loading of the heating oven is presented in Fig. 5 and 6.
(marker tiles: F70201024/293, F70201026/103, F70201026/335, F70201025/463, F70201025/458, F70201026/082, F70201026/293, F70201024/290)

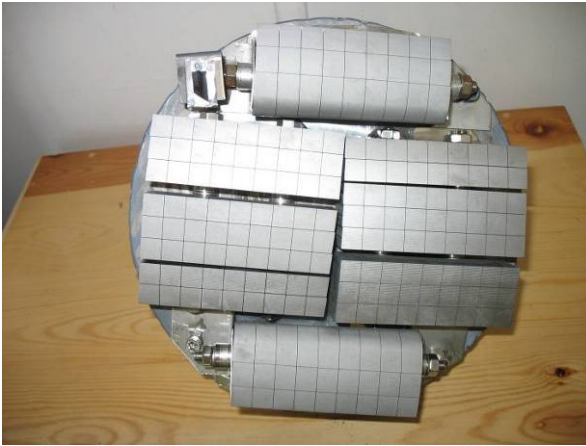


Fig. 5 Photograph of two marker tiles before deposition

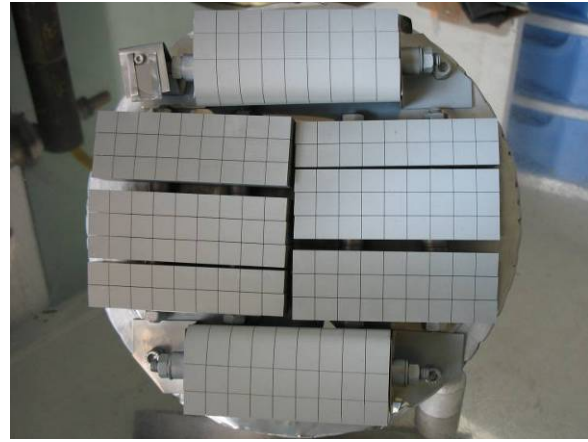


Fig. 6 Photograph of of two marker tiles after Ni/Be deposition

PRODUCTION-Run 4

After coatings, the tiles were double heat sealed; packed in carton crates and put together in a wooden box. The plastic bag surfaces, carton crates and wooden box were smeared and the smear products (25 mm paper filters) were sent to NFC-Pitesti in order to analyzed the Be contamination. The results of the measurements show the Be content under the detection limit ($< 0.1 \mu\text{g}/\text{filter}$). The marker tiles lots were accompanied by the requested documents: Technological records, Packing list for Consignment to JET, Certificate of Conformity for Consignment to JET (marker tiles), Invoices.

Conclusion

Thermionic vacuum arc (TVA) method was used to obtain thin film layers of 2-3 μm Ni and 7-9 μm Be for coating on a number of **45 marker tiles** (two lots), as part of the ITER-like fusion reactor wall. By TVA method were evaporated from two different sources Nickel and Beryllium materials, without opening the vacuum chamber between the two deposition processes. The control of the ion energy and of the electron flux by handling the exterior plasma parameters ensured realization of dense Ni and Be layers, similar to the bulk materials used for the ITER-like Wall beryllium block tiles.

The original findings during the project accomplishment were published in scientific journals [1-5].

References

- [1] C. P. Lungu, I. Mustata, V. Zaroschi, A. M. Lungu, A. Anghel, P. Chiru, M. Rubel, P. Coad G. F. Matthews and JET-EFDA contributors, Beryllium Coatings on Metals: Development of Process and Characterizations of Layers, Phys. Scr. T128 (March 2007) 157–161
- [2] C. P. Lungu, I. Mustata, V. Zaroschi, A. M. Lungu, P. Chiru, A. Anghel, G. Burcea, V. Bailescu, G. Dinuta, F. Din, Spectroscopic study of beryllium plasma produced by thermionic vacuum arc Vol. 9, Iss. 4, 2007, J OPTOELECTRON ADV M, Vol. 9, No. 4, 2007, 884-886.
- [3] T. Hirai, J. Linke, M. Rubel, J.P. Coad, J. Likonen, C.P. Lungu, G.F. Matthews, V. Philipps, E. Wessel and JET-EFDA contributors, Thermal load testing of erosion-monitoring beryllium marker tile for the ITER-LikeWall Project at JET, Fusion Engineering and Design, Fusion Engineering and Design, Volume 83, Issues 7-9, December 2008, Pages 1072-1076.
- [4] Cristian P. LUNGU, Ion MUSTATA, Alexandu ANGHEL Corneliu POROSNICU, Ionut JEPU, Catalin TICOS Ana M. LUNGU, Mihai GANCIU, Arcadie SOBETKII Gheorghe HONCIUC and Patrick CHAPON Preparation and Characterization of Multifunctional, Nanostructured Coatings Using Thermionic Vacuum Arc Method, Frontier of Applied Plasma Technology (Edited by Osaka University, Japan), Vol.2 July 2009, pp1-6.
- [5] C. P. Lungu, J. Likonen, C. Porosnicu, A. Anghel, I. Jepu, V. Zaroschi, A. M. Lungu, P. Chiru, I. Mustata, SIMS analysis of beryllium films prepared by TVA method, SOFT Conference, September 2010, Porto, Portugal

National Research and Development Institute for Cryogenics and Isotopic Technologies

National Institute for Laser, Plasma and Radiation Physics

SCIENTIFIC REPORT

To the Contract 1EU-4/08/08.2008

July-Dec 2010

Project BS-15-N: KM6T Tandem Collimators

Project leader: S. Soare

EFDA-JET Task Agreement: JW9-TA-EP2-TCS-01

Etapa II: Evaluation of the KM6T pre-collimator

S. Soare¹, T. Craciunescu², M. Curuia¹, M. Gherendi², V. Zoita²

¹ National Research and Development Institute for Cryogenics and Isotopic Technologies

² National Institute for Laser, Plasma and Radiation Physics

Introduction

Plasma diagnostics based on the gamma-ray emission spectrometry is one of the important techniques used in the JET tokamak for studying fast ions [1-3]. The intense gamma-ray emission is produced in JET plasma when fast ions (ICRF-driven ions, fusion products, NBI-injected ions) react either with fuel ions or with the main plasma impurities such as carbon and beryllium. Gamma-ray energy spectra have been measured in the JET tokamak with three independent spectrometers looking at the plasma along different lines of sight. Two spectrometers look at the plasma in octant 8 along horizontal and vertical lines of sight. A third one has a vertical line of sight in octant 5. The gamma-rays are continuously recorded in all JET discharges over the energy range 1–28MeV, with an energy resolution of about 4% at 10MeV. The project addresses certain components of the horizontal, quasi-tangential gamma-ray spectrometer (the KM6T gamma-ray spectrometer). More precisely, the present enhancement project (TCS, Tandem Collimator System) deals with the first two components of the upgraded diagnostics line-of-sight, the tandem collimator system (KM6T-TC) for the KM6T tangential gamma-ray spectrometer.

The main aim of the TCS project is to provide a proper collimation for the gamma-ray (BGO) detector of the tangential gamma-ray spectrometer, with a well-defined field of view at the plasma end of the diagnostics line-of-sight. The collimation system should at the same time improve the signal-to-background ratio at the detector end of the line-of-sight.

Tandem collimators

The collimation system was initially developed as a tandem configuration. The main aim of the tandem collimators is to provide a proper collimation for the gamma-ray (BGO) detector of the tangential gamma-ray spectrometer, with a well-defined field of view at the plasma end of the diagnostics line-of-sight. The collimation system should at the same time improve the signal-to-background ratio at the detector end of the line-of-sight.

In order to fulfil these requirements the tandem collimators should:

- Provide an adequate neutron and gamma-ray shielding factor. A value of at least 10^2 is usually required for this factor

- Reduce as much as possible any parasitic gamma-ray sources which may fall within the spectrometer field-of-view.

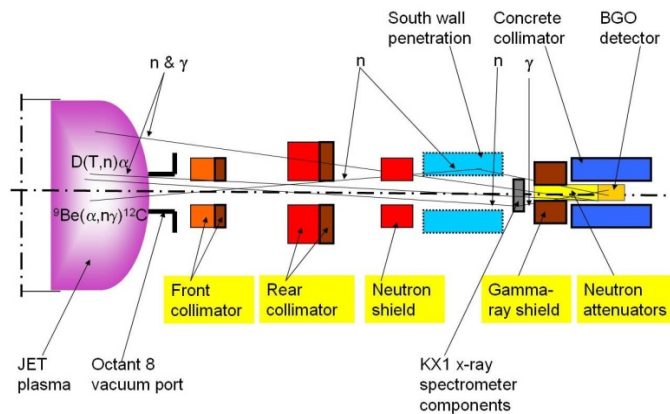


Figure 1 - Schematic representation of the evolution of the KM6T diagnostics configuration

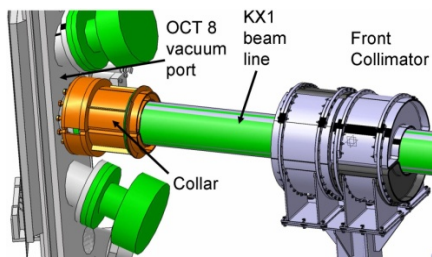


Figure 2 - View of the new system component (the collar) together with the front collimator.

Recently, due to mechanical reasons, the clearance between the front collimator and the KX1 flight tube had to be increased. In order to keep the initial field of view, a third component – a collar (see Fig. 2-3) - is proposed to be inserted in the system. This leads to a request for a new evaluation of the performances of the tandem collimators.

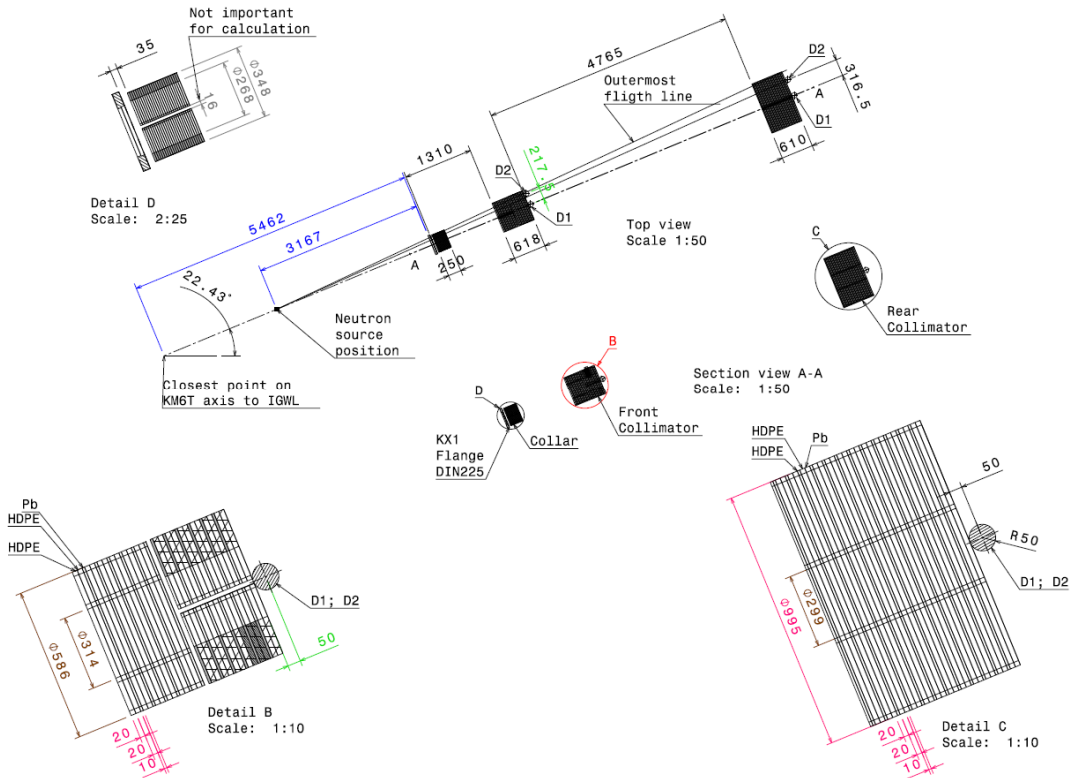


Figure 3 – Updated configuration (CONFIG4-NEW)

KM6T Pre-collimator. Components and Location.

As mentioned earlier, the clearances between the collimators bore and the KX1 flight tube had to be increased. This led to an increment in the field of view determined by the collimators and thus additional sources of parasitic gamma-rays will fall into the field of view. To overcome this, a third object was proposed to be inserted into the system (originally designed as a tandem collimator) called TCS pre-collimator.

The TCS pre-collimator is proposed to be installed on the OCT8 vacuum port flange, clamped onto the KX1 flight tube flange, figure 4. The collimating (for gamma radiation) material will be Pb nuclear grade encased in a steel structure (all welded). Total weight of the pre-collimator is 205kg.

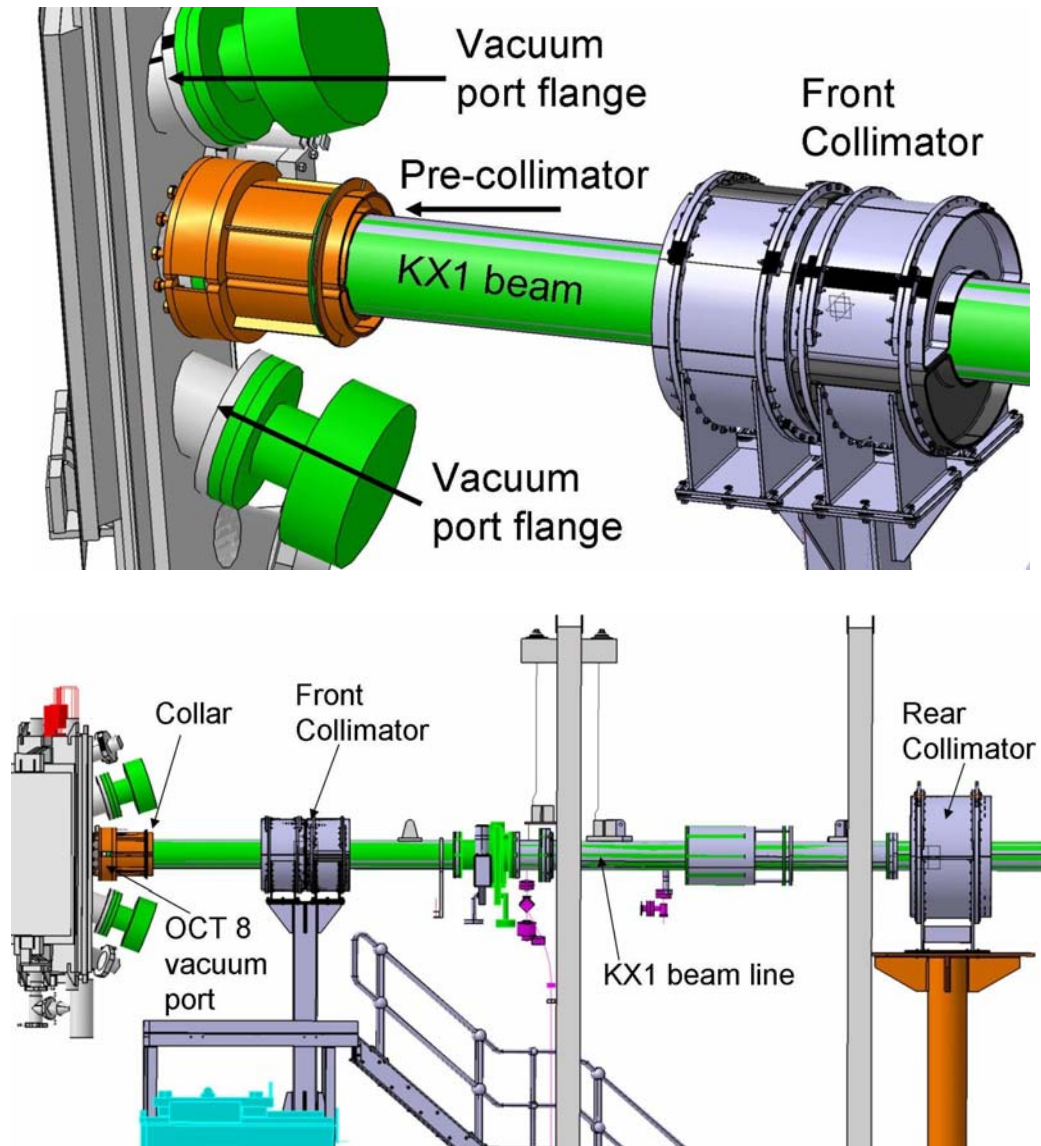


Figure 4 Proposed position of the KM6T pre-collimator

The main components of the pre-collimator are, figure 5:

- collimating material: half rings, Pb nuclear grade
- two identical casings: SS304, all 5mm sheets but clamping parts that are thicker
- connectors: M10 screws
- two flanges

collimator. One detector (cell 87) is placed on the KX1 axis, and the other (cell 88) is placed at the mid-radius of the collimator (216 mm from the axis). Another two detectors were placed behind the rear collimator, with their centre in a plane at a distance of 50 mm behind the rear face of the collimator. One detector (cell 85) is placed on the KX1 axis, and the other (cell 86) is placed at the mid-radius of the rear collimator (403.5 mm from the axis). The front collimator made up of 12 alternating polyethylene (thickness 40 mm) and lead (thickness 10 mm) plates. A polyethylene plate is placed at the front face of the front collimator. The rear collimator made up of 12 alternating polyethylene (thickness 40 mm) and lead (thickness 10 mm) plates. The rear collimator has an additional 10 mm lead plate at the rear face. A polyethylene plate is placed at the front face of the rear collimator.

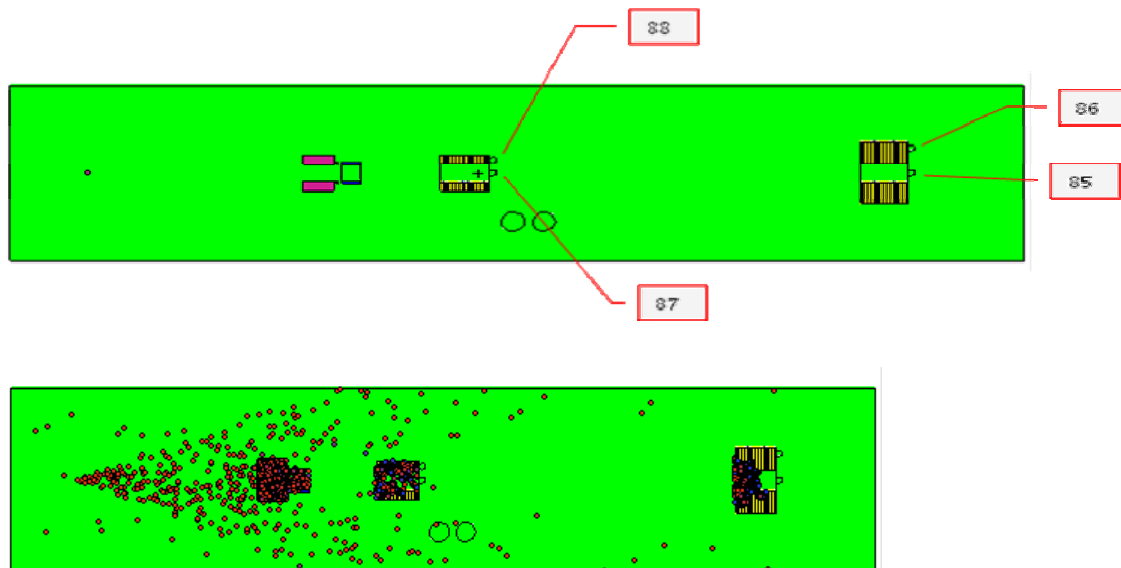


Figura 8 – MCNP simplified geometry

The neutron and photon transport calculations the radiation sources, approximated by point sources, have specific positions:

- a point neutron source placed at the intersection of the KX1 axis with the (vertical projection of) magnetic axis. This is at a distance of 4.512 m from the front face of the front collimator. The point neutron source has a Gaussian shape neutron spectrum with the mean energy at $E_0 = 2.45$ MeV and a full width at half maximum (FWHM) of 0.5 MeV.

- a point photon (gamma-ray) source placed at the intersection of the KX1 axis with a plane perpendicular to the surface of the inner wall guard limiter in Octant 2. This is at a distance of 6.807 m from the front face of the front collimator. The 9 MeV gamma-ray line corresponds to the most intense nickel neutron capture gamma-ray line expected.

In order to reduce the computation time, the propagation space was limited to a reduced solid angle (see again Fig. 6). This conical collimation preferentially biases the emission of particles in the desired direction. The angle subtended by the front face of the front collimator was increased using a factor of 5.0 in order to avoid biasing of the evaluated tally.

In this geometry the numerical simulations provided, at the detector positions, the integrated neutron and photon fluxes and also neutron and photon spectra. The shielding characteristics of the tandem collimators were defined in terms of a shielding factor, which is the ratio of the radiation fluxes in two detectors: one placed on the axis of the system and another placed behind the collimators, at a mid-radius position.

The evaluation performed for DD discharges (2.5 MeV neutron emission) is reported in comparison with the evaluation obtained for the previous configuration. The energy distribution of the neutrons reaching the detectors was calculated in 8 energy bins. The energy distribution for both neutrons and neutron induced gamma rays, at the location of the virtual detectors are presented in Fig. 9. The shielding characteristics of the tandem collimators is defined in terms of a shielding factor, which is the ratio of the radiation fluxes in the two detectors placed behind the collimators. The fluxes at the location of the virtual detectors and the shielding factors are listed in Table 1.

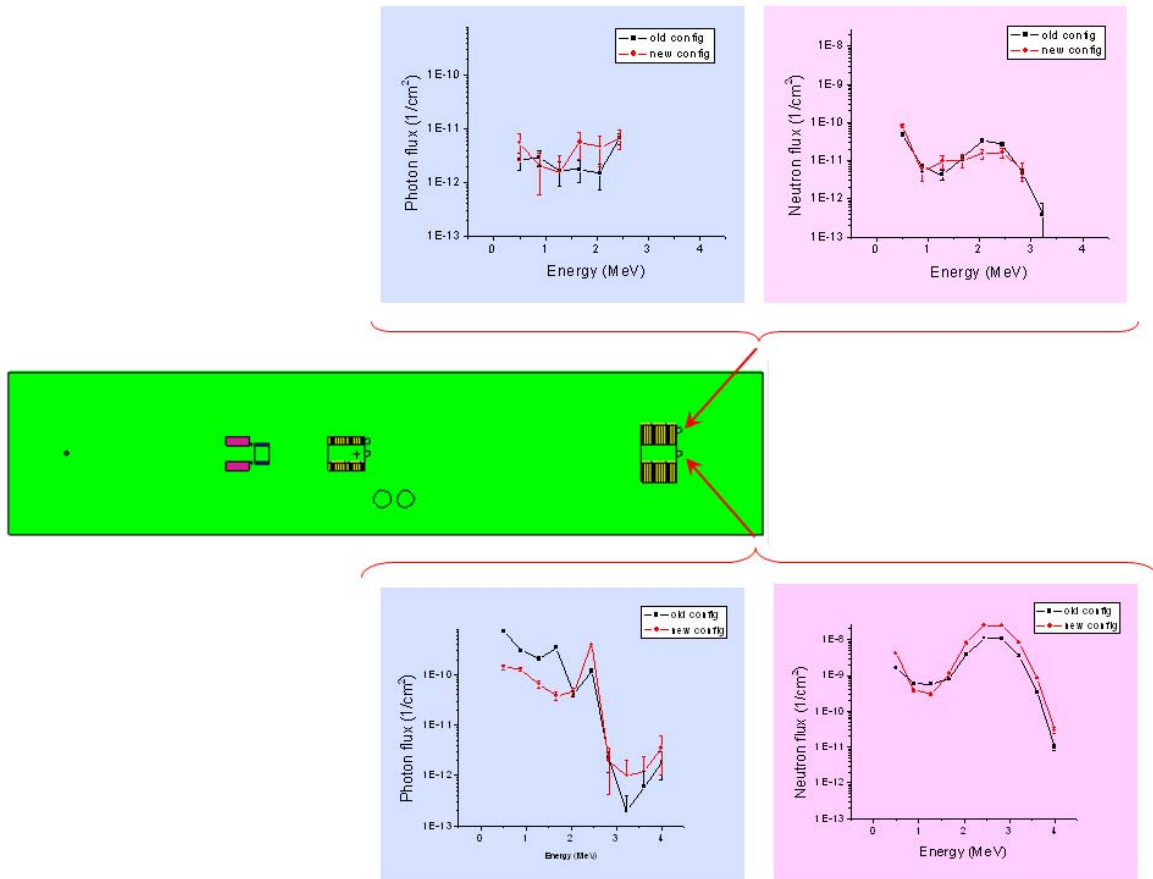


Figure 9- Neutron and photon induced spectra and at locations of the virtual detectors.

Table 1 – MCNP results obtained for DD discharges (2.5 MeV neutron emission) for the old (right) and new (left) configuration.

Old configuration			New configuration		
Rear collimator			Rear collimator		
n in 85	$(3.39 \pm 0.01)E-08$	$n(85/86) = 246 \pm 5$	n in 85	$(7.33 \pm 0.03) E-08$	$n(85/86) = 509 \pm 12$
n in 86	$(1.38 \pm 0.07)E-10$		n in 86	$1.44 \pm 0.10)E-10$	
p in 85	$(1.65 \pm 0.02)E-09$	$p(85/86) = 96 \pm 14$	p in 85	$(8.22 \pm 0.34)E-10$	$p(85/86) = 31 \pm 4$
p in 86	$(1.71 \pm 0.25)E-11$		p in 86	$(2.63 \pm 0.60)E-11$	
Front collimator			Front collimator		
n in 87	$(1.54 \pm 0.01)E-07$	$n(87/88) = 19 \pm 1$	n in 87	$(3.23 \pm 0.01)E-07$	$n(87/88) = 23 \pm 1$
n in 88	$(7.94 \pm 0.05)E-09$		n in 88	$(1.01 \pm 0.01)E-08$	
p in 87	$(7.39 \pm 0.05)E-09$	$p(87/88) = 5 \pm 1$	p in 87	$(2.76 \pm 0.60)E-09$	$p(87/88) = 3 \pm 0.5$
p in 88	$(1.53 \pm 0.02)E-09$		p in 88	$(1.08 \pm 0.04)E-09$	

The 9 MeV gamma-ray line corresponds to the most intense nickel neutron capture gamma-ray line expected to be emitted by the INCONEL support of the IWGL. For its propagation the energy distribution of the photons reaching the detectors is calculated in 10 energy bins. The photon energy distribution is shown in Fig. 8 and the shielding factors are presented in Table 2. It can be seen from this figure that the transmission of the 9 MeV photons through the tandem collimator structure has been reduced by at least two orders of magnitude.

Table 2 - MCNP results obtained for the 9 MeV parasitic gamma-ray line.

Rear collimator		
p in 85	$(3.03 \pm 0.01)E-08$	$p(85/86) = 464 \pm 50$
p in 86	$(6.53 \pm 0.70)E-11$	
Front collimator		
p in 87	$(9.61 \pm 0.02)E-08$	$p(87/88) = 45 \pm 0.7$
p in 88	$(2.13 \pm 0.03)E-09$	

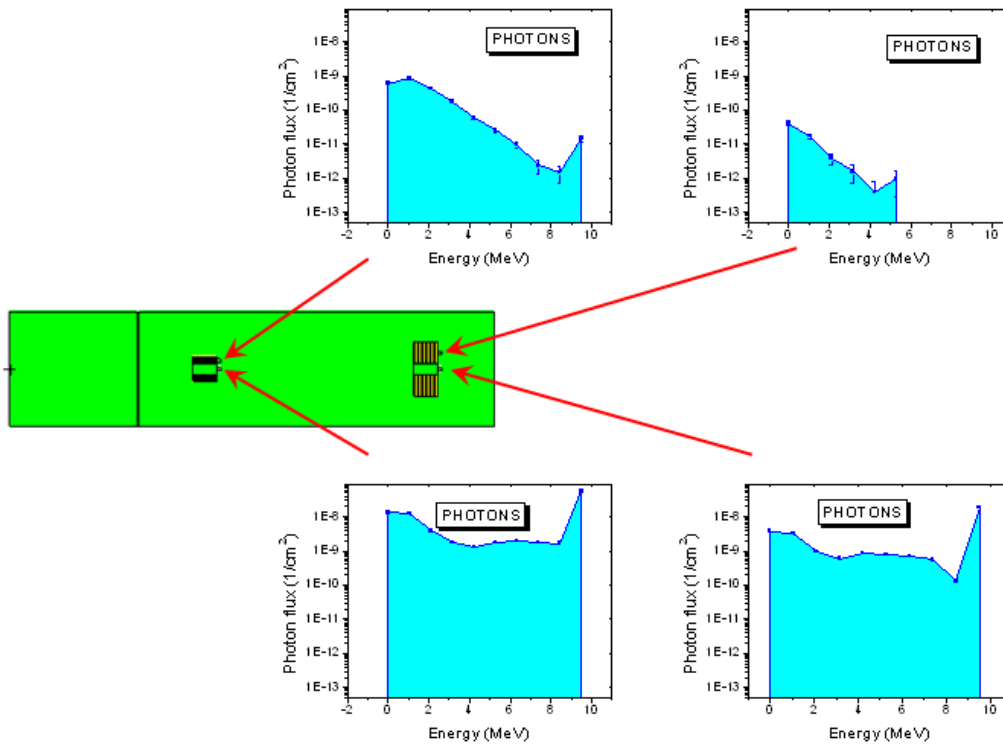


Figure 8 – Parasitic photon spectra and at locations of the virtual detectors.

Conclusion

The tandem collimators designed for the JET TGRS were evaluated by means of MCNP calculations. The final configuration developed for deuterium discharges provides improved shielding factors of about 500 for 2.45 MeV neutrons. For neutron-capture photons induced within the collimation structure the shielding factor decreased 3 times (~30 instead of ~90). For the parasitic gamma-ray line of 9 MeV the shielding factor is ~450. The results prove that the tandem collimators are able to restore and improve the radiation protection offered by the KJ5 radiation shield (X-ray camera) removed at the 2004 JET shut-down.

References

- [1] V.G. Kiptily , F.E. Cecil, O.N. Jarvis , M.J. Mantsinen, S.E. Sharapov, L. Bertalot, S. Conroy, L.C. Ingesson, T. Johnson, K.D. Lawson, S. Popovichev, *γ-ray diagnostics of energetic ions in JET*, Nucl. Fusion 42(2002)999.

- [2] O.N. Jarvis, J Adams, P.J.A. Howarth, F.B. Marcus, E. Righi, G.J. Sadler, D.F.H. Start, P. Van Belle, C.D. Warrick, N. Watkins, *Gamma ray emission profile measurements from JET ICRF-heated discharges*, Nucl. Fusion, 36(1996) 1513.
- [3] V. G. Kiptily, Yu. F. Baranov, R. Barnsley, L. Bertalot, N. C. Hawkes, A. Murari, S. Popovichev, S. E. Sharapov, D. Stork, V. Yavorskij, *First Gamma-Ray Measurements of Fusion Alpha Particles in JET Trace Tritium Experiments*, Phys. Rev. Lett. 93(2004)115001.